Gene Regulatory Network in Schwann cell Disorders

Marta Palomo Irigoyen

2020

Gene Regulatory Network in Schwann cell Disorders

Marta Palomo Irigoyen 2020

CIC bioGUNE
CENTER FOR COOPERATIVE RESEARCH IN BIOSCIENCES

EXCELENCIA SEVERO OCHOA

UPV EHU

eman ta zabal zazu
Universidad del País Vasco
Euskal Herriko Unibertsitatea

eman ta zabal zazu

Universidad del País Vasco
Euskal Herriko Unibertsitatea

Departamento de Neurociencias

Gene Regulatory Network in Schwann cell Disorders

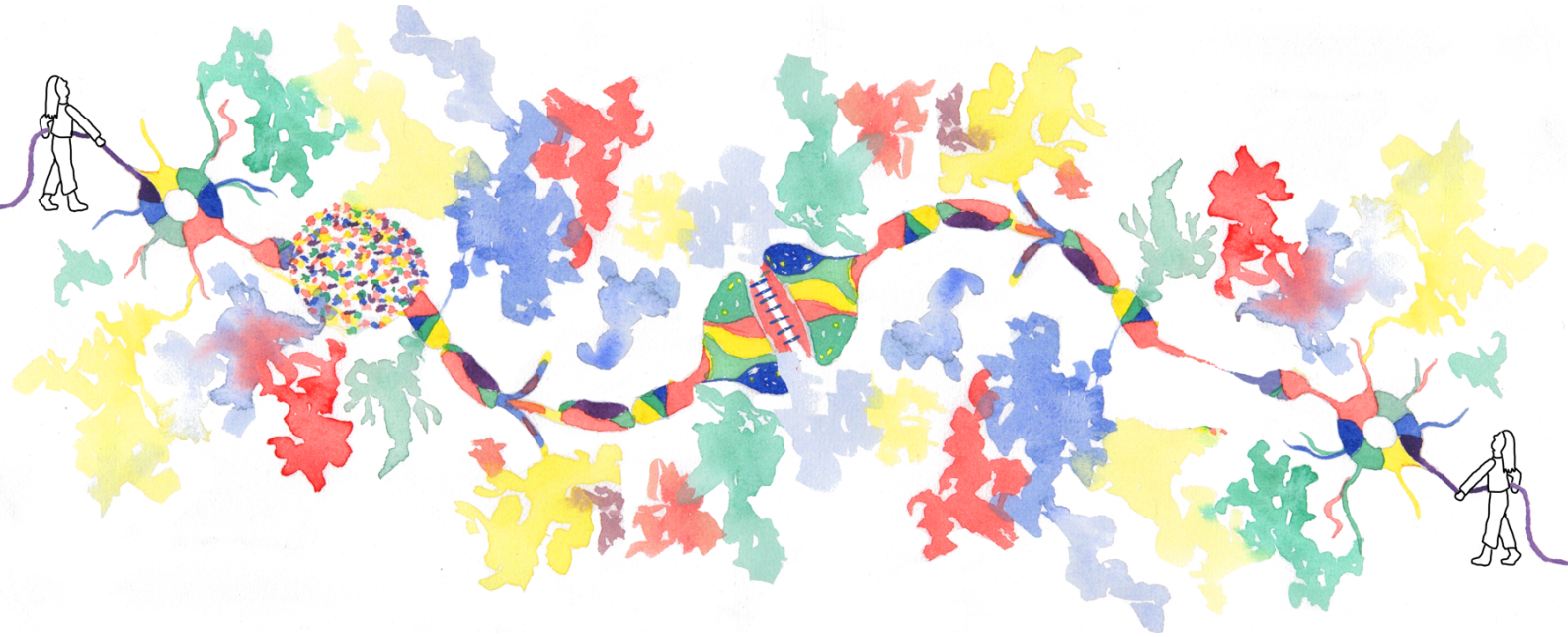

Marta Palomo Irigoyen

Supervisors: Ashwin Woodhoo, José María Mato

2020

On the cover: *Representation of Malignant Peripheral Nerve Sheath Tumour, derived from Schwann cells (represented as colorful dots mimicking aberrant tumour growth) (left) (see chapter 2) and representation of peripheral nerves demyelination (right), that could be due to a wide range of conditions, including pathogen-mediated infections, in this case Borrelia burgdorferi-induced demyelination (see chapter 3). Colorful spots represent systemic immune system activation, except in the area around B. burgdorferi-mediated demyelination.*
(Ilustration painted by Nagore Vitallé).

Live, because life is flying away so fast like a nerve impulse

Theodor Schwann

Jakin-minak mugiarazten duen horrentzat, aztertu nahi duten horientzat

Para todo aquel que se mueva por la curiosidad, para todo aquel que quiera descubrir

Financial Support

The doctoral candidate is grateful for the support of the following grants achieved for this work: Predoctoral grant from the Basque Government, CIC bioGUNE research associate contract, Boehringer Ingelheim travel grant and Severo Ochoa travel grant.

Experimental work has been funded by grants from Spanish Association Against Cancer (AECC; JP Vizcaya), MCIU/AEI/FEDER, EU (Subprograma Ramon y Cajal RYC2010-06901; Proyectos Retos Investigacion RTI2018-097503-B-I00, SAF2015-65360-R; Proyectos Explora Ciencia SAF2015-72416-EXP; Proyectos Europa Excelencia SAF2015-62588-ERC), the BBVA foundation, Basque Department of Industry, Tourism and Trade (Elkartek) and Education (PI2013-46), and Fundación Vasca de Innovación e Investigación Sanitarias EiTB Maratoia (BIO13/CI/015).

Scientific contributions

Results obtained in this doctoral thesis, explained hereafter, have been presented in several scientific meetings either national or international congresses. Publications produced during these years are highlighted below:

Publications

✓ **Marta Palomo-Irigoyen,** Encarni Pérez-Andrés, Marta Iruarrizaga-Lejarreta, Marta Varela-Rey, Adrián Barreira-Manrique, Miguel Tamayo-Caro, Nagore Beitia, Daniela Medrano, Juan José Lozano, Satoshi Okawa…Ashwin Woodhoo. RNA-binding protein HuR/ELAVL1 amplifies multiple oncogenic programs essential for Malignant Peripheral Nerve Sheath Tumour growth and metastasis. *J Clin Invest*, **2020**, pii: 130379.

✓ Daniela Mestre, Francisco González-Romero, Igor Aurrekoetxea, Colm J. Ó Rourke, Jesper B. Andersen, Ashwin Woodhoo, Miguel Tamayo-Caro, Marta Varela-Rey, **Marta Palomo-Irigoyen**, Beatriz Gómez-Santos…Patricia Aspichueta. E2F2 is a metabolic driver that mediates nonalcoholic fatty-liver disease development and progression to hepatocarcinogenesis. *J Hepatology, **submitted***.

✓ **Marta Palomo-Irigoyen**, Encarni Pérez-Andrés, Adrián Barreira-Manrique, Nicolás Navasa, Hector Rodriguez, Aize Pellon, Miguel Tamayo-Caro, Marta Varela-Rey, Monika González-Lopez, Nuria Macías-Cámara, Elsa González…Juan Anguita, Ashwin Woodhoo. *Borrelia burgdorferi* bacterium: a direct inducer of Schwann cells demyelination. ***In preparation***.

✓ **Marta Palomo Irigoyen**, Miguel Tamayo-Caro, Encarnacion Pérez Andrés, Adrián Barreira Manrique, Marta Varela Rey and Ashwin Woodhoo. Isolation and purification of primary rodent Schwann cells. Methods in Molecular Biology "Myelin". *Springer Protocols*, **2018**, 81-93.

✓ Miguel Tamayo Caro, **Marta Palomo Irigoyen**, Encarnacion Pérez Andrés, Adrián Barreira Manrique, Marta Varela Rey and Ashwin Woodhoo**.** Analyzing autophagic flux in nerve cultures**.** Methods in Molecular Biology "Myelin". *Springer Protocols*, **2018**, 193-206.

✓ Jose A. Gomez-Sanchez, Lucy Carty, Marta Iruarrizaga-Lejarreta, **Marta Palomo-Irigoyen**, Marta Varela-Rey, Megan Griffith, Janina Hantke, Nuria Macias-Camara, Mikel Azkargorta, Igor Aurrekoetxea… Ashwin Woodhoo and Kristján R. Jessen. Schwann cell autophagy, myelinophagy, initiates myelin clearance from injured nerves. *J Cell Biol*, **2015**, 210, 153-168.

*This publication is commented in J Cell Biol by Dr. Michael Thumm (University of Göttingen) and Dr. Mikael Simons (Max Planck Institute of Experimental Medicine) in: Myelinophagy: Schwann cells dine in. (J Cell Biol, **2015**; 210, 9-10).*

Participation in congresses

✓ **VIBes in Biosciences**. **Marta Palomo-Irigoyen,** Encarni Pérez-Andrés, Adrián Barreira-Manrique, Miguel Tamayo-Caro, Marta Varela-Rey and Ashwin Woodhoo. *Borrelia burgdorferi* bacterium: a direct inducer of Schwann cells demyelination. Poster 50, Leuven, Belgium, **2020.**

✓**ASEMV** (American Society for exosomes and Microvesicles). Participation as part of Prof. Randy Schekman's lab. Pacific Grove, California, USA. **2019.**

✓**MikrobioGUNE** (1st Basque Microbiology Meeting). **Marta Palomo-Irigoyen,** Encarni Pérez-Andrés, Marta Iruarrizaga-Lejarreta, Adrián Barreira-Manrique, Miguel Tamayo-Caro, Marta Varela-Rey and

Ashwin Woodhoo. The *Borrelia burgdorferi* bacterium: a novel contact-dependent inducer of peripheral nerve demyelination. Flash communication and Poster, BM03. Bilbao, Spain, **2018**.

✓**Neurogune** (Basque Neuroscience meeting). **Marta Palomo-Irigoyen,** Encarni Pérez-Andrés, Marta Iruarrizaga-Lejarreta, Adrián Barreira-Manrique, Miguel Tamayo-Caro, Marta Varela-Rey and Ashwin Woodhoo. The *Borrelia burgdorferi* bacterium: a novel contact-dependent inducer of peripheral nerve demyelination. Poster, T2-28. Vitoria, Spain, **2018**.

✓**Neurogune** (Basque Neuroscience meeting). **Marta Palomo-Irigoyen,** Encarni Pérez-Andrés, Marta Iruarrizaga-Lejarreta, Adrián Barreira-Manrique, Miguel Tamayo-Caro, Marta Varela-Rey and Ashwin Woodhoo. The RNA-binding protein HuR/Elavl1 controls a core transcriptional regulatory circuity essential for MPNST growth and metastasis. Poster, T2-29. Vitoria, Spain, **2018**.

✓**Neurogune** (Basque Neuroscience meeting). **Marta Palomo-Irigoyen,** Marta Iruarrizaga-Lejarreta, Marta Varela-Rey and Ashwin Woodhoo. The RNA-binding protein HuR/Elavl1 controls a core transcriptional regulatory circuity essential for MPNST growth and metastasis. Poster, IDO05. Bilbao, Spain, **2016**.

✓**Euroglia** (XII European Meeting on Glial Cells in Health and Disease). **Marta Palomo-Irigoyen,** Marta Iruarrizaga-Lejarreta, Marta Varela-Rey and Ashwin Woodhoo. *The RNA-binding protein HuR/Elavl1 controls a core transcriptional regulatory circuity essential for MPNST growth and metastasis.* Poster, T17-04B. Bilbao, Spain, **2015**.

Participation in research projects

- Role of post-translation modifications in Swann cell myelination and demyelination, and in peripheral nervous system regeneration (*Spanish Ministry of Science and Innovation, Universities. RTI2018-097503-B-I00, 01/01/2019 - 31/12/2021. Head of research: Ashwin Woodhoo, CIC bioGUNE, Spain*).

- Dissecting the master regulatory control of Schwann cell reprogramming. (*Spanish Ministry of Economy, projects "I+D+I Retos" SAF2015-65360-R, 01/01/2016 - 3/12/2018. Head of research: Ashwin Woodhoo, CIC bioGUNE, Spain*).

- The *Borrelia burgdorferi* bacterium: a novel contact-dependent inducer of peripheral nerve demyelination. (*Spanish Ministry of Economy, projects "Explora Ciencia" SAF2015-72416-EXP", 06/2016 - 30/05/2018. Head of research: Ashwin Woodhoo, CIC bioGUNE, Spain*).

- Role of the histone methyltransferase Ezh2 in Schwann cell reprogramming. (*BBVA, 01/10/2015 - 30/11/2016. Head of research: Ashwin Woodhoo, CIC bioGUNE, Spain*).

- Identifying the master regulatory signal that initiates Schwann cell reprogramming. (*Spanish Ministry of Science and Innovation, Universities. SAF2015-62588-ERC, 01/08/2015 - 30/09/2016. Head of research: Ashwin Woodhoo, CIC bioGUNE, Spain*).

- The role of autophagy in Schwann cells dedifferentiation and axon regeneration. (*Instituto de Salud Carlos III PFIS (PI12/00005), 01/01/2013 - 31/12/2015. Head of research: Ashwin Woodhoo, CIC bioGUNE, Spain*).

- The role of the RNA binding protein HuR (Elavl1) in MPNST (Malignant Peripheral Nerve Sheath Tumors). (*Dept. of Education of the Basque Government, 01/2013 - 12/2015. Head of research: Ashwin Woodhoo, CIC bioGUNE, Spain*).

Research stay

Visiting scholar at Prof. Randy Schekman's Nobel laureate laboratory (UC Berkeley, California, USA) for 3 months, in 2019.

Collaborations (Research projects not included in the thesis)

🔎 E2F2 is a metabolic driver that mediates nonalcoholic fatty-liver disease development and progression to hepatocarcinogenesis. (*Principal Investigator*: *Patricia Aspichueta, Universidad del País Vasco/Euskal Herriko Unibertsitatea UPV/EHU).*

🔎 Role of secretome and mesenchymal stem cells derived-exosomes in sciatic neuropathy (*Principal Investigator: Maria Vega Villar, Universidad de León).*

🔎 Deciphering RBPMS role in normoxic and hypoxic conditions in retinal ganglion cells (*Principal Investigator: Elena Vecino, UPV/EHU*).

🔎 Guanine-7 methylation of RNA in stem cells and prostate cancer (*Principal Investigator: Sandra Blanco, Centro de Investigación del Cancer, Universidad de Salamanca-CSIC*).

🔎 Extracellular vesicles derived from primary human epidermal keratynocites and human dermal fibroblasts promote migration of skin cells (*Principal Investigator: Arup Indra, Oregon State University*).

Table of Contents

LIST OF FIGURES

Chapter 1

Chapter 2

Chapter 3

LIST OF TABLES

Chapter 2

Chapter 3

ABBREVIATIONS

3´-UTR	3´-untranslated region
5´-UTR	5´-untranslated region
AAALAC	Assessment and Accreditation of Laboratory Animal Care
AC	Adenylate cyclase
ACA	Acrodermatitis chronica atrophicans
ADS	Antibody diluyent solution
AMP	Adenosine monophosphate
ANOVA	Analysis of variance
APC	Allophycocyanin
AraC	Cytosine arabinoside
ATP	Adenosine triphosphate
ATCC	American Type Culture Collection
AU	Adenylate/uridylate
Bb	*Borrelia burgdorferi*
BCA	Bicinchoninic acid
BDNF	Brain-derived neurotrophic factor
BosR	Borrelia oxidative stress regulator
BrdU	5-bromo-2-deoxyuridin
BSA	Bovine serum albumin
BSK-H	Barbour-Stoenner-Kelly
cAMP	3´-5´-cyclic adenosine monophosphate
Cdk	Cyclin-dependent kinase
Cdk1	Cyclin dependent kinase 1
CD11b	Macrophage-1 antigen (Mac-1)
CD14	Cluster of differentiation 14
CD204	Scavenger receptor-A
CD45	Protein tyrosine phosphatase receptor type C
CD64	Cluster of differentiation 64
CHAPS	3-[(3-Cholamidopropyl)dimethylammonio]-1-propanesulfonate
CHIP	Cromatin immunoprecipitation
CIC	Collision-induced dissociation
CMT4D	Charcot Marie Tooth disease type 4 D
CNS	Central Nervous System
CREB	cAMP response element
CSF	Cerebrospinal fluid
DAPI	4 ',6-diamino-2-fenilindol
db cAMP	N^6,2'-O-Dibutyryladenosine 3',5'-cyclic monophosphate
DCAR1	Dendritic cell activating receptor
Dhh	Desert hedgehog
DMEM	Dulbecco's Modified Eagle Medium
DMSO	Dimethyl sulfoxide
DNA	Deoxyribonucleic acid

DRG	Dorsal root ganglia
DTT	Dithiothreitol
ECL	Enhanced chemiluminescent
EDTA	2,2',2'',2'''-(Ethane-1,2-diyldinitrilo)tetraacetic acid
EDU	5-ethynyl-2'-deoxyuridine
EGFR	Epidermal growth factor receptor
ELAV	Embryonic lethal abnormal vision
ELISA	Enzyme-Linked Immunosorbent Assay
FA	Formic acid
FBS	Fetal bovine serum
FDA	Food and Drug Administration
FITC	Fluorescein isothiocyanate
GalC	Glycolipid galactocerebroside
GAPDH	Glyceraldehyde 3-phosphate dehydrogenase
GDNF	Glial cell line-derived neurotrophic factor
GFAP	Glial fibrillary acidic protein
GFP	Green fluorescent protein
GPI	Glycosylphosphatidylinositol
HGFR	Hepatocyte growth factor receptor
HIF	Hypoxia-inducible factor
HNS	Nucleo-cytoplasmic shuttling domain
HRP	Horseradish peroxidase
HuR	Human antigen R
IA	Iodoacetamide
iSC	Immature Schwann cell
ICC	Immunocytochemistry
IgG	Immunoglobulin G
IGF	Insulin growth factor
IgM	Immunoglobulin M
IHC	Immunohistocehistry
Il-1β	Interleukin 1β
Il-6	Interleukin 6
IP	Immunoprecipitation
IPL	Interperiod lines
IRES	Internal ribosome entry sites
KD	Knockdown
LC-MS	Liquid chromatography–mass spectrometry
LC3	Microtubule-associated protein 1A/1B-light chain 3
LPS	Lipopolysaccharide
MAG	Myelin associated glycoprotein
MAPK	Mitogen-activated protein kinase
MARCO	Macrophage receptor with collagenous structure
MBP	Myelin basic protein

MDL	Major dense line
MOI	Multiplicity of infection
MPNST	Malignant peripheral nerve sheath tumour
MPZ	Myelin protein zero
MR	Mannose receptor
mRNA	Messenger RNA
MRS	De Man-Rogosa-Sharpe
NES	Nuclear export sequence
NF	Neurofibroma
NFKB	Nuclear factor kappa-light-chain-enhancer of activated B cells
NF1	Neurofibromatosis type 1
NGF	Nerve growth factor
NLS	Nuclear localization sequence
NRG1	Neuregulin 1
NT3	Neurotrophin-3
OP-puro	O-propargy-lpuromycin
OspA	Oter surface protein A
OspC	Oter surface protein C
PAMPs	Pattogen-associated molecular patterns
PBS	Phosphate Buffer Saline
PDGFRA	Platelet-derived growth factor receptor A
PDL	Poly-D-lysine
PI	Propidium Iodide
PKA	Protein kinase A
PLL	Poly-L-lysine
PMP22	Peripheral Myelin Protein 22
PNS	Peripheral Nervous System
PP	Pyrvinium pamoate
Ras	Rat sarcoma
RBP	RNA-binding protein
RNA	Ribonucleic acid
Rpm	Revolutions per minute
RRM	RNA recognition motifs
RT	Room Temperature
RT-PCR	Reverse transcription polymerase chain reaction
SDS	Sodium dodecyl sulfate
SCP	Schwann cell precursors
SEM	Standard error of the mean
SEM	Scanning electron microscopy
SLI	Schmidt-Lanterman incisures
TBS	Tris buffer saline
TBS-T	Tris buffer saline-Tween20
TEM	Transmission electron microscopy

TF	Transcription factor
TGF β	Transforming growth factor β
TLR	Tool like receptor
TNF	Tumor necrosis factor
TROSPA	Tick receptor for OspA
TTP	Tristretaprolin
TUNEL	TdT-mediated dUTP nick end labeling
T3	3,3’,5-Triiodo-L-thyronine
Ub	Ubiquitin
WNT	Wingless-type MMTV integration site family
WT	Wildtype

SUMMARY

Peripheral nervous system (PNS) of the vertebrates, together with central nervous system, form the essential connexions in all the body leading to movement and sensation. Schwann cells are the main non-neuronal cells or so called glial cells in PNS, which in association with neuronal axons, are essential for the correct conexion from the CNS to the rest of the body. This is feasible due to a specific structure which wraps axons, called myelin (mainly composed by water, lipids and proteins), which is crucial for the rapid saltatory conduction of nerve impulses.

Schwann cells which form myelin sheath, named myelinating Schwann cells, derived from the neural crest via two main transitional stages. Initially, neural crest cells give rise to Schwann cell precrusors (SCP), which subsequently generate immature Schwann cells (iSC). At birth, iSC differentiated into mature non-myelinating (Remak) or myelinating Schwann cells. Myelination is an essential process which starts after birth and continue long during life. Nonetheless, myelin breakdown, demyelination, is a universal outcome of a remarkably wide range of conditions that involve disturbance to Schwann cells or the nerve environment, whether due to genetic or acquired diseases, toxicity or microbial infections. Schwann cells are also described as the crucial pathogenic cell type in Neurofibromatosis type 1 (NF1), an autosomal dominant disorder leading to peripheral nerve sheath tumours (MPNSTs), which are highly aggressive sarcomas with still no effective treatments.

Cancer cells can develop a strong addiction to discrete molecular regulators, which control the aberrant transcription programs that drive and maintain the cancer phenotype. Here, we report the identification of the RNA-binding protein HuR as a central oncogenic driver for malignant peripheral nerve sheath tumours (MPNSTs), which are highly aggressive sarcomas that originate from cells of the Schwann cell lineage. HuR was found to be bound to a multitude of cancer-associated transcripts in human MPNST samples. Accordingly, genetic and pharmacological inhibition of HuR had potent cytostatic and cytotoxic effects on tumour growth, and strongly supressed metastatic capacity *in vivo*. Importantly, we linked the profound tumorigenic function of HuR to its ability to simultaneously regulate multiple essential oncogenic pathways in MPNST cellls, including the Wnt/β-Catenin, YAP/TAZ, Rb-E2F and BET proteins, which converge on key transcriptional networks. Given the exceptional dependency on HuR for MPNST cell survival, proliferation, and dissemination, we propose that HuR represents an ideal therapeutic target for MPNST treatment (see chapter 2).

Strikingly, PNS involvement has been observed in Lyme disease-associated clinical manifestations, known as Lyme neuroborreliosis, which is perhaps one of the most dangerous

of all manifestations of Lyme disease, the most common arthropod-borne infectious disease in temperate regions of the northern hemisphere. It is caused by infection with the spirochete *Borrelia burgdorferi,* which is transmitted by a tick bite. The early local reaction to the deposition of the bacteria in the skin is followed by the hematogenous dissemination of the spirochete, which results in the colonization of different tissues and organs such as the skin, heart and nervous system. In this study, we showed that Schwann cells recognize *B. burgdorferi* which leads to demyelination in *in vitro* myelinated Schwann cells in the absence of immune cells, as well as in dorsal root ganglia (DRG) and Schwann cell cocultures and peripheral nerves. We suggest that *B. burgdorferi* regulates intracellular signaling pathways, including Wnt/β-Catenin, to strongly repress myelin gene and protein expression, throwing light on one of the most intriguing pathological features of Lyme neuroborreliosis (see chapter 3).

RESUMEN (versión extendida)

El sistema nervioso periférico, junto con el sistema nervioso central, forman en conjunto el sistema nervioso de los vertebrados, que permite el movimiento y la percepción sensorial. Las células de Schwann, llamadas así gracias al descubrimiento del fisiólogo alemán Theodor Schwann, son las células no neuronales dominantes del sistema nervioso periférico, o las llamadas células gliales, que en asociación con los axones neuronales, son primordiales para la correcta conexión entre el sistema nervioso central y resto del organismo. Las células de Schwann concretamente, además de ser esenciales para el movimiento y la sensación normal en el adulto, controlan la supervivencia neuronal en el embrión, la regeneración y reparación en los nervios dañados y forman la vaina de mielina, una estructura específica que recubre a los axones. Esta vaina de mielina está compuesta principalmente por H_2O, lípidos y proteínas y, es crucial para la conducción rápida y saltatoria de los impulsos nerviosos. Las células de Schwann maduras que forman la mielina, llamadas células de Schwann mielinizantes, derivan de células de la cresta neural a través de dos etapas de transición principales. Inicialmente, las células de la cresta neural dan lugar a precrusores de células de Schwann, que posteriormente generan células de Schwann inmaduras y, éstas en el nacimiento, se diferencian en células de Schwann maduras no mielinizantes (llamadas también células Remak, en honor a su descubridor Robert Remak) y mielinizantes, dependiendo del diámetro del axón que rodeen, siendo menor o mayor que 1 μm, respectivamente. Sin embargo, una gama amplia de afecciones que implican la alteración de las células de Schwann o del entorno nervioso, ya sea debido a enfermedades genéticas (p.ej. Charcot-Marie-Tooth) o adquiridas (p.ej. síndrome de Guillain-Barré), toxicidad o infecciones microbianas (p.ej. lepra) o producidas por virus (p.ej. Zika), afectan a la vaina de la mielina provocando la degradación de los componentes que la forman, proceso denominado desmielinización.

El daño del nervio promueve una cadena de respuestas en un proceso conocido como degeneración Walleriana, en la que se observa degredación de la mielina, degeneración de los axones y una subsiguiente regeneración axonal y, por lo tanto del nervio, gracias a la plasticidad que presentan las células de Schwann diferenciadas. Estas células se transdiferencian en un nuevo fenotipo celular conocido como células de Schwann reparadoras, que presentan un transcriptoma diferente al de las células dediferenciadas del desarrollo embrionario y a las células maduras en el adulto. Varios factores afectan a la capacidad regeneradora, incluidos la edad, el daño prolongado, el tamaño de la lesión del nervio, etc.

La vaina de mielina también se ve afectada en los diferentes tipos de cáncer de las células de Schwann, denominados Neurofibtomatosis. Estas células son las principales responsables de la patogenicidad de la Neurofibromatosis tipo 1 (NF1), trastorno autosómico dominante que se caracteriza por la falta del gen que codifica la proteína neurofibromina y se presenta en 1 de cada 3,500 nacimientos. NF1 conduce a la formación de tumores benignos llamados neurofibromas y otros síntomas clínicos no-tumorales, como por ejemplo manchas de pigmentación, deformidades de los huesos y deficiencia cognitiva. Los neurofibromas pueden transformarse en tumores malignos de la vaina del nervio periférico, que son sarcomas altamente agresivos capaces de metastatizar diferentes tejidos, sobretodo los pulmones. Estos tumores no tienen aún tratamiento efectivo y además se desconocen todas las bases moleculares que conducen a la transformación de los neurofibromas a tumores malignos.

Las células tumorales pueden desarrollar una fuerte adicción a reguladores moleculares concretos capaces de regular varios programas de transcripción que impulsan y mantienen el fenotipo del cáncer. Por ello, las proteínas de unión al ácido ribonucleico (ARN) son muy estudiadas en enfermedades como el cáncer ya que presentan la capacidad de regular post-transcripcionalmente un inmenso número de dianas, ARN mensajeros, que a su vez pueden regular dianas de diversas vías intracelulares. La proteína de unión al ARN HuR/ELAVL1 ejerce un papel fundamental en la regulación post-transcripcional de la expresión génica en las células de mamíferos, controlando numerosos procesos biológicos. Esta proteína reconoce y se une a elementos adenilato/uridilato (AREs) en la región no traducida 3′ (3′ UTR) y 5′ (5′ UTR) de sus ARN mensajeros (ARNm) diana, generalmente promoviendo la estabilidad de dichos ARNm y la posterior traducción a proteína. En un estudio previo de nuestro laboratorio se observó que HuR está altamente expresado en las células de Schwann inmaduras, en las que regula coordinadamente la expresión de varios genes para promover la proliferación e inhibir la apoptosis. La expresión de HuR es elevada en varios tipos de cáncer (páncreas, próstata, colon, piel…) donde regula multitud de ARN mensajeros oncogénicos. Además, en un estudio preliminar de nuetsro laboratorio se confirmó la expresión elevada de HuR en los tumores malignos del nervio periférico, en comparación a muestras humanas de neurofibromas y nervios no dañados.

Por consiguiente, en el primer proyecto de esta tesis doctoral (**capítulo 2**) hemos analizado el papel funcional de HuR en la malignicidad de los tumores malignos de la vaina del nervio periférico. Hemos comprobado que HuR se une a un mayor número de dianas oncogénicas en los tumores malignos del nervio periférico en comparación a muestras humanas de neurofibromas, promoviendo el crecimiento tumoral y metástasis. Como consecuencia, la

inhibición genética y farmacológica de HuR tuvo potentes efectos citostáticos y citotóxicos sobre el crecimiento tumoral y la supresión de la capacidad metastásica *in vivo*. Sin embargo, hemos comprobado que HuR no es suficiente para inducir la transformación oncogénica de las células de Schwann, es decir, la sobreexpresión de *HuR* en células de Schwann humanas no condujo a la formación de tumores malignos del nervio periférico *in vivo*. Es importante destacar que vinculamos la función tumorigénica de HuR con su capacidad para regular simultáneamente múltiples vías oncogénicas esenciales en líneas celulares extraídas en su origen de este tipo de tumores malignos de la vaina del nervio periférico. Las principales vías reguladas positivamente por HuR en este tipo de tumores malignos promoviendo la traducción de sus dianas, incluyen Wnt/β-Catenina, YAP/TAZ, Rb-E2F y BET. La sobreexpresión de *β-Catenina* redujo el efecto del silenciamiento de HuR, aumentando la capacidad oncogénica de las líneas celulares provinentes de estos tumores malignos. Sin embargo, la sobreexpresión de las otras dianas de HuR no tuvo ese mayor efecto observado con la sobreexpresión de *β-Catenina*. Por lo que sugerimos, que HuR regula diferentes vías oncogénicas que, convergen en redes transcripcionales clave para la progresión y malignicidad asociada con los tumores malignos de la vaina del nervio periférico.

Dada la excepcional dependencia de HuR para la supervivencia, proliferación y diseminación de estos tumores malignos, proponemos que HuR representa una diana terapéutica óptima para el tratamiento de los tumores malignos de la vaina del nervio periférico (ver capítulo 2).

Sorprendentemente, la desmielinización también se ha observado en pacientes que presentan la enfermedad de Lyme, la enfermedad infecciosa más común transmitida por artrópodos en el hemisferio norte. El sistema nervioso puede estar afectado en un 13 % de los casos, lo que se denomina neuroborreliosis de Lyme y, probablemente la afección del sistema nervioso sea una de las manifestaciones clínicas más peligrosas. La enfermedad de Lyme, llamada así por el lugar de origen donde se descubrió (Lyme, Connecticut), es causada por la transmisión por garrapatas de la espiroqueta *Borrelia burgdorferi.* La reacción local temprana a la deposición de la bacteria en la piel es seguida por la diseminación hematógena del patógeno, lo que resulta en la colonización de diferentes tejidos y órganos como la piel, el corazón, y el sistema nervioso. Las manifestaciones clínicas pueden deberse a una activación excesiva del sistema immunológico, pero las consecuencias y mecanismos moleculares implicados en la infección del sistema nervioso periférico son mayoritariamente desconocidos.

Por consiguiente, en un segundo proyecto de esta tesis doctoral (**capítulo 3**) estudiamos el efecto directo del patógeno *Borrelia burgdorferi* que produce la enfermedad de Lyme en cultivos puros de células de Schwann de rata, en los que previamente se había inducido la respuesta de mielinización mediante la adición de un análogo de Adenosín monofosfato cíclico (AMPc),

denominado dibutiril AMPc (dbAMPc). Hemos demostrado que las células de Schwann son dianas directas de *B. burgdorferi*. Observamos una unión directa entre la bacteria y las células de Schwann mediante el uso de varias técnicas, como el microscopio de fluorescencia, microscopio confocal y electrónico de barrido. La unión del patógeno con las células de Schwann promovió una respuesta de desmielinización en absencia de células immunes. Además, la presencia de *B. burgdorferi* en cultivos puros de células de Schwann no indujo la expresión y secreción de citoquinas, que podrían estar provocando la desmielinización previamente observada en presencia del patógeno. Estas células gliales pueden reconocer el patógeno metabólicamente inactivo (la bacteria expuesta a una alta temperatura) e incluso residuos de la superficie o intracelulares de la bacteria (obtenidos al sonicar el microorganismo previamente), lo que resultó en una respuesta similar de desmielinización a la observada en presencia del patógeno vivo. Esta unión de lipoproteínas presentes en la superficie del microorganismo y su material genético a las células de Schwann podría deberse a que éstas presentan en su membrana receptores implicados en el sistema immunológico y en el reconocimiento de patógenos, incluyendo MARCO y CD64. Sin embargo, la presencia de *B. burgdorferi* no incrementó los niveles de estos receptores.

También se observó desmielinización en cultivos de nervios periféricos (plexo braquial y nervio ciático) y en cocultivos de células de Schwann y ganglios de la espina dorsal. Además, comprobamos que *B. burgdorferi* es capaz de inhibir la inducción de mielinización en las células de Schwann no diferenciadas al añadir la bacteria simultáneamente con dbAMPc, lo que podría estar asociado con la degeneración axonal prolongada y por consiguiente con las manifestaciones clínicas duraderas relacionadas con el sistema nervioso periférico que se han observado en pacientes con neuroborreliosis de Lyme. Este efecto en desmielinización no es una respuesta común que pueda inducirse en las células de Schwann en presencia de todo tipo de bacterias taxonómicamente diferentes, ya que en este proyecto analizamos la respuesta de estas células gliales a la estimulación de diferentes bacterias que pertenecen a géneros *Lactobacillus* y *Mycobacterium* y no se observó unión de los microorganismos ni tampoco desmielinización.

Los resultados obtenidos de la secuenciación del ARN y proteómica, sugieren que *B. burgdorferi* desregula varias vías intracelulares, incluídas dianas que intervienen en la adhesión celular y la vía Wnt/β-Catenina. Observamos un claro aumento de la expresión de *Wnt5a,* proteína que puede participar tanto en la vía no canónica de Wnt como en la vía canónica Wnt/β-Catenina en este caso disminuyendo los niveles del factor de transcripción β-Catenina; lo que podría sugerir que en presencia de *B. burgdorferi* el aumento aberrante de *Wnt5a* podría disminuir los niveles de β-Catenina observados en este sistema, originando la represión de la

expresión de genes que codifican proteínas asociadas a la mielina y a un incremento de la degradación de éstas vía proteasoma, asi como por autofagia. La sobreexpresión de *β-Catenina* aumentó los niveles de la proteína de mielina MPZ ("Myelin Protein Zero"), disminuyendo el efecto de *B. burgdorferi* en la desmielinización de las células de Schwann.

Por lo tanto, proponemos que *B. burgdorferi* desregula varias vías de señalización intracelular en las células de Schwann, incluida Wnt/β-Catenina, disminuyendo los niveles de β-Catenina y reprimiendo así la expresión de genes y proteínas asociadas a la mielina, lo que arroja luz sobre una de las características patológicas más intrigantes de la neuroborreliosis de Lyme (ver capítulo 3).

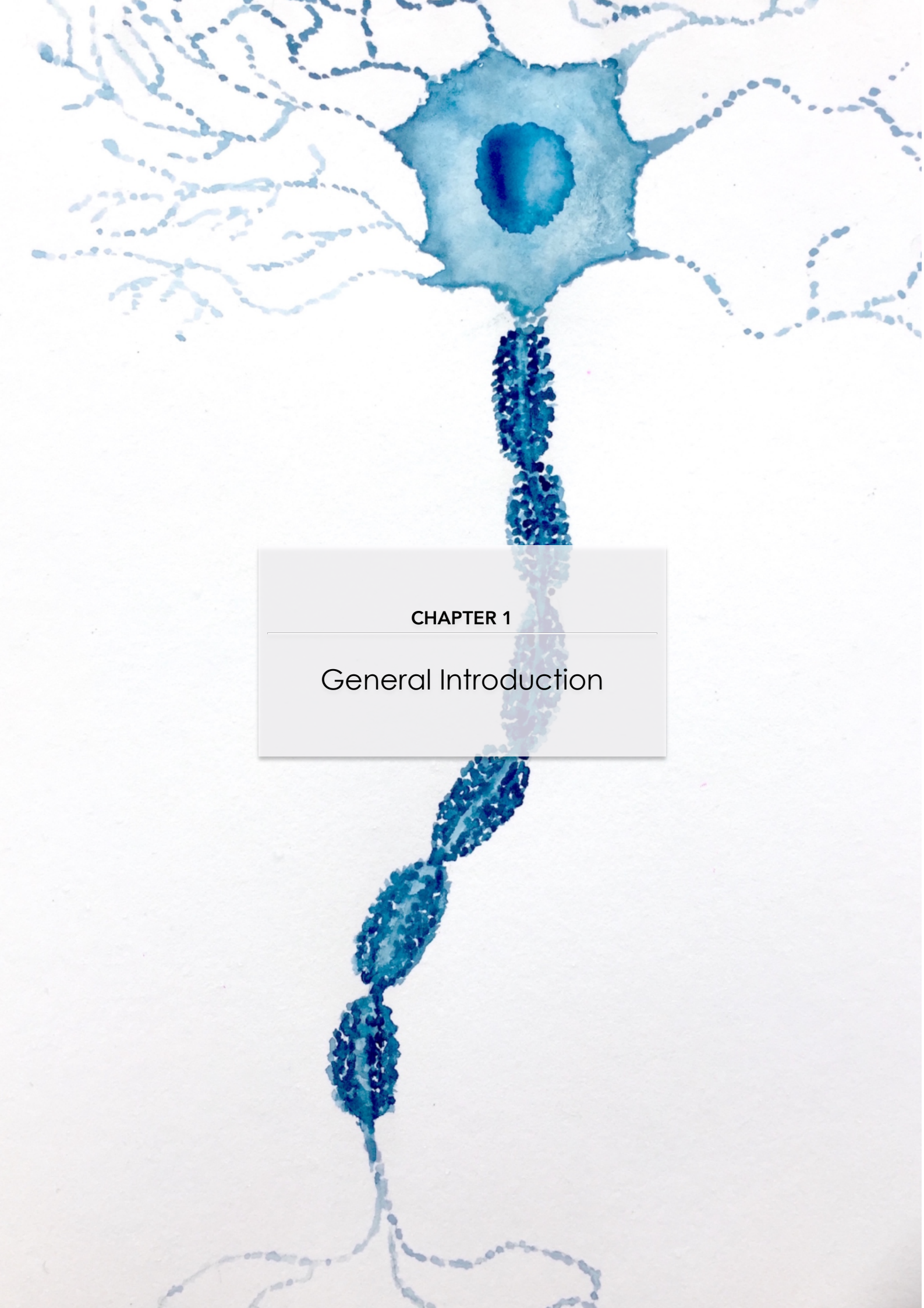

CHAPTER 1

General Introduction

General Introduction

1. An overview of Schwann cell lineage

The vertebrate nervous system consists of the peripheral nervous system (PNS) and central nervous system (CNS), which in turn, is formed by the brain and spinal cord. The PNS connects CNS to the rest of organs and limbs, coordinating body functions. It is made up of several components, including motor, sensory, and autonomic neurons, their afferent and efferent axons and, connective tissue components (endoneurium, perineurium, epineurium, blood and lymphatic vessels) (Katona and Weis, 2017). Nerves are made up of different types of cells including neurons and non-neuronal cells, named glial cells, constituting the vast majority of the PNS cells, in addition of macrophages and fibroblasts, among others (Jessen, 2004) (**Figure 1**).

Schwann cells, named after the physiologist Theodor Schwann (1810-1882), are the main glial cells of PNS. Two different types of mature Schwann cells exist in adult nerves: non-myelin Schwann cells, known also as Remak Schwann cells (named after embryologist Robert Remak) (Boullerne, 2016) and myelinating Schwann cells. In addition to the function of saltatory nerve impulse transmission, Schwann cells are specially needed for axonal trophic support, regulation of axonal diameter and axonal regeneration after a nerve insult (see section 1.4).

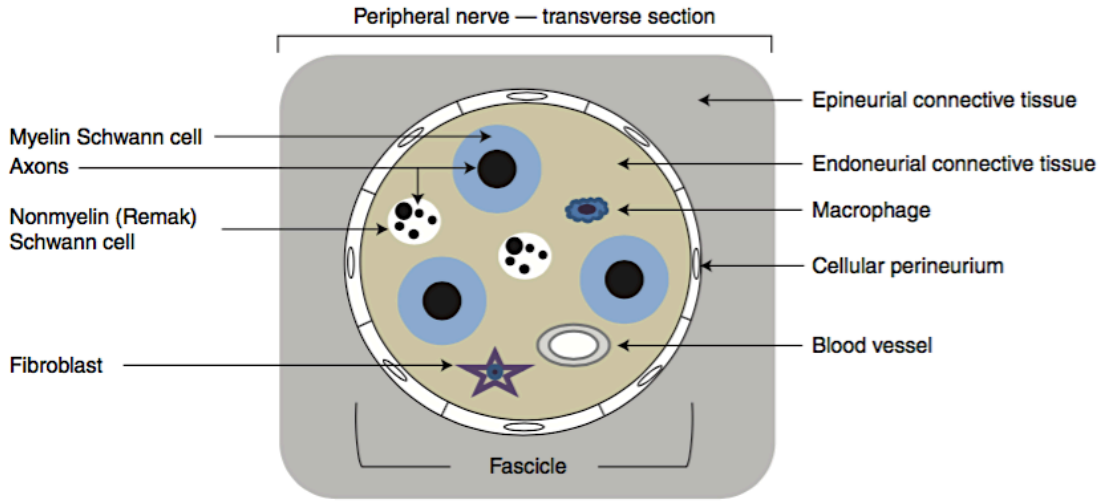

Figure 1. **Adult peripheral nerve and its main components**. The main cellular structures within the nerve are indicated in the image. This nerve contains one fascicle. The perineurium shown here as a single cell layer is most often multilayered. Basal lamina is not shown (Adapted from Jessen *et al*., 2015).

The other glial cells found in the PNS include satellite cells that associate directly with neuronal cell bodies in sympathetic, parasympathetic and sensory ganglia (Pannese, 1981), terminal glia of somatic motor nerve terminals, also known as teloglia or perisynaptic glia, which regulate synaptic transmission and maintain stability of the neuromuscular junction (Robitalle, 1998; Auld and Robitalle, 2003); enteric glial cells in the autonomic ganglia of the gut (Gabella, 1981;

Jessen and Mirsky, 1983), olfactory ensheathing cells (Chuah and West, 2002), which associate with both CNS and PNS axons (Jessen, 2004), and specialized glial cells that function as mechanosensory end organs, including Meissner's corpuscles, Pacinian corpuscles, lanceolate endings, Merkel cells, and Ruffini corpuscles (Fleming and Luo, 2013).

2. Schwann cells development

2.1. First embryonic stage: Schwann cell precursors

Adult differentiated Schwann cells are derived from neural crest cells, a group of multipotent cells that arise from the dorsal part of the neural tube, through two main developmental steps. First, neural crest cells give rise to Schwann cell precursors (SCP) at embryo day E12/13 in mice (E14/E15 in rat) (**Figure 2**). Signals controlling this transition are still poorly known (Jessen *et al*., 2015). SCP retain multipotency, giving rise to different type of cells, such as neurons (Uesaka *et al*., 2015; Espinosa-Medina *et al*., 2017), fibroblasts (Joseph *et al*., 2004), chromaffin cells (Furlan *et al*., 2017), melanoblasts (Adameyko *et al*., 2009) and mesenchymal cells developing into odontoblasts (Kaukua *et al*., 2014) and immature Schwann cells (iSC) (Jessen and Mirsky, 2019a). SCP are strictly dependent on axonal signals for their survival and further differentiation. Thus, when SCP are isolated from embryonic nerves and cultured *in vitro* in the absence of axons, they survive poorly. Nonetheless, addition of molecules to the cell culture such as neuregulin1 (NRG1) can promote SCP survival and prevent death, as well as promoting differentiation to iSC (Jessen *et al*., 2019a). Neural crest cells, when converted to SCP, change expression of several genes, some of them being downregulated in SCP phenotype while three-fold higher number of genes are upregulated. Several genes, such as genes encoding for myelin basic protein (MBP), PLP22, BFABP and desert hedgehog (Dhh) persist or further up-regulated during next Schwann cells developmental stages (Jessen *et al*., 2019a).

2.2. Second embryonic stage: Immature Schwann cells

SCP at embryo day E15/16 in mice (E17/18 in rat) give rise to iSC, which then will differentiate to mature non-myelin (Remak) or myelinating Schwann cells after birth (see 2.3 section) (**Figure 2**). iSC associate with connective tissue and basal lamina and do not depend on axons for survival, however axonal signal is essential for giving rise iSC from SCP, as these cells cannot survive without axonal signals (Jessen *et al*., 2019a), as explained above. The transition of SCP to iSC is characterized by an upregulation of several genes in iSC, such as S100 and glial fibrillary acidic protein (GFAP), and downregulation of SCP markers, including AP2, α4 integrin and Ncadherin (Wanner *et al*., 2006). The differentiation of SCPs to iSC is promoted by Notch

signaling pathway (Woodhoo *et al*., 2009) and negatively regulated by endothelins (Brennan *et al*., 2000).

iSC have less migration capacity than SCP but are more proliferative, reaching a DNA synthesis peak just before birth (Jessen and Mirsky, 2019a). Proliferation of iSC is controlled by wide range of factors, such as axonal contact, NRG1 and Notch, laminins expressed in basal lamina, and transforming growth factor β (TGF β), among other signals. Hippo and cAMP pathways also contribute to the regulation of Schwann cells proliferation in developing nerves *in vivo* (Jessen *et al*., 2019a).

Schwann cells can also undergo apoptosis during development, which is controlled mainly by TGF-β, acting through TGF-β type II receptors (Parkinson *et al*., 2001; D' Antonio *et al*., 2006). Even though nerve growth factor (NGF), acting through $p75^{NTR}$ receptor, is not implicated in Schwann cells survival during development, NGF signaling controls Schwann cells death in injured nerves (Syroid, *et al*., 2000). Apoptosis during normal development or in nerve injury is inhibited by exogenous NRG addition (Grinspan *et al*., 1996).

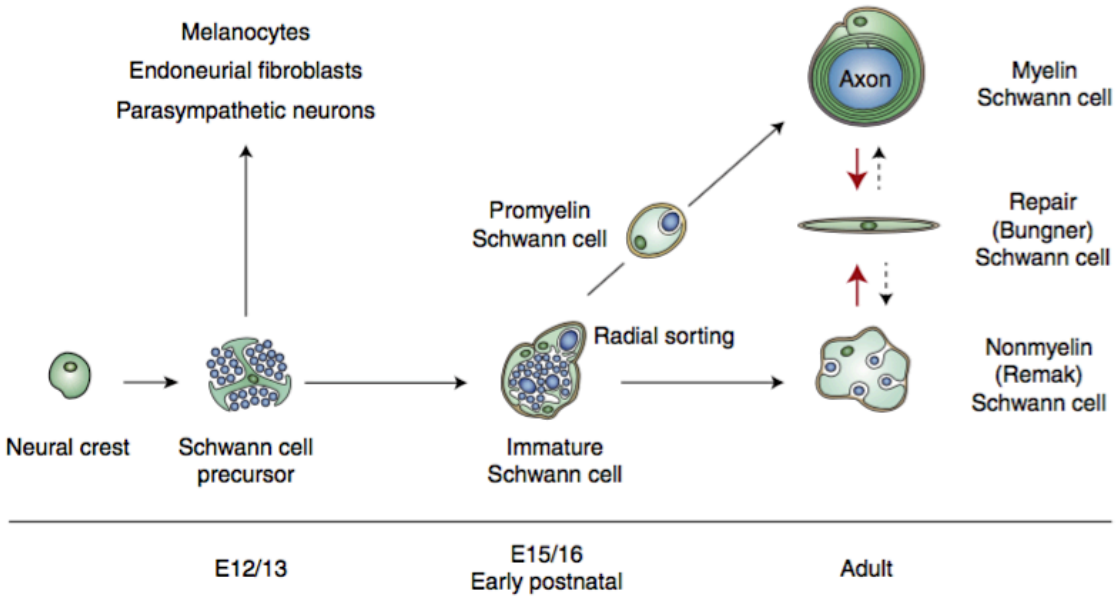

Figure 2. Developmental stages of Schwann cell lineage and nerve injury-induced transitions. Normal development is represented in black uninterrupted arrows, whereas red arrows indicate Schwann cell injury response; stippled arrows specify formation of myelin and Remak from repair Schwann cells. Embryonic days (E) refer to mouse development (modified from Jessen *et al*., 2015).

2.3. Mature Schwann cells: Remak and myelinating Schwann cells

At birth, iSC are able to segregate large diameter axons found in the Schwann cell-axon families, such that an individual large-diameter axon (>1 µm) is surrounded by a unique Schwann

cell in a 1:1 relation (a pro-myelinating Schwann cell), a process known as radial sorting. After radial sorting, these pro-myelinating Schwann cells then differentiate to myelinating Schwann cells (Feltri *et al*., 2016). Schwann cells wrap axons up to one and a half times before myelination is arrested. Remak Schwann cells can surround more than one small diameter axon (<1 µm) (Jessen and Mirsky, 2003). Several factors are involved in regulating the radial sorting, such as NRG1, insulin growth factor (IGF), neurotrophin-3 (NT3) and brain-derived neurotrophic factor (BDNF). The extracellular signals that control fate choice in Schwann cell lineage stages are not well understood; however, If a Remak Schwann cell was placed in contact with a large diameter axon rathert than a smaller one, myelin phenotype would be promoted giving rise to myelinating Schwann cell instead of a Remak Schwann cell, and conversely (Jessen and Mirsky, 2019b). Differentiated mature Schwann cells and iSC are characterized by different antigenic profiles (**Figure 3**). iSC destined to form myelin start to express the glycolipid galactocerebroside (GalC) at around E19 and Remak cells only express GalC shortly after iSC differentiation into mature Remak Schwann cells around third postnatal week (Jessen *et al*., 1985). Furthermore, iSC driven to give rise myelinatig Schwann cells downregulate expression of GFAP, N-CAM and $p75^{NTR}$, among others (**Figure 3**) (Jessen and Mirsky, 2003)

After the fifth week of birth, mature Schwann cells become quiescent. Strikingly though, Remak and myelinaring Schwann cells are highly plastic cells, and can undergo a switch in their phenotypic identity; after injury, they can undergo a reprogramming process to convert to repair Schwann cells, which is a specific Schwann cell phenotype essential for axonal regeneration (see 2.4 section) (Stierli *et al*., 2018).

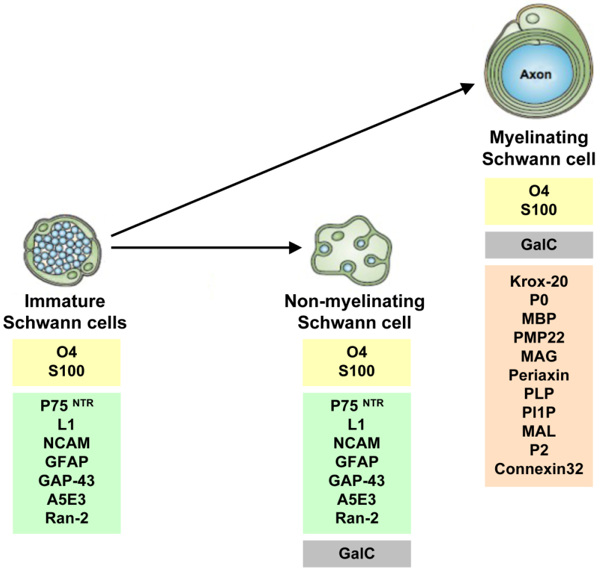

Figure 3. Antigenic profile of immature Schwann cells (iSC) and differentiated adult Schwann cells. Proteins inside the yellow box are present in all three Schwann cells phenotypes, from iSC to mature Schwann cell stages. Glycolipid galactocerebroside (GalC) (grey box) is only present in mature Schwann cells (Remak and myelinating Schwann cells). Proteins present in iSC and Remak Schwann cells, but downregulated in myelinating Schwann cells, are represented in the green box, and antigens in the orange box are only upregulated in mature myelinating Schwann cells (adapted from Jessen and Mirsky, 2003 with minor modifications).

2.4. Repair Schwann cells in Wallerian degeneration

After peripheral nerve injury, mature Schwann cells lose axonal contact and transdifferentiate giving rise to repair Schwann cells as mentioned above, also known as Bungner cells, in a process referred to Wallerian degeneration (**Figure 2**) (Chen et al., 2007; Arthur-Farraj *et al*., 2017). Although axonal degeneration after a nerve injury is observed after 2-4 days, activation of Schwann cells is seen earlier, even at hours of the injury, through mechanisms that are still poorly known (Rotshenker, 2011). Formation of repair Schwann cells was commonly described as a dedifferentiation process where adult denervated cells revert to an earlier stage similar to those iSC, re-expressing genes of iSC phenotype; however nowadays there is evidence that repair Schwann cells are different in structure to iSC and have a different molecular profile and function. Furthermore, oligodendrocyte transcription factor1 (*Olig 1)* and sonic hedgehog (*Shh*) genes which are upregulated by c-Jun, differentiate repair Schwann cells from the rest of the Schwann cell phenotypes of developmental stages (Arthur-Farraj *et al*., 2012; Jessen and Mirsky, 2019a). These facts, suggest that repair Schwann cell phenotype is a specific and transitory stage, suggesting these repair Schwann cells are formed by transdifferentiation of mature Schwann cells rather than dedifferentiation (Arthur-Farraj *et al*., 2012). Moreover, this repair response after a nerve insult is controled by several factors, such as Notch and c-Jun transcription factors (Harrisingh *et al*., 2004; Napoli *et al*., 2012), glial cell line-derived neurotrophic factor (GDNF), BDNF, NT3, NGF, vascular endothelial growth factor (VEGF), artemin and, pleiotrophin that promote survival of injured neurons and axonal elongation (Arthur-Farraj *et al*., 2012; Fontana *et al*., 2012; Brushart *et al*., 2013; Jessen and Mirsky, 2019a). Denervated cells activate cytokines expression, including TNF, IL-6 and IL-1β, promoting attraction and activation of macrophages that help Schwann cells to digest myelin by autophagy, term known as myelinophagy (Gomez-Sanchez *et al*., 2015), which is essential for the following axonal elongation and repair. In addition, some cytokines can also act directly in neurons, promoting axonal regeneration (Barrette *et al*., 2008). Howerver, for a complete axonal regeneration remyelination is needed and several factors regulate remyelination after nerve injury, such as extracellular matrix molecules (laminins, dystroglycans), cell adhesion molecules (N-cadherin, NCAM), neurotrophic factors and receptors (BDNF, p75NTR), intracellular regulators (e.g. PI3K/AKT signaling pathway) and hormones (progesterone, thyroid hormone…) (Chen *et al*., 2007).

Repair and mature Schwann cells not only differ in gene expression profile, but also in morphology. Repair Schwann cells are more elongated than myelin or Remak Schwann cells, which leads to the formation of the regeneration tracks that will connect the proximal stump

with the distal part of the injured nerve, by establishing 1:1 relationship with the axons and remyelinating them, but, in this case, the myelin sheaths are thinner and the internodes (see section 3.1) are usually shorter than in normal nerves (Schroder, 1972; Beuche and Friede, 1985; Glenn and Talbot, 2013).

Wallerian degeneration occurs in the distal stump of cut or crushed nerves, wherein number of Schwann cells is increased due to the activation of proliferation. Nonetheless, inhibition of proliferation does not affect final nerve regeneration, suggesting proliferation is not essential for axonal regeneration (Yang *et al*., 2008).

3. Myelination

Myelination is an indispensable process, that occurs in both central and peripheral nervous system after birth and continue long during life. Myelin sheaths are important not only for accelerating action potential conduction but for providing trophic and metabolic support to axons.

Myelinating Schwann cells insulate a unique axon as explained above, extending around the axonal segment and leaving a non-myelinated space from one myelin sheath to another, regions known as nodes of Ranvier (named after the discovery in 1877 by Louis-Antoine Ranvier; Garbay *et al*., 2000; Boullerne, 2011). Nerve impulses travel through one node to the next, which is essential for the rapid saltatory impulse of action potential, discovered in 1939 by Tasaki (Boullerne, 2016).

Myelin formation starts with the radial sorting of large diameter axons (>1 µm) by iSC (Geren, 1954), to give rise to pro-myelinating Schwann cells, which then differentiate to myelinating Schwann cells, as explained above (see section 2.3). Axonal signals, such as NRG1 type III which is associated with axonal membranes (see section 3.3.1), promote axonal wrapping, where Schwann cells nuclear circumnavigation of the axon is observed (Bunge *et al*., 1989) and plasma membrane can be expanded about 20 mm^2 in order to form myelin sheath (Kidd *et al*., 2013).

Profound gene expression changes occur during the myelination process, with upregulation of myelin-related genes (MBP, Periaxin, MAG, etc.) together with downregulation of some iSC markers, such as NCAM, GFAP and $p75^{NTR}$ (Jessen and Mirsky, 2019a) (**Figure 3**). Several pro-myelin transcription factors regulate myelination, including NF-kB, Pou3f1 (Oct6), Pou3f2 (Brn2), NFATc4, YY1 (Yin Yang), and subsequent Krox20 (Salzer, 2015). Furthermore, sterol regulatory element binding proteins (SREBP) induces lipid biosynthesis necessary for myelin sheath (Svaren and Meijer, 2008) (**Figure 4**).

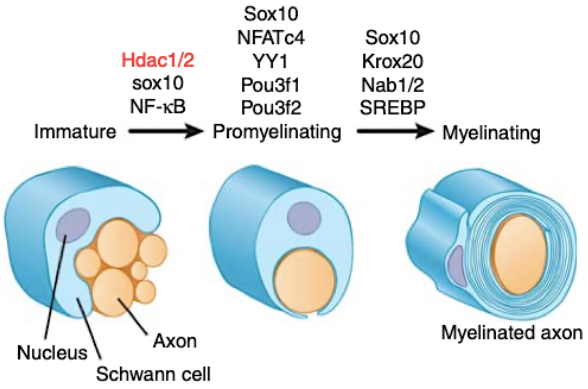

Figure 4. Transcriptional control of myelinating Schwann cell. Sox10 and Hdac1/2 (in red) expression is essential for progression from immature Schwann cells (iSC) to the promyelinating stage. NF-kB also promotes this transition. Differentiation from the promyelinating stage to the myelinating phenotype requires Pou3f1 (Oct6), Pou3f2 (Brn2), Sox10, NFATc4, and YY1. These proteins promote expression of Krox20 and together with Nab1 and Nab2, are essential for the formation of the myelinating Schwann cells. Sterol regulatory element binding proteins (SREBP) induces lipid biosynthesis (edited from Salzer, 2015).

Myelination, is also regulated by epigenetic modifications, including DNA methylation (Varela-Rey *et al*., 2014), posttranslational modifications of nucleosomal histones (e.g. acetylation, methylation and citrullination), and noncoding RNAs, specially microRNAs (miRNAs) (Pereira *et al*., 2012).

3.1. Myelinated fiber structure

Myelinating Schwann cells are longitudinally and radially polarized cells that organize into distinct membrane domains (**Figure 5**). Longitudinal polarity is demostrated by the organization into nodal, paranodal, juxtaparanodal, and internodal compartments of the myelinated axon. Radial polarity is evident because of the different inner (adaxonal) and outer (abaxonal) membranes which are present at each end of the cell on opposite sides. Between these membrane surfaces remains the compact part of the myelin sheath (Salzer, 2015). Initially, Schwann cells start surrounding axons and bringing together the two sides of its plasma membrane, a region known as inner mesaxon, that elongates forming like a spiral around the axon (**Figure 5**) and continue surrounding the axon in order to form several spiral layers (myelin lamellae). At the same time of the myelin lamellae formation, mesaxon starts condensing because of myelin related proteins, such as MPZ, forming compact myelin (Kidd *et al*., 2013). Adaxonal membrane is separated from the plasma membrane (axolemma) by a space of about 15 nm. It is enriched in adhesion molecules and receptors that mediate interaction with axonal ligands (Slazer, 2015). The abaxonal membrane, which is above adaxonal membrane, mediates interactions with laminin of the basal lamina notably by integrins, such as, α6β1 and α6β4 and,

β dystroglycan (Previtali *et al*., 2003). This outer surface is interrupted by periodic appositions that delineate several cytoplasmic channels called Cajal bands (Court *et al*., 2004). These channels provide a conduit for transport of RNA and proteins formed in cell soma and going towards the paranodal region. Basal lamina is wrapping around the Schwann cell plasma membrane, surrounding the whole axon-Schwann cell unit (Scherer and Arroyo, 2002). Myelin sheath is composed of about 40 or more lamellae (Peters *et al*., 1991) (**Figure 5**).

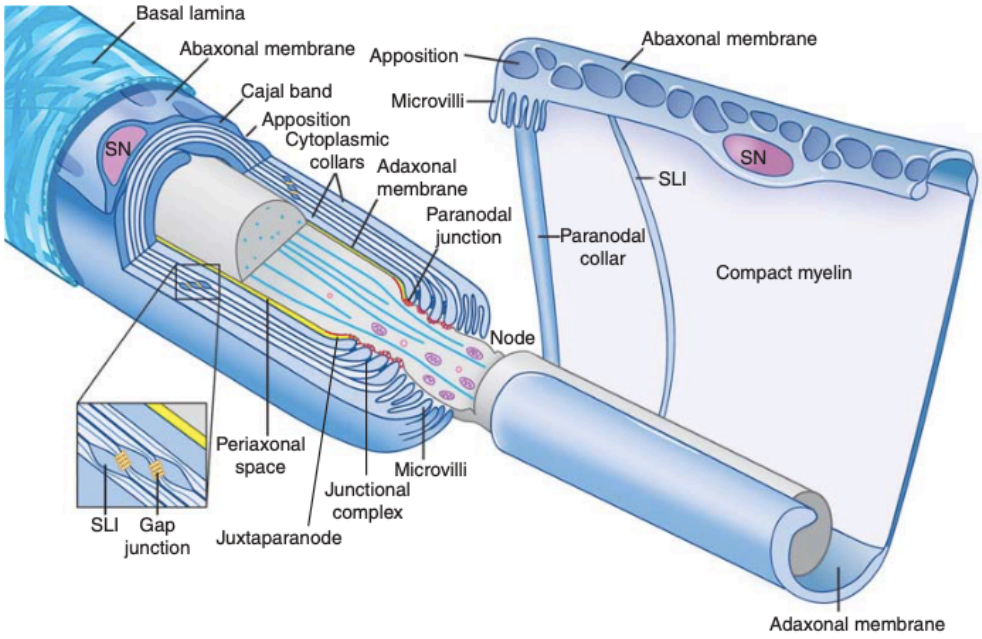

Figure 5. Structural composition of a myelinated nerve fiber. A schematic diagram of myelinated nerve structure is shown, indicating the axon and Schwann cell layers surrounding the axon, which forms the myelin sheath, separated by Nodes of Ranvier. Compact myelin is interrupted by Schmidt-Lanterman incisures (SLI) and Cajal bands (original in Salzer, 2003; modified in Nave, 2010; Salzer, 2015).

The internode, located between two nodes of Ranvier, is the largest longitudinal part of the Schwann cell (99 % of the total Schwann cell length) extending up to 2 mm (Hildebrand *et al*., 1994). It consists of compact and non-compact myelin, name proposed by German pathologist Rudolf Ludwig Virchow (1821-1902) (Boullerne, 2016). Electron micrographs show compact myelin as a compartment with light and dark lines. Major dense lines (MDL) are about 2.5 nm thick and are formed by two cytoplasmic lipid bilayers that are separated from each other by extracellular light interperiod lines (IPL) (Salzer, 2015) (**Figure 6**).

Compact-myelin is interrupted by Schmidt-Lanterman incisures (SLI) from the adaxonal to the abaxonal membrane, which form non-compact myelin (**Figure 5**, **Figure 6**). SLI generate a Schwann cell cytoplasm network throughout the compact myelin allowing intracellular

communication (Small *et al*., 1987; Hall and Williams, 1970). SLI are observed once myelin is formed, so its late origin suggests that they are not essential for myelin formation, but may serve in myelin maintenance (Gillespie *et al*., 2000). Adherens, gap and tight junctions found in SLI and channels also contribute to connect the different parts of the Schwann cell. Cajal bands are located perpendicular to SLI (Pereira *et al*., 2012) (**Figure 5**).

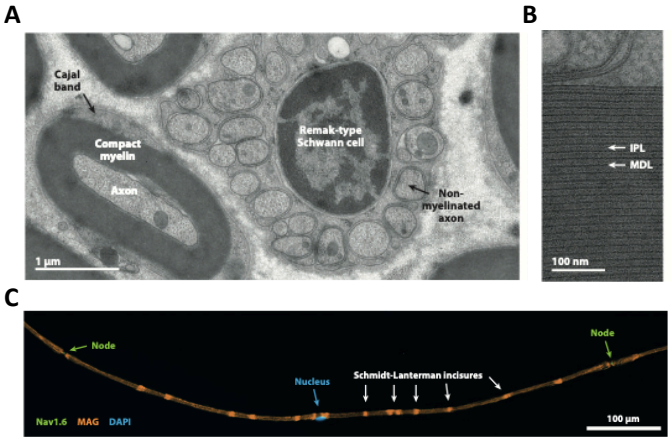

Figure 6. Structural morphology of peripheral nervous system (PNS) axons. A) Myelinated and smaller non-myelinated axons of a sciatic nerve are shown in an electron microscopy micrograph. Remak Schwann cell enwraps multiple small axons (< 1µm diameter), whereas myelinating Schwann cell forms myelin by ensheathing one axonal segment with multiple periodic membrane layers. **B)** Electron-dense intraperiod lines (IPL) and major dense lines (MDL) are indicated in a sciatic nerve myelin sheath. **C)** A single internodal segment is shown. Nodes of Ranvier, labeled with antibodies specific for the axonal sodium channel Nav1.6 (green), and Schmidt-Lanterman incisures, labeled with antibodies against myelin-associated glycoprotein (MAG, orange), are indicated. The nucleus of the myelinated Schwann cell is represented in blue, by DAPI staining (adapted from Nave and Werner, 2014).

Axons and Schwann cells contact directly at the paranodal region in nodes of Ranvier, through septate-like junctions. The juxtaparanodes are small areas located between the paranodal junction and the internode (**Figure 5**) that contain voltage-sensitive potassium channels, which play a role in repolarization, maintenance of resting potential and prevention of ectopic impulses (Salzer *et al*., 2008).

Recent works reported that axons destined to be myelinated are larger and biochemically different than the ones destined not to be myelinated (Salzer, 2015). In unmyelinated axons, nerve impulse is propagated by local circuits of ion current from the active region of the axonal membrane through the axon to the adjacent sections, while in myelinated fibers, action potential flows from an excitable part of the membrane, which corresponds to the node of Ranvier, to the next node of Ranvier, in a high saltatory velocity (**Figure 7**).

3.2. Myelin composition

Myelin content is divided into a liquid part of about 40 % water and about 60 % of dry mass, which is composed of about 75 % lipids and a low proportion of proteins (about 20 %) (Morell and Quarles, 1999; Nave and Werner, 2014). The main lipids found in myelin are galactosphingolipids, saturated long-chain fatty acids and cholesterol.

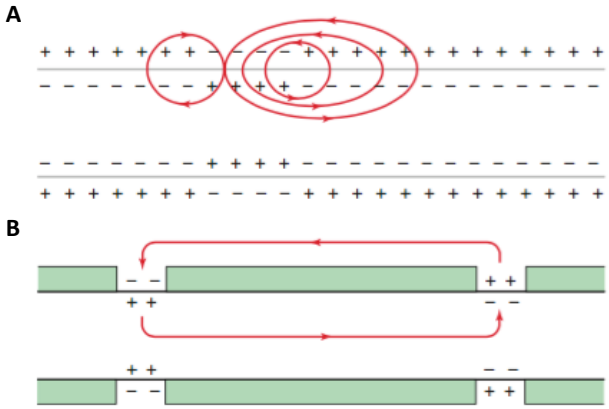

Figure 7. Nerve impulse conduction throughout axons. A) In unmyelinated fiber the arrows show the flow of action currents in local circuits into the active region of the membrane going throw adjacent axonal membrane. **B)** In myelinated axons action potential flows in a saltatory conduction, jumping from one node to the next node (adapted from Quarles *et al*., 2006).

One of the biochemical characteristics that distinguish myelin from other biological membranes is its high lipid content, around 1 to 186 lipid-protein ratio, which contributes to the insulating properties of the myelin internode. Strictly speaking, however, there are no myelin specific lipids (Garbay *et al*., 2000). The ratio of cholesterol, phospholipids and glycosphingolipids in most membranes is about 25%: 65%: 10%, whereas in myelin sheath it represents a range of 40%: 40%: 20% (Schmitt *et al*., 2014). PNS lipid content varies quantitatively from one species to another (Garbay *et al*., 2000). Furthermore, PNS and CNS myelin present similar lipid content with quantitative differences (Nave and Warner, 2014). PNS myelin has considerably more sphingomyelin, accounting for 10-35 % of the total lipids, but less cerebroside and sulfatide than CNS myelin (Garbay *et al*., 2000). A characteristic difference of PNS myelin is the presence of ganglioside LM1, also known as sialosyl-lactoneotetraosylceramide (Morell and Quarles, 1999). Cholesterol is essential for the formation and maintenance of myelin and represents about 28 % of myelin dry mass (Saher *et al*., 2011). The glycolipids GalC and galactosulfatide are involved in myelin stability and are required for node and paranode formation. Oleic acid is the major fatty acid of PNS, representing about 30-40 % of fatty acids in sciatic nerve.

Some proteins of PNS are shared with CNS, whereas others are unique. MPZ is the major protein of PNS, accounting for more than the half of myelin protein composition (Uyemura *et al*., 1993; Raasakka *et al*., 2019). In addition to MPZ glycoprotein, compact myelin also contains PMP22, which represents about 5 % of total protein amount and it is thought to control myelin thickness (Sutter and Snipes, 1995). MBP accounts for 5 to 18 % of the protein content (in contrast to CNS, where it accounts for about 30 % of total proteins). Four different isoforms have been found in either CNS or PNS (Lees and Brostoff, 1984). MBP, together with MPZ, contributes to the formation and compaction of MDL (Martini *et al*., 1995). Myelin associated glycoprotein (MAG) is found in non-compact myelin, including SLI (Morell and Quarles, 1999). P_2 is another protein of PNS which seems to be involved in lipid assembly or turnover in myelin sheath (Martenson and Uyemura, 1992). There are also other proteins expressed in PNS myelin, such as proteolipid protein, which is the major myelin protein in CNS (Kamholz *et al*., 1992).

3.3. Regulation of myelination

3.3.1. NRG1

NRG1 comprises a family of transmembrane and secreted proteins that are encoded by four genes (*NRG1 - 4*), in which NRG1 is the best characterized. Six different proteins of NRG1 have been described (types I - VI) with at least 31 isoforms, which differ in the amino-terminal region. Each NRG1 has an extracellular domain containing two extracellular cysteine-rich regions, a transmembrane domain, a short intracellular juxtamembrane region, a tyrosine kinase domain and a carboxy-terminal tail. All of them share an epidermal growth factor (EGF)-like signaling domain located in the extracellular region. The expression pattern of the isoforms differ in the tissues. Types I - III are the most common NRG1, with type III being the most abundant in peripheral axons. NRG1 stimulates transmembrane tyrosine kinases called ErbB receptors (Mei and Xiong 2008; Salzer, 2015) NRG1 promotes ErbB dimerization and activates the ErbB kinase domain, which results in auto- and trans-phosphorylation of the intracellular domains. This ErbB activation results in the activation of several pathways, including Raf–MEK–ERK and PI3K–Akt–S6K (Gu *et al*., 2005; Mei and Xiong 2008) and an increase of the intracellular Ca^{2+} (Pereira *et al*., 2012).

NRG1 type III plays an important role in the regulation of PNS myelination by activating ErbB2-ErbB3 in Schwann cells (Lemke, 2006; Birchmeier and Nave, 2008). Importantly, inactivation of NRG1 receptors and reduced levels of NRG1 lead to hypomyelination of peripheral nerves (Garrat *et al*., 2000; Michailov *et al*., 2004), while overexpression of NRG1 promotes hypermyelination (Michailov *et al*., 2004). Furthermore, increased levels of NRG1 promotes a

higher number of Schwann cells required for myelination (Taveggia *et al*., 2005), but once myelination is complete, no more axonal NRG1/ErbB signal is required to maintain myelination. In addition, NRG1 is not essential for remyelination after nerve injury (Fricker *et al*., 2013).

3.3.2. cAMP

Myelin formation is, in part, regulated by cyclic adenosine monophosphate (cAMP). Upon ligand binding, the G protein coupled receptor activates adenylyl cyclase, converting ATP into the second messenger cAMP, which activates the protein kinase A (PKA), promoting cAMP response element (CREB) signal transduction pathway. The G protein-coupled receptor 126 (Gpr126) is the only receptor identified to drive Schwann cells differentiation by elevating cAMP levels; but, once myelination is initiated, elevation of Gpr126 and cAMP levels are no longer required for myelin maintenance (Glenn and Talbot 2013). Mutation in Gpr126 causes hypomyelination and retarded axonal segregation in the PNS, however treatment with cAMP-elevating compound forskolin was sufficient to restore myelination (Monk *et al.*, 2009; Monk *et al*., 2011).

Elevation of intracellular cAMP levels in Schwann cell cultures with cell-permeable and non-hydrolyzable cAMP analogues, together with exogenous NRG1 addition, can upregulate myelin-related genes expression, including MPZ, MBP, Periaxin and Krox20, whereas negative myelin regulators are decreased, including c-Jun and Sox2 transcription factors and Remak Schwann cells' or iSC' markers, such as $p75^{NTR}$ and GFAP (Arthur-Farraj *et al*., 2011). cAMP is need to change NRG1-mediated Schwann cells survival and proliferation into a differentiation, myelination response.

3.3.3. Termination of myelination

Is there any mechanism to regulate termination of myelination? Increasing evidences are emerging which suggest a regulation of myelin termination. As mentioned above (section 3.3.1), once myelin sheaths are formed, NRG1 and ErbB signals are decreased. Similarly, expression of *ErbB2* and *Akt* are downregulated in Schwann cells. Conversely, negative regulators of myelination are upregulated (Salzer, 2015). Moreover, basal lamina, which is required for the initial radial sorting by Schwann cells, also limits myelin amount. Laminins, including α2 and α4 are suggested to act also as negative regulators of myelin, as knockout mice showed hypermyelinated fibers (Slazer, 2015), even if it was also observed a failure in myelin initiation (Wallquist *et al*., 2005).

4. Peripheral nervous system disorders

PNS disorders are broadly classified in two main type of diseases: cancer and peripheral neuropathies.

4.1. Schwann cells-origin cancer: Neurofibromatoses

Neurofibromatoses constitute a group of cancer syndromes classified in 3 different groups that exhibit tumor and non-tumorigenic manifestations (MacCollin *et al*., 2005; Ferner, 2010). Autosomic dominant neurofibromatosis type 1 (NF1) (OMIM:162200), caused by *NF1* gene mutation, is the most common of all the three types of neurofibromatosis, with an incidence of 1 in 3,500 births and it can progressed to an aggressive malignant profile, named malignant peripheral nerve sheath tumour (MPNST) (Griffiths *et al*., 2007) (see chapter 2). Neurofibromatosis type 2 (OMIM:101000) is caused by mutation of the *NF2* gene, which encodes for the tumor suppressor Merlin (Xiao *et al*., 2005; Ferner, 2007), and schwannomatosis (OMIM:162091) develops from mutation of the *INI1/SMARCB1* gene (Hulsebos, et al., 2007). Although these groups differ in their genetic bases, it is widely believed that tumorigenesis arises in cells of the Schwann cell lineage (Zhu *et al*., 2002; Parrinello and Lloyd, 2009). Currently, the therapeutic strategies available for the different Schwann cells cancer types are very limited.

4.2. Peripheral neuropathies

Peripheral neuropathies are common debilitating neurological diseases with a prevalence of about 2.4 % in the general population rising to 8 % in people over the age of 55 years. They have a broad clinical spectrum that can range from weakness and pain, severe disability and even death. A central feature of several of these neuropathies is the destruction of myelin, or demyelination. Strikingly, peripheral neuropathies have a wide variety of causes, ranging from immune assaults, metabolic disturbances or genetic defects (Martyn and Hughes, 1997). Axonal injury can promote cell body damage. In neurodegenerative diseases, prominent axonal pathology often results also in cell body loss (Wang *et al*., 2012). Certain systemic disorders with metabolic origin, such as, hepatic failure, vitamin deficiencies and uremia, among others, can cause axonal or myelin alterations. Moreover, exposure to toxins can also lead to myelin sheath disruption and breakdown, including chemotherapy (e.g. platinum drugs, vinca alkaloids and myeloma treatments, such as bortezomib), alcohol consumption, exposure to heavy metals and other toxins (Katona and Weis, 2017). Pathogen-induced disorders can also affect PNS, such as *Mycobacterium leprae*-caused leprosy (Rambukkana et al., 2002), *Borrelia burgdorferi*-induced Lyme disease (see chapter 3), human immunodeficiency virus (HIV) (Jones *et al*., 2005; Datta *et al*., 2019) and virus-associated hepatitis (Chin *et al*., 2010). A hyperactivation of immune system

can lead to autoimmune diseases (sarcoidosis, Guillain–Barré syndrome, chronic inflammatory demyelinating polyneuropathy, and diverse forms of vasculitis), which can result in demyelination (Katona and Weis, 2017), as well as hereditary disorders (e.g. Charcot-Marie-Tooth) (Berger *et al*., 2006) or unknown origin disorders, such as primary palmar hyperhidrosis (Tu *et al*., 2012).

Main goals

Malignant peripheral nerve sheath tumours (MPNSTs) are aggressive sarcomas that can arise in the context of Neurofibromatosis type 1 (NF1) in 50 % of the cases or can be formed spontaneously. MPNST has poor prognosis and 5-years survival rate. Although we have broadened our understanding of the molecular mechanisms implicated in the malignant progression of NF1-derived and sporadic MPNSTs, there are currently no specific treatments available. A better insight of the master molecular mechanisms leading to MPNST formation could lead to the development of effective and durable therapies for patients with MPNST (chapter 2).

Similarly, one of the most dangerous clinical manifestations of Lyme disease involves peripheral nervous system impairment. It is still not clear whether the pathological manifestations of the disease in the PNS are the consequence of a systemic inflammation generated by the activation of the immune system by the causative agent *Borrelia burgdorferi* or wether the bacterium could target peripheral nerves directly, including Schwann cells, which might lead to demyelination (chapter 3).

Thus, the main objectives of this thesis are summarized and highlighted below:

To investigate the molecular mechanisms driving the malignant transformation of Schwann cells to MPNSTs in order to identify novel therapeutical targets (see chapter 2).

To broaden our understanding of the molecular mechanisms involved in the phatological manifestations of Lyme disease in the PNS (see chapter 3).

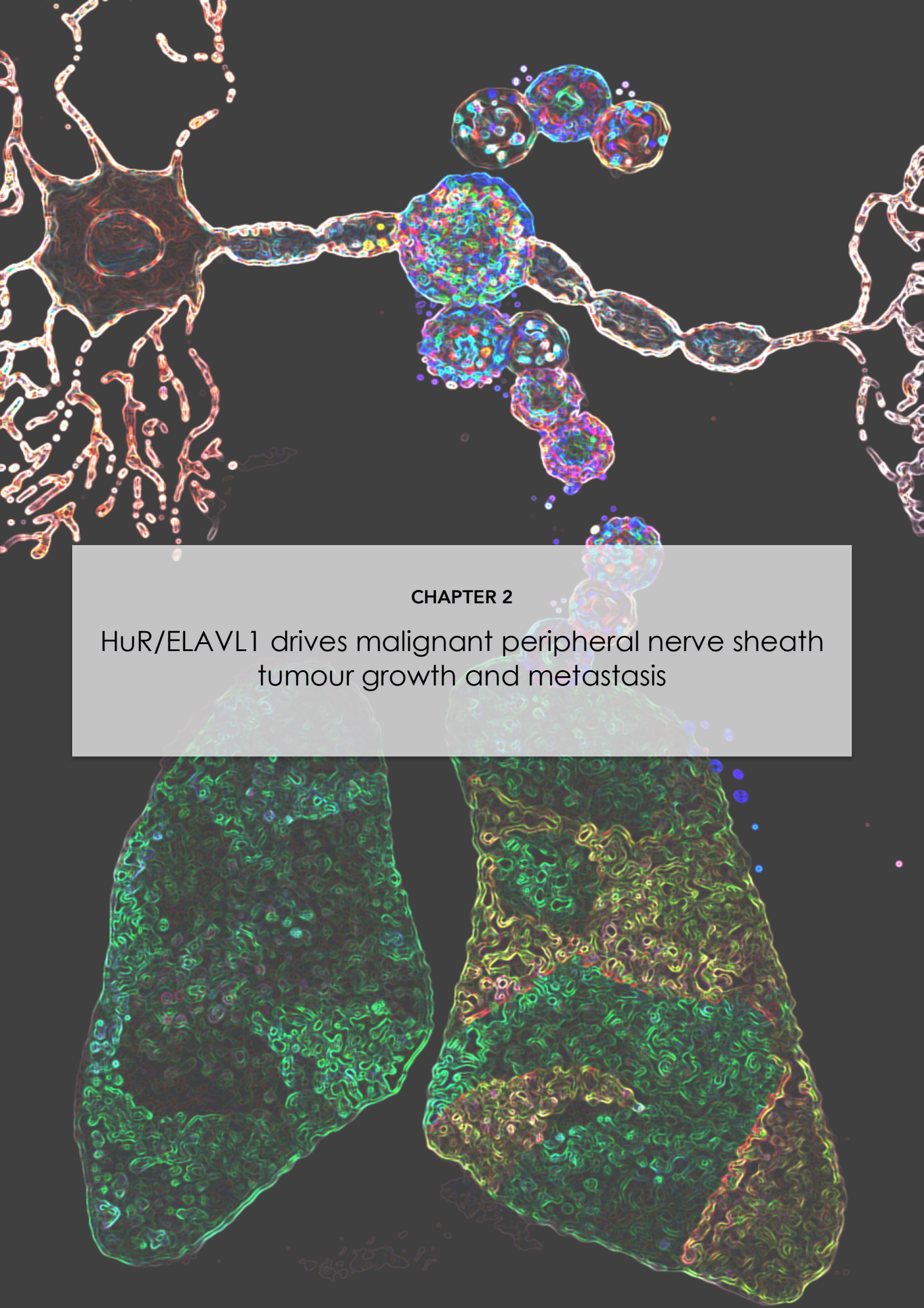

CHAPTER 2

HuR/ELAVL1 drives malignant peripheral nerve sheath tumour growth and metastasis

Introduction

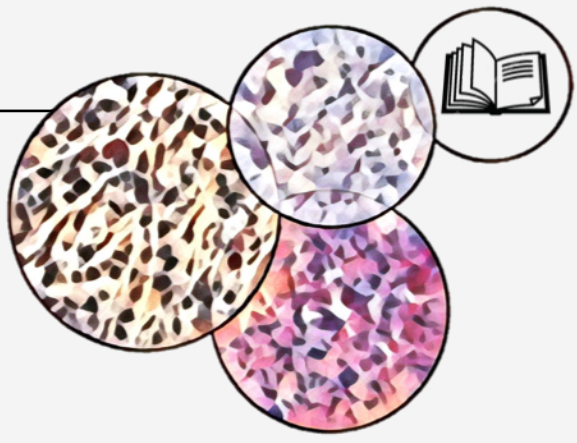

Introduction

1. Neurofibromatosis type I

Neurofibromatosis type I (NF1) is an autosomal dominant disorder which is caused by loss of the *NF1* gene, indentified in 1990 (Gutman *et al*., 1991). *NF1* encodes the tumour suppressor neurofibromin, a rat sarcoma (RAS) GTPase-activating protein, which converts active RAS-GTP to its inactive form RAS-GDP, thus negatively regulating Ras signal transduction pathway (**Figure 8**). Neurofibromin can also regulate the adenylyl cyclase (AC)/cAMP/protein Kinase A (PKA) pathway by positively controlling AC activity and intracellular cAMP levels (Tong *et al*., 2002). Nonetheless, mechanisms underlying neurofibromin-mediated cAMP regulation are still unclear, and both RAS-dependent and RAS-independent mechanisms have been implicated (Hannan *et al*., 2006).

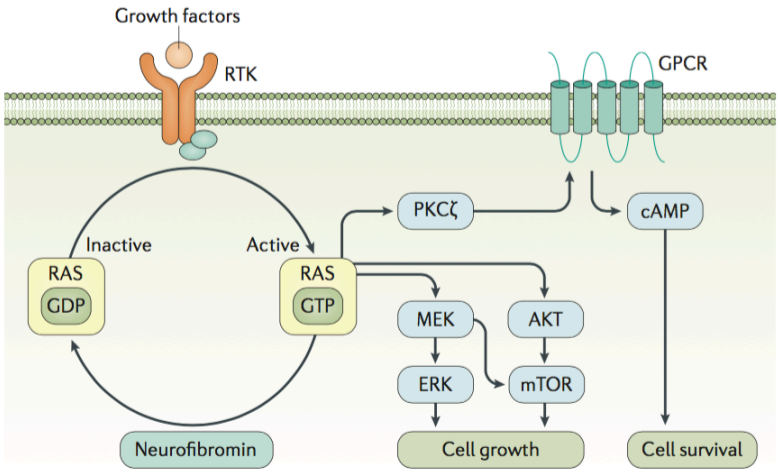

Figure 8. RAS activation and its Intracellular signaling pathways. Neurofibromin acts a RAS GTPase-activating protein, converting active RAS-GTP to its inactive form RAS-GDP, which inhibits Ras intracellular signaling pathways and thereby regulating cell growth and cell survival. Growth factors can bind to receptor tyrosine kinases (RTKs) to activate RAS signaling. RAS also controls the generation of cyclic AMP (cAMP) through protein kinase C-ζ (PKCζ) following the activation of G protein-coupled receptors (GPCRs) (adapted from Gutmann *et al*., 2017).

Loss of *NF1* gene product leads to development of benign peripheral nerve sheath tumours named neurofibromas, that are located on the skin (cutaneous neurofibromas) or can be deep-seated in large peripheral nerves (plexiform neurofibromas) (**Figure 9**.) Plexiform neurofibromas undergo malignant transformation, giving rise to malignant peripheral nerve sheath tumours (MPNSTs), a highly aggressive sarcomas which have no effective treatments. Furthermore, MPNSTs can also occur spontaneously (sporadic MPNSTs) or even after radiotherapy (Gutman *et al*., 2007).

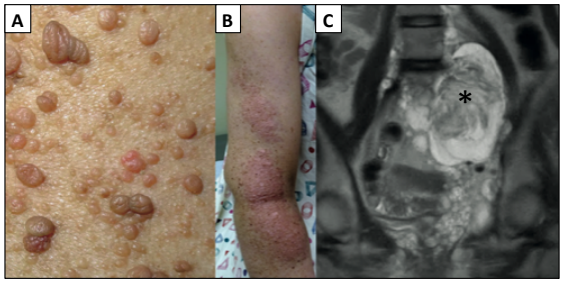

Figure 9. Dermal and plexiform neurofibromas. A) Neurofibromas can grow as nodules, found on the skin as dermal neurofibromas and **B, C**) tumours can also involve multiple branches of larger nerves (plexiform neurofibromas) which can be seen on the skin (B) or can be internal (C). **C**) MRI scan of an intra-abdominal plexiform neurofibroma (asterisk) (edited from Gutmann *et al*., 2017).

1.1. Clinical manifestations

Formation of tumours (**Figure 9**) and a wide range of non-tumoral pathological consequences are linked with neurofibromatosis 1, including pigmentary lessions known as café au lait macules (**Figure 10**), axillary and groin freckling, Lisch nodules, optic gliomas, neoplasias of the haematopoietic system, myeloid leukemias, epilepsy and learning disabilities (Ferner, 2007). About 60 % of NF1 patients present cognitive disabilities, such as defects in attetntion and social behaviour (Costa *et al*., 2002; Ferner, 2010; Anastasaki and Gutmann, 2014).

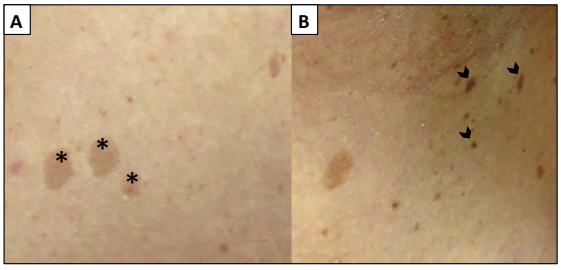

Figure 10. Pigmentary features of Neurofibromatosis 1. A) Dark spots known as café au lait macules are highlithed with asterisk. **B)** Arrowheads point axillary freckles (edited from Gutmann *et al*., 2017).

Moreover, bone abnormalities have also been linked to NF1, including osteopenia (reduction in bone mineral density) which is considered a precursor of osteoporosis, dystrophic scoliosis and tibial dysplasia. The main clinical presentations that are used as diagnostic criteria of NF1 were established by the 1987 NIH Consensus Development Conference (**Table 1**).

Table 1. 1987 NIH Consensus Development Conference diagnostic criteria. (modified from Gutmann *et al*., 2017; *see original* NIH, 1998).

NF1 Diagnostic criteria
Six or more café-au-lait macules of ≥5 mm in diameter before puberty or ≥1.5 mm in diameter after puberty
Axillary or inguinal skinfold freckling
Two or more dermal neurofibromas or one plexiform neurofibroma
Two or more iris hamartomas (Lisch nodules)
An optic pathway glioma
A distinctive long bone dysplasia involving the sphenoid wing or thinning of the long bone cortex with or without pseudarthrosis
first-degree relative with neurofibromatosis type 1

1.2. Neurofibroma development

Schwann cells homeostasis is tightly controlled by axonal signals. During embryogenesis, axons provide survival and proliferative signals, while in adult nerves, axons are required for maintaining Schwann cells differentiation state. In the NF1 context, loss of *NF1* gene in mice at E12.5, which corresponds to the late Schwann cell precursors (SCP) and early-immature Schwann cells (iSC) stage of embryonic Schwann cells development (see **Figure 2** from chapter 1), leads to neurofibroma formation. This is based on studies in which deletion of *Nf1* at E12.5 using *P0A-Cre,Nf1*$^{fl/-}$ (Zheng *et al*., 2008) and *DhhCre;Nf1*$^{fl/fl}$ mice (Wu *et al*., 2008) results in development of neurofibromas (**Figure 11**).

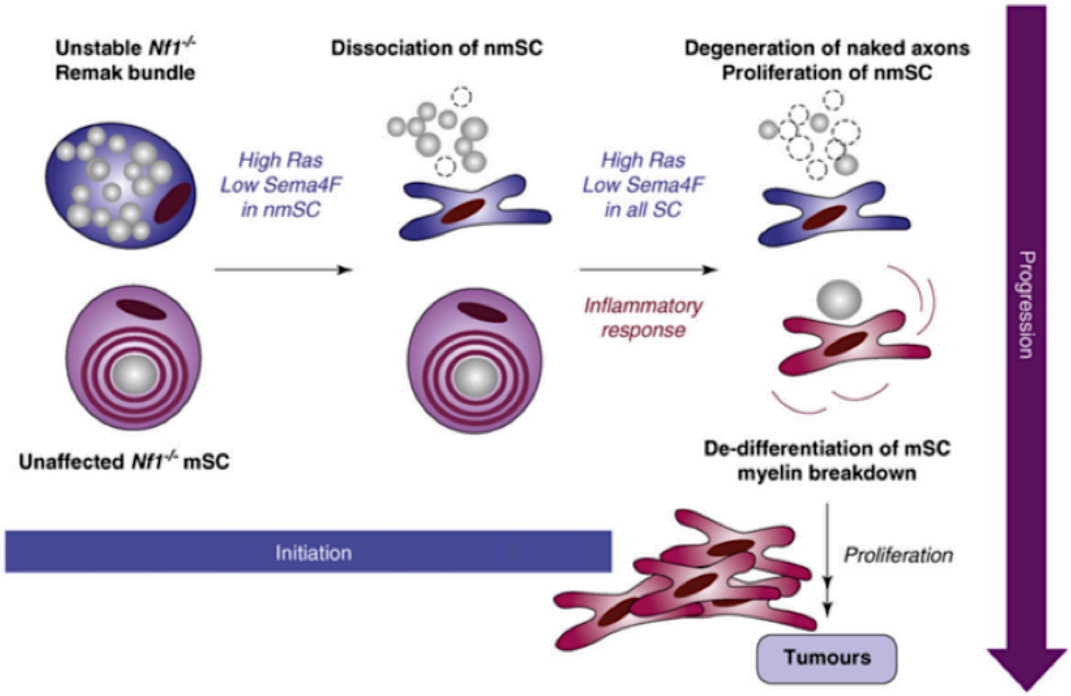

Figure 11. Schematic diagram of neurofibroma development and progression. Embryonic loss of *Nf1* in Schwann cell precursors (SCP) results in Nf1$^{-/-}$ non-myelinating (nmSC) and myelinating (mSC) mature Schwann cells. *Nf1* loss leads to Ras-Raf-ERK pathway hyperactivation in adulthood and consequent semaphoring 4F (Sema4F) downregulation, which give rise to abnormal unstable Remak bundles. Naked axons degenerate, thereby initiating an inflammatory response, a process that mimics nerve injury. Inflammatory cytokines and growth factors stimulate the proliferation of dissociated nmSC and the de-differentiation of mSC and maintenance of elevated Ras signaling. As a result, Schwann cells cannot reassociate to axons and differentiation is impaired, whereas proliferation is promoted, which finally leads to bening tumour formation (neurofibromas) (edited from Parrinello and Lloyd, 2009).

However, when *NF1* loss was triggered later at E15.5, in iSC using the *krox20Cre*,*Nf1*$^{fl/-}$ mice, neurofibromas were not formed in peripheral nerves (Zheng *et al*., 2008). Therefore, the timing of *Nf1* gene inactivation seems to be crucial for the development of neurofibromas and could be responsible for the significant variability in the severity of the clinical phenotypes of the Schwann cells disorder. SCP lacking *Nf1*, which is caused by a somatic inactivation, are not

tumorigenic but promote loss of axonal contact in Remak Schwann cells due to the loss of neurofibromin, which upregulates Ras-Raf-Erk signaling leading to a downregulation of Semaphorin 4F (Sema4F) in adulthood. These changes promote Remak Schwann cells proliferation and lead to an unestable Remak bundles with naked axons, which results in axonal degeneration and thereby an increase of inflammation and mast cells recruitment. Inflammatory response leads to demyelination and further axonal loss, whereby myelinating Schwann cells, without anti-proliferative axonal signals, dedifferentiate and continue proliferating. Thus, a favourable *Nf1*$^{+/-}$ microenvironment promotes neurofibroma progression (Parrinello *et al*., 2008; Parrinello and Lloyd, 2009) (**Figure 11**).

1.3. Malignant peripheral nerve sheath tumours (MPNSTs)

MPNSTs are highly aggressive sarcomas with a strong metastatic potential, usually to the lung (Farid *et al*., 2014). Patients with MPNSTs are largely refractory to current treatments that include radical surgical resection and/or radiation and chemotherapy, and have very poor 5-year survival rates ranging between 15 % and 50 % (Farid *et al*., 2014). Half of MPNSTs are sporadic and other 50 % of MPNST cases might arise in the context of NF1. These aggressive tumours are a leading cause of death in NF1 patients. As explained above in neurofibromas formation, it is thought that neoplastic transformation of Schwann cells is crucial for MPNST development (Farid *et al*., 2014; Carroll, 2016).

In addition to *Nf1* loss and a hyperactivated RAS signaling, MPNST formation requires the accumulation of additional genetic mutations. A number of mutations that drive MPNST pathogenesis have been identified with a surprising degree of overlap in NF1-associated and sporadic forms. These include molecular variants of the *Nf1* tumour suppressor gene that are present in all NF1 patients, and in a majority of sporadic and radiation-induced MPNSTs (Carroll, 2016; Longo *et al*., 2018). Other commonly known and essential cancer-driving genetic aberrations are found in MPNSTs, including loss of *CDKN2A*, *TP53*, *RB*, *PTEN*, or the genes encoding the PRC2 components *SUZ12* or *EED*, and amplification of platelet-derived growth factor receptor A (*PDGFRA)*, epidermal growth factor receptor (*EGFR)* or hepatocyte growth factor receptor (*HGFR*) (Natalie and Lu, 2019; Korfhage and Lombard, 2019). In addition, recent studies have shown that activation of multiple signalling pathways that include the PI3K/AKT/mTOR, RAS-RAF-MEK-ERK, WNT/β-Catenin and HIPPO-YAP/TAZ pathways, and other less ubiquitous molecular alterations involving aurora kinases and transcription factors, such as SOX9, also contribute to MPNST pathogenesis (Farid *et al*., 2014; Longo *et al*., 2018; Wu *et al*., 2018).

1.4. Treatments for neurofibroma and MPNSTs

The complexity and variability of the phenotypes observed in NF1 patients present challenges for a common effective treatment for all clinical manifestations. In addition, it is still unclear the optimal time to initiate treatment and whether treatment at a specific time can prevent the growth of tumours permanently or whether there is a need for continued treatment, which may increase treatment-related toxicity. Moreover, we still do not know whether a single therapy could be effective for at least one, never mind all, clinical manifestations. Chemotherapeutic intervention and radiation therapy are not considered good choices for the vast majority of MPNST treatment due to their slow-growing nature. Furthermore, mechanisms of chemotherapy resistance have been found in MPNSTs, including overexpression of survivin (Alaggio *et al*., 2013), Bcl-xl (Lee *et al*., 2012) and topoisomerase II (Skotheim *et al*., 2008), as well as autophagy induction (Lopez *et al*., 2011). Surgical resection of the tumour is the primary therapy for dermal neurofibromas, but plexiform neurofibromas and MPNSTs are mostly unresectable, due to their association with nerves and close localization to vital structures.

Most clinical approaches so far have targeted the hyperactivated RAS signalling pathway (Gutmann *et al*., 2013) (**Figure 12**), which is associated with neurofibroma development and has also been observed in MPNSTs, as explained above (see section 1.2 and 1.3).

Different types of drugs have emerged that inhibit promising targets involved in neurofibroma and MPNST formation, including mast cell inhibitors, MAPK pathway inhibitors, inhibitors of PI3K-AKT-mTOR pathway, canonical Wnt/ signaling inhibitors, aurora kinase inhibitors and epigenetic regulators among others have been described. MEK inhibitors are usually used for the treatment of plexiform neurofibromas (Jessen *et al*., 2013). Selumetinib is one of the most effective drugs tested so far, which partially reduces the volume of plexiform neurofibroma tumour, but not total tumour regression (Gutmann *et al*., 2017). Moreover, trying to restore neurofibromin function has been successful in cystic fibrosis (Gutmann *et al*., 2017), thus could be a promising future target to avoid neurofibroma and MPNSTs formation. However, although drugs in phase II clinical trials have been successfully tested, there is at present no Food and Drug Administration (FDA)-approved drug with proven benefits currently available.

2. RNA-binding proteins (RBPs) in cancer

Gene dysregulation is a hallmark of cancer cells. Genetic alterations in cancer cells invariably lead to a global remodelling of their transcriptome allowing them to acquire advanced functional capabilities for survival, proliferation and dissemination. MPNSTs have a unique transcriptomic signature that is clearly distinct from normal or even neurofibroma-derived primary Schwann

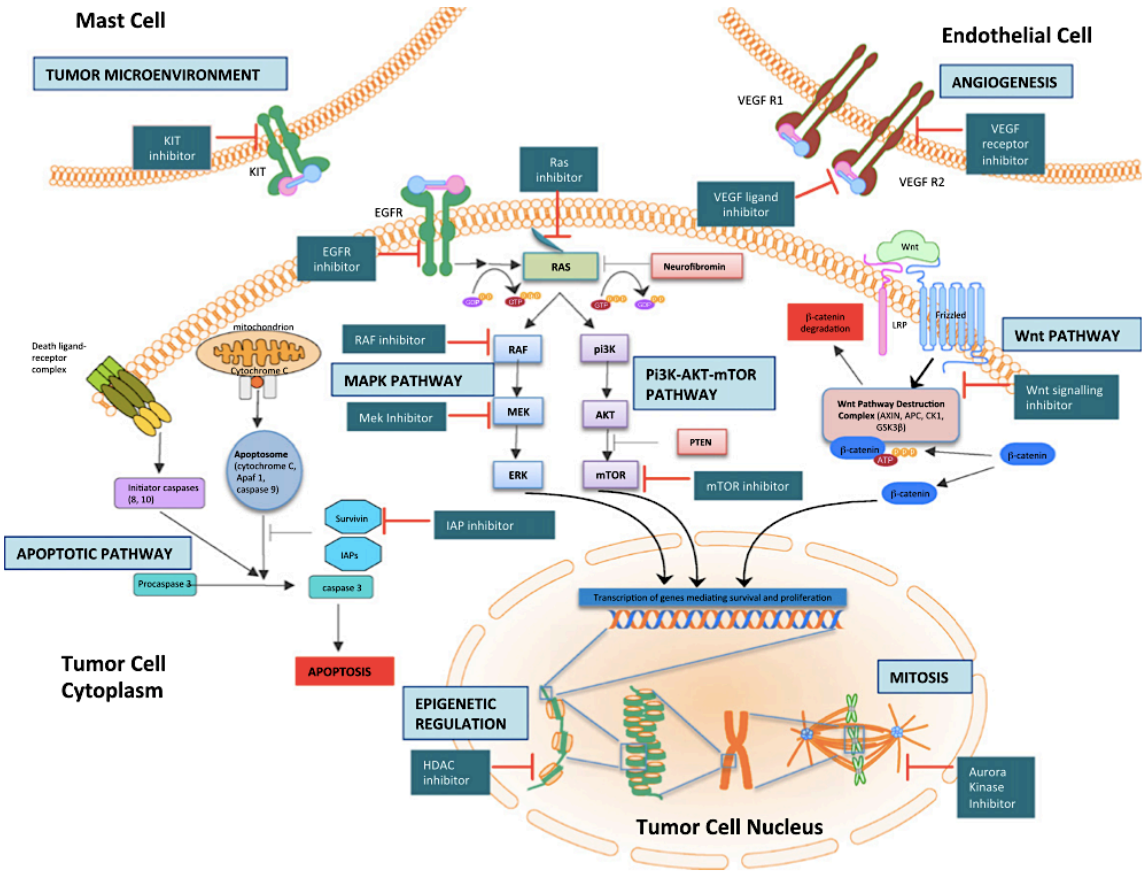

Figure 12. Pathways implicated in malignant peripheral nerve sheath tumour (MPNST) formation, and inhibitors of potential drug targets. Intracellular signaling pathways, epigenetic regulation, mitosis, angiogenesis and interactions with the tumour microenvironment are implicated in MPNST formation. Pharmacological agents inhibiting several potential targets are shown, which leads to retardation in tumour growth and brings therapeutic benefit. IAP, inhibitor of apoptotic proteins. (adapted from Farid *et al*., 2014).

cells or tumours (Miller *et al*., 2009; Jessen *et al*., 2013) and that is strongly associated with key genes controlling Schwann cells survival and proliferation.

Targeting dysregulated gene expression programs in cancers has emerged as a promising therapeutic strategy, and there is an intense focus on identifying the key molecular regulators that govern these programs (Gonda and Ramsay, 2015; Bradner *et al*., 2017). In particular, RNA-binding proteins (RBPs) are increasingly recognised as attractive targets because of their ability to regulate the type and abundance of hundreds of transcripts by modulating every aspect of their post-transcriptional life, including splicing, transport, localization, translation, stabilization and decay. Furthermore, each RBP can bind to multiple overlapping groups of functionally related RNAs, forming “RNA regulons” that control many biological functions (Bisogno and Keene, 2018).

3. Human antigen R (HuR) RBP

The Hu family of RBPs are the mammalian homologues of Drosophila embryonic lethal abnormal vision (ELAV) proteins. Three of the four members of the family, known as the neuronal Hu proteins, are highly enriched in neurons, including HuB (Hel-N1), HuC (PLE21) and HuD, that have been implicated in neuronal development, plasticity and memory (Deschênes-Furry *et al*., 2006; Pascale *et al*., 2008). The fourth member, known as Human antigen R (HuR), HuA or ELAV-like 1 (ELAVL1), is ubiquitously expressed and is involved in the regulation of many cellular processes (Ma *et al*., 1996).

3.1. HuR structure

HuR is the product of *Elavl1* gene, located on chromosome 19p13.2 (Ma and Furneaux, 1997). Its structure consists of 3 RNA recognition motifs (RRMs), termed RRM1, RRM2 and RRM3, which are highly conserved among the four Hu members, and a hinge region containing the HuR nucleo-cytoplasmic shuttling (HNS) domain (Winseck *et al*.,2002). It is localized between RRM2 and RRM3 regions and is responsible for the shuttling of HuR from the nucleus to the cytosol due to a nuclear localization sequence (NLS) and a nuclear export sequence (NES) (Wolpowitz *et al*., 2000).

3.2. HuR function

HuR can bind to its mRNA targets through poly-A tail recognintion by RRM3 domain or when RRM1 and RRM2 regions recognize and bind to the adenylate/uridylate (AU) and U-rich elements (AREs) of its target transcripts, which are conserved sequences located in the 3′ untranslated region (3′ UTR) and 5′ UTR of its target mRNAs (López de Silanes *et al*., 2004). The direct interaction between HuR and AREs generally promotes mRNA stability and protein translation. HuR usually competes with microRNAs and other RBP by blocking the association with target transcripts and therefore preventing the recruitment of those targets to sites of mRNA decay (Durie *et al*., 2011). Nevertheless, HuR can also cooperate with different microRNAs and RBP (Srikantan and Gorospe, 2012) and it has also been implicated in supressing translation of mRNAs, such as *Wnt5a* (Leandersson *et al.,* 2006) and *p27* (Kullmann *et al*., 2002).

In basal conditions, HuR is predominantly nuclear, where it associates with pre-mRNA introns affecting splicing, regulating the export of mature mRNAs and antagonizing microRNA-mediated repression of miRNAs (Mukherjee *et al*., 2011; Srikantan and Gorospe, 2012). However, upon stimulus, HuR shuttles to the cytoplasm (described in section 3.3), where it modulates the stabilization and translation of its target mRNAs, such as hypoxia-inducible factor *(HIF)-1α*, *p53* (Mazan-Mamczarz *et al*., 2003), prothymosin α (Lal *et al*., 2005), cytochrome c (Kawai *et al*.,

2006), heme oxygenase-1 (Kuwano *et al*., 2009), among many others. After completing the stabilization of target mRNAs, HuR returns to the nucleus (**Figure 13**).

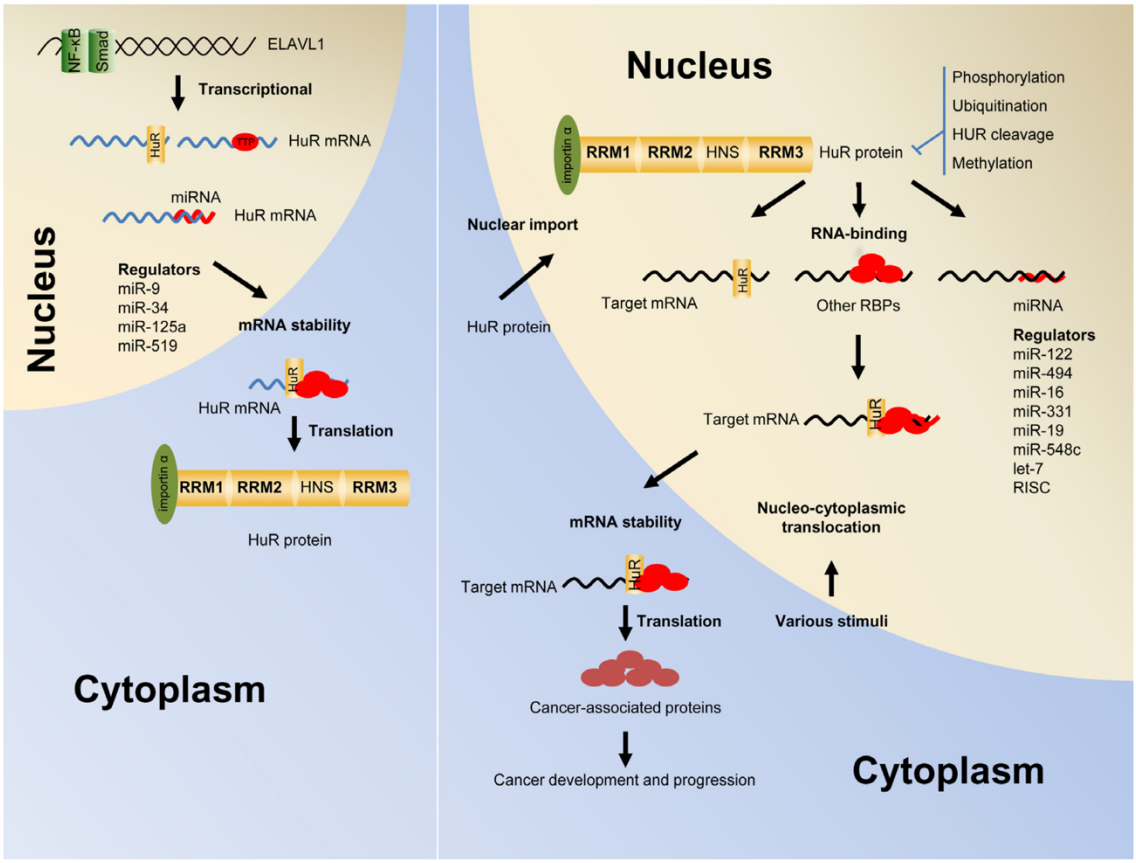

Figure 13. HuR autoregulation and its function. Nuclear factor-κB and Smad control the HuR mRNA expression at the transcriptional level. HuR mRNA is also regulated by other RBPs (such as TTP and RNP C1), miRNAs and HuR protein itself, regulating HuR stabilization and translation (**left panel**). In the nucleus, HuR binds to the pre-mRNAs participating in their splicing and nuclear processing and collaborates with the mRNA export. In the cytosol, HuR enhances (and could also inhibit) mRNA stability and translation of several proteins implicated in cancer development and progression (**right panel**). The nucleocytoplasmic shuttling mechanism of HuR is regulated by HuR phosphorylation, ubiquitinylation, methylation and HuR cleavage. Moreover, other RBPs and several miRNAs compete or cooperate with HuR (modified from Wang *et al*., 2013).

3.3. HuR regulation and nucleocytoplasmic transport

The association of HuR and mRNA targets is modulated through posttranslational modifications, including phosphorylation by protein kinase C (Doller *et al*., 2008), the mitogen-activated protein kinase (MAPK) p38 (Lafarga *et al*., 2009), and the checkpoint kinase Chk2 (Abdelmohsen *et al*., 2007), which also modulates HuR levels by influencing its ubiquitination (Abdelmohsen *et al*., 2009).

Nucleocytoplasmic transport of HuR across nuclear envelope involves HNS either several transport machinery components, including CRM1, transportins 1 and 2, and importin-1α

(Güttinger *et al*., 2004; Rebane *et al*., 2004). Furthermore, stress signals have been reported to induce HuR shuttling from the nucleus into the cytosol, such as ultraviolet radiation (Wang *et al*., 2000), chemical compounds (McMullen *et al*., 2003), lipopolysaccharide (LPS) (Lin *et al*., 2011), hypoxia (Levy *et al*., 1998), viral infection (Dickson *et al*., 2012) and hormone treatment (Sheflin *et al*., 2001), among others. Most of the reported exogenous stress stimuli result in the accumulation of HuR protein in the cytoplasm.

Nuclear factor-κB and Smad control the HuR mRNA expression at the transcriptional level. HuR mRNA stabilization and consequent protein translation is also regulated by other RBPs, such as tristretaprolin (TTP) and RNP C1, miRNAs and HuR protein itself (Srikantan and Gorospe, 2012; Wang *et al*., 2013) (**Figure 13**).

3.4. HuR in cancer

The first evidence about the implication of Hu/ELAV proteins in carcinogenesis was came with the discovery of HuD protein as a tumour antigen present in people suffering from paraneoplastic encephalomyelitis (a condition associated with small-cell lung cancer) (Szabo *et al*., 1991). HuR family member was reported to play a critical role in carcinogenesis and cancer progression in several cancers. In fact, clinical data supports evidence to link HuR overexpression with advanced stage, positive lymph nodes, and poor survival in cancer patients (Wang *et al*., 2013). HuR upregulation is frequently observed in different cancer types, including prostate, skin, kidney, ovarian, colon, pancreatic and breast cancer, wherein regulates all essential cancer traits for cancer development and progression (proliferation, survival, angiogenesis, evasion of immune response, invasion and metastasis) by regulating specific mRNA targets, such as *Cyclin D1*, *SIRT1*, *Mdm2*, *VEGF,* and *Snail* among many others (Abdelmohsen and Gorospe, 2010) (**Figure 13**).

Aims of the study

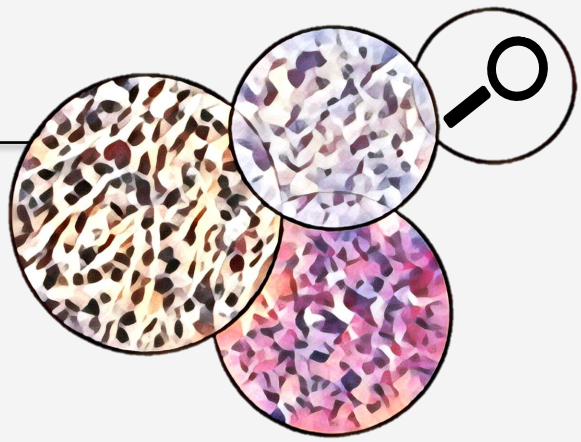

Aims of the study

Human antigen R (HuR) RNA-bindig protein (RBP) is frequently upregulated in different cancers and it has been linked with regulation of several essential aspects for cancer progression. Work in our laboratory previously showed that HuR was highly expressed in immature Schwann cells (iSC), a stage of development characterized by a peak in Schwann cell proliferation, wherein HuR was bound to and regulated several key mRNAs, co-ordinately regulating them at the post-transcriptional level (Iruarrizaga-Lejarreta *et al*., 2012). As iSC subsequently differentiate, they lost HuR expression, coinciding with a decrease in the production of HuR targets encoding proliferation and apoptosis proteins were downregulated. Notably, many of the HuR targets in iSC become re-expressed in MPNSTs, and those mRNAs protein products play key roles in tumour growth, as shown for SOX9 (Miller *et al*., 2009) and BRD4 (De Raedt *et al*., 2014).

In unpublished work from our group, we have found that HuR is strongly upregulated in both NF1-derived and sporadic malignant peripheral nerve sheath tumours (MPNSTs) (**Figure 14**).

Overall, the high abundance and cytoplasmic localisation of HuR in MPNSTs lead us to hypothesize that HuR might have a key role in driving essential transcriptomic programs in sporadic and NF1-derived MPNSTs. Therefore, the main **objectives** of this project are highlighted below:

Aim 1. To investigate the role of Human antigen R (HuR) in MPNSTs:

- **1.1.** Identify intracellular pathways regulated by HuR leading to MPNST formation/progression.

Aim 2. To explore whether HuR can induce malignant transformation of Schwann cells, leading to MPNST formation.

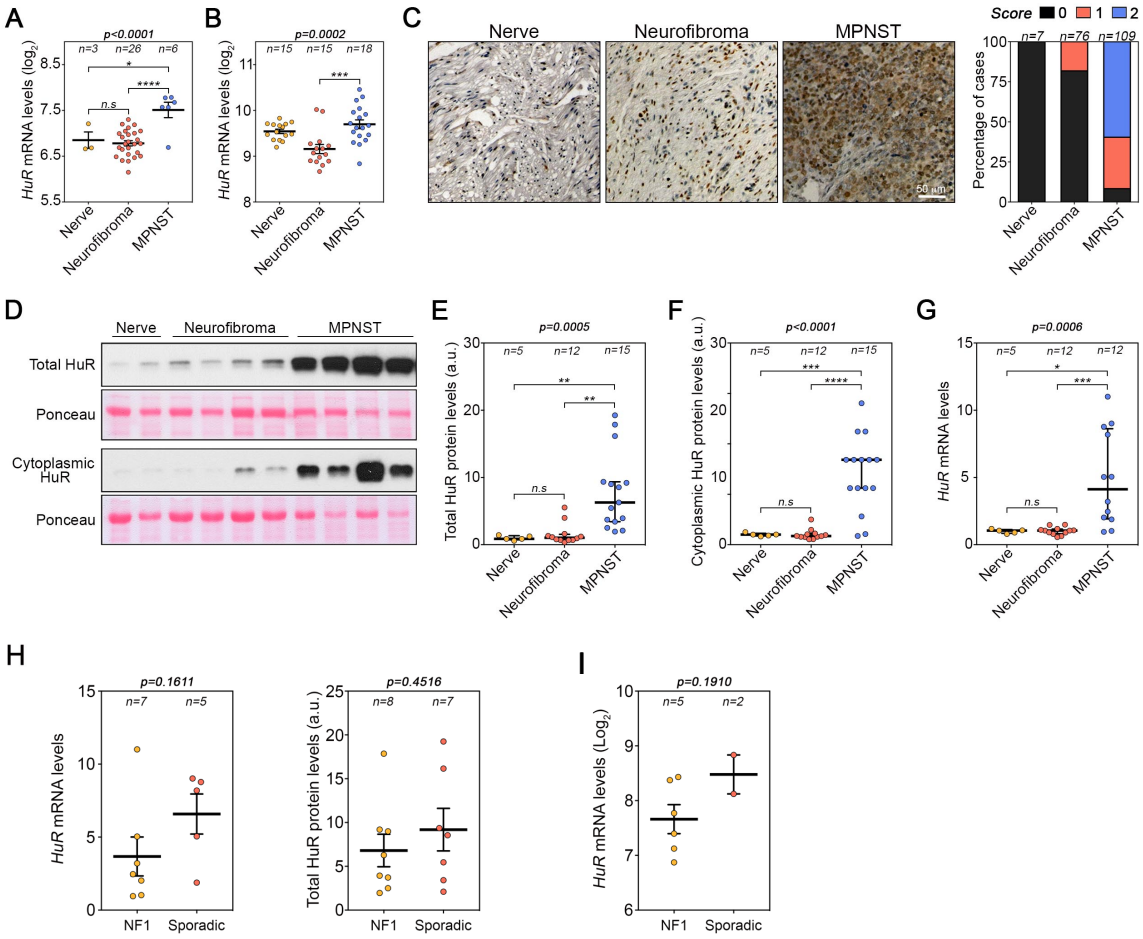

Figure 14. HuR is upregulated in human MPNSTs. A, B) HuR mRNA levels in nerves, neurofibromas and MPNSTs from **A)** patients and **B)** mouse models from the Jessen cohort (GSE 41747) (Jessen *et al*., 2013). **C)** Representative immunohistochemistry micrographs of endogenous HuR protein levels (brown) in a tissue microarray panel of human nerves (n=7), benign neurofibromas (n=76) and MPNSTs (n=109) (Pytel *et al*., 2010). Score 0 represent low HuR staining, Score 1 intermediate staining and Score 2 represent high HuR staining. **D–G)** Western blot and RT-qPCR analysis of HuR levels in a panel of human nerves (n=5), benign neurofibromas (n=12) and MPNSTs (n=15) obtained from Stanmore Musculoskeletal Biobank. **D)** Representative immunoblots showing total and cytoplasmic HuR levels in a selection of samples. **E–F)** Graphs representing densitometry analysis of **E)** total HuR protein levels, corrected for Ponceau red signals, **F)** cytoplasmic HuR protein levels, corrected for Ponceau red signals. **G)** HuR mRNA levels as measured by RT-qPCR analysis. **H, I)** Assesment of HuR expression levels in NF1-derived MPNSTs and sporadic MPNSTs. **H)** *HuR* mRNA and protein levels from a human frozen cancer panel (D-G), and **I)** the average HuR mRNA levels in MPNST cell lines in Miller cohort (GSE 14038) (Miller *et al*., 2009). Data are presented as mean ± SEM (A,B) or median with interquartile range (E–G); one-way ANOVA with Tukey's multiple-comparisons test. Individual p-values and number of samples (n) per group is indicated. n.s= not significant; *p<0.05; **p<0.01, ***p<0.001; ****p<0.0001 (modified from Iruarrizaga-Lejarreta, 2014; thesis version) .

Material and methods

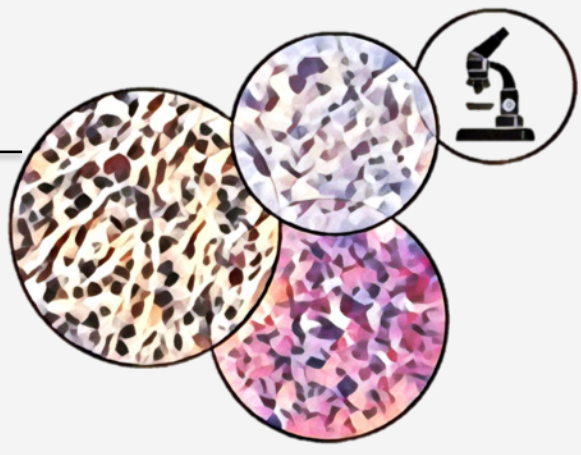

Material and Methods

1. Animals

All experiments were performed in accordance with Spanish Guide for the Care and use of Laboratory animals, and by the International Animal Care and Use Committee Standards. All procedures were performed following the ethical guidelines established by the Biosafety and Welfare Committee at CIC bioGUNE.

Animals were handled in accordance with the European Communities Council Directive at CIC bioGUNE [Assessment and Accreditation of Laboratory Animal Care (AAALAC) accredited facility], under conventional housing conditions (22 ± 2 °C, 55 ± 10 % humidity, 12-hour day/night cycle) and fed with a standard diet (Harlan Teklad) with *ad libitum* access to food and water. All possible efforts were made to minimize animal suffering and the number of animals used.

Female Hsd:Athymic Nude-Foxn1$^{nu/nu}$ mice of 8–12 weeks of age were used for xenograft experiments (purchased from Harlan Laboratories) and experimental lung metastasis.

2. Patient samples

Patient samples were obtained from different sources in accordance with the ethical standards of the institutional and/or national research committee and with the 1964 Helsinki declaration and its later amendments or comparable ethical standard:

1) the Stanmore Musculoskeletal Biobank, a satellite of the UCL/UCLH Biobank (HTA Licence Number 12055), which was approved by the National Research Ethics Committee (reference 15/YH/0311). This specific study was approved by the NREC-approved UCL/UCLH Biobank Ethical Review Committee (reference EC17.14).

2) Peripheral nerves for Schwann cell culture were retrieved from donors after consent under NHS Blood and Transplant (NHSBT) research study entitled 'Collection of peripheral nerves for control cells for brain tumour treatment research', NHSBT study 61. Full research project title was 'Identifying and validating molecular targets in low grade brain tumours; REC number: 14/SW/0119; IRAS reference: 153351.

3. Cell lines

3.1. Malignant Peripheral Nerve Sheath Tumours' (MPNSTs') derived cell lines: S-462, ST-88-14, 90-8 and STS-26T

MPNST cell lines S-462, ST88-14, 90-8 and sporadic MPNST STS-26T cell line were obtained from Nancy Ratner (Cincinnati Children's Hospital Medical Centre) (Miller *et al*., 2006; Watson

et al., 2013). ST-8814, 90–8 and S462 were derived from neurofibromatosis 1 (NF1) patients with confirmed loss of heterozygosity at the *NF1* locus for all 3 cell lines, and with the 90–8 cell line additionally showing a known microdeletion of *NF1*, whereas the sporadic MPNST line STS26T had no mutations detected in the 60 exons of the *NF1* gene. The cells were maintained in Dulbecco's modified Eagle Medium (DMEM; Thermo Fisher Scientific) supplemented with 10 % (v/v) fetal bovine serum (FBS; Thermo Fisher Scientific) and 1 % (v/v) antibiotic/antimycotic (A/A; Thermo Fisher Scientific) under standard culture conditions at 37 °C and 5 % CO_2.

3.2. immortalized human Schwann cells (iHSCλ2)

Immortalized normal human Schwann cell line (iHSCλ2) was obtained from Nancy Ratner (Cincinnati Children's Hospital Medical Centre). The cells were maintained in DMEM supplemented with 10 % FBS and 1 % A/A under standard culture conditions at 37 °C and 5 % CO_2.

3.3. immortalized plexiform Schwann cells (ipNF SC)

Immortalized plexiform neurofibroma-derived Schwann cells [hTERT NF1 ipNF95.11b (ATCC® CRL3390™); hereafter ipNF SC] was purchased from ATCC. The cells were maintained in DMEM supplemented with 10 % FBS and 1 % A/A under standard culture conditions at 37 °C and 5 % CO_2.

3.4. Normal human Schwann cells (NH SC)

Normal human Schwann cells (hereafter NH SC) were isolated from the sural nerves of donors with informed consent (see below). Withdrawn nerves were stripped of their epineurium and fascicles were separated from the remaining interfascicular epineurium. Fascicles were cut into 2 mm-long pieces and incubated in humidified conditions and 10 % CO_2 for 7-14 days in DMEM (Gibco) with 10 % FBS (Sigma-Aldrich); 500 U/mL penicillin/streptomycin (Gibco) and 2.5 mg/mL Amphotericin (Gibco). Fascicles were then digested in DMEM with 10 % FBS; 500 U/mL penicillin/streptomycin; 0.8 U/mL dispase grade I (Sigma-Aldrich) and collagenase type 1A 160 U/mL (Sigma-Aldrich). The resulting Schwann cells were then amplified on plates coated with 0.1 mg/mL Poly-L-lysine in DMEM with 20 % FBS; 100 U/mL penicillin/streptomycin; 0.5 mM Forskolin (Sigma-Aldrich); 2.5 mg/mL Amphotericin 2.5 mg/mL; 2.5 mg/ml Insulin (Sigma-Aldrich); 10 nM β1-heregulin (Sigma-Aldrich) and 0.5 mM IBMX (Sigma-Aldrich). Amplified Schwann cells were plated in DMEM with 10 % FBS in the absence of β1-heregulin for at least 24 hours before analysis.

3.5. HEK293FT

HEK293FT cells were maintained in complete growth medium [DMEM, 10 % FBS, 0.1 mM non-essential amino acids (Gibco), 1 mM sodium pyruvate (Gibco), 2 mM L-glutamine (Gibco) and 1% A/A] under standard culture conditions at 37 °C and 5 % CO_2.

4. *In vitro* experimental procedures

4.1 Silencing or overexpression of genes by lentivirus

4.1.1 Production and concentration of lentivirus in HEK293FT cells

HEK 293FT cells were plated in their complete growth medium [DMEM, 10 % FBS, 0.1 mM non-essential amino acids (Gibco), 1 mM sodium pyruvate (Gibco), 2 mM L-glutamine (Gibco) and 1 % A/A] three days before transfections.

For each transfection, DNA-Lipofectamine 2000 (Invitrogen) complexes were prepared as follows: 36 µl of Lipofectamine 2000 were diluted in 1.5 ml Opti-MEM (Gibco) in a sterile 5 ml tube and incubated for 5 minutes at room temperature (RT). During those 5 minutes, packaging Mix (PSPAX2 and VSVG) and each pLenti expression plasmid DNA (**Table 2**) were diluted in 1.5 ml of Opti-MEM in a separate sterile 5 ml tube. After the 5 minutes incubation period, diluted DNA was combined with the diluted Lipofectamine 2000 and incubated for 20 minutes at RT to allow the DNA-Lipofectamine complexes to form. During this time, HEK293FT cells were trypsinized and resuspended at a density of 1.2 x 10^6 cells/ml in Opti-MEM containing 10 % FBS. 5 ml of cell suspension (6 x 10^6 cells) are required for each lentivirus. After the 20 minutes incubation, DNA-Lipofectamine 2000 complexes and the 5 ml of the HEK293FT cells' suspension were added to a 100 mm tissue culture dish containing 5 ml Opti-MEM with 10 % FBS. Cells were incubated overnight in a humidified 5 % $C0_2$ incubator, at 37 °C. The next day, the transfection mix was replaced with 10 ml complete growth medium, without antibiotics and cells were incubated overnight at 37 °C and 5 % $C0_2$. Virus-containing supernatants were harvested 72 hours post-transfection by removing medium into a 15 ml sterile tube. Supernatants were centrifuged and filtered through a Millex-HV 0.45 µm PVDF filter (Millipore). Three volumes of clarified supernatants were then combined with 1 volume of Lenti-X concentrator (Millipore) and the mixture was incubated overnight at 4 °C in a rotator. Next day, samples were centrifuged, supernatants discarded and pellet containing the viral particles resuspended in 1 ml sterile phosphate buffer saline (PBS, Gibco). Viruses were kept in 250 µl aliquots into single-use microtubes and stored at -80 °C.

Table 2. List of plasmids used for lentivirus production.

Recombinant DNA	Abbreviation used in manuscript	Source
pLKO.puro.empty	sh Ctrl	Sigma-Aldrich
pLKO.puro.shHuR#1	sh HuR#1 (sh H#1)	Sigma-Aldrich
pLKO.puro.shHuR#2	sh HuR#2	Sigma-Aldrich
pLKO.puro.shβ-cat#1	sh β-Cat#1	Addgene
pLKO.puro.shβ-cat#2	sh β-Cat#2	Addgene
pLKO.puro.shBRD2#1	sh BRD2#1	GE Healthcare
pLKO.puro.shBRD2#2	sh BRD2#2	GE Healthcare
TRIPZ -non-silencing shRNAmir-Ctrl	TRIPZ-sh *i*Control	Dharmacon
TRIPZ -shHuR#3	TRIPZ-sh *i*HuR	Dharmacon
pcw107.puro.empty	pcw107–EV	Addgene
pcw107.puroBETA-CATENIN (S33A, S37A, T41A, S45A)	pcw107–β-Cat (4A)	Addgene
pLKO.neo.empty	sh Control (shC)	Addgene
pLKO.neo.shHuR	sh HuR#3 (shH#3)	Sigma-Aldrich
pCDH-EF1-FHC	pCDH-EV	Addgene
pCDH-puro-cMyc	pCDH-c-MYC	Addgene
plenti6.2 EGFP-SOX9	pLenti6.2-EV	Kindly provided by Vincent J Hearing, NCI
plenti6.2 EGFP	pLenti6.2-SOX9	Kindly provided by Vincent J Hearing, NCI
pWPI-EV	pWPI-EV	Addgene
pWPI-E2F1	pWPI-E2F1	Addgene
pWPI-E2F2	pWPI-E2F2	Addgene
pWPI-E2F3	pWPI-E2F3	Addgene
pCDH-empty	pCDH-EV	Kindly provided by Ruben D. Carrasco, Harvard University
pCDH-BCL9	pCDH-BCL9	Kindly provided by Ruben D. Carrasco, Harvard University
TRIPZ-HA	TRIPZ-HA	Kindly provided by Ruben D. Carrasco, Harvard University
TRIPZ-HuR	TRIPZ-HuR	Kindly provided by Ruben D. Carrasco, Harvard University

4.1.2 Infection of cells with lentiviral particles

For lentiviral infections, MPNST cells, iHSCl2 and ipNFSC were treated with the corresponding lentiviral particles in the presence of hexadimethrine bromide (8 μg/ml) (comercial name Polybrene, Merck). After 48 h of transduction, medium was replaced with freshly supplemented growth medium and infected cells were then selected by treatment with either 4 μg/ml puromycin (Thermo Fisher Scientific) for 2 days or G418 sulfate (Thermo Fisher Scientific) at 50

µg/mL for 5 days in growth medium without A/A. Puromycin or geneticin-resistant cells were grown or frozen for future use.

For the inducible knockdown plasmids, after infection and selection, MPNST cells were treated with 0.5 µg/ml doxycycline every 24 h for 3 days. Infection efficacy was tested by western blot and RT-qPCR analysis. For rescue experiments, cells were first infected with control or β-Catenin overexpressing plasmids and selected with puromycin, and then further infected with shHuR#3 lentiviral particles followed by selection with geneticin, as above. After infection and selection, MPNST cells were replated at specific densities for the different functional assays. All assays were conducted in triplicate, with at least 3 independent experiments performed for each assay.

4.2. ATP assay

1,000 lentivirus-transduced cells per well were seeded in triplicate in 96-well plates and 3 days after plating, ATP levels were measured with the ATPlite Luminescence Assay System (Perkin Elmer) following the manufacturer' s instructions. Luminescence values were collected in a Veritas Microplate Luminometer (Turner Biosystems), quantification performed using a standard curve and values normalized with values obtained at 1 day after plating.

4.3. Colony formation assay

For colony formation assay, 150 lentivirus-transduced cells per well were seeded in triplicate in 12-well plates and cultured in supplemented growth medium for up to 10 days. Cells were then washed with 1X PBS, fixed with 10 % formalin solution (Merck) and stained with 0.1 % (w/v) crystal violet (Merck) in 20 % methanol. After gentle rinsing with ddH_2O, the retained dye was extracted with 10 % (v/v) acetic acid and the absorbance measured at 595 nm on a Synergy HT spectrophotometer (Biotek).

4.4. Anchorage-independent growth assay (Soft agar)

Soft agar assay was used to study the anchorage-independent growth capacity of lentivirus-transduced cells. A total of 45,000 cells were mixed in supplemented growth medium (at 37 °C) containing 0.3 % low-melting-point agar (Fermentas) and then seeded in triplicate in a 6-well plate on top of a layer of 0.6 % agar (Thermo Fisher Scientific). Cells were allowed to grow for 3-4 weeks in culture, with supplementation of complete growth medium every week until colonies were visible by eye. The soft agar plates were scanned (HP Scanjet G4050, Hewlett Packard) and colonies (composed of at least 20 cells) quantified using the ImageJ software (https://imagej.nih.gov/ij/).

4.5. 5-bromo-2-deoxyuridin (BrdU) incorporation assay

To assess DNA synthesis and proliferation, 5,000 lentivirus-transduced MPNST cells were seeded in triplicate onto glass coverslips in 24-well plates, and cultured in supplemented growth medium for 2 days. Cells were incubated with 10 µM BrdU (Merck) for the last 2 h of culture before fixation with 2 M hydrochloric acid and immunolabeling with anti-BrdU antibody (1:1000 dilution; Roche) diluted in antibody diluent solution (ADS; PBS containing 5 % goat serum and 1 % BSA) overnight at 4 °C. Next day, samples were incubated in goat anti-mouse Cy3 secondary antibody (dilution 1:100; Jackson ImmunoResearch Laboratories) and nuclear stained with 50 ng/ml DAPI (Merck) for 30 minutes. Then, samples were mounted in Dako fluorescence mounting medium (Dako) and analyzed by 20x AxioImager.D1 fluorescent microscope objective (Zeiss). The number of BrdU+ cells were counted and expressed as a percentage of total number of DAPI+ cells.

4.6. Cell growth assay

Transduced cells with corresponding lentivirus, 10,000 cells per well were seeded in triplicate in 24-well plates and cultured in supplemented growth medium for 2 days before trypsinization and counting using a hemocytometer. Growth was determined relative to the number of cells initially plated (10,000). For culture under growth-limiting conditions, cells were cultured in 2 % FBS for 3 days before counting. Log2 of fold growth (as above) was determined (negative values indicate cell death).

4.7. Cell cycle analysis

Lentivirus-transduced MPNST cells were seeded in triplicate on 6-well plates (150,000 cells per well) and 2 days after seeding, adherent and non-adherent cells were collected, washed with PBS, and fixed and permeabilized with cold 75 % ethanol at –20 °C overnight. DNA staining was performed with 50 µg/ml propidium iodide (PI) solution (Thermo Fisher Scientific) in the presence of 50 µg/ml RNase A (Macherey-Nagel). Cell cycle was analysed using a FACS CANTO (BD Biosciences) flow cytometer. Data were analyzed using FACSDiva software (BD Biosciences).

4.8. Apoptosis

For apoptosis analysis, lentivirus-transduced MPNST cells were seeded in triplicate on 6-well plates (150,000 cells per well) and 48 h later, adherent and non-adherent cells were collected and stained with Annexin V–FITC and PI (Immunostep) following the manufacturer's instructions. Cells were fixed with 1 % formaldehyde before analysis using a FACS CANTO flow cytometer. Data were analyzed using FACSDiva software.

4.9. Senescence associated-X-gal staining

To assess senescence, MPNST transduced cells were seeded in triplicate onto glass coverslips (10,000 per coverslip) in 24-well plates, and cultured in supplemented growth medium for 2 days. Cells were fixed and analyzed for SA-β-Gal activity using the Senescence Detection Kit (Calbiochem) following the manufacturer's instructions at 37 °C overnight or until blue colour was developed. Cells were rinsed with PBS and mounted using fluorescent mounting medium (Dako). Pictures were acquired using an optical microscope and β-Gal+ cells were counted and expressed as a percentage of total number of cells.

4.10. Protein extraction and analysis

4.10.1. Total protein extraction and quantification.

150,000 cells were seeded per well (6-well plates) in duplicate and after 48 h total proteins were extracted. Cells were washed twice with PBS and scraped in 200 µl RIPA lysis buffer [500 ml stock solution: 1.6 mM NaH_2PO_4 (Merck), 8.4 mM Na_2HPO_4 (Merck), 0.1 % Triton X-100 (VWR), 0.1 M NaCl (Ambion), 0.1 % SDS (Fisher Scientific) and ddH_2O] supplemented with sodium deoxycholate (Merck), 1 mM sodium fluoride and 1X protease and phosphatase inhibitor cocktails (Roche). Next, lysates were snap frozen, defrosted, vortexed and incubated on ice in order to enhance the lysis process. After that, lysates were centrifuged for 30 minutes, at 13,000 rpm and 4 °C) and the supernatants were collected. Total protein content was quantified using BCA protein assay (Bio-Rad) in a Synergy HT spectrophotometer (Biotek). Bovine serum albumin (BSA) was used as protein standard.

For xenograft tumours and human cancer samples, a small piece of tissue was excised and homogenized in supplemented RIPA buffer using the Precellys Homogenizer (Bertin technologies).

For cytosolic, cell membrane and nuclear lysates isolation from cells, the subcellular proteome extraction kit (Calbiochem) was used as described by the manufacturer. Protein content was quantified as described above (for protein quantification from total cell lysis) using BCA protein assay. The purity of cytoplasmic and nuclear fractions was examined by Western blotting using antibodies anti-GAPDH and anti-Histone H3, respectively.

4.10.2. Western blotting

Protein aliquots (8–20 µg each) were denaturalized in 5X loading buffer [0.25 M Tris, pH 6.8 (VWR), 5 % SDS, 2-mercaptoethanol (Merck), 50 % glycerol and bromophenol blue powder (Merck)] for 5 min at 95 °C. Samples were separated on 8 %, 11 % or 15 % tris-glycine SDS-

polyacrylamide gels with 1X Tris-Glycine-SDS buffer (Bio-Rad) and transferred to a 0.2 μm nitrocellulose membranes (Amersham) with 1X transfer buffer [Glycine (VWR), Tris (Trizma base, VWR), 20 % Methanol (Panreac AppliChem) and ddH_2O]. Membranes were blocked with 5% non-fat dry milk in 1X TBS [50 mM Tris, 150 mM NaCl (Sigma-Aldrich), pH 8.0) containing 0.1% Tween20 (TBS-T, Sigma-Aldrich)] and then incubated with specific primary antibodies (**Table 3**) at 1/1000 concentration in TBS-T overnight at 4 °C. Next day, membranes were washed three times with TBS-T, incubated with HRP (Horse peroxidase)-linked rabbit or mouse secondary antibodies at 1/5000 concentration in blocking solution for 1 h, at RT and samples were developed with ECL substrate (BioRad). Membranes were exposed to X-ray films (Fujifilm) in a Curix 60 Developer (Agfa).

Table 3. List of Antibodies used for Western blotting.

Target protein	Host	Company
AURKA	Rabbit	Cell Signaling
AURKB	Rabbit	Cell Signaling
BRD2	Rabbit	Abcam
BRD3	Mouse	Abcam
BRD4	Rabbit	Abcam
β-ACTIN	Mouse	Sigma-Aldrich
β-CATENIN	Rabbit	Santa Cruz Biotechnology
BCL-9	Mouse	Santa Cruz Biotechnology
CDK2	Rabbit	Cell Signaling
CDK4	Rabbit	Cell Signaling
CDK6	Rabbit	Cell Signaling
C-MYC	Rabbit	Cell Signaling
CYCLIN D1	Rabbit	Cell Signaling
CYCLIN D2	Rabbit	Cell Signaling
CYCLIN E	Rabbit	Cell Signaling
E2F1	Rabbit	Cell Signaling
E2F2	Rabbit	Abcam
E2F3	Mouse	Santa Cruz Biotechnology
GAPDH	Mouse	Abcam
HISTONE-H3	Mouse	Abcam
HISTONE-H3 (ACETYL K27)	Mouse	Abcam
HUR	Mouse	Santa Cruz Biotechnology
p21	Rabbit	Cell Signaling
P27	Rabbit	Cell Signaling
p-RB (SER780)	Rabbit	Cell Signaling
RB	Rabbit	Santa Cruz
SOX9	Rabbit	Cell Signaling
TAZ	Rabbit	Cell Signaling
TEAD1	Rabbit	Cell Signaling
TEAD2	Rabbit	Cell Signaling
TEAD3	Rabbit	Cell Signaling
TWIST1	Rabbit	Cell Signaling
YAP1	Rabbit	Cell Signaling
Mouse IgG HRP linked	-	Cell Signaling
Rabbit IgG HRP linked	-	Cell Signaling

4.11. Immunohistochemistry (IHC)

Tumour xenografts and lungs were dissected out, fixed in 10 % formalin solution overnight and embedded in paraffin. Sections (5-µm thick) were dried, deparaffinized, rehydrated and subjected to antigen retrieval and then incubated overnight with primary antibodies. After three washes with PBS, sections were incubated for 1 h with secondary antibodies, followed by EnVision+ System HRP system (Dako) and incubated with peroxidase/diaminobenzidine (DAB) for colour development. The slides were washed in ddH_2O, counterstained with Haematoxylin, dehydrated and mounted with permanent media. Standard haematoxylin and eosin staining was also performed. For analysis of HuR expression in patient samples, a tissue microarray panel consisting of 7 normal nerve, 76 neurofibromas and 109 MPNSTs (Pytel *et al.*, 2010) was subjected to HuR IHC. Digital images were then acquired with an AXIO Imager A1 microscope (Carl Zeiss AG). The sections were scored in a blinded manner for staining intensity (0–2). Antibodies used for IHC are highlighted below (**Table 4**).

Table 4. List of Antibodies used for Immunohistochemistry (IHC).

Target protein	Host	Company
Cleaved Caspase-3	Rabbit	Cell Siganaling
HuR	Mouse	Santa Cruz Biotechnology
Ki67	Rabbit	Abcam

4.12. Ribonucleic acid (RNA) extraction and processing

4.12.1. RNA isolation

Total RNA was isolated from MPNST cells (150,000 cells/ well in 6-well plate), after washing in PBS, with Trizol Reagent (Thermo Fisher Scientific) according to the manufacturer's instructions. Total RNA was treated with DNase I (Invitrogen) and cleaned with Genejet RNA Cleanup and Concentration Kit (Thermo Scientific). RNA concentration was determined using RNA BR Qubit® assay kit (Life Technologies) in a Qubit® 2.0 Fluorometer (Life Technologies) according to the manufactureŕs instructions. RNA integrity was assessed by electrophoresis in a 1 % agarose gel.

4.12.2. Reverse transcription (RT) followed by quantitative Polymerase Chain Reaction (qPCR) analysis

A minimum of 200 ng of total RNA and up to 1 µg was reversed transcribed in a 20 µl reaction containing dNTPs (Invitrogen), random hexamer primers (Invitrogen), 0.1 M DTT (Invitrogen), RNaseOUT inhibitor (Thermo Fisher Scientific), 5X Buffer (Invitrogen) and M-MLV Reverse Transcriptase (Thermo Fisher Scientific) according to the manufacturer's instructions. Reactions

were carried out in a Thermocycler (Biometra). Resulting cDNA was diluted 1/5 with 80 µl RNase-free H_20 (Sigma-Aldrich). qPCR was performed in a 5 µl reaction mix containing 2.5 µl PerfeCTa® SYBR® Green SuperMixes and FastMixes™ with low ROX reference dye (Quanta Biosciences), 0.5 µl 10 µM primers and 2 µl cDNA. All reactions were performed in triplicates in a Viia7 Real-Time PCR System (Applied Biosystems). 40 cycles with a melting temperature of 60 °C, and 30 seconds of each step were used. Specific primers were designed with Primer Blast database (https://www.ncbi.nlm.nih.gov/tools/primer-blast/) (**Table 5**) and synthesized by Sigma-Aldrich. Quantification was performed using the ΔΔCT method and data was normalized using *GAPDH* mRNA as a standard.

Table 5. Human primers used for qPCR.

Target gene	Forward (5'->3')	Reverse (5'->3')
AurkA	GCTGGAGAGCTTAAAATTGCA	TTTTGTAGGTCTCTTGGTATGTG
AurkB	TGAGGAGGAAGACAATGTGTGGCA	AGGTCTCGTTGTGTGATGCACTCT
Bcl9	CTGGAGAGGAAGCGTGTGAG	GTCTTGATACCAGGAGGCCAG
BRD2	CGGTTCCTTGCGGTCAAGAT	CAGCAACCCTGCATTCCCTT
BRD3	CCATGGTGAGCAAGGGCGCT	GCACGGCCTTCAGCTGCTCC
BRD4	AACCTGGCGTTTCCACGGTA	GCCTGCACAGGAGGAGGATT
CDK2	CTCCACCGAGACCTTAAACCTCAG	TCGGTACCACAGGGTCACCA
CDK4	CTTCTGCAGTCCACATATGCAACA	CAACTGGTCGGCTTCAGAGTTTC
CDK6	GATCTCTGGAGTGTTGGCTGCATA	GGCAACATCTCTAGGCCAGTCTTC
c-Myc	AATGAAAAGGCCCCCAAGGTAGTTATCC	GTCGTTTCCGCAACAAGTCCTCTTC
Ctgf	ACCGACTGGAAGACACGTTTG	CCAGGTCAGCTTCGCAAGG
Ctnnb1	CATCTACACAGTTTGATGCTGCT	GCAGTTTTGTCAGTTCAGGGA
CyclinD1	CAGCAACCCTGCATTCCCTT	TGTGAAGTTCATTTCCAATCCG
CyclinD2	CTTCAAGTGCGTGCAGAAGGA	CCAAGAAACGGTCCAGGTAAT
CyclinE	ACAATAATGCAGTCTGTGCA	ATAGACTTCACACACCTCCA
Cyr61	TGAAGCGGCTCCCTGTTTT	CGGGTTTCTTTCACAAGGCG
E2f1	TATGGTGATCAAAGCCCCTC	AGATGATGGTGGTGGTGACA
E2f2	GCCTATGTGACTTACCAGGATATCC	CCTTGACGGCAATCACTGTCT
E2f3	GAGACTGAAACACA AGTCC	CCTGAGTTGGTTGAAGCC
Gapdh	ACCCACTCCTCCACCTTTGA	CTGTTGCTGTAGCCAAATTCGT
HuR	GGTTCGGAGGCCCCGTTCAC	CCAGCCGGAGGAGGCGTTTC
Lef1	ACCCCACCTCTTGGCTGGCA	TGTGGGGACCAGGAGGACCG
p16	GGCACCAGAGGCAGTAACCA	GGACCTTCGGTGACTGATGATCTAA
p21	AAGACCATGTGGACCTGTCACTGT	GAAGATCAGCCGGCGTTTG
p27	GAAGCCTGGCCTCAGAAGAC	CCATTCCATGAAGTCAGCGAT
Sox9	TATGGTGATCAAAGCCCCTC	AGATGATGGTGGTGGTGACA
Tead1	GAGACTGAAACACA AGTCC	CCTGAGTTGGTTGAAGCC
Tead2	ACCCACTCCTCCACCTTTGA	CTGTTGCTGTAGCCAAATTCGT
Tead3	GGTTCGGAGGCCCCGTTCAC	CCAGCCGGAGGAGGCGTTTC
Tead4	TTGCCAGGCCAAGCCGGAAC	CGGGCCCTGCAGGAGACTCA
TAZ	GCCTATGTGACTTACCAGGATATCC	CCTTGACGGCAATCACTGTCT
Twist1	ACCCCACCTCTTGGCTGGCA	TGTGGGGACCAGGAGGACCG
YAP1	GGCACCAGAGGCAGTAACCA	GGACCTTCGGTGACTGATGATCTAA

4.13. RNA immunoprecipitation

Immunoprecipitation (IP) protocol of endogenous mRNA-HuR complexes was performed as described before (Jayaseelan *et al.*, 2014; Keene *et al.*, 2006). In brief, whole MPNST cell lines (S-462, STS-26T, ST88-14 and 90-8) were cultured in 150 mm plates until they were 80 % confluent. Whole cell lysates were homogenized in lysis buffer [100 mM KCl (Ambion), 5 mM $MgCl_2$, 10 mM HEPES pH 7.0 (Sigma-Aldrich), 0.5 % NP-40, 1 mM DTT (Invitrogen), 100 units/ml RNase OUT (Invitrogen) and 1X Protease Inhibitor Cocktail (Roche) in ddH_2O], incubated for 30 min on ice, and centrifuged at 13 000 rpm, 4 °C for 30 minutes. 500 µl of lysates were pre-cleared by incubating with 25 µl of protein A-sepharose 4B beads (Merck) and anti-mouse IgG (BD Biosciences) in 1 ml of NT2 buffer (50 mM Tris pH 7.4, 150 mM NaCl, 1 mM $MgCl_2$, 0.05 % NP-40) and incubating under rotation for 30 min. The pre-cleared extracts were then divided and incubated with 50 µl of protein A-sepharose 4B beads, pre-coated 1 h with 15 µg anti-HuR (Santa Cruz Biotechnology) or anti-mouse IgG antibodies (BD Biosciences Pharmingen). After incubation, beads were washed 5 times with 1 ml NT2 buffer and bound RNA recovered after proteinase K digestion (Roche) and phenol chloroform extraction. An equal volume of extracted RNA from each sample was then used for cDNA synthesis and analysed by qPCR.

4.14. RNA Sequencing

ST88-14 cells were infected with shHuR#1 ot its control (shCtrl) lentivirus, selected with puromycin for 2 days, replated and then RNA was isolated 2 days later with TRIzol Reagent (Thermo Fisher Scientific) following manufacturer's instructions. The quantity and quality of the RNAs were evaluated using Qubit dsDNA Assay Kit (Thermo Fisher Scientific) in a Qubit® 2.0 Fluorometer (Life Technologies) and Agilent RNA Nano Chips (Agilent Technologies), respectively. Next, RNA samples were processed by Genome Analysis platform at CIC bioGUNE and bioinformatic analysis was performed by Dr. José Luis Lavín (CIC bioGUNE) and Dr. Juanjo Lozano (CiberEHD). In brief, TruSeq RNA Sample Preparation v2 kit (Illumina Inc.) was used following the TruSeq® RNA Sample Preparation v2 Guide (Part #15026495 Rev. F). In brief, starting from 500 ng of total RNA, mRNA was purified, fragmented and primed for cDNA synthesis. cDNA first strand was synthesized with SuperScript-II Reverse Transcriptase (Thermo Fisher Scientific) for 10 min at 25 °C, 15 min at 42 °C, 15 min at 72 °C and pause at 4 °C. cDNA second strand was synthesized with Illumina reagents at 16 °C for 1 hour. Then, A-tailing and adaptor ligation were performed. Finally, enrichment of libraries was achieved by PCR (30 sec at 98 °C; 15 cycles of 10 sec at 98 °C, 30 sec at 60 °C, 30 sec at 72 °C; 5min at 72 °C and pause at 10 °C). Afterwards, libraries were visualized on an Agilent 2100 Bioanalyzer using Agilent High

Sensitivity DNA kit (Agilent Technologies) and quantified using quantitative PCR with Kapa Library Quantification Kit (Master Mix and DNA Standards, KAPA – Biosystems) and Qubit dsDNA HS DNA Kit (Thermo Fisher Scientific). RNAseq-libraries single-Read sequencing of 50 nucleotides was carried out in a HiScanSQ platform (Illumina Inc.). Reads were trimmed for adapters using cutadapt (Martin, 2011) and aligned to hg38 genome using STAR (Dobin *et al.*, 2013). All libraries were divided in 2 pools, and each pool was sequenced in 2 lanes at a final concentration of 4.3 pM (each library was intended to be sequenced at 0.473 and 4.3 pM per lane, respectively). Quantification in expected counts from genes and isoforms were computed by RSEM (Li and Dewey, 2011) using genecode annotation v.26 [*https://www.gencodegenes.org/*]. We use TMM method to estimate scale factors between samples followed by the voom function in *limma* to convert them into $\log_2$counts per million (logCPM). Finally, differential expression between shCtrl and shHUR#1-infected cells were evaluated by LIMMA bioconductor package (Ritchie *et al.*, 2015). Genes with a fold change of 2 and FDR < 0.05 were considered as significantly different.

4.15. ChIP-Seq

Chromatin immunoprecipitation was performed essentially as described (Fontanals-Cirera *et al.*, 2017). In brief, ST88-14 cells were infected with shHuR#1 or its control (shCtrl) lentivirus, selected with puromycin for 2 days, replated and then 2 days later cross-linked with 1 % formaldehyde for 10 min at RT and reaction quenched with 125 mM glycine for 5 min. The isolated nuclei were resuspended in nuclei lysis buffer and sonicated using a Bioruptor Sonicator (Diagenode). The samples were immunoprecipitated with the appropriate antibodies overnight at 4 °C. Protein G beads (Thermo Fisher Scientific) were added and incubated for 1 h, and the immunoprecipitates were washed twice, each with low-salt, high-salt and LiCl buffer. The eluted DNA was reverse-crosslinked and purified using PCR purification kit (Qiagen). The quantity and quality of the DNAs were evaluated with Qubit dsDNA HS DNA Kit (Thermo Fisher Scientific) and Agilent High Sensitivity DNA kit (Agilent Technologies), respectively. Sequencing libraries were prepared by Genome Analysis Platform at CIC bioGUNE, following TruSeq® ChIP Sample Preparation Guide with the corresponding kit (Illumina Inc.). Input ChIP DNA (5–10 ng) was blunt–ended and phosphorylated. A single 'A' nucleotide was added to the 3' ends of the fragments in preparation for ligation to an adapter that has a single-base 'T' overhang. The ligation products were purified and accurately size-selected by agarose gel electrophoresis. Size-selected DNA was purified and PCR-amplified to enrich for fragments that have adapters on both ends. Resulting libraries were visualized on an Agilent 2100 Bioanalyzer using Agilent High Sensitivity DNA kit (Agilent Technologies) and quantified using Qubit dsDNA HS DNA Kit (Thermo

Fisher Scientific). ChIPseq libraries were single-read sequenced for 51 nucleotides in a HiSeq2500 (Illumina).

The sequencing data were mapped to the hg38 genome assembly, biological replicates merged and peak calling was performed using Model-based analysis of ChIP-seq (MACS) 2 (Zhang *et al.*, 2008) to identify regions of ChIP-Seq enrichment over background (input) with an enrichment threshold of adjusted p-value < 0.01.

4.16. Data Analysis

4.16.1. BRD proteins occupancy

The BRD samples were processed using NaviSE (Ascension *et al.*, 2017) with default parameters (bowtie2 aligner with --very-sensitive parameter). In order to find the signal at enriched regions, occupancy was calculated using a sliding window of 50 nucleotides, and counting the number of reads within each window. Values were adjusted to reads per million (rpm)/bp units. Enriched regions were determined as the set of peaks obtained in MACS2 in shCtrl cells with q-value < 10^{-5}. The windows lying within the enriched regions were selected and used for the violin plots. The difference in the distributions of BRD4 was compared using a Welch's t test.

4.16.2. Gene Ontology Analyses

Gene ontology analyses for RNA-Seq dataset were performed using Gene Set Enrichment v3.0 (GSEA, http://www.broadinstitute.org/gsea/index.jsp) (Subramanian *et al.*, 2005). Gene sets used were obtained from the Molecular Signatures Database v6.0 (MSigDB, http://www.broadinstitute.org/gsea/msigdb/index.jsp, C1 hallmark gene sets or C6 oncogenic signatures) or were manually curated from published data set. Normalized enrichment score (NES) denotes the degree to which the gene-set is overrepresented at the top or bottom of a ranked list of genes. Genes categorized with negative or positive NES are downregulated or upregulated, respectively. The nominal P value describes the statistical significance of the enrichment score. The FDR q value is the estimated probability that a gene set with a given NES represents a false positive finding. The GSEA summary plots in Figure 2R.2B, 2R.6C and 2R.9A were plotted with Microsoft Excel software, and show upregulated and downregulated gene sets. Circle size is proportional to the core enriched genes, i.e. the subset of members within a gene set that shows statistically significant, concordant differences between two biological states and contribute most to the NES. Gene sets with FDR q values < 0.25 are plotted as a function of NES. Circle colours represent FDR q values. Gene enrichment analysis for transcriptional network was performed using ToppGene suite

(https://toppgene.cchmc.org/enrichment.jsp (Chen *et al.*, 2009a).

4.16.3. Gene Expression datasets

We collected the microarray expression profiles of human normal nerves, neurofibromas and MPNSTs from the GEO public resource (http://www.ncbi.nlm.nih.gov/geo/) and the accession numbers are GSE41747 (Jessen *et al.*, 2013) and GSE14038 (Miller *et al.*, 2009). RNA-Seq data of control and Lats1/2-deficient Schwann cells were from GSE99040 (Wu *et al.*, 2018). The normalized values from these datasets were analysed for gene expression scores. YAP activated signature was according to the list of activated genes provided in (Tremblay *et al.*, 2014), and PD901 activated genes and JQ1 activated/repressed genes (FC of 1.5 and FDR values < 0.05) in MPNST cells were obtained from (De Raedt *et al.*, 2014).

4.16.4. Supervised network analysis

4.16.4.1. Assignment of active promoters and enhancers bound by BRD proteins

Hg19 TSS coordinates were obtained from (ftp://ccg.vitalit.ch/epdnew/H_sapiens/005/db/promoter_ucsc.txt) and active promoter regions were defined as H3K4me3 peaks lying within the +/-5kb range of TSSs. If one peak falls within more than one promoter region, the one whose TSS coordinate was the closest to the peak midpoint was assigned to that peak. Human enhancer regions and their target genes were obtained from the GeneHancer database (Fishilevich *et al.*, 2017). H3K4me1 and H3K27ac peaks were defined as overlapping if the midpoint of either peak was falling within the peak range of the other and only the overlapping region was considered as the range. If H3K4me1 + H3K27ac overlapping peaks resided within an enhancer region, this enhancer was considered active. If more than one enhancer contained a H3K4me1 + H3K27ac overlapping peak, the one whose midpoint was the closest to the midpoint of the overlapping peak was assigned to that peak. Binding peaks of BRD2, BRD3 and BRD4 were assigned to active promoters and enhancers if the peak midpoint fell within their regions. If a peak fell within more than one active promoter/enhancer region, the one whose midpoint was the closest to the midpoint of the peak was considered the target of the peak.

4.16.5. Gene Regulatory Network (GRN) inference and analysis

GRNs for shHuR and its control (shCtrl) phenotypes were inferred from RNA-seq data, BRD-bound active promoters and enhancers, and literature knowledge. First, differentially expressed genes between the two phenotypes were identified with the p-value cutoff 0.001 and the

absolute fold change 1.5. In addition, genes were not considered differentially up-regulated if logCPM was below 10 in at least one of the three RNA-seq replicates. Since not only BRD proteins but also Transcription factors targeted by BRD proteins could contribute to the gene expression changes between shCtrl and shHuR samples, we retrieved from MetaCore (Clarivate Analytics) (Nikolsky *et al.*, 2005) experimentally validated transcriptional regulatory interactions among differentially expressed, direct and indirect BRD target Transcription factors whose promoters and/or enhancers are active (download date: May 2018). Then, these retrieved interactions were merged with BRD-target binding interactions to form the prior knowledge network (PKN) and this PKN was "contextualized" to each of the two phenotypes using an algorithm developed in (Crespo *et al.*, 2013). Briefly, this algorithm assumes that each cellular phenotype is a Boolean stable steady state attractor of a given network, and removes interactions that are inconsistent with the Booleanized gene expression states. This gene expression Booleanization was performed by treating differentially up-regulated genes as "1" and down-regulated genes as "0". The GRN was clustered based on Gene Ontology categories, and was visualized in Cytoscape version 2.7.0 (Shannon *et al.*, 2003).

5. *In vivo* experimental procedures

5.1. Mouse xenografts

Xenograft experiments were carried out following the ethical guidelines established by the Biosafety and Welfare Committee at CIC bioGUNE following the recommendations from AAALAC. All inoculations were carried out in female Hsd:Athymic Nude-*Foxn1*$^{nu/nu}$ mice of 8–12 weeks of age. For constitutive HuR inactivation experiments, STS-26T cells were infected with shCtrl or shHuR#1 lentivirus (**Table 2M.1**). For HuR overexpression studies, iHSCλ2 or ipNFSC were infected with control (TRIPZ-HA) or HA-tagged (TRIPZ-HuR) (Zhou *et al*., 2018) lentivirus. Cells were selected with puromycin for 2 days. 1 X 10^6 cells mixed in 1:4 PBS:Matrigel were injected subcutaneously in the right back flank of mice under standard procedures and iHSCλ2 or ipNFSC-injected mice were fed with doxycycline diet (Open Standard Diet with 2,000 ppm Doxycycline, Research Diets Inc). Tumour volume was measured biweekly with calipers, and mice were sacrificed 5 weeks after injections.

For inducible HuR inactivation experiments, STS-26T cells were infected with sh *i*Ctrl or sh *i*HuR#1 lentivirus and selected with puromycin for 2 days. 1 X 10^6 cells mixed in 1:4 PBS:Matrigel were injected subcutaneously in the left and right back flanks of mice respectively under standard procedures. After the tumour reached 100 mm^3 average volume (about 20 days), as assessed by palpation and calliper measurements, mice were randomized into 2 groups and fed

with either a standard chow or doxycycline diet (Open Standard Diet with 2,000 ppm doxycycline, Research Diets Inc), as above, for a further 10 days when maximal tumour volume allowed under institutional protocol was reached. The mice were then sacrificed, tumours extracted and processed for biochemical and histological analyses. Tumour weight was measured at endpoints. Tumour volume was measured biweekly with callipers. For both experiments, tumour volume was calculated using the formula: $V = (\pi \times length \times width^2)/6$, where length is the longest tumour diameter and width the perpendicular diameter. For inducible HuR inactivation experiment, endpoint volume of each individual xenograft was normalized to tumour volume at start of doxycycline diet treatment, and expressed as log2 fold change.

5.2. Experimental lung metastasis assay

To examine metastatic capacity, the experimental lung extravasation assay was used, which models the late phases of the invasion-metastasis cascade. For constitutive HuR inactivation experiments, STS-26T cells were infected with shCtrl or shHuR#1 lentivirus and selected with puromycin for 2 days. 1 X 10^6 cells were resuspended in PBS and injected in the lateral tail vein of mice. Mice were euthanized 4 weeks later, and lungs were processed for histology upon perfusion with 10 % formalin through the trachea. Lung architecture was analysed by standard H&E staining, and number and area of visible lung metastases were quantified using ImageJ software. For inducible HuR inactivation and HuR overexpression experiments, STS-26T cells were infected with sh *i*Ctrl or sh *i*HuR#1 lentivirus and selected with puromycin for 2 days. 1 X 10^6 cells, resuspended in PBS, were injected in the lateral tail vein of mice. Three mice from each group were euthanized 2 weeks after injection to examine basal formation of lung metastases. The rest of mice were randomized into 2 groups and fed with either a standard chow or doxycycline diet (Open Standard Diet with 2,000 ppm doxycycline, Research Diets Inc) for a further 3 weeks, after which formation of lung metastases were examined and quantified as above. For HuR overexpression studies iHSCλ2 and ipNFSC were infected with control (TRIPZ-HA) or HA-tagged (TRIPZ-HuR) (Zhou *et al*., 2018) lentivirus and selected with puromycin for 2 days. 1 X 10^6cells were resuspended in PBS and injected in the lateral tail vein of mice, as above. Mice were fed with doxycycline diet, and then euthanized 5 weeks later and lungs were processed for histology upon perfusion with 10% formalin through the trachea.

6. Statistics

All analyses were done using Microsoft Excel or GraphPad Prism 6.00 (San Diego California,

www.graphpad.com). Data are shown in dot plots or histograms as mean ± SEM, $p < 0.05$ is deemed statistically significant. Statistical analysis was performed by two-tailed unpaired Student's t tests, Mann Whitney U test, one-way ANOVA with post hoc analysis by Tukey's multiple comparison test, or Two-way ANOVA with Tukey's multiple comparisons test, or as indicated. Quantifications were performed from a minimum of three experimental groups.

7. Accession Codes

All the microarray, RNA-seq and ChIP-Seq data are deposited in the NCBI Gene Expression Omnibus (GEO) with the accession number GSE120687.

Results

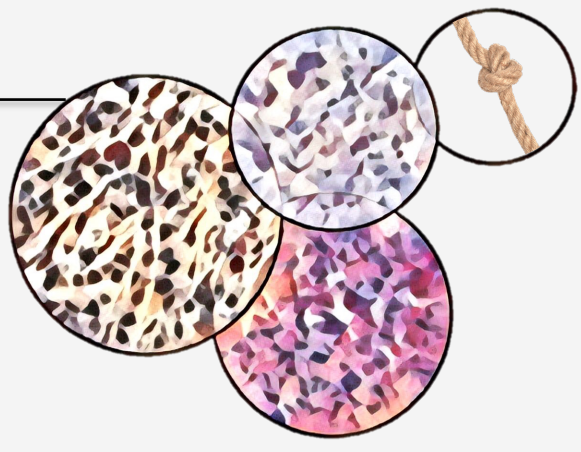

Results

1. RIP-Chip identifies Human antigen R (HuR) mRNA targets associated with key cancer traits

The high abundance and cytoplasmic localisation of HuR in malignant peripheral nerve sheath tumours (MPNSTs), as described above (in Chapter 2: Aims of the study), point to a potentially important role in both sporadic and NF1-derived MPNSTs. Thus, to examine the biological significance of the high HuR levels in MPNSTs, we analysed HuR-associated mRNAs on a genome-wide scale by ribonucleoprotein (RNP) immunoprecipitation (RIP) under conditions that preserve endogenous RNA-protein interactions, followed by microarray detection of bound RNAs (RIP-Chip) (Keene *et al*., 2006; Jayaseelan *et al*., 2014). Notably RIP-chip preferentially enriches for the stably–bound subsets of putative mRNA targets rather than transient targets that might be detected by RNP crosslinking. This favours the identification of targets forming part of functional complexes that lead to mRNA target stabilization and increased translation (Simone and Keene, 2013).

RIP analysis was performed using an anti-HuR antibody or control anti-IgG antibody in cytoplasmic extracts from human neurofibroma (n=8) and MPNST (n=12) tumour samples from a frozen cancer panel obtained from the Stanmore Musculoskeletal Biobank (UK). The isolated RNA was identified by microarray analysis (**Figure 15**).

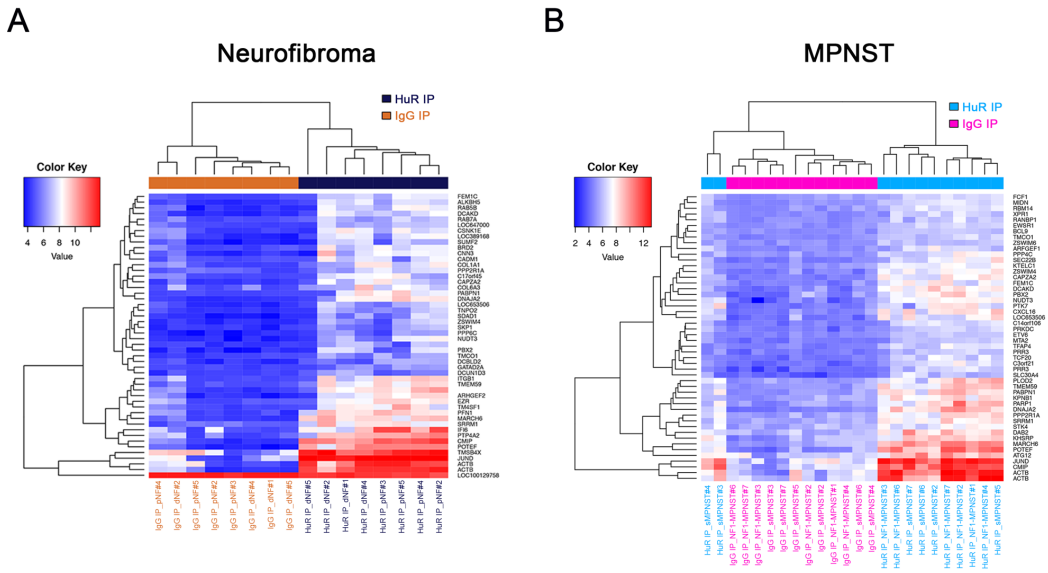

Figure 15. HuR is bound to key tragets in human malignant peripheral nerve sheath tumours (MPNSTs). A) Heatmap showing exprssion of the top transcripts most significantly bound to HuR (HuR IP) compared with control IgG (IgG IP) in neurofibroma samples (n=8) and **B)** MPNST samples (n=12), obtained from Stanmore Musculoskeletal Biobank. The colour scales indicate the degree of enrichment (red-blue ratio scale). dNF = dermal neurofibroma; pNF = plexiform neurofibroma; sMPNST = sporadic MPNST; NF1-MPNST = NF1-derived MPNST.

Background mRNAs identified in side-by-side control IP reactions using mouse anti-IgG antibody were subtracted to identify *bona fide* HuR-interacting mRNAs. We found that HuR was specifically bound to 71 and 276 mRNAs in neurofibroma and MPNST samples respectively (**Figure 16 A; supplemental Table 1, 2**). The large majority of neurofibroma targets (60 out of 71; 85 %) were also associated with HuR in the MPNST samples, whereas 216 HuR-bound transcripts were exclusively expressed in MPNST samples (**Figure 16 A**), in line with the high HuR expression in MPNST samples, and supporting a role for HuR in malignant Schwann cell tumours.

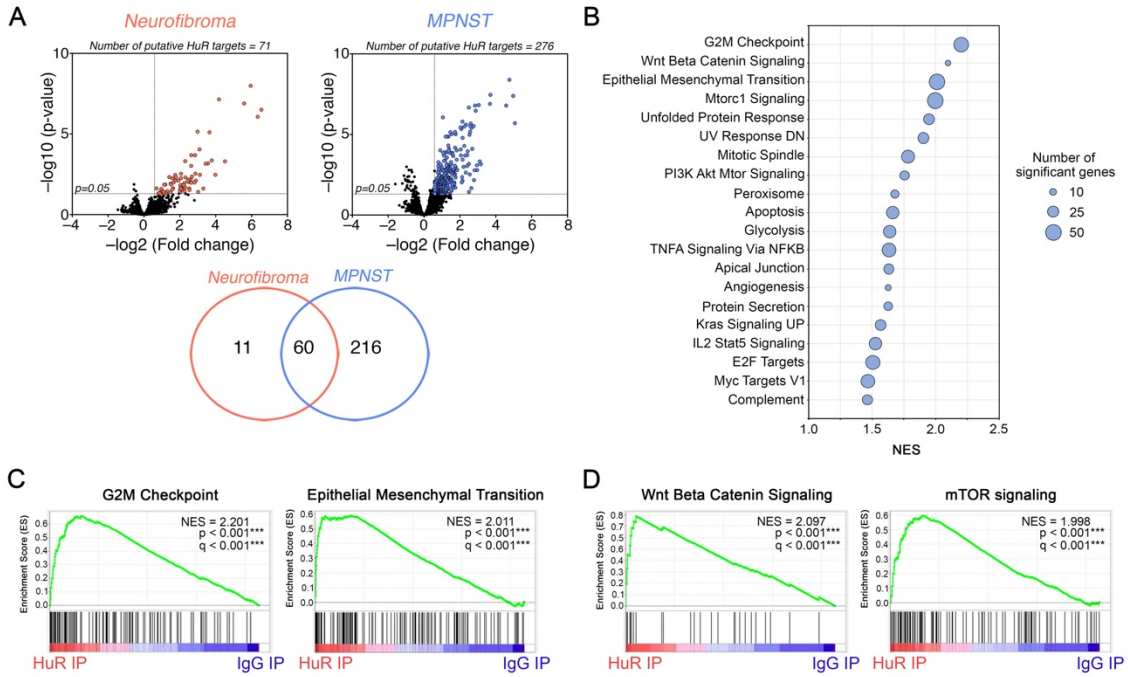

Figure 16. mRNA targets bound to HuR in Neurofibroma and MPNST samples. A) Volcano plots show enrichment of transcripts most significantly bound to HuR compared with control IgG in neurofibromas (left panel) (n=8) and MPNSTs (right panel) (n=12) obtained from Stanmore Musculoskeletal Biobank. (Red or blue coloured dots: fold-change >1.5; adjusted p-value<0.05). Venn diagram shows overlap between putative HuR mRNA targets from neurofibromas and MPNSTs. **B)** GSEA analysis of putative HuR mRNA targets in MPNSTs for MSigDB hallmarks. The top 20 gene sets (FDR q-values <0.1) are plotted relative to normalized enrichment score (NES). Circles denote the number of enriched genes in each category. **C, D)** GSEA plots of HuR IP and Control IgG IP for **C)** key cancer traits and **D)** oncogenic pathways in MPNSTs.

To identify molecular pathways associated with HuR-bound transcripts in MPNST, we performed gene set enrichment analysis (GSEA) using Molecular Signature Database (MSigDB) hallmarks (Subramanian *et al.*, 2005) GSEA revealed significant enrichment of signatures associated with oncogenic traits that include cell cycle progression, EMT and angiogenesis (Hanahan and Weinberg, 2011) as well as signatures for key oncogenic transcription factors MYC and E2F (Chen *et al.*, 2009b; Kress *et al.*, 2015) (**Figure 16 B**). In addition, key signalling pathways

in MPNSTs that include the Wnt/β-Catenin, PI3K/AKT/mTOR and RAS pathways (Farid *et al*., 2014; Carroll, 2016), were also enriched (**Figure 16 B–D; supplemental Table 3**).

Together, these data point to a potentially important biological function for HuR in MPNSTs, possibly regulating key signalling pathways that control oncogenic traits in these malignant tumours.

2. HuR promotes MPNST cell growth *in vitro* and *in vivo*

To characterize the functional importance of HuR, we first evaluated its abundance in established MPNST cell lines. Using a publicly available expression dataset (GEO: GSE14038) (Miller *et al*., 2009) we found that *HuR* mRNA levels were significantly upregulated in MPNST cell lines compared to neurofibroma-derived Schwann cells (NFSC) (**Figure 17 A**). Furthermore, higher *HuR* mRNA and protein levels were observed in 4 commonly used MPNST cell lines (ST88-14, 90-8, S462, STS-26T), compared to freshly isolated Schwann cells derived from human nerves (NHSC) (**Figure 17 B, C**).

We then silenced HuR in these 4 MPNST cell lines by lentiviral delivery of two distinct HuR-specific short hairpin (sh) RNAs and examined cellular growth. Three of the cell lines (ST-8814, 90–8 and S462) were derived from NF1 patients with confirmed loss of heterozygosity at the *NF1* locus for all 3 cell lines; the 90–8 cell line additionally showed a known microdeletion of *NF1*, whereas the sporadic MPNST line STS–26T had no mutations detected in the 60 exons of the *NF1* gene. These MPNST cell lines share a common gene expression profile distinct from that of normal Schwann cells, although they differ in proliferation rates and in expression of cell cycle proteins (Miller *et al*., 2006). Both constitutively expressed shRNAs reduced HuR levels efficiently, and suppressed cell growth, as shown by measuring ATP levels and by direct cell counts in all 4 cell lines (**Figure 17 D-F**).

Furthermore, *HuR* silencing significantly reduced the clonogenic and anchorage-independent growth capacity (**Figure 18 A**), shown by number of foci growth after 10 days culture conditions (**Figure 18 B**) and soft agar assay, which showed a reduction in formation of colonies after lentivirus-based *HuR* silencing in 4 MPNST cell lines (**Figure 18 C**).

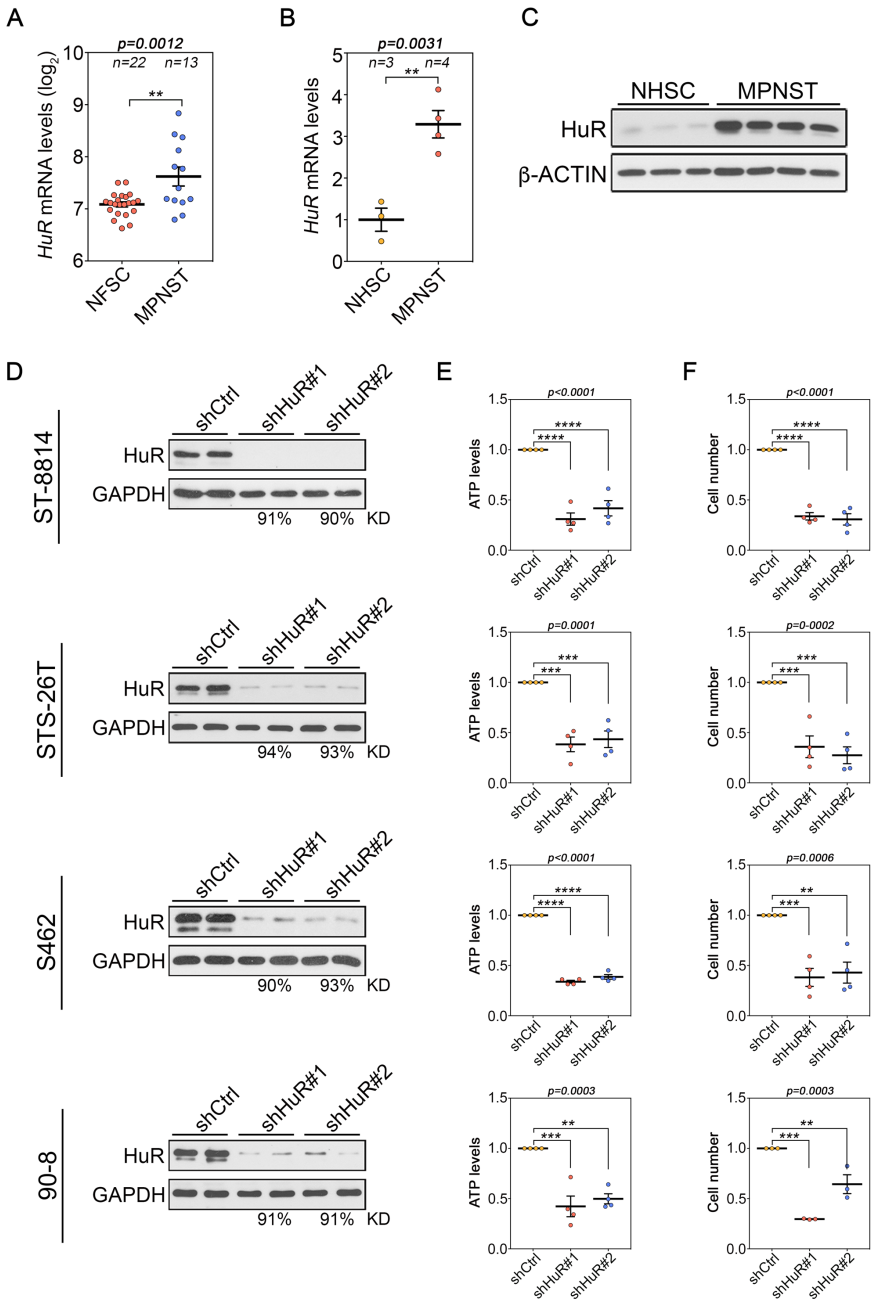

Figure 17. HuR promotes MPNST cell growth *in vitro.* A) HuR mRNA expression levels in Neurofibroma-derived Schwann cells (NFSC) and MPNST cell lines from Miller cohort (GSE14038) (Miller *et al.*, 2009). Data are presented as mean ± SEM, two-tailed unpaired Student's t-test. The number of samples (n) per group is indicated. **B)** RT-qPCR analysis of HuR mRNA levels and **C)** Western blot analysis of HuR levels, in normal human Schwann cells (NHSC) (n=3), obtained from NHSBT study no. 61 and MPNST cell lines (n=4). **D-F)** Growth of MPNST cell lines ST88-14, STS-26T, S462 and 90-8 is sensitive to constitutive *HuR* silencing *in vitro*. **D)** Representative immunoblots of HuR expression after shRNA-mediated knockdown with two distinct HuR-specific sh RNAs (sh HuR #1 and sh HuR #2). β-ACTIN expression was used as a loading control. The percentage of HuR knockdown (KD) was quantified by densitometry. Technical duplicates are shown, and similar results were obtained in at least 3 independent experiments. **E, F)** *HuR* silencing leads to a reduction in cell growth in MPNST cell lines, as determined by **E)** ATP luminescence assays and **F)** counts of cell numbers, 5 days after puromycin selection. Data are normalized to shCtr cells and are presented as mean ± SEM; n=3–4 independent experiments; one-way ANOVA with Tukey's multiple-comparisons test. *p<0.05; **p<0.01, ***p<0.001; ****p<0.0001.

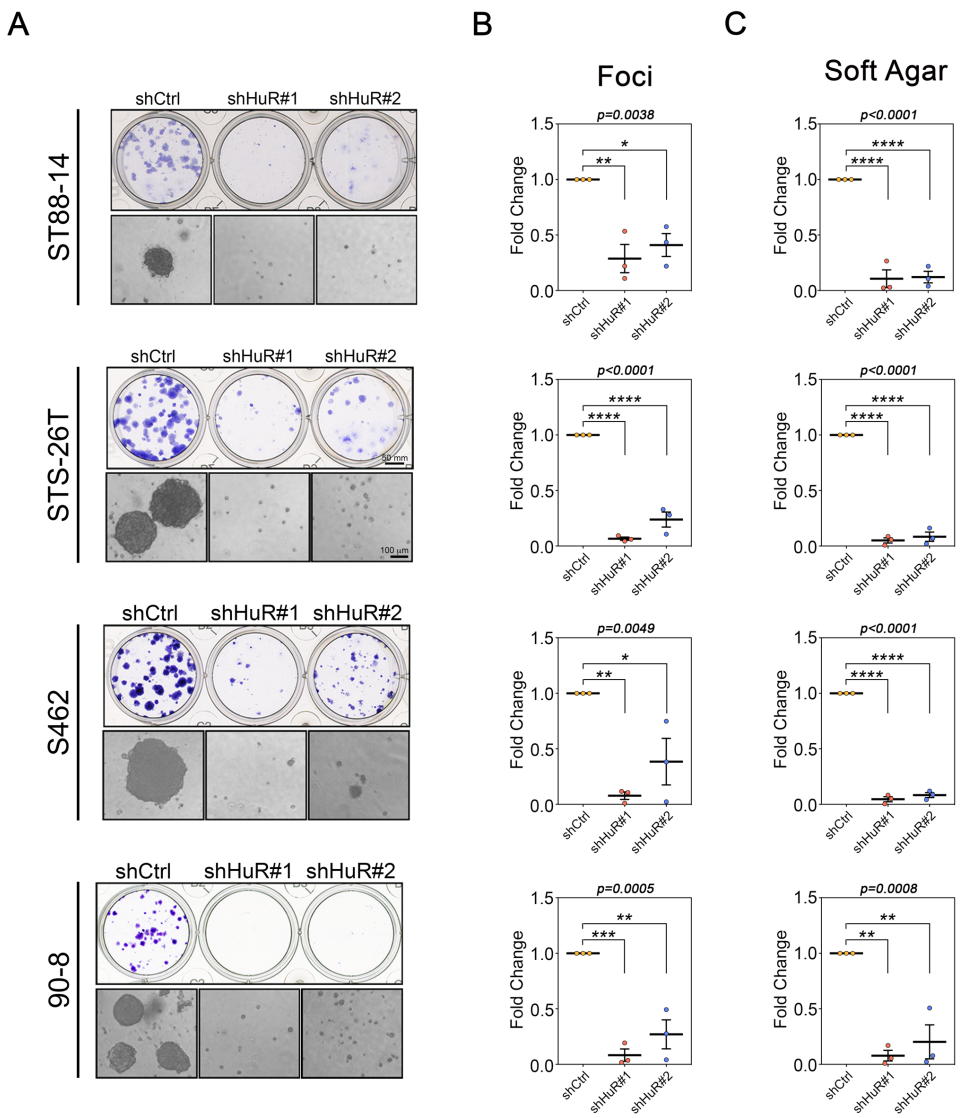

Figure 18. MPNST cell growth reduction *in vitro* after *HuR* silencing. A) Representative pictures of crystal-violet stained colonies in clonogenic assays (top panels), and colonies in soft agar assays (bottom panels) are shown for each cell line. **B)** Graphs represent absorbance of crystal-violet stained colonies for clonogenic assays. **C)** Number of colonies in soft agar assays, presented in Graphs. Data are normalized to control (shCtrl) cells and are presented as mean ± SEM; n=3 independent experiments; one-way ANOVA with Tukey's multiple-comparisons test. *p<0.05; **p<0.01, ***p<0.001; ****p<0.0001.

Since the *in vitro* consequences of HuR perturbation were shared by all MPNST cell lines, we selected as representative STS-26T for *in vivo* validation. STS-26T cells in which HuR levels were normal or reduced by silencing, consequtively, were implanted subcutaneously in immunodeficient mice. Subsequent analysis revealed that whereas control cells efficiently formed tumours (5/5), tumour formation was completely abolished in HuR-silenced cells (0/5) (**Figure 19 A, B**). Next, we examined the effects of HuR depletion on the growth of already established tumours. To this end, we used a doxycycline-inducible lentiviral shRNA system targeting HuR and its respective control. STS-26T cells expressing pTRIPZ-sh Control (sh *i*Ctrl) or

pTRIPZ-sh HuR (sh *i*HuR) were injected subcutaneously in the left and right flanks of immunodeficient mice respectively, and tumours were allowed to form for about 20 days until they were palpable (~100 mm^3 average).

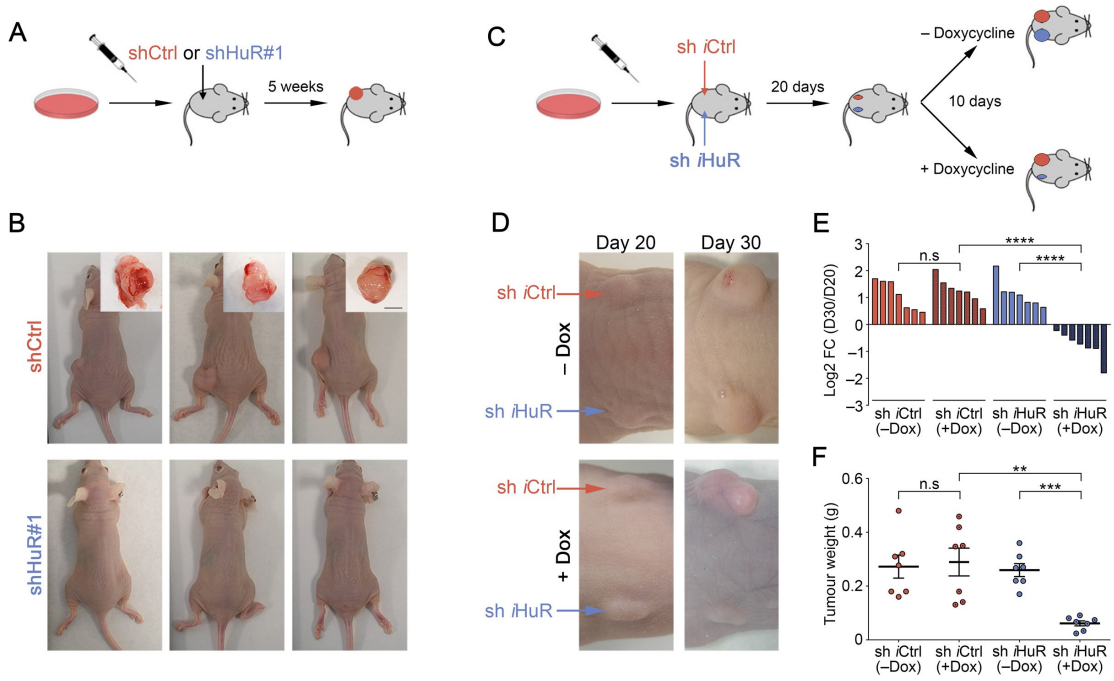

Figure 19. HuR promotes MPNST cell growth *in vivo*. A, B) Constitutive *HuR* silencing prevents tumour formation *in vivo*. **A)** Schematic representation of xenotransplantation experiments. **B)** Representative pictures of tumours from nude mice injected with control (sh Ctrl) or sh HuR#1 STS-26T MPNST cells on the left flank, 5 weeks after transplant (n=5) for each condition. Scale bar= 5 mm. **C-F)** Inducible *HuR* silencing promotes tumour regression *in vivo*. **C)** Schematic representation of xenotransplantation experiments using inducible *HuR* silencing strategy. **D)** Representative pictures of tumours from nude mice injected with sh *i*Ctrl or sh *i*HuR STS-26T MPNST cells on left and right flank respectively at 20 days after injection (Day 20), and 10 days later (Day 30) with doxycycline (+Dox) or without doxycycline diet (-Dox). **E**) Waterfall plot showing change in tumour volume (represented as log2 fold-change) of individual tumours formed at 20 days after transplant, and after 10 days with or without doxycycline treatment for each 4 groups of mice: sh *i*Ctrl (-Dox) (n=7), sh *i*Ctrl (+Dox) (n=7), sh *i*HuR (-Dox) (n=7) and sh *i*HuR (+Dox) (n=7). **F)** Graph showing weight of excised tumours for the 4 groups of mice. Each data point represents 1 mouse; one-way ANOVA with Tukey's multiple-comparisons test. n.s= not significant; **p<0.01, ***p<0.001; ****p<0.0001.

Mice were randomly assigned to standard chow diet or doxycycline diet for a period of 10 days, whereupon mice were sacrificed and tumours extracted (**Figure 19 C**). Remarkably, induction of *HuR* shRNA by doxycycline treatment severely blunted tumour growth, and even led to visible tumour regression (**Figure 19 D**). Tumour regression was observed in all mice following HuR depletion, and on average tumours shrank by 40 % (**Figure 19 E**), and weighed significantly less than control tumours (**Figure 19 F**).

Furthermore, HuR-depleted cells formed smaller tumours, and the efficiency of *HuR* silencing was confirmed in those tumours by Western blotting analysis (**Figure 20 A, B**). Notably, tumours

arising from sh *i*HuR cells without doxycycline treatment were indistinguishable in all parameters from tumours arising from sh *i*Ctrl cells with or without doxycycline treatment, supporting the efficiency and specificity of the inducible system used.

We also documented a marked reduction in the proliferation marker Ki67 and a rise in an apoptotic marker, active Caspase-3, in HuR-depleted tumours (**Figure 20 C**).

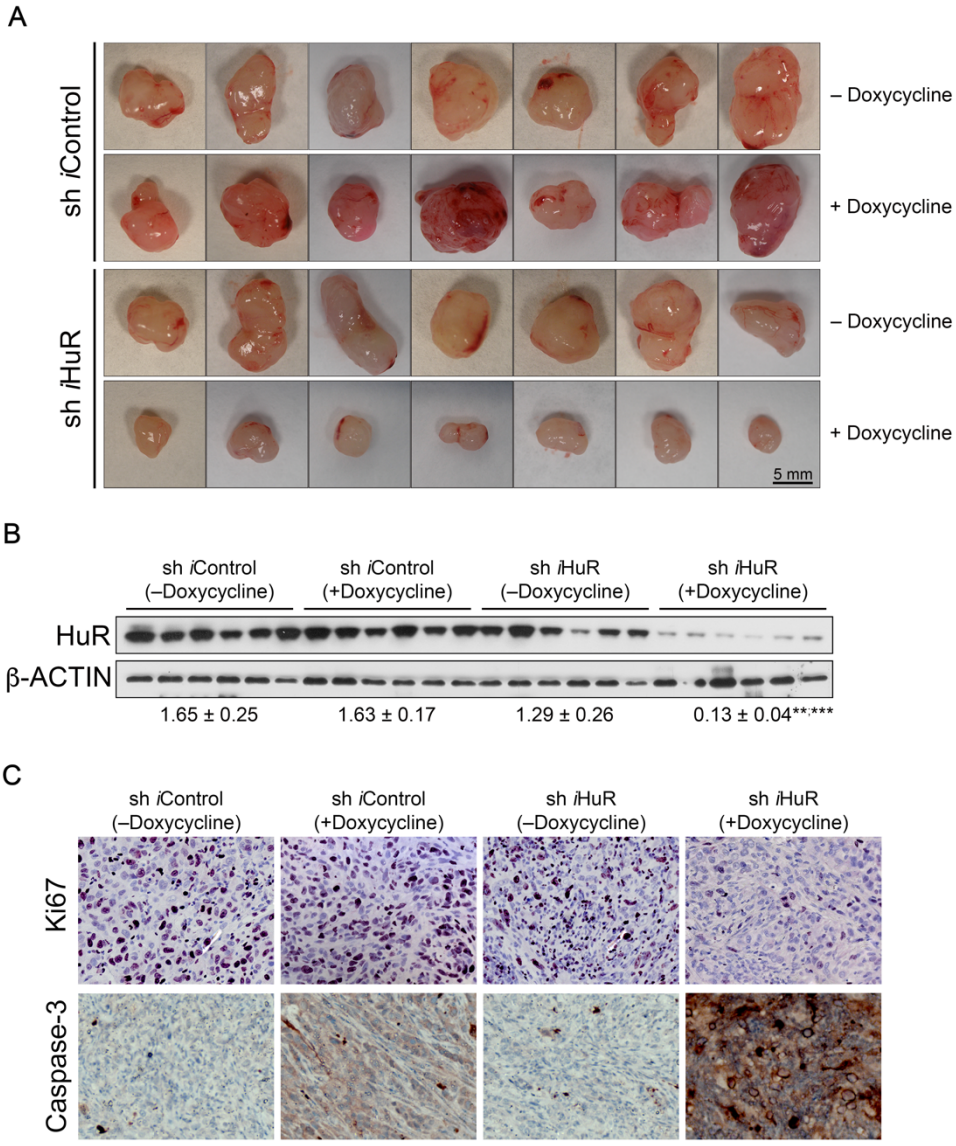

Figure 20. *HuR* silencing *in vivo* blocks proliferation and induces apoptosis in MPNSTs. A) Pictures of all tumours extracted from nude mice for 4 groups of mice: sh *i*Control (-Doxycycline) (n=7), sh *i*Control (+Doxycycline) (n=7), sh *i*HuR (-Doxycycline) (n=7) and sh *i*HuR (+Doxycycline) (n=7), as per experiment described in Figure 5 C. **B)** Representative Western blot of total HuR levels from extracted tumours (A). Densitometry analysis of HuR levels corrected for β-ACTIN was performed for panel of tumours. Statistical significance was calculated by one-way ANOVA with Tukey's multiple-comparisons test. **p<0.01 [sh *i*HuR (+Doxycycline) v sh *i*HuR (-Doxycycline)]; ***p<0.001 [sh *i*HuR (+Doxycycline) v sh *i*Control (+Doxycycline)]. **C)** Representative immunohistochemistry images of ki67-positive proliferative cells (violet) and apoptotic active Caspase-3 positive (brown) from tumours from A.

Then, we validated these results in the panel of cultured MPNST cell lines, where, similarly, genetic depletion of HuR in the 4 cell lines potently reduced cell proliferation as measured by (1) cell cycle analysis by flow cytometry, which showed a general increase in the percentage of cells in the G1 phase and a decrease in cells in the S and G2M phases, consistent with a G1 cell cycle arrest, and (2) BrdU incorporation (**Figure 21 A, B**).

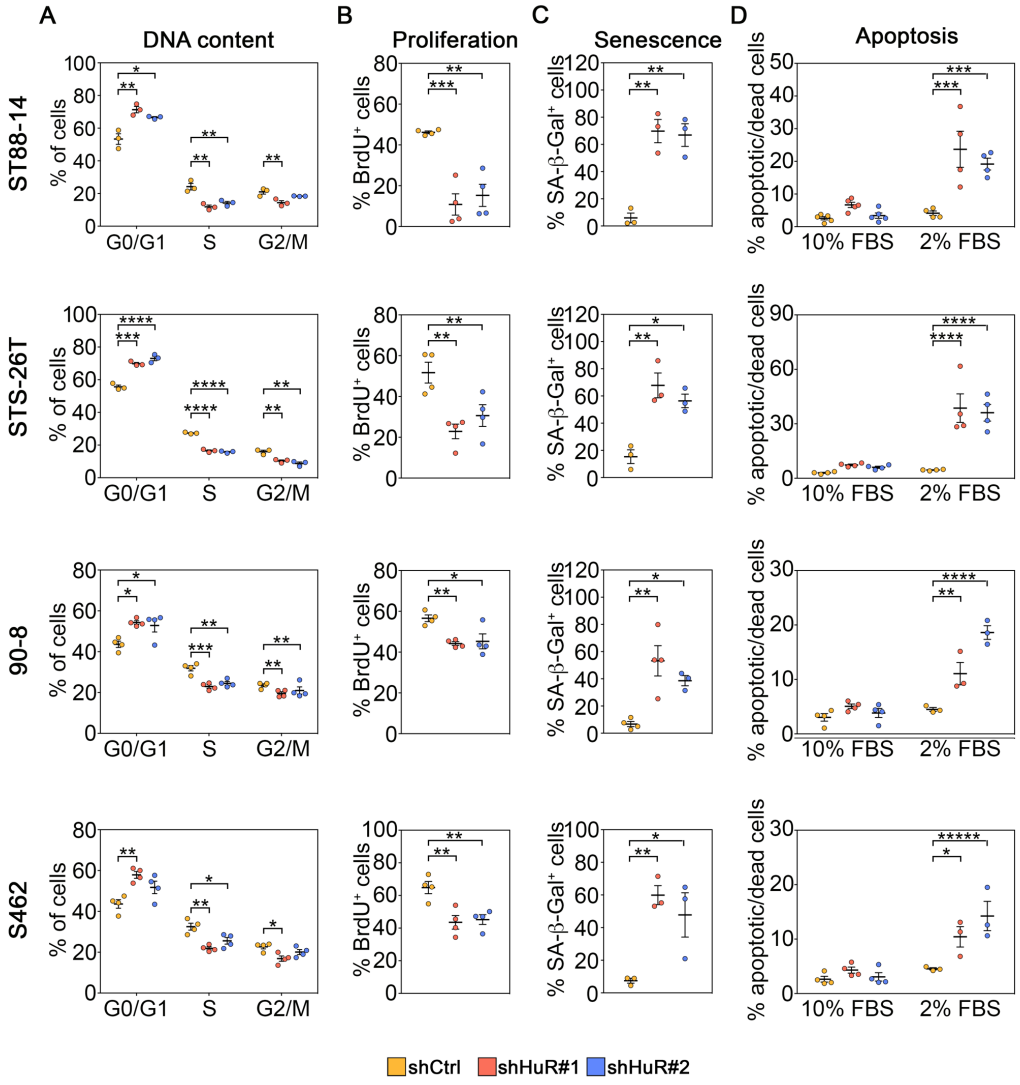

Figure 21. HuR depletion induces cell cycle arrest, apoptosis and senescence in MPNST cells. A) Cell cycle analysis of Propidium Iodide-stained nuclei of MPNST cells after constitutive *HuR* silencing in vitro with two distinct HuR-specific shRNAs (shHuR#1 and shHuR#2) in 4 cell lines. Data are presented as mean ± SEM; n=3-4 independent experiments; one-way ANOVA with Tukey's multiple-comparisons test. **B)** Percentage of BrdU positive proliferative cells after *HuR* silencing. Data are presented as mean ± SEM; n=4 independent experiments; one-way ANOVA with Tukey's multiple-comparisons test. **C)** Percentage of SA-β-Gal-positive cells after *HuR* silencing. Data are presented as mean ± SEM; n=3–4 independent experiments; one-way ANOVA with Tukey's multiple-comparisons test. **D)** Apoptosis induction as measured by flow cytometry analysis for Annexin V (+) cells after *HuR* silencing after culture in growth-promoting (10 % FBS) and growth-limiting conditions (2 % FBS). Data are presented as mean ± SEM; n=3-4 independent experiments; two-way ANOVA with Tukey's multiple-comparisons test. *p<0.05; **p<0.01, ***p<0.001; ****p<0.0001.

We also found a marked increase in senescence after *HuR* silencing in all 4 cell lines (**Figure 21 C**). Moreover, detection of Annexin V by flow cytometry indicated a trend towards increased apoptosis in all 4 cell lines after HuR knockdown when cells were cultured under basal, growth-promoting conditions (10% serum). Exposure to cellular stress, such as culture of cells under growth-limiting conditions (2% serum) (De Raedt *et al*., 2014) exaggerated this effect and led to a marked increase in apoptotic and necrotic cell death after HuR depletion (**Figure 21 D**).

Together, these data indicate that HuR play an important functional role in MPNST cell biology by controlling key features such as survival, proliferation and replicative immortality.

3. HuR promotes MPNST metastasis *in vivo*

MPNSTs have a high metastatic potential, and up to 50 % of patients develop metastatic disease, usually to the lung, further worsening 5-year survival rates of patients (Farid *et al*., 2014; Kim *et al*., 2015). Yet, metastasis is one of the least understood aspects of MPNSTs. Given the profound tumoral effects of HuR in MPNST cells, and the identification of EMT signature as one of the top enriched categories of HuR targets from GSEA analysis (**Figure 16 C**), we decided to examine whether HuR could be important for MPNST metastasis, using a surrogate model of lung metastasis. Briefly, this model measures the ability of cells injected in the lateral tail vein of immunodeficient mice to survive in circulation, arrest at a distant organ, extravasate, adapt to growth in the foreign microenvironments of a distant tissue, and grow into metastatic lesions, recapitulating many of the essential late steps in metastasis (Lambert *et al*., 2017).

We silenced HuR constitutively in STS-26T cells, an MPNST cell line which exhibits metastatic tropism to the lung (Ghadimi *et al*., 2012), injected them in the tail vein, and examined metastatic colonization of the lung 4 weeks later by histology (**Figure 22 A**). Remarkably, very few metastatic lesions were observed in HuR-depleted cells in contrast to control cells, which formed numerous and large metastatic foci (**Figure 22 B, C**). Next, we used our inducible lentiviral silencing system to examine the effect on *HuR* silencing on the colonization step of the metastatic process, i.e. the survival of the cells in these foreign microenvironments during the metastatic process, and the reactivation of their proliferation programs to form overt metastatic lesions. We injected STS-26T cells expressing pTRIPZ-sh Control (sh *i*Ctrl) or pTRIPZ-sh HuR (sh *i*HuR) in the tail vein, and allowed them to begin to form metastases for 2 weeks. Mice were randomly assigned to standard chow or doxycycline-containing diet for 4 weeks, whereupon mice were sacrificed and lungs extracted for histological analysis (**Figure 22 D**).

Induction of HuR shRNA by doxycycline treatment blocked the conversion of micrometastases into the macroscopic neoplastic growth seen in the control cells with or without doxycycline treatment and in sh *i*HuR cells without doxycycline treatment (**Figure 22 D-F**).

These data support a key role for HuR in MPNST metastasis, potentially controlling key aspects of the metastatic process, from the survival of the cells in the bloodstream to their colonization and proliferation within distant organs.

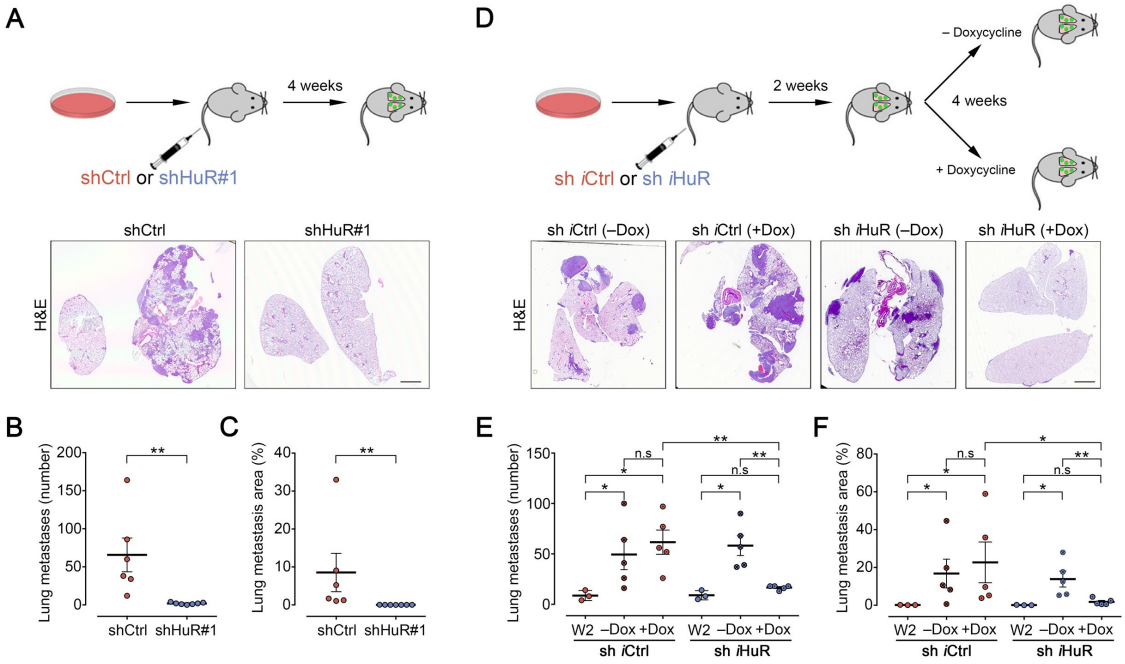

Figure 22. HuR promotes MPNST metastasis *in vivo*. A–C) Constitutive *HuR* silencing prevents lung metastasis of STS26T MPNST cells. **A)** Schematic representation of lung metastasis experiments. Sh Control (n=6) or shHuR#1-expressing (n=7) STS26T MPNST cells were injected in the tail vein of nude mice, and mice sacrificed 4 weeks later and lung architecture analysed by haemaoxylin & eosin (H&E) staining. Representative pictures of lung histology for each group is shown. **B)** Number of lung metastases **C)** and lung metastatic area, expressed as a percentage of total lung area, was quantified by H&E histology. Scale bar, 2 mm. Each data point represents 1 mouse. Data are presented as mean ± SEM, two-tailed unpaired Mann-Whitney U test. **p<0.01. **D–F)** Inducible *HuR* silencing prevents growth of established lung metastatic nodules *in vivo*. **D)** Schematic representation of experiments. Sh *i*Control (sh *i*Ctrl) or sh *i*HuR-expressing STS–26T MPNST cells were injected in the tail vein of nude mice. A group of mice (n=3, for each condition) was sacrificed at 2 weeks (W2) to analyse basal formation of lung metastases, and the rest of mice fed with normal diet (–Doxycycline, –Dox) or doxycycline diet (+Dox) to induce expression of shRNAs for a further 4 weeks, before sacrifice and analysis of lung histology by H&E staining. Representative pictures of lung histology for the following groups are shown: sh *i*Ctrl with normal diet (sh *i*Ctrl; –Dox) (n=5), sh *i*Ctrl with doxycycline diet (sh *i*Ctrl; +Dox) (n=5), sh *i*HuR with normal diet (sh *i*HuR; –Dox) (n=5), sh *i*HuR with doxycycline diet (sh *i*HuR; +Dox) (n=5). Scale bar, 2 mm. **E)** Number of lung metastases and **F)** lung metastatic area, expressed as a percentage of total lung area, was quantified for each of 6 groups by histology. Each data point represents 1 mouse; Data are presented as mean ± SEM, two-tailed unpaired Mann-Whitney U test. n.s= not significant; *p<0.05; **p<0.01.

4. HuR overexpression in Schwann cells is not sufficient to trigger oncogenic transformation or dissemination

Since HuR is expressed at notably higher levels in MPNST compared to Schwann cells (**Figure 17A–C**), we next examined whether elevating HuR levels in human Schwann cells was sufficient elicit to cell transformation and dissemination. For that, we ectopically expressed HA-tagged HuR using a doxycycline-inducible lentiviral system (Zhou *et al*., 2018) in immortalized normal human Schwann cells (iHSCλ2) (**Figure 23 A**).

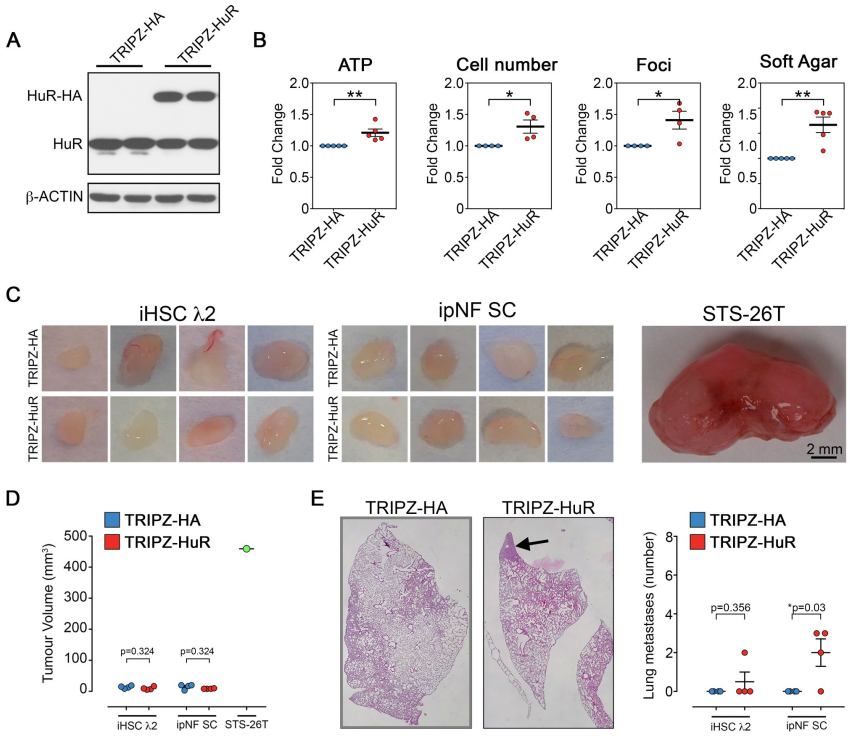

Figure 23. HuR overexpression does not lead to tumour formation and overt metastasis in normal (iHSCλ2) or plexiform neurofibroma Schwann cells (ipNF SC). A) Representative immunoblots showing increased expression of HuR tagged with HA after infection with a lentiviral vector (TRIPZ-HuR) in immortalized normal human Schwann cell line (iHSCλ2). β-ACTIN expression was used as a loading control. Technical duplicates are shown, and similar results were obtained in at least 3 independent experiments. **B)** HuR overexpression leads to a slight increase in cell growth in immortalized normal human Schwann cell line, as determined by ATP luminescence assays, counts of cell numbers, clonogenic assays (foci), and anchorage-independent growth using soft agar assays. Data are normalized to control TRIPZ-HA infected cells and are presented as mean ± SEM; n=3–4 independent experiments; two-tailed unpaired Student's t tests. **C–D)** HuR overexpression does not induce an increase in tumour size in iHSCλ2 or immortalized plexiform neurofibroma Schwann cells (ipNF SC). In comparison, tumour formed by MPNST cell line STS-26T is comparatively much larger. **C)** Pictures of tumours extracted from nude mice **D**) Graph shows volume of extracted tumours. **E)** HuR overexpression does not lead to overt formation of metastatic nodules in iHSCλ2 or ipNF SC. Pictures shows formation of a small metastatic nodule in HuR-overexpressing ipNF SC (arrows). A small but significant increase in formation of metastatic nodules was observed only in the case of HuR-overexpressing ipNF SC, but not in HuR-overexpressing iHSCλ2 cell lines. Data are normalized to control TRIPZ-HA infected cells and are presented as mean ± SEM; n=4 mice; two-tailed unpaired Student's t tests. *p<0.05; **p<0.01.

HuR overexpression also led to a small but significant increase in cell growth, as shown by measuring ATP levels, direct cell counts, and increased the clonogenic and anchorage-independent growth capacity (**Figure 23 B**). However, no major effect was observed in tumour formation *in vivo* using mouse xenograft models (**Figure 23 C, D**). We also did not observe any major effect on tumour formation after ectopic expression of HuR in immortalized plexiform neurofibroma-derived human Schwann cells (ipNF SC). These data suggest that while HuR overexpression promotes proliferation in Schwann cells in culture, it is not sufficient to induce Schwann cell-derived tumours in mice.

Similarly, we examined metastatic properties using tail vein injections of control (TRIPZ-HA) or HuR-overexpressing (TRIPZ-HuR) iHSCλ2 and ipNF SC. We did not find any metastatic nodules in either cell line. Unexpectedly, we found the presence of small micrometastases in HuR-overexpressing iHSCλ2 (1 out of 4) and ipNF SC (3 out of 4) (**Figure 23 E**), although these were far fewer and smaller than after injection of STS-26T MPNST cell line (**Figure 22**).

Taken together, HuR overexpression in normal or plexiform neurofibroma Schwann cells was not sufficient to trigger oncogenic transformation but modestly increased their metastatic capacity.

5. Pharmacological inhibition of HuR reduces MPNST growth and metastasis

Our results demonstrate that elevated HuR levels in MPNST cells are required for cell growth and metastasis. We next ascertained whether the inhibition of HuR could be exploited as a therapeutic strategy using small molecule HuR inhibitors.

Pharmacological inhibition of HuR with MS-444, which inhibits HuR homodimerization to prevent the binding of 3'UTR AU-rich elements (Meisner *et al*., 2007), pyrvinium pamoate (PP), an FDA-approved anthelminthic drug that blocks HuR nucleocytoplasmic translocation (Guo *et al*., 2016), and tanshinone mimic 6N (TM-6N), which inhibits HuR-RNA complex formation (Manzoni *et al*., 2018) each strongly reduced MPNST cell growth in culture, in ST88-14 and STS-26T cells (**Figure 24 A, B**), similar to what we found through the genetic inhibition of HuR (**Figure 17, Figure 18**).

Importantly, intra-peritoneal injection with MS-444 (25 mg/kg body weight; treatment every 48 h for 10 days) of nude mice bearing already established tumours (formed 20 days after xenograft transplant of STS-26T cells in flanks) severely blunted tumour growth, and even led to tumour regression in some cases. In addition, MS-444-treated tumours weighed significantly less than control tumours (**Figure 24 C-E**).

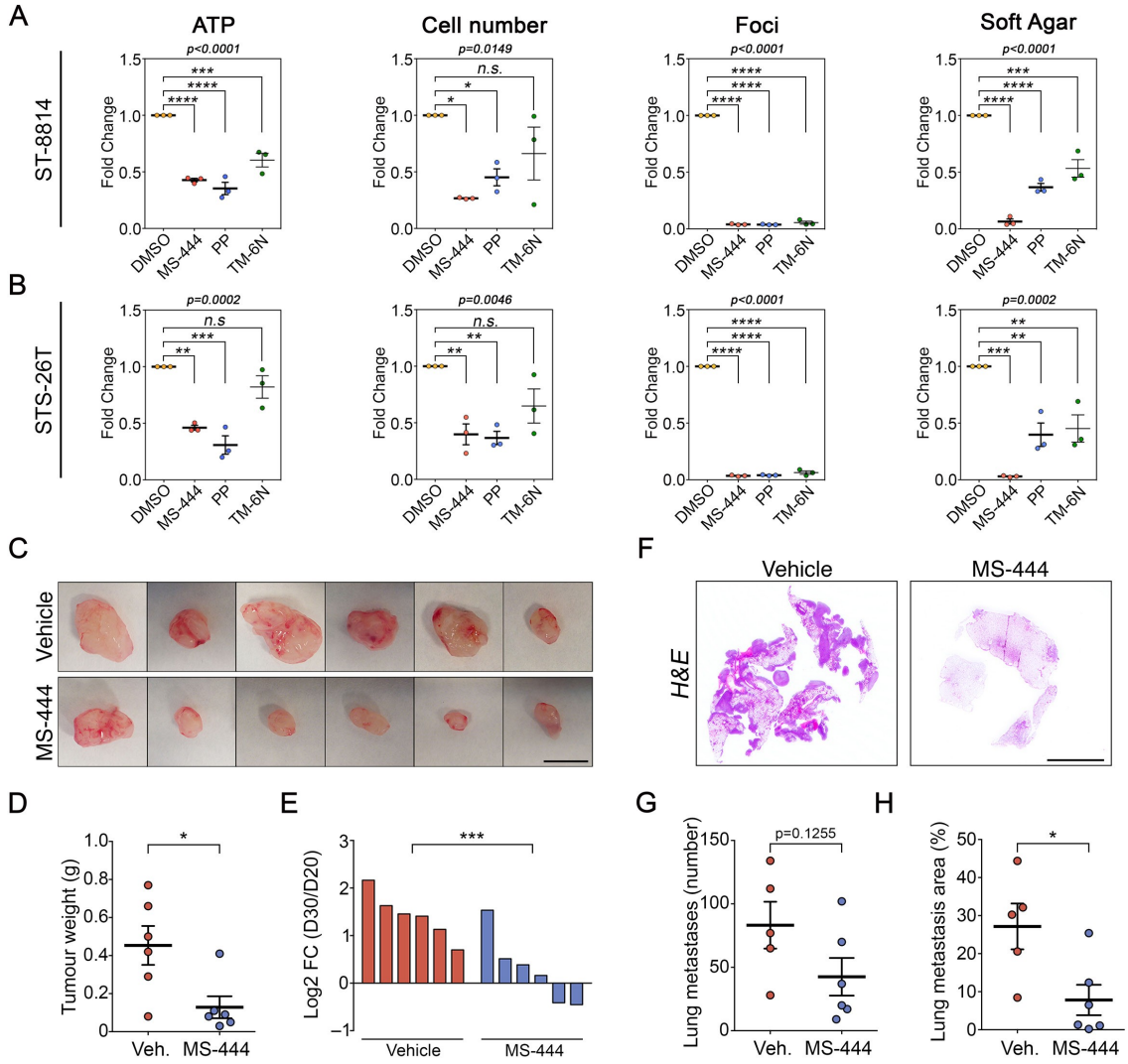

Figure 24. Pharmacological inhibition of HuR blocks MPNST cell growth and metastasis *in vitro* and *in vivo*. A) Pharmacological inhibition of HuR activity leads to a reduction in cell growth in MPNST cell lines ST-8814 and STS-26T, as determined by ATP luminescence, counts of cell numbers, clonogenic assays (foci), and anchorage-independent growth using soft agar assays. Graphs represent absorbance of crystal-violet stained colonies for clonogenic assays, and number of colonies in soft agar assays. Data are normalized to DMSO-treated and are presented as mean ± SEM; n=3 independent experiments; one-way ANOVA with Tukey's multiple-comparisons test. **C–E)** Pharmacological inhibition of HuR activity by MS-444 promotes tumour regression *in vivo*. **C)** Pictures of tumours from nude mice injected with STS-26T MPNST cells after vehicle or MS-444 treatment. Scale bar, 10 mm. **D)** Graph showing weight of excised tumours for both groups of mice. **E)** Waterfall plot showing change in tumour volume (represented as log2 fold-change) of individual tumours formed at 20 days after transplant, and after 10 days with pharmacological inhibition. Each data point represents 1 mouse. Data are presented as mean ± SEM, two-tailed unpaired Mann-Whitney U test. **F–H)** Pharmacological inhibition of HuR activity by MS-444 prevents growth of established lung metastatic nodules *in vivo*. **F)** Representative pictures of lung histology from nude mice injected with STS-26T MPNST cells after vehicle or MS-444 treatment. **G)** Number of lung metastases and **H)** lung metastatic area, expressed as a percentage of total lung area was quantified. Scale bar, 5 mm. Each data point represents 1 mouse; Data are presented as mean ± SEM, two-tailed unpaired Mann-Whitney U test. *p<0.05; **p<0.01, ***p<0.001; ****p<0.0001.

Remarkably, MS-444 treatment of nude mice (intra-peritoneal injection every 48 h for 2 weeks; 25 mg/kg body weight) with established micrometastases that had formed for 2 weeks after intravenous injection of STS-26T cells, also reduced the conversion of these micrometastases into the macroscopic neoplastic growth, and smaller metastatic areas were measured in MS-444-treated mice than in vehicle-treated mice (**Figure 24 F-H**).

Our results show that pharmacological inhibition of HuR reduces MPNST growth and metastasis, thus highlighting the relevance of HuR as a potential therapeutical target for MPNST.

6. Molecular mechanisms implicated in HuR-mediated MPNST malignancy

6.1. HuR regulates key oncogenic transcriptional programs

Next, we sought to define the mechanisms by which HuR exerts such profound effects on MPNST cells. We silenced HuR using lentiviral vectors expressing constitutively shRNA directed at HuR in the MPNST ST88-14 cell line, and performed RNA-sequencing (RNA-seq). We identified distinct transcriptomic profiles between the control (sh Ctrl) and HuR-depleted cells (shHuR#1) (**Figure 25 A**).

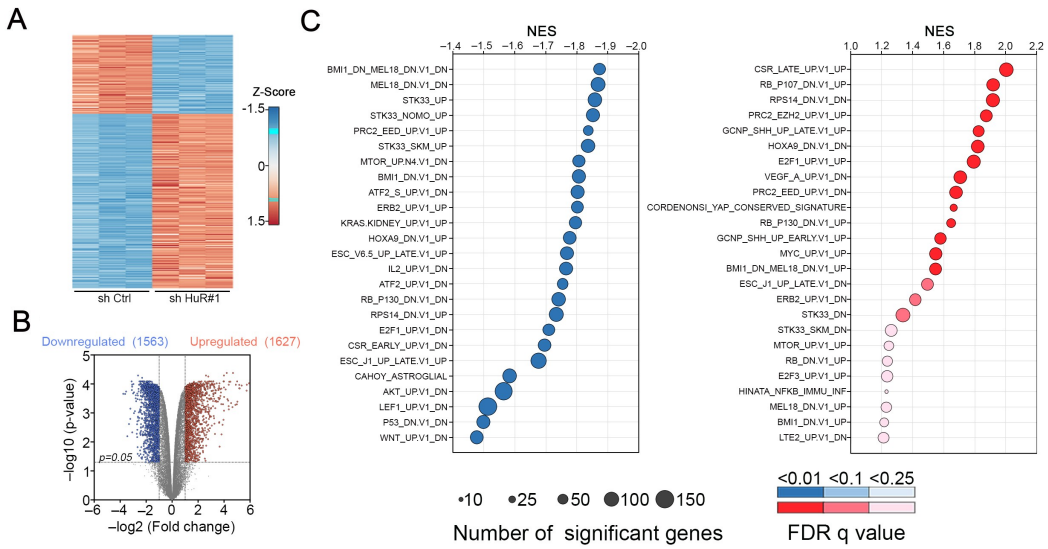

Figure 25. RNA-Seq reveals that HuR controls key oncogenic pathways in MPNST cells. A) Heatmap representation of differentially expressed genes between control (sh Ctrl) (n=3) or shHuR#1-expressing (n=3) ST88-14 MPNST cells (fold change >2 and adjusted p-value<0.05). **B)** Volcano plot of transcriptome profiles between sh Ctrl (n=3) and shHuR#1-expressing (n=3) ST88-14 MPNST cells. Red and blue dots represent genes significantly upregulated and downregulated in shHuR#1-expressing cells respectively (Red or blue dots: fold change >2 and adjusted p-value<0.05). **C)** GSEA analysis of sh Ctrl and shHuR#1-expressing ST88-14 MPNST cells for MSigDB Oncogenic signatures. Gene sets with FDR q values <0.25 are plotted relative to normalized enrichment score (NES). Categories with negative (left) and positive (right) NES are down- or upregulated, respectively, in sh Ctrl cells. Circles denotes the number of enriched genes in each category and colour codes represent FDR q values as indicated.

Differential expression analysis revealed that a notable proportion of the transcriptome in MPNST cells changed significantly. There were similar numbers of significantly upregulated and downregulated transcripts exhibiting >2-fold changes (1563 and 1627 respectively) (**Figure 25 B**). GSEA analysis revealed an inhibition of several tumorigenic pathways in MPNST cells by *HuR* silencing, including the YAP/TAZ, Wnt/β-Catenin, PI3K/AKT/mTOR and RAS pathways, in addition to signatures for the key oncogenic transcription factors MYC and E2F (**Figure 25 C, supplemental Table 4, 5**). There was also significant overlap between the signature sets we identified by this RNA-Seq analysis and the RIP-chip analysis for putative HuR mRNA targets (**Figure 25 B**). These results strongly suggested that HuR could be affecting MPNST cells by directly regulating these pathways, several of which have already been established to play key roles in MPNST tumorigenesis (Rahrmann *et al*., 2013; Watson *et al*., 2013; Patel *et al*., 2014; Wu *et al*., 2018). We thus set out to examine the importance of HuR for these pathways.

We first focused on the YAP/TAZ pathway. In an elegant study, it was recently shown that human MPNSTs exhibit elevated HIPPO-TAZ/YAP expression, and hyperactivation of YAP/TAZ in Schwann cells activated an oncogenic program with development of MPNSTs (Wu *et al*., 2018). GSEA analysis of RNA-Seq data showed that *HuR* silencing in MPNST cells led to a strong suppression of a YAP-conserved signature (Cordenonsi *et al*., 2011), as well as a functionally validated YAP-activated signature (Tremblay *et al*., 2014) (**Figure 26 A, B**). Notably, GSEA also showed a strong negative correlation of genes regulated by YAP/TAZ hyperactivation in Schwann cells (Wu *et al*., 2018) and genes regulated by *HuR* silencing in ST88-14 MPNST cells (**Figure 26 C**), suggesting that HuR could be responsible for regulating expression of YAP/TAZ pathway components. To test this hypothesis, we examined whether HuR associated with mRNAs encoding key protein components of the YAP/TAZ pathway by performing RIP followed by reverse transcription and quantitative PCR analysis (RIP-qPCR) in MPNSTs. To avoid possible confounding effects of cell type heterogeneity in tumour samples, we used MPNST cell lines instead. We found that there was a strong enrichment of *YAP1* mRNA, encoding YAP1, and *TEAD1* and *TEAD2* mRNAs, encoding TEAD1 and TEAD2, two transcriptional partners of YAP1, in HuR RIP samples (**Figure 26 D**). Notably, HuR depletion led to a striking reduction in the levels of these proteins in both the NF1-derived ST88-14 cell line and the sporadic cell line STS-26T (**Figure 26 E**). Suppressing the YAP/TAZ pathway by *HuR* silencing reduced the mRNA levels of downstream YAP/TAZ target genes in both cell lines (**Figure 26 F**). Interestingly, although we did not find that *TAZ* or *TEAD4* mRNAs were direct targets of HuR, HuR depletion led to a strong reduction in their expression levels, likely due to an indirect effect on their transcription, mRNA stability or translation.

Our results indicate that HuR can regulate expression of key YAP/TAZ pathway components in MPNST cells, which could lead to the aberrant elevated HIPPO-TAZ/YAP expression seen in mouse and human tumour tissue samples and the hyperactivation of this essential oncogenic pathway for MPNST pathogenesis.

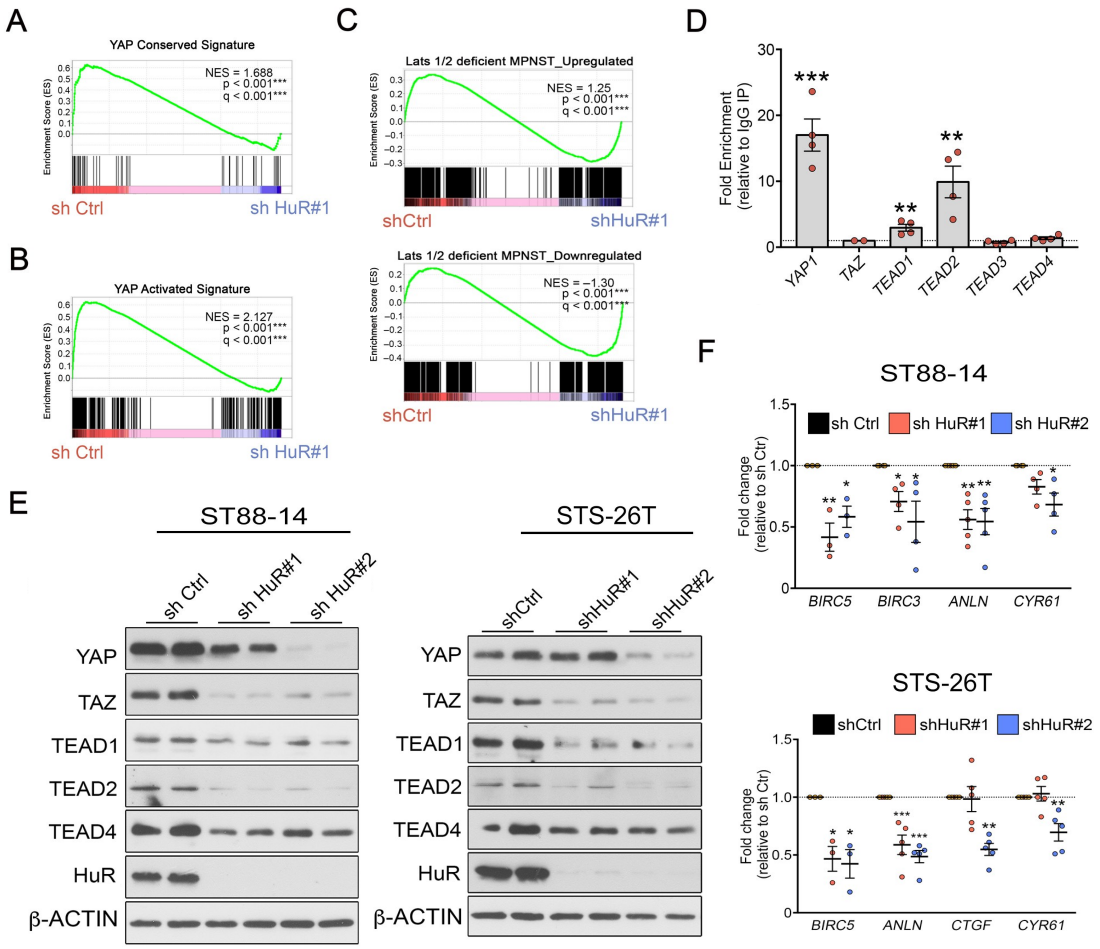

Figure 26. HuR regulates the YAP/TAZ pathway in MPNST cells. A, B) GSEA plots showing enrichment of **A**) Yap conserved signature from Figure 25 C, and **B**) Yap activated signature set (36), in control (sh Ctrl) compared to sh HuR#1-infected ST88-14 MPNST cells. **C**) GSEA plots showing enrichment of genes upregulated and downregulated by YAP/TAZ activation in mouse Schwann cells (after Lats 1/2 ablation), in sh Ctrl and sh HuR#1 ST88-14 cells respectively. **D**) RIP-qPCR analysis showing binding of HuR to YAP1, TEAD1 and TEAD2 in 4 MPNST cell lines (ST88-14, 90-8, S462, STS-26T). Data are normalised to control IgG IPs and are presented as mean ± SEM, two-tailed unpaired Student's t-test. n= 4 MPNST cell lines. **E**) Representative Western blots showing a general downregulation of key YAP/TAZ pathway components after *HuR* silencing in ST88-14 and STS-26T MPNST cells. Technical duplicates are shown, and similar results were obtained in at least 3 independent experiments. **F**) RT-qPCR analysis showing downregulation of YAP/TAZ pathway effector genes (Wu *et al*., 2018) after *HuR* silencing in ST88-14 and STS-26T MPNST cells. Data are normalized to sh Ctrl cells and are presented as mean ± SEM; Each data point represents 1 independent experiment; one-way ANOVA with Tukey's multiple-comparisons test. *p<0.05; **p<0.01, ***p<0.001.

6.2. HuR regulates key cell cycle genes in MPNST via a RB-E2F axis

The RAS-MEK-ERK and PI3K-AKT-mTOR are two other major signalling pathways that are upregulated in MPNSTs and have important roles in MPNST pathogenesis (Farid *et al*., 2014; Carroll, 2016). GSEA analysis revealed that many components of these pathways were significantly downregulated by *HuR* silencing, including activation of receptor tyrosine kinases such as PDGF (**Figure 27 A, B**).

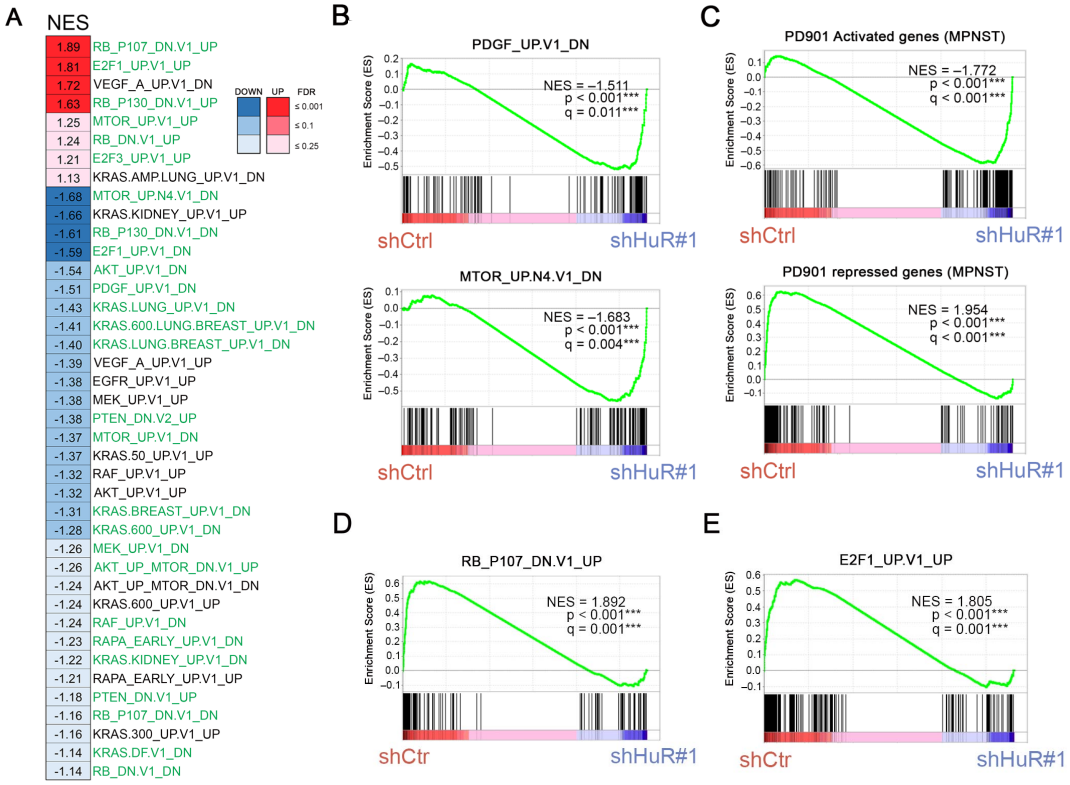

Figure 27. HuR regulates key cell cycle genes in MPNST cells. A) Compendium of normalized enrichment scores (NES) of all target gene sets associated with RAS-MEK-ERK, PI3K-AKT-mTOR and Rb-E2F pathways after GSEA analysis of RNA-sequencing in HuR–silenced ST88-14 MPNST cells. Notably, there is a general positive correlation in the activation of the pathways (highlighted in green) in control (sh Ctrl-infected) compared to sh HuR#1-infected ST88-14 MPNST cells. The colour codes represent FDR q values (red-blue ratio scale). **B**) GSEA plots showing enrichment of genes downregulated by PDGF receptor activation and mTOR pathway activation in sh HuR#1-infected compared to sh Ctrl-infected ST88-14 MPNST cells. **C**) GSEA plots showing enrichment of genes activated by PD901 treatment of MPNST cells (FC >2 and adjusted p-value<0.05) (Jessen *et al*., 2013) in sh HuR#1-infected compared to sh Ctrl-infected ST88-14 MPNST cells, and conversely, enrichment of genes repressed by PD901 treatment in sh Ctrl-infected compared to sh HuR#1-infected ST88-14 MPNST cells. **D**) GSEA plots showing enrichment of functionally defined RB and **E**) E2F1 signature set in sh Ctrl- and sh HuR#1-infected ST88-14 MPNST cells from Figure 25 C.

Along the same lines, GSEA also showed a strong positive correlation among genes regulated by the MEK inhibitor PD0325901 in the MPNST cell line 90-8TL (De Raedt *et al*., 2014) and genes

regulated by *HuR* silencing in ST88-14 MPNST cells (**Figure 27 C**). In addition, several signatures of downstream effectors of these pathways, including the RB and E2F transcription factors, were inhibited by *HuR* silencing (**Figure 27 D, E**). These effectors are frequently dysregulated in cancer and play an important role in cell cycle regulation (Chen *et al*., 2009b). To examine the specific function of HuR in controlling RB and E2F tumorigenic pathways, we examined whether HuR was bound to and regulated expression of different components of these pathways (**Figure 28 A**). By RIP-qPCR analysis, we found that HuR was bound to *CCND1, CCND2, CDK2, CDK6, p27, E2F1, E2F2* and *E2F3* mRNAs (**Figure 28 B**). In both the ST88-14 and STS-26T cell lines, we found that silencing *HuR* strongly reduced the levels of several proteins encoded by these mRNAs, accordingly to the role of HuR in promoting mRNA stability and translation (**Figure 28 C**).

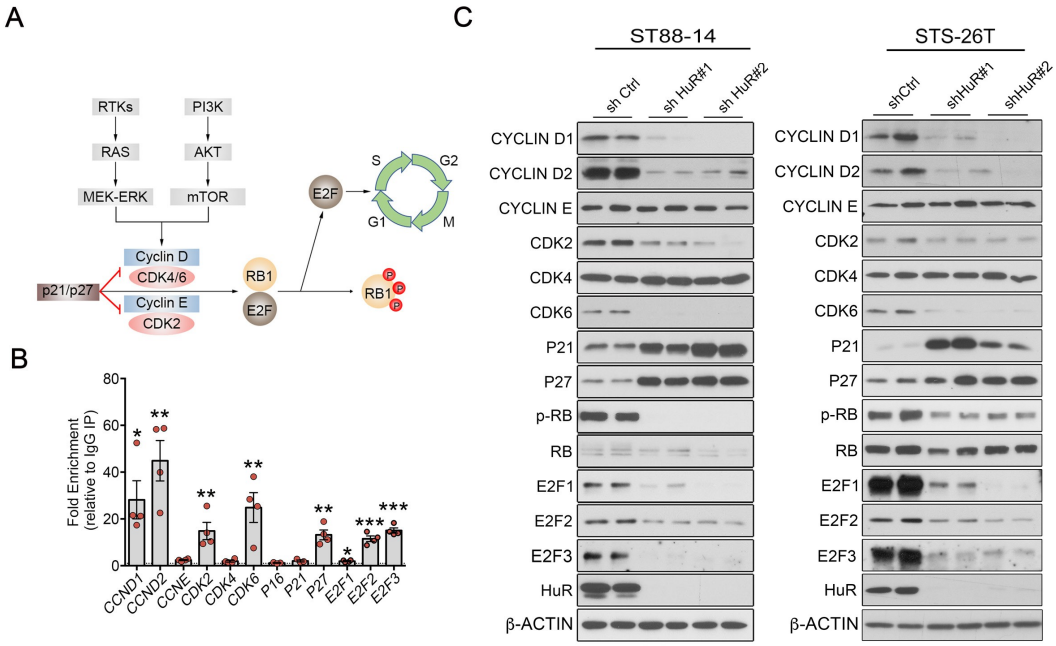

Figure 28. HuR regulates the Rb-E2F pathway in MPNST cells. A) Schematic diagram depicting regulatory components of the Rb-E2F pathway in cell cycle regulation. Cyclins form complexes by interacting with CDKs (cyclin D with CDK4/6 and cyclin E with CDK2) that phosphorylate RB1 (phosphorylated RB1 is inactive). When Rb1 is phosphorylated, E2F is released and can transcriptionally activate its target genes, enabling the G1/S transition of cell cycle. Cyclins can be regulated at the transcription level by the RAS-MEK-ERK pathway and at the translation level by mTOR via S6K and 4EBP1. P21 and p27 can bind to and inhibit Cyclin-CDK complexes. **B**) RIP-qPCR analysis showing binding of HuR to multiple genes in the Rb-E2F pathway in 4 MPNST cell lines (ST88-14, 90-8, S462, STS-26T). Data are normalised to control IgG IPs and are presented as mean ± SEM, two-tailed unpaired Student's t-test. **C**) Representative Western blots showing downregulation of several key Rb-E2F pathway components after *HuR* silencing in ST88-14 and STS-26T MPNST cells, in general concordance with RIP-qPCR data. Technical duplicates are shown, and similar results were obtained in 3 independent experiments. *p<0.05; **p<0.01, ***p<0.001.

However, in specific cases, HuR can also inhibit protein translation (Hinman and Lou, 2008) as described for *P27* (Kullmann *et al*., 2002). Here, similarly, we found that HuR depletion led to an

increase in P27 protein levels. P21 protein levels were also induced, not as a direct target of HuR, but possibly as one of the key proteins increasing in abundance during cell senescence (**Figure 28 C**).

Collectively, our results suggest that HuR may play a direct role in driving cell cycle progression via E2F transcription factors in MPNST cells by acting at several levels: (1) by enhancing the expression of specific cyclins and CDKs to promote phosphorylation of RB1 to release E2F family members (2) by repressing production of P27, an inhibitor of CDKs, and (3) by directly regulating the levels of E2F transcription factors.

6.3. HuR activates a key Wnt/β-Catenin oncogenic program in MPNST

Using the *Sleeping Beauty* forward genetic screen, signalling through the canonical Wnt/β-Catenin pathway was recently identified as a key genetic driver of MPNST tumorigenesis (Rahrmann *et al*., 2013; Watson *et al*., 2013). Canonical Wnt pathway is activated after Wnt stimulation leading to an inhibition in degradation of β-Catenin, which then enters the nucleus and binds to a member of the lymphoid-enhancing factor 1/T-cell factor (LEF1/TCF) and other transcriptional cofactors including BCL9 and Pygopus to regulate the expression of target genes involved in diverse cellular processes (Anastas and Moon, 2013). We found that *HuR* silencing led to a downregulation of *MYC*, *SOX9* and *AURKA/B* mRNAs, which have previously been identified as downstream targets of the Wnt/β-Catenin pathway in different cell systems (Dutta-Simmons *et al*., 2009; Blache *et al*., 2004; Chapuy *et al*., 2013). Here, we confirmed that these genes were also downstream target genes in MPNST cells by silencing *β-Catenin* using specific shRNAs in the ST88-14 and STS-26T cell lines (**Figure 29 A**). In line with this set of targets, GSEA analysis showed that several signature data sets associated with this pathway were significantly downregulated by *HuR* silencing (**Figure 29 B, C; supplemental Table 4 and 5**). RIP analysis showed that HuR associated with *CTNNB1* mRNA, which encodes β-Catenin, as well as *BCL9* mRNA, which we also identified as a target of HuR from our RIP-Chip analyses (**Figure 29 D**; **supplemental Table 2**). A functional role of β-Catenin in controlling MPNST cell growth and viability had already been shown using shRNA-mediated silencing of *CTNNB1* (Watson *et al*., 2013).

Furthermore, we showed that *HuR* silencing led to a notable reduction in the levels of β-CATENIN and BCL9 in ST88-14 and STS-26T cells (**Figure 30 A**), showing that HuR controlled protein production from these mRNAs. HuR depletion also significantly lowered the levels of the key downstream targets, including c-MYC, SOX9, AURKA and AURKB, further supporting a role for HuR in regulating Wnt/β-Catenin-mediated gene transcription.

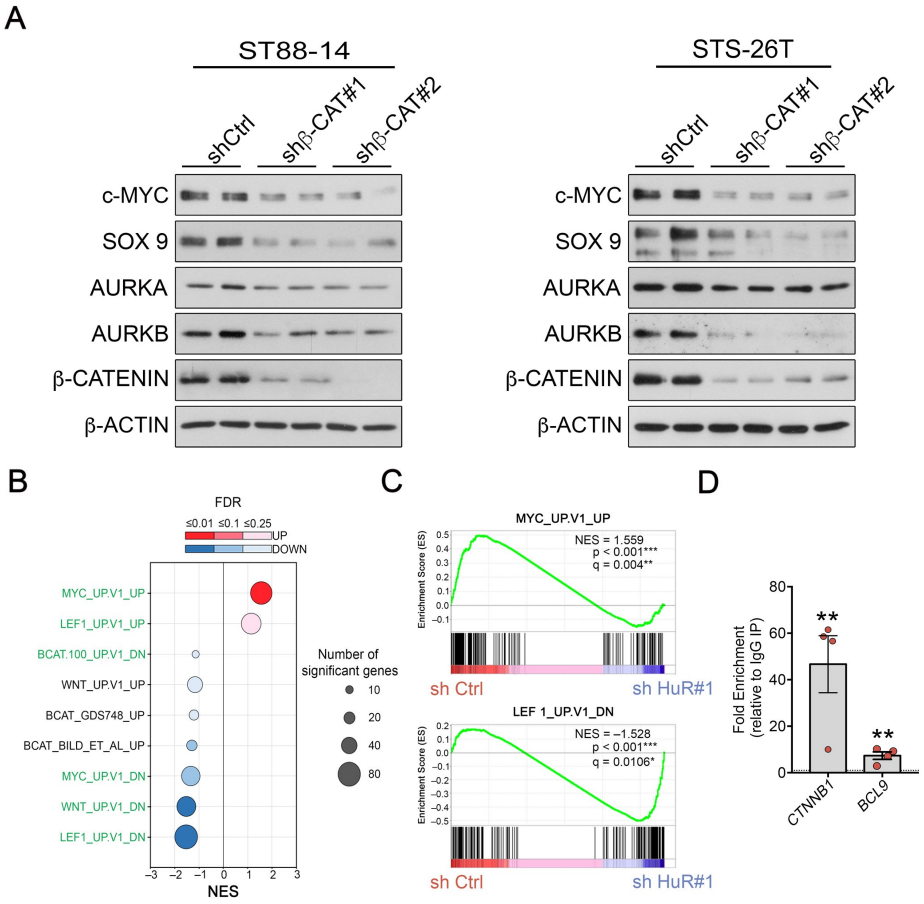

Figure 29. HuR activates key oncogenic programs in MPNST cells. A, B) Representative Western blot showing a general downregulation of Wnt/β-Catenin pathway components, including key oncogenic downstream regulators, after *β-Catenin* silencing in **A**) ST88-14 and **B**) STS-26T MPNST cells. Technical duplicates are shown, and similar results were obtained in 3 independent experiments. **C**) Compendium of normalized enrichment scores (NES) of target gene sets associated with Wnt/β–Catenin pathway after GSEA analysis of HuR–silenced ST88-14 MPNST cells after RNA-sequencing. Notably, there is a general positive correlation in the activation of the pathways (highlighted in green) in sh Control-infected compared to sh HuR#1-infected ST88-14 MPNST cells. Circles denotes the number of enriched genes in each category and colour codes represent FDR q values as indicated. **D**) GSEA plots showing enrichment of a MYC-induced target gene set (top panel) and LEF1-repressed target gene set (bottom panel) in sh Ctrl-infected compared to sh HuR#1-infected ST88-14 MPNST cells. **E**) RIP-qPCR analysis showing binding of HuR to *CTNNB1* and *BCL9* in 4 MPNST cell lines (ST88-14, 90-8, S462, STS-26T). Data are normalised to control IgG IPs and are presented as mean ± SEM, two-tailed unpaired Student's t-test. *p<0.05; **p<0.01, ***p<0.001, ****p<0.001.

To confirm previous results, we examined the capacity of ectopically expressing a degradation-resistant form of β-Catenin to abrogate the effects of *HuR* silencing in MPNST cells. Constitutive expression of the β-Catenin mutant partially blocked the effects of *HuR* silencing on downregulation of the downstream Wnt pathway targets in NF1-derived ST88-14 MPNST cells and sporadic MPNST STS-26T cell line (**Figure 30 B**). In line with this, although silencing *HuR* still reduced ATP levels and cell number in cells overexpressing the β-Catenin mutant, there was a

significant recovery in these parameters when compared to *HuR*-silenced cells expressing the empty vector plasmid in both MPNST cell lines (**Figure 30 C**).

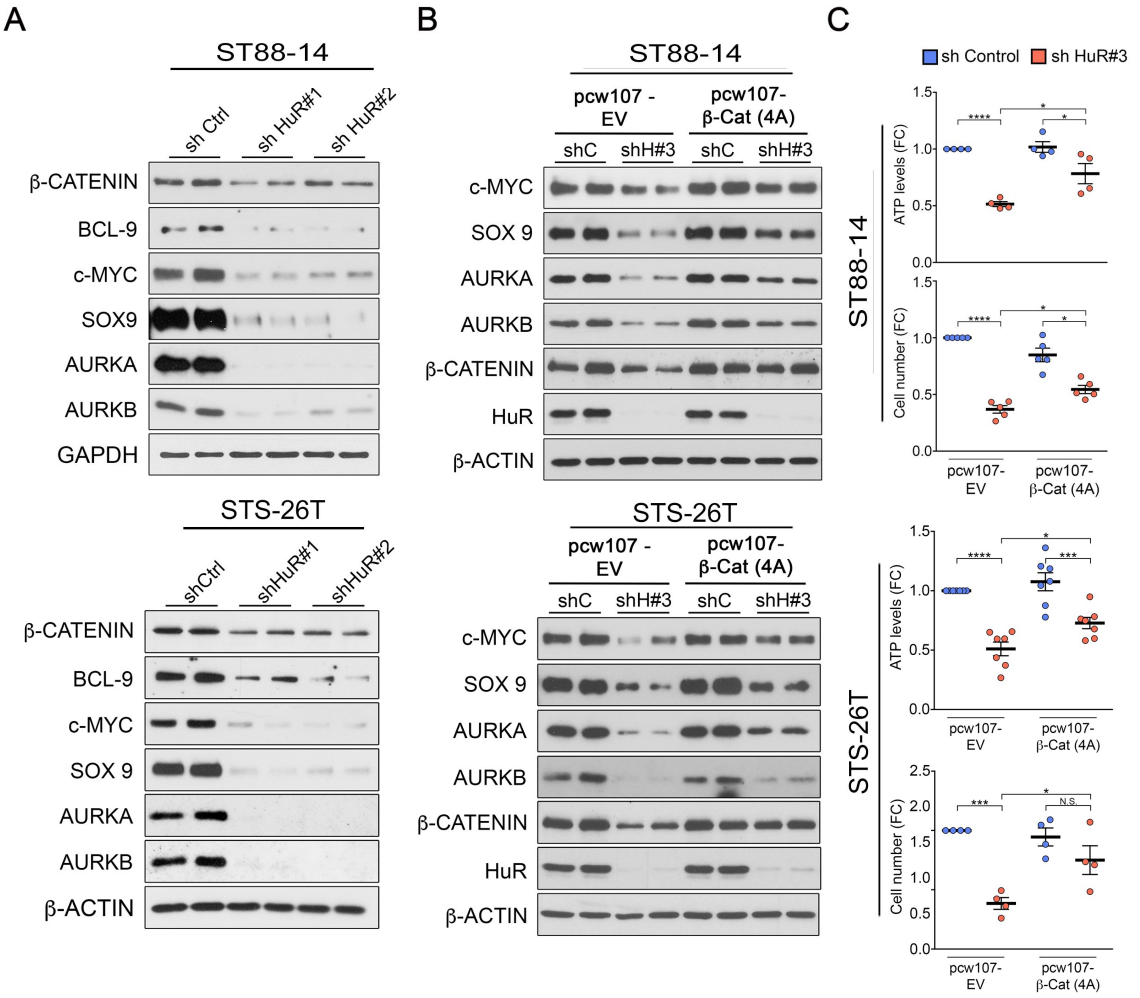

Figure 30. HuR activates key oncogenic programs by regulating the Wnt/β-Catenin pathway. A) Representative Western blots showing a general downregulation of Wnt/β-Catenin pathway components, including key oncogenic downstream regulators, after *HuR* silencing in ST88-14 and STS-26 T MPNST cells. Technical duplicates are shown, and similar results were obtained in 3 independent experiments. **B)** Representative Western blots showing that lentivirus-based expression of constitutively active β-Catenin 4A mutant [pcw107- β Cat (4A)] harbours alanine substitutions at S33, S37, T41, and S45 which prevents its degradation, partially blocks the downregulation of the key downstream regulators c-MYC, SOX9, AURKA and AURKB by *HuR* silencing in ST88-14 and STS-26 T MPNST cells. Technical duplicates are shown, and similar results were obtained in 3 independent experiments. **C)** Ectopic expression of constitutively active β-catenin 4A mutant partially blocks the effects of *HuR* silencing on cell numbers and ATP levels in ST88-14 and STS-26 T MPNST cell lines. Data are normalized to shC + pcw107-EV cells and are presented as mean ± SEM; n=4–5 independent experiments; one-way ANOVA with Tukey's multiple-comparisons test. *p<0.05; **p<0.01, ***p<0.001, ****p<0.001.

Our results above also show that a number of key oncogenic transcription factors, including c-MYC, SOX9 or E2Fs, were downregulated by *HuR* silencing. Thus, we attempted to overexpressed these transcription factors and determined whether we could rescue *HuR*-

silencing effect in MPNST cell lines. However, we found no major effect on MPNST growth when the expression of *E2F* family members were restored (**Figure 31 A**) using lentiviral overexpression constructs after *HuR* silencing in ST88-14 and STS-26T MPNST cells, shown by ATP levels and cell numbers (**Figure 31 B**).

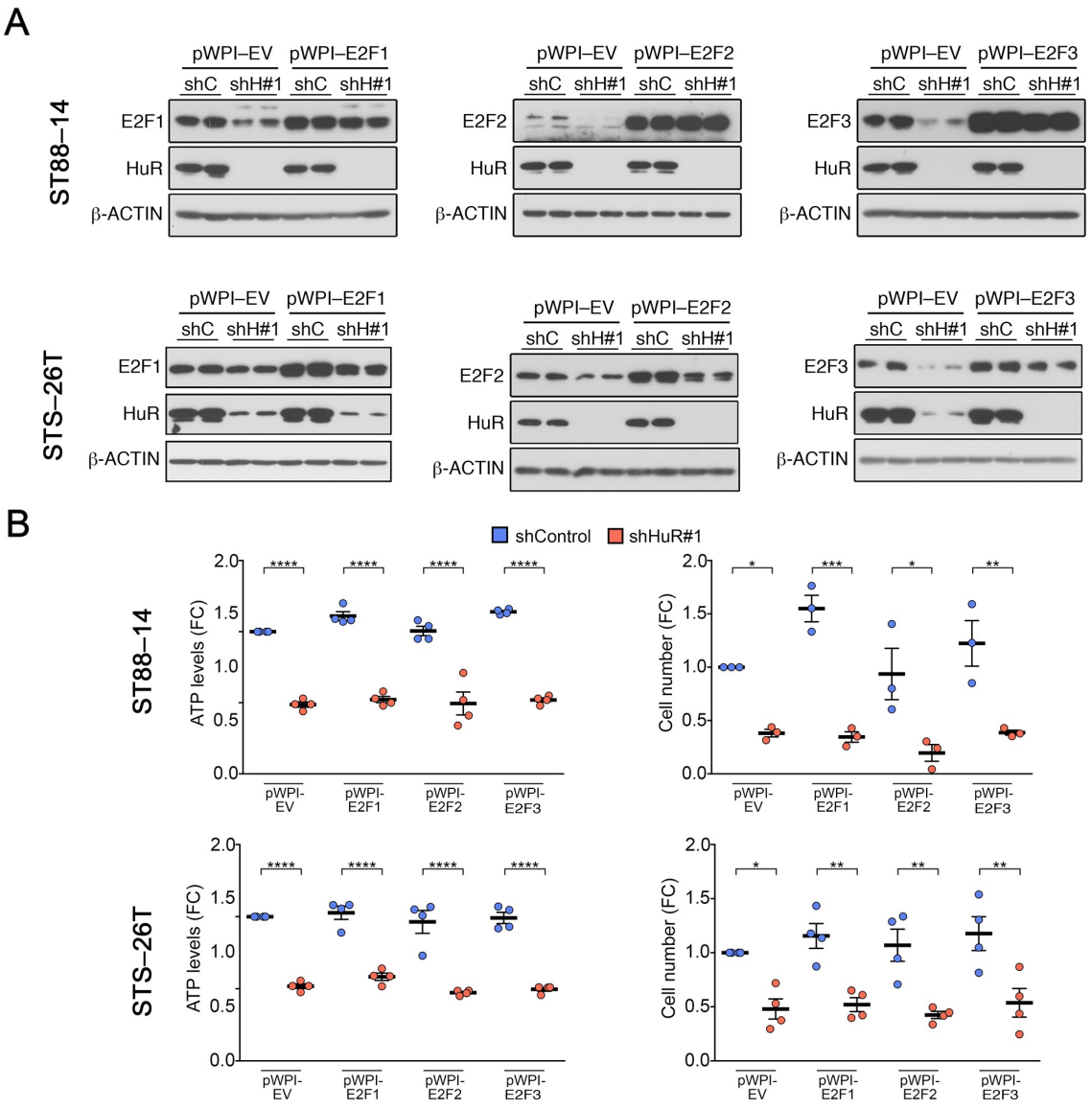

Figure 31. *HuR* silencing-mediated effects on cell growth cannot be rescued by overexpression of E2F transcription factors. A) Representative Western blots showing that expression of E2Fs and HuR after lentivirus-based expression of E2Fs and *HuR* silencing in ST88-14 and STS-26T MPNST cells. Technical duplicates are shown, and similar results were obtained in 3 independent experiments. **B)** Ectopic expression of E2Fs cannot rescue effects of *HuR* silencing on cell numbers and ATP levels in ST88-14 and STS-26T MPNST cells. Data are normalized to shControl + pWPI-EV cells and are presented as mean ± SEM; n=4 independent experiments; one-way ANOVA with Tukey's multiple-comparisons test. *p<0.05; **p<0.01, ***p<0.001, ****p<0.001.

Similarly, no major differences were observed when *c-MYC* and *SOX9* transcription factors were ectopically expressed using lentiviral overexpression constructs after *HuR* silencing compared to empty vector-infected ST88-14 and STS-26T MPNST cells (**Figure 32**).

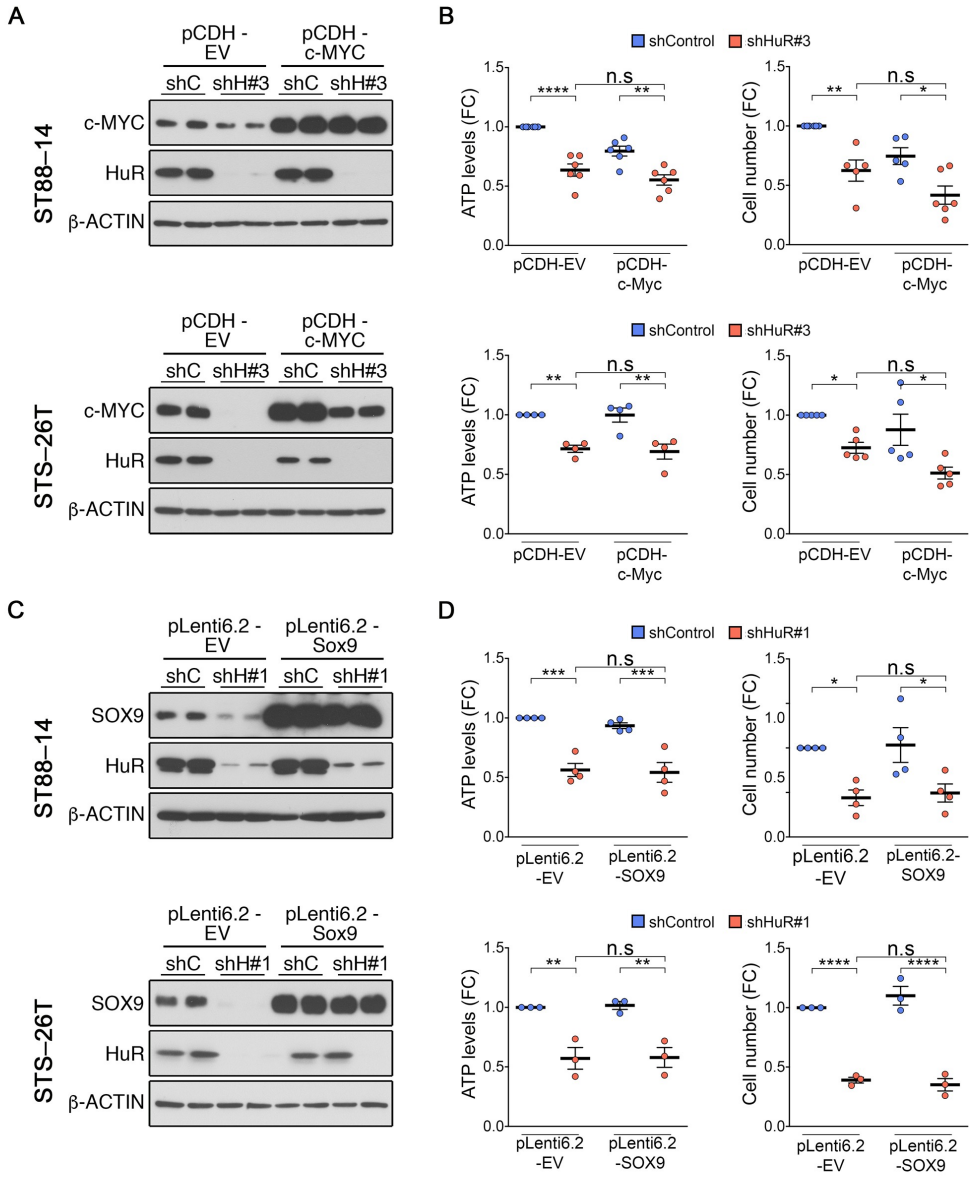

Figure 32. *HuR* silencing-mediated effects on cell growth cannot be rescued by c-MYC or SOX9 overexpression. A) Representative Western blots showing that expression of c-MYC and HuR after lentivirus-based expression of *c-MYC* and *HuR* silencing in ST88-14 and STS-26T MPNST cells. Technical duplicates are shown, and similar results were obtained in 3 independent experiments. **B**) Ectopic expression of *c-MYC* cannot rescue effects of *HuR* silencing on cell numbers and ATP levels in ST88-14 and STS-26T MPNST cells. Data are normalized to shControl + pCDH-EV cells and are presented as mean ± SEM; n=4–6 independent experiments; one-way ANOVA with Tukey's multiple-comparisons test. **C**) Representative Western blots showing SOX9 and HuR protein levels after lentivirus-based expression of *SOX9* and *HuR* silencing in ST88-14 and STS-26T MPNST cells. Technical duplicates are shown, and similar results were obtained in 3 independent experiments. **D**) Ectopic expression of *SOX9* cannot rescue effects of HuR silencing on cell numbers and ATP levels in ST88-14 and STS-26T MPNST cells. Data are normalized to shControl + pLenti6.2-EV cells and are presented as mean ± SEM; n=3–4 independent experiments; one-way ANOVA with Tukey's multiple-comparisons test. *p<0.05; **p<0.01, ***p<0.001, ****p<0.001.

Overall, these data suggest that there is a hierarchical prioritization for HuR function in MPNSTs: HuR primarily regulates the expression of key master regulators (e.g., β-Catenin, YAP/TAZ), which in turn control the production of cell cycle proteins and transcription factors.

6.4. HuR regulates a core transcriptional circuitry in MPNST cells by controlling expression of BRD proteins

Deregulation of the epigenome has also emerged as an important component of the pathogenesis of MPNST. In particular, two recent studies pointed to a role of bromodomain (BRD) and extra-terminal domain (BET) proteins in the activation and maintenance of an aberrant transcriptional program (De Raedt *et al*., 2014; Patel *et al*., 2014). BET proteins (BRD2, BRD3 and BRD4) bind to hyperacetylated lysines in promoter/enhancer regions, and subsequently recruit cofactors to control transcription of oncogenic drivers, such as MYC and E2F (He *et al*., 1998).

In MPNST cells, a small-molecule inhibitor of the BET proteins, JQ1, blocks proliferation and can induce apoptosis in MPNST cells in vitro and in vivo, highlighting the importance of these proteins in MPNST pathogenesis (De Raedt *et al*., 2014; Patel *et al*., 2014). Using GSEA analysis, we found a striking enrichment of genes activated by JQ1 treatment in MPNST cells (De Raedt *et al*., 2014) and genes upregulated by *HuR* silencing in our dataset (**Figure 33 A**). Furthermore, in line with our RIP-Chip analyses, where we found enrichment of *BRD2* mRNA in HuR-bound fractions (**Supplemental Table 2**), we found that mRNAs encoding all 3 BET family members, BRD2, BRD3 and BRD4, were highly enriched in HuR fractions in RIP-qPCR analyses of MPNST cell lines (**Figure 33 B**). *HuR* silencing strongly reduced all three BET proteins in both the ST88-14 and STS-26T cell lines, suggesting a role for HuR in promoting the stability and/or translation of the corresponding mRNAs (**Figure 33 C**). A functional role of BRD4 in controlling cell growth and viability in MPNST cells had already been shown using shRNA-mediated silencing (De Raedt *et al*., 2014; Patel *et al*., 2014). Here, we found that silencing *BRD2* using two distinct *BRD2*-specific shRNAs also led to a reduction in cell growth and viability (**Figure 33 D**–**F**), underscoring the importance of this transcriptional regulator in MPNST.

Key recent studies have shown that JQ1 treatment in melanoma and multiple myeloma cells depletes BRD2 and BRD4 from promoter and enhancer regions of the genome and this was associated with the disruption of transcriptional programs in these cells (Loven *et al*., 2013; Fontanals-Cirera *et al*., 2017). To gain mechanistic insight into the role of HuR in mediating the function of BET proteins in MPNST cells, we investigated changes in BET occupancy on a genome

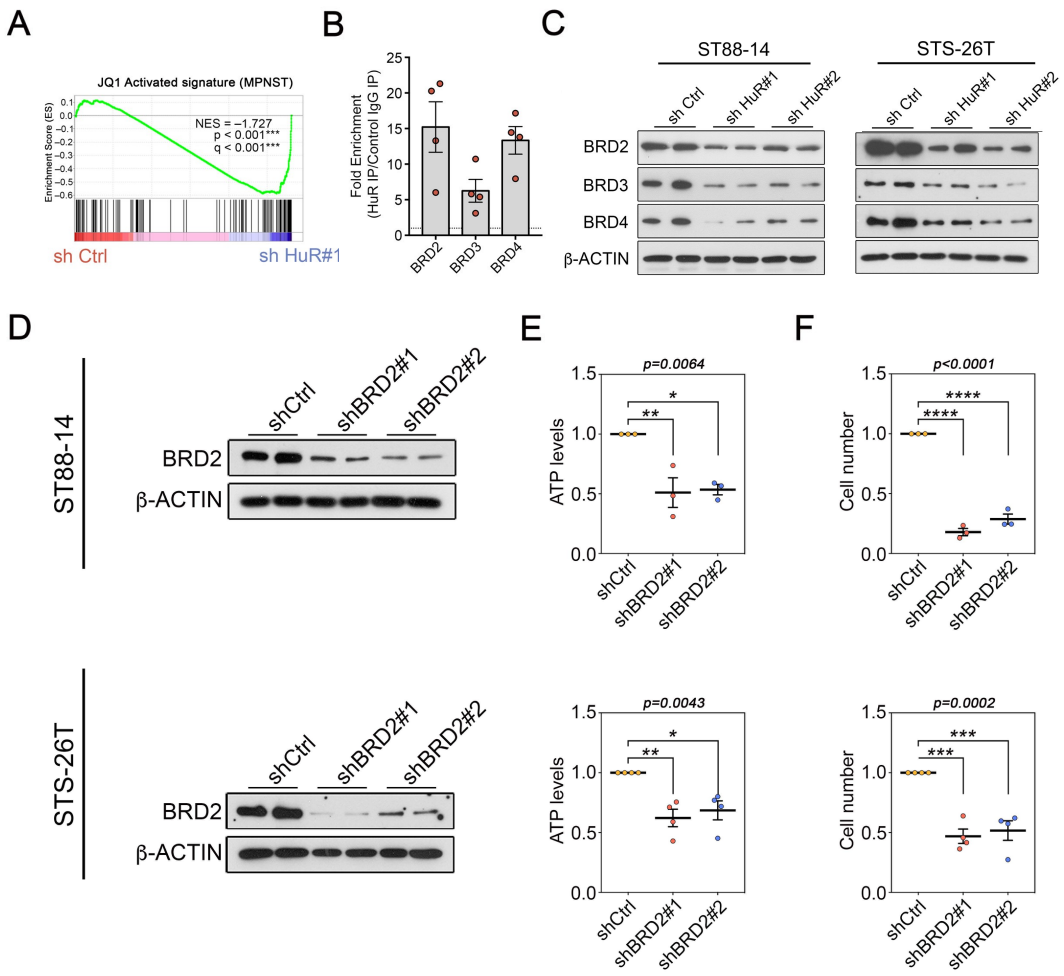

Figure 33. HuR regulates expression of BRD proteins in MPNST cells. **A**) GSEA plot showing an enrichment of genes upregulated in MPNST cells by JQ1 treatment (FC >1.5 and adjusted p-value<0.05) (De Raedt *et al.*, 2014) and sh HuR#1-infected ST88-14 MPNST cells. **B**) RIP-qPCR analysis showing binding of HuR to *BRD2*, *BRD3* and *BRD4* in 4 MPNST cell lines (ST88-14, 90-8, S462, STS-26T). Data are normalised to control IgG IPs and are presented as mean ± SEM, two-tailed unpaired Student's t-test. **C**) Representative Western blots showing downregulation of BRD proteins after *HuR* silencing in ST88-14 and STS-26T MPNST cells. Technical duplicates are shown, and similar results were obtained in 3 independent experiments. **D**–**F**) Growth of MPNST cell lines ST88-14 and STS-26T are sensitive to constitutive *BRD2* silencing *in vitro*. **D**) Representative immunoblots of BRD2 protein levels after shRNA-mediated knockdown with two distinct *BRD2*-specific sh RNAs (sh BRD2 #1 and sh BRD2#2). β-ACTIN was used as a loading control. Technical duplicates are shown, and similar results were obtained in at least 3 independent experiments. **E**, **F**) *BRD2* silencing leads to a reduction in cell growth in both cell lines, as determined by **E**) ATP luminescence assays and **F**) counts of cell numbers, 5 days after selection. Data are normalized to shCtrl cells and are presented as mean ± SEM; n=3–4 independent experiments; one-way ANOVA with Tukey's multiple-comparisons test. *p<0.05; **p<0.01, ***p<0.001, ****p<0.001.

scale by ChIP-Seq in ST88-14 cells after *HuR* silencing. We found that *HuR* silencing significantly reduced genome-wide BRD2, BRD3 and BRD4 occupancy by ~60 %, ~50 % and ~45 % respectively (**Figure 34 A**). Next, to examine the functional effects of the BETs occupancy on transcriptional regulation, we generated a chromatin landscape in ST88-14 cells using H3K4me3

to identify promoters, H3K4me1 to identify enhancers, and H3K27ac to identify active promoter/enhancer regions.

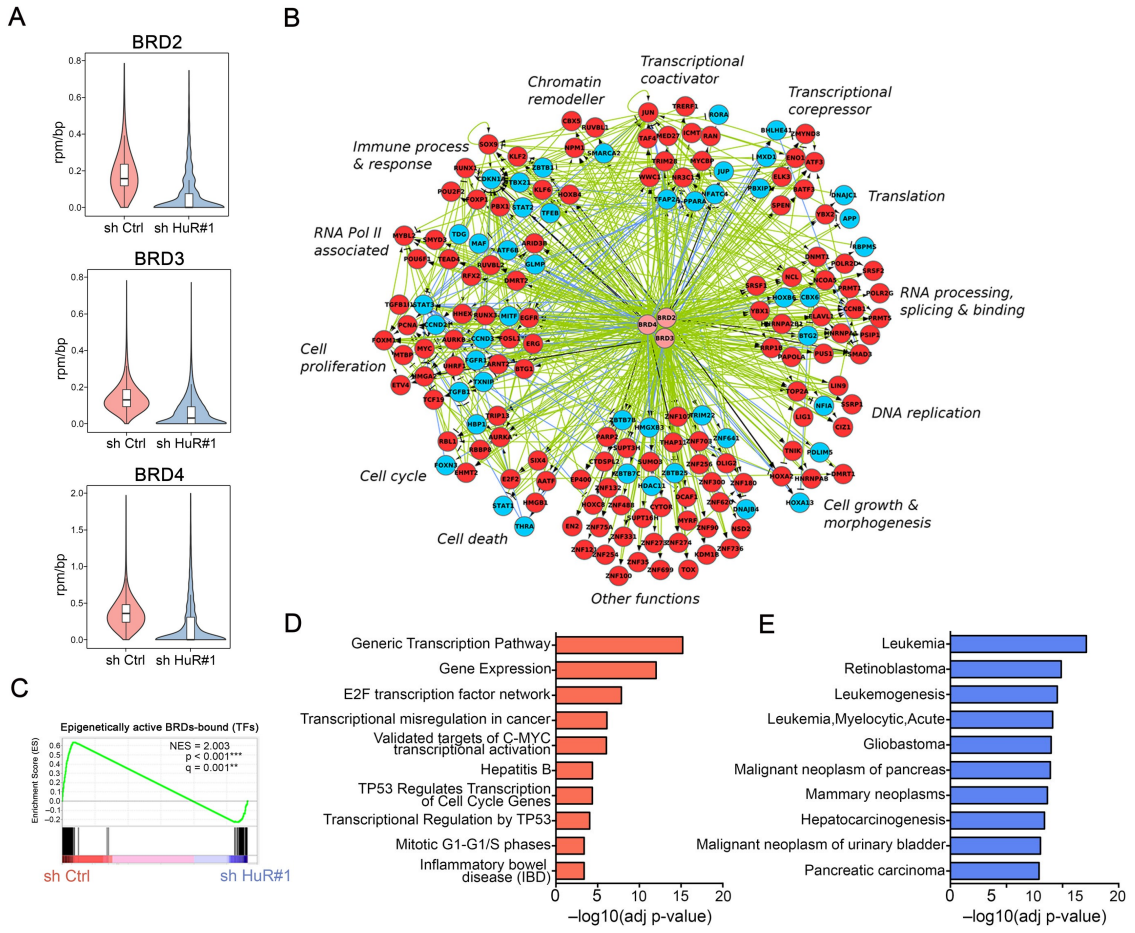

Figure 34. HuR regulates a core transcriptional circuitry in MPNST cells by controlling expression of BRD proteins. A) Violin plot showing the distributions of BRD2, BRD3 and BRD4 ChIP-seq signal at enriched regions in control (sh Ctrl)-infected and sh HuR#1-infected ST88-14 MPNST cells. The y axis shows BRD ChIP-seq signal in units of reads per million (rpm)/bp. The loss of BRD occupancy at BRD-enriched regions after *HuR* silencing is highly significant (BRD2: P = 4.44 x 10^{-16}, BRD3: P = 1.332 x 10^{-15}, BRD4: P = 1.332 x 10^{-15}, Welch's t-test). **B**) Gene regulatory networks among differentially expressed, epigenetically active transcription factors (TFs) that are either direct or indirect targets of BRD proteins. Red and blue circles represent differentially up-regulated TFs in sh Ctrl-infected cells and down-regulated TFs in sh Ctrl-infected cells respectively. Light green edges indicate regulatory interactions unique to sh Ctrl cells, light blue edges indicate those unique to sh HuR#1-infected cells, and black edges indicate those present in both phenotypes. Pointed arrows indicate activation and blunted arrows indicate inhibition. Functional categories are based on Gene Ontology Biological Processes. **C**) GSEA plot showing strong enrichment of epigenetically active TFs that are either direct or indirect targets of BRD proteins in sh Ctrl or sh HuR#1-transduced ST88-14 MPNST cells. **D**, **E**) ToppGene analysis of HuR-regulated TF network in MPNST cells (Epigenetically active TFs that are either direct or indirect targets of BRD proteins in sh Ctrl-infected cells and are downregulated in sh HuR#1-transduced cells; red circles from B), as classified according to **D**) pathway categories or **H**) disease.

Using the chromatin landscape information explained above, we performed network analysis to generate a network of transcriptional regulators that are targets of BRD proteins and

regulated by HuR expression. In brief, we identified BRD-bound epigenetically active (active promoters and enhancers) and differentially regulated transcription factors in control and *HuR*-silenced cells (**Figure 34 B**). It is apparent from this analysis that there is a considerable number of transcriptional regulators in MPNST cells that are associated with BRD proteins and that control key processes, such as proliferation. Importantly, we found that a substantial proportion of these transcriptional regulators were especially sensitive to HuR inhibition, which depleted BRD proteins from their promoter/enhancer regions and downregulated their expression (red circles). Thus, GSEA analysis of BRD-bound transcriptional regulators demonstrated a significant enrichment of genes activated in control cells and repressed by HuR silencing (**Figure 34 C**). Gene enrichment analysis by ToppGene suite (Chen *et al*., 2009a) identified these repressed regulators as being overrepresented in different oncogenic pathways, including E2F and MYC transcription factor networks, proliferation and TP53-regulated pathways, and for different cancers (**Figure 34 D**, **E**).

Collectively, these data demonstrate that BRD proteins are enriched at promoter/enhancer regions of key transcriptional regulators in MPNST cells, and that a reduction in their levels and genome occupancy by HuR silencing suppresses this oncogenic transcriptional circuitry.

***** See Supplementary Material for **supplemental tables**

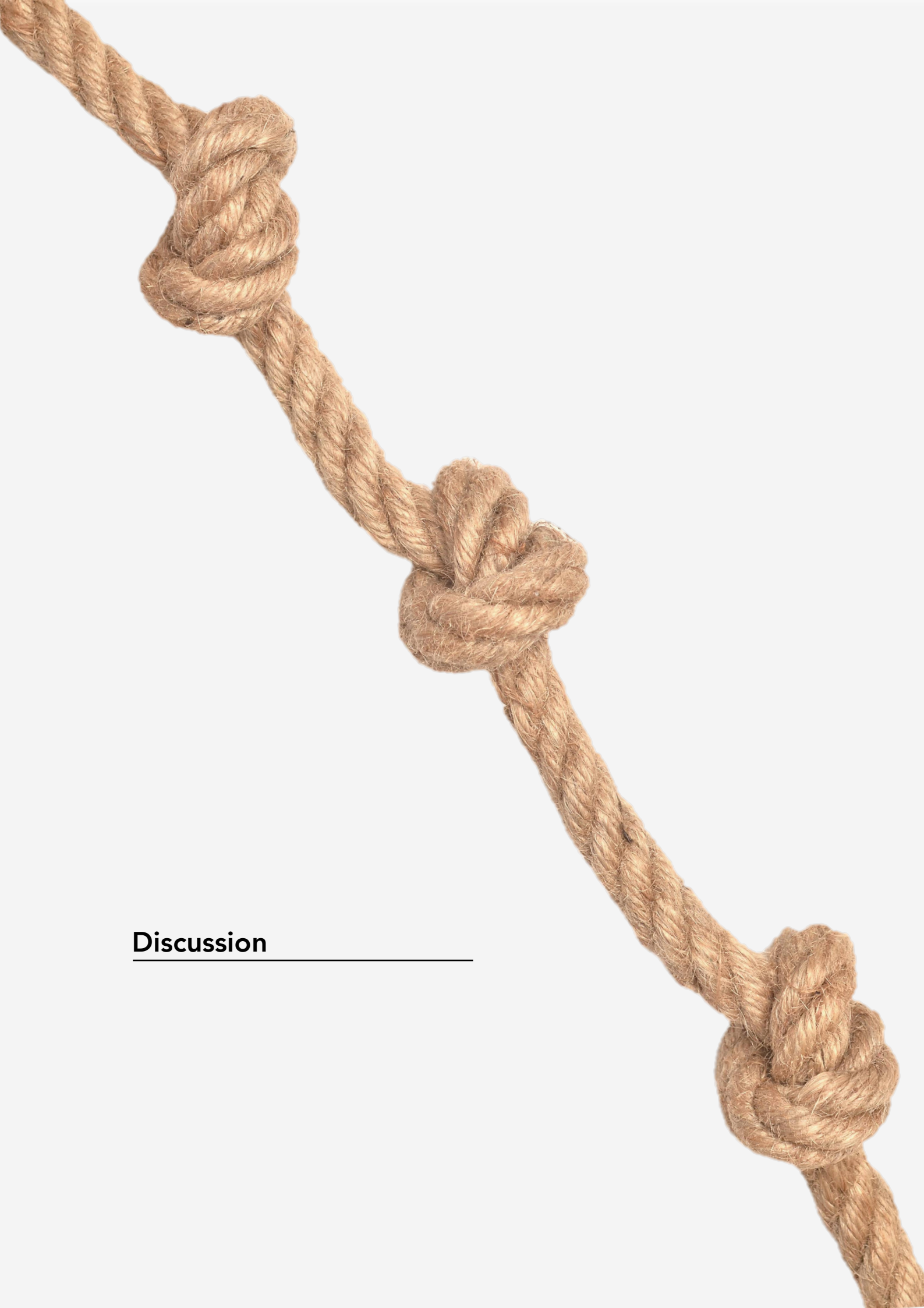

Discussion

Discussion

Cancer arises from multiple genetic lesions that lead to aberrant gene expression programs, which are increasingly being recognised as fundamental for the acquisition, development and maintenance of cancer phenotypes. Compelling recent evidence shows that cancer cells can develop absolute dependencies on discrete molecular regulators – out of the thousands of human proteins that contribute to control of gene expression – that drive these dysregulated transcriptional programs. There is nowadays an intense search for these key regulators through focussed mechanistic studies, since they represent attractive targets for effective and enduring therapies in cancer (Gonda and Ramsay, 2015; Bradner *et al*., 2017).

In this study, we present evidence that MPNST cells exhibit an exceptional reliance on the RNA-binding protein HuR for their abilities to survive, proliferate and disseminate. HuR inhibition prevented the formation of tumours in xenograft models, and even induced a striking regression of tumour volume in established tumours. Furthermore, HuR strongly promoted the metastatic capacity of MPNST cells, one of the worst prognostic features of this cancer. We propose that HuR-regulated transcriptomes promotes the survival and adaptation strategies that allow the disseminated cancer cells to survive in the circulation, migrate to, extravasate and thrive in incompatible foreign microenvironments of distant tissues. Consistent with these results, we found that HuR regulated essential biological capabilities of MPNST cells, including cell cycle progression and sustained proliferation, resisting cell death in stress conditions and enabling replicative immortality. Notably, the functional consequences of HuR inhibition was largely comparable in a representative panel of 4 MPNST cell lines, obtained from patients with different NF1 status, even though these exhibit heterogeneous cellular growth rates and alterations in expression of a number of cell cycle proteins (Miller *et al*., 2006). This lack of major differences, functionally or mechanistically, between NF1-derived and sporadic MPNSTs after *HuR* silencing support the view that relatively similar molecular mechanisms are involved in the pathogenesis of MPNST, and that HuR can be a broad target for MPNSTs, irrespective of NF1 status (Fraid *et al*., 2014).

Mechanistically, our RIP-Chip and transcriptomics data showed a global dysregulation of several signalling pathways and molecular regulators in these cancer cells, including the HIPPO-YAP/TAZ, PI3K/AKT/mTOR, RAS/RAF-MEK-ERK and Wnt/β-Catenin pathways and bromodomain regulation of gene transcription, while our focused analyses revealed that regulation by HuR of specific components of these pathways likely led to the aberrant signalling. Several of these pathways, including WNT/β-Catenin, seem to be specific to MPNSTs, since we find that HuR cannot regulate them in normal Schwann cells (data not shown). We posit that this capacity of

HuR to simultaneously control several essential molecular regulators that operate in these cancer cells explains in large part the striking effects of HuR inhibition in MPNST cells. All these pathways have been shown to contribute to MPNST pathogenesis in seminal studies from several laboratories using various genetically engineered mouse models or culture systems (Patel *et al*., 2012; Watson *et al*., 2013; De Raedt *et al*., 2014; Farid *et al*., 2014; Patel *et al*., 2014; Carroll, 2016; Wu *et al*., 2018). However, genetic or pharmacological inhibition of these targets individually have, in general, been modestly effective and largely cytostatic. Instead, concurrent targeting of different pathways has been proved to be more potent. Thus, combined inhibition of YAP/TAZ and PDGFR signalling activity (Wu *et al*., 2018), BRD proteins and MEK activity (De Raedt *et al*., 2014), or the mTOR and Wnt/β-Catenin pathways (Watson *et al*., 2013) are strongly synergistic in blocking tumour growth, and can even induce apoptosis.

These observations strongly support the view that parallel and redundant pathways control the oncogenic traits in MPNST cells, a phenomenon that has been associated with the emergence of therapeutic resistance in cancer cells (Hanahan and Weinberg, 2011; Gonda and Ramsay, 2015). This is particularly true for targeted therapies against kinase-mediated signalling cascades, which are organized in a linear and hierarchical manner, with different receptor tyrosine kinases at the top, activating a reduced number of kinase signalling cascades, including RAS/RAF-MEK-ERK, PI3K-AKT and JAK-STAT that operate in parallel but which can crosstalk with one another (Gonda and Ramsay, 2015). This linear and redundant architecture facilitates bypassing of a signalling pathway after its inhibition for another, thus blocking the therapeutic effects of the drugs. This paradigm is also consistent with the disappointingly poor results obtained from Phase I and Phase II clinical trials from targeting individual components of kinase cascades in MPNST patients. Because of the superior results obtained from additive effects of cotargeting multiple pathways, current clinical trials are more focused on combination drug therapy (Farid *et al*., 2014; Kim *et al*., 2017). Our results strongly argue that targeting HuR could be as equally effective as the combined treatments, as we find that HuR inhibition potently suppresses several of the oncogenic signals in MPNSTs, leading to the profound cytostatic and cytotoxic effects on tumour growth, as well as on their metastatic capacity.

Strikingly, we find that targeting HuR can both prevent the formation of tumours and metastatic nodules, as well as lead to shrinkage of fully established tumours and metastases. Thus, therapeutic intervention could be equally effective in newly diagnosed or recurrent tumours, which has particularly appealing translational importance, since timing of intervention and stage of disease has been raised as a possibility for negative clinical trials in MPNSTs. However, even though our promising data on pharmacological inhibition of HuR could represent a viable therapy for patients with MPNST, it is still unclear whether the preclinical efficacy

observed in this study using cell lines and mice can be translated to the clinic. Whether HuR is a valid therapeutic target in MPNST warrants direct investigation.

Our ChIP-Seq data reveal a large network of transcriptional regulators operating in MPNST cells that are associated with key biological functions. Notably, we find that this network is highly sensitive to levels of HuR that regulate expression of these regulators via regulation of BRD protein levels, and/or signalling pathways. An essential role for BRD proteins in regulating gene expression has also been shown in several malignancies, including MPNST, and interestingly, we find that HuR silencing in MPNST phenocopies to a large extent treatment with the BET inhibitor JQ1, at least in terms of gene expression profiles. In addition, the displacement of BRD proteins on promoter/enhancer regions of active cancer-related genes by JQ1 in haematological malignancies and melanoma (Chapuy *et al*., 2013; Loven *et al*., 2013; Fontanals-Cirera *et al*., 2017) is similar to the reduced promoter/enhancer occupancy on transcriptional regulators in MPNSTs we found after *HuR* silencing. Thus, our data suggest that the dysregulation of the transcriptional program in MPNST by *HuR* silencing, could be in large part mediated by the influence of HuR on the MPNST transcriptional network.

Remarkably, we found that HuR depletion led to strong suppression of MYC and E2Fs levels that was accompanied by a highly significant reduction in the abundance of MYC- and E2F-transcribed gene sets, pointing to a general suppression of transcription at E2F- and MYC-driven targets by HuR inhibition. These proto-oncogenic transcription factors (TFs) are among the most important drivers of tumorigenesis, as they regulate cell growth, proliferation, apoptosis and metabolic pathways (Chen *et al*., 2009b; Kress *et al*., 2015), and represent some of the important targets for cancer therapy, although efforts to directly target these TFs have proved unsuccessful so far (Bradner *et al*., 2017). Our work could thus have far-reaching implications for cancer therapy, since it suggests an alternative strategy to effectively target these TFs. MYC regulation also represents one of the best examples of the "multifunctional" capacity of HuR in driving expression of particular oncoproteins. MYC levels are regulated by major growth-regulatory and oncogenic signalling pathways, including the Wnt/β-Catenin, JAK-STAT and Notch pathways that induce *MYC* transcription and mTOR pathway that increases the efficiency of *MYC* mRNA translation, together with function of the PI3K and RAS signalling, and AURKA/B in increasing the stability of MYC protein (Chen *et al*., 2009b; Dauch *et al*., 2016). The striking downregulation of MYC levels in MPNST cells by HuR inhibition could potentially be mediated by a combinatorial action at several of these nodes of regulation, that are themselves under strong HuR influence. Similarly, E2F levels/function in MPNST cells could be determined by HuR by affecting multiple regulatory mechanisms, including Cyclin-CDK expression, RB phosphorylation and *E2Fs* transcription/translation.

RBPs play a central role in regulation of gene expression, and thus it is not surprising that their dysregulation has been linked to several human diseases, including neurological disorders and cancer (Wurth and Gebauer, 2015; Pereira *et al*., 2017). These dynamic regulators can bind to and regulate thousands of functionally related genes, regulating every hallmark of cancer cells. Recent detailed studies have shown that RBPs are rapidly emerging as key oncogenic drivers in a variety of malignancies (Ortiz-Zapater, *et al*., 2011; Nguyen *et al*., 2014; Pereira *et al*., 2017; Perron *et al*., 2018). In this study, we show the RBP HuR has pleiotropic functions in MPNST, driving tumour growth and metastasis by, quite strikingly, influencing almost all key signalling pathways and regulators discovered in MPNSTs so far, including the PI3K/AKT/mTOR, RAS/RAF-MEK-ERK, WNT/β-Catenin and HIPPO-YAP/TAZ pathways, and transcriptional regulators that include SOX9, AURKA/B, BRD proteins, as well as the proto-oncogenic TFs MYC and E2Fs. Over 1500 RBPs have been described and several of them are dysregulated in MPNSTs (data not shown). It would be interesting to examine their biological and mechanistic functions in MPNSTs, and whether they have broad functions similar to HuR or regulate distinct pathways

This function of HuR in establishing the highly intricate regulatory networks operating in MPNSTs to coordinate multiple cancer hallmark traits supports a “master” regulatory function for HuR in MPNST. Thus, by elevating HuR levels, MPNST cells have elaborated an adaptive mechanism to amplify and regulate key oncogenic signals and modulate transcriptional programs to confer a competitive advantage to these cancer cells, promoting MPNST growth and metastatic spread (**graphical abstract**).

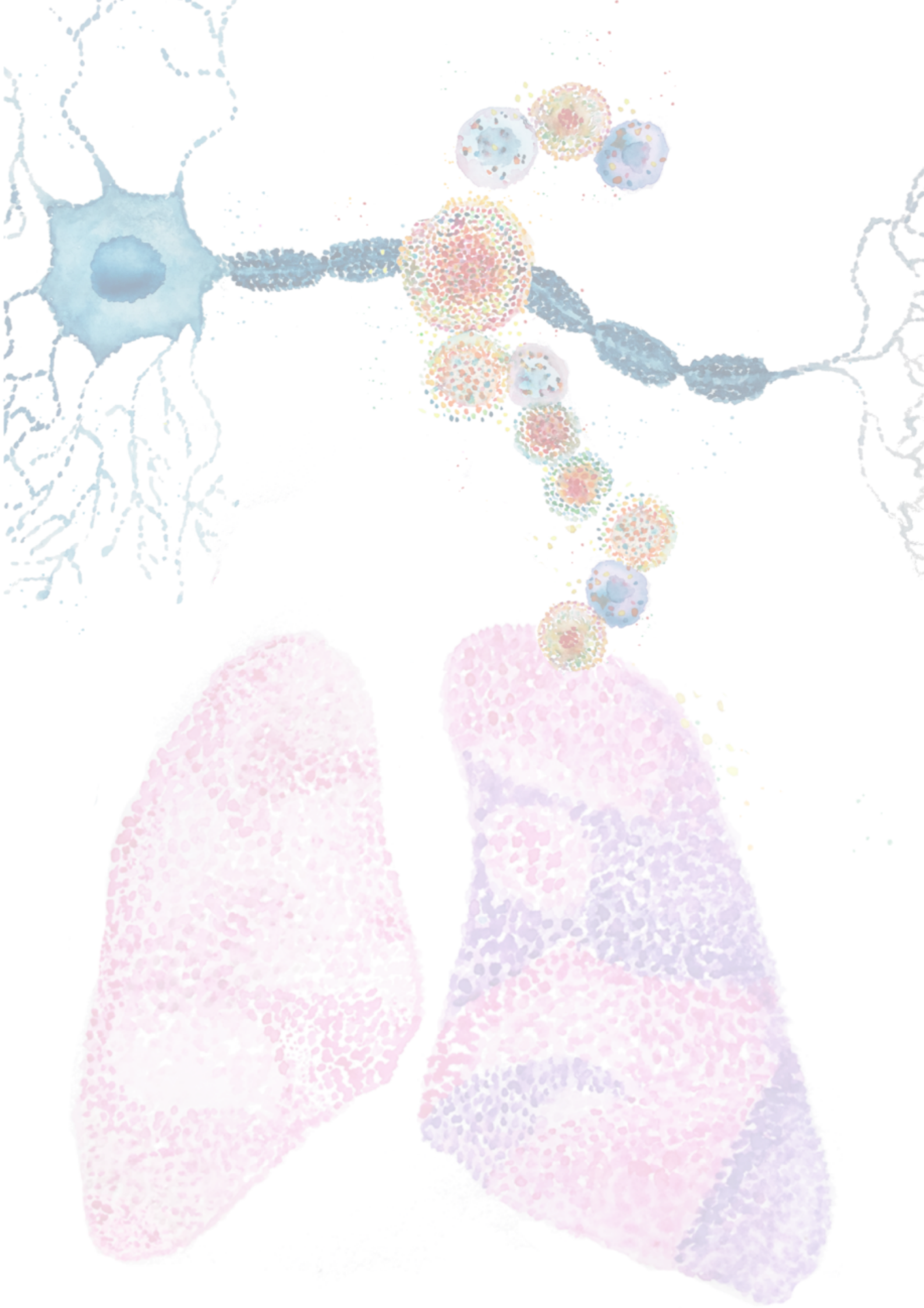

Conclusions

☑ Human antigen R (HuR) RNA-binding protein (RBP) regulates multiple oncogenic pathways in malignant peripheral nerve sheath tumours (MPNSTs) by promoting the expression of β-Catenin, BRD proteins and YAP/TAZ transcription factors, which converge on key transcriptional networks essential for MPNST growth and metastasis (**graphical abstract**).

Graphical abstract

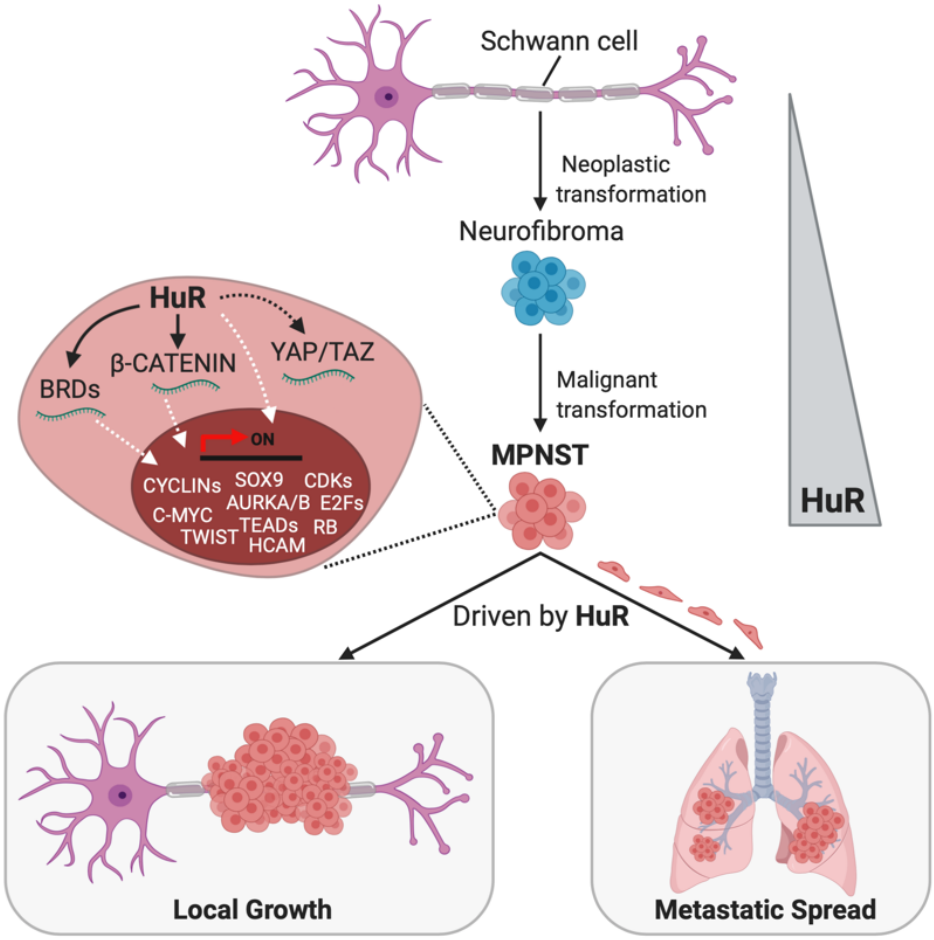

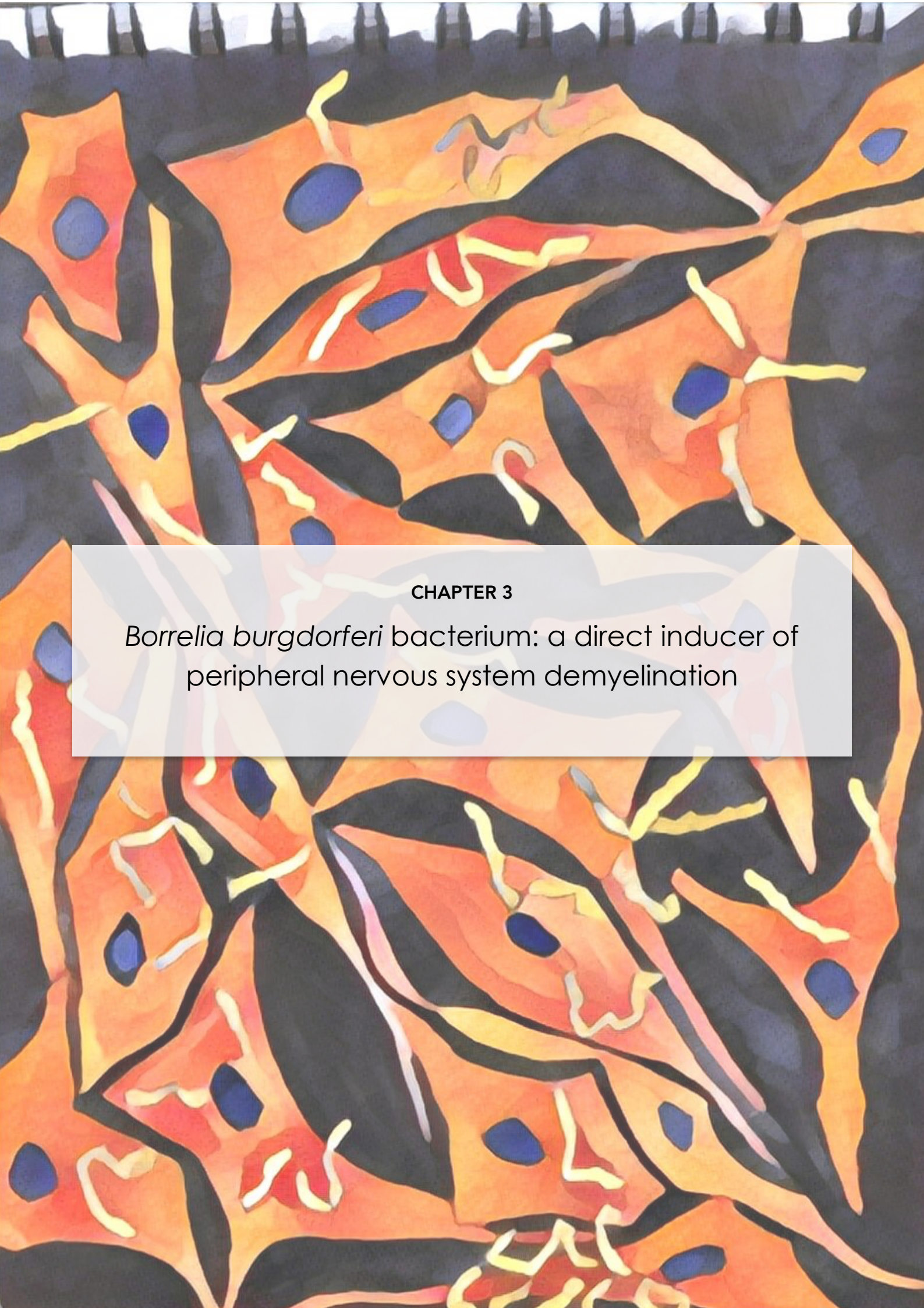

CHAPTER 3

Borrelia burgdorferi bacterium: a direct inducer of peripheral nervous system demyelination

Introduction

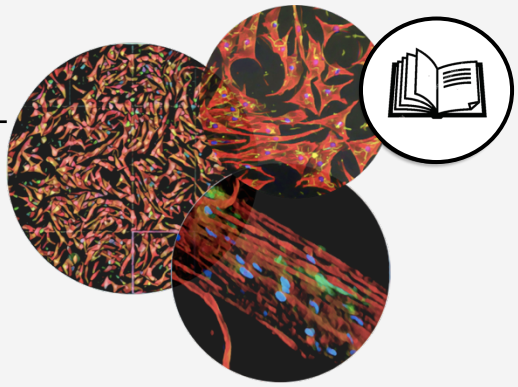

Introduction

1. Lyme disease

Vector-borne diseases represent more than 17 % of all infectious diseases, which are responsible for more than 700,000 deaths annually (World Health Organization, https://www.who.int/news-room/fact-sheets/detail/vector-borne-diseases).

Lyme disease, caused by a bacteria, is the most commonly reported vector-borne disease, with an estimation of about 300,000-400,000 cases per year in the US (Hinckley *et al.*, 2014; Nelson *et al.*, 2015) with a prevalence of 20 to 100 cases per 100,000 people and about 100,000-200,000 cases per year in Europe with an estimation of 100 to 130 cases per 100,000 people (van den Wijngaard *et al*., 2017). Furthermore, incidence has increased during the last decades because climate change is leading to the expansion of tick vectors habitat (Lindgren and Jaenson, 2006; Medlock and Leach, 2015; Jones *et al.*, 2018). Clinical manifestations of Lyme disease, if left untreated or even in some cases after antibiotic treatment, can persist for long periods leading to nervous system damage, perhaps one of the most dangerous and poorly understood manifestations of the infectious disease (Rupprecht *et al*., 2008) affecting up to 15 % of Lyme disease patients (Koedel *et al*., 2015; Halperin, 2017).

Lyme disease, also called Lyme borreliosis, is transmitted to humans by a bite of a tick belonging to the *Ixodes* genus, which has previously acquired the causative agent from an infected animal. The causative agent of Lyme disease was not described until 1982, named as *B. burgdorferi* in honor of medical entomologist Willy Burgdorfer, who discovered the bacterium in the mid-gut of a nymphal *Ixodes scapularis* tick (Johnson *et al.*, 1984; Burgdorfer *et al.*, 1982; Barbour and Benach, 2019). Ticks were also observed in the skin of patients when disease was first described, in 1976 in Lyme, Connecticut. In Europe, on the other hand, *B. burgdorferi* spirochete was not isolated from skin samples of patients until 1983 (Asbrink *et al.*, 1984). Furthermore, there are different *Borrelia* genospecies (*B. afzelii*, *B. garinii* and *B. burgdorferi*) that can cause Lyme disease in humans, hereafter refered to as *B. burgdorferi sensu lato* (s.l.). *B. afzelii* and *B. garinii* are the responsible for the vast majority of Lyme disease cases in Eurasia, whereas *B. burgdorferi* sensu stricto (hereafter referred as *B. burgdorferi*) is the only one known to cause the disease in North America, and it is the only one observed in all tick habitats (Samuels and Radolf, 2010, Stanek *et al.*, 2012). Recently, newly identified strains of *Borrelia* causing Lyme disease have been reported, including *B. mayonii* (Pritt et al., 2016).

1.1. Transmission: Vectors

Ticks are obligate ectoparasites, bloodsucking arthropods that can transmit multitude of pathogens to humans. There are about 900 tick species, which almost all belong to the two main familes, Ixodidae (known as "hard ticks") and Argasidae (known as "soft ticks"). There is a third family, Nuttalliellidae, with only one species, *Nuttalliella namaqua*, which presents features of both main families (Argasidae and Ixodidae) (Guglielmone *et al*., 2010; Mans *et al.*, 2012). These two main families are divided based on differences not only in life cycles, but also in morphology and physiological features (Estrada-Peña, 2015) (**Figure 35**). Ticks usually live in forests where the relative humidity is of 80 % and there is low incidence of desiccation and can live up to 1350 m of altitude (Stünzner *et al*., 2006). The six-legged larvae and the eight-legged nymphs, are found in low vegetation, and thus the hosts are small animals, such as rodents, insectivores, and birds. Adult ticks, on the other hand, tend to live higher up on vegetation, which allows them to infest larger hosts, especially deer. Hard ticks feed on hosts for longer periods than soft ticks and can ingest more than 100 times their body mass in blood, by anchoring to the host with a calcified structure called hypostome (Samuels and Radolf, 2010) (**Figure 35 B**), while soft ticks ingest blood until their weight increase from 5 to 10-fold compared to unfed state.

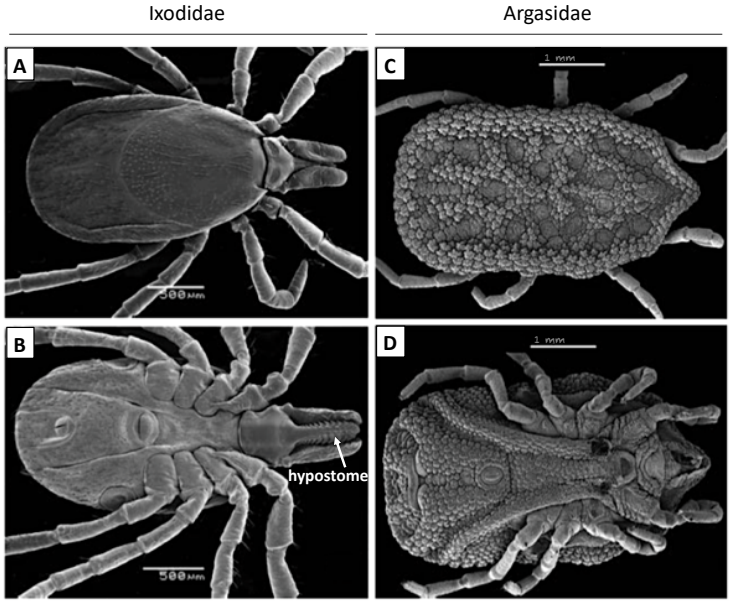

Figure 35. External morphology of ticks belonging to Ixodidade and Argasidae families. A) Dorsal and **B)** ventral side of a female *Ixodes ricinus*, representative of Ixodidade family. Hypostome is marked by the arrow. **C)** Dorsal and **D)** ventral views of an argasid tick, *Ornithodoros puertoricensis* (modified from Estrada-Peña, 2015).

The four principal hard tick species that transmit Lyme disease causative agents belong to *Ixodes scapularis* in eastern North America, *I. pacificus* in western North America, *I. persulcatus* in Asia and some areas of eastern Europe, and *I. ricinus* in all Europe (Masuzawa, 2004; Piesman

and Gern, 2004; Steere *et al.*, 2004; Ogden *et al.*, 2009) (**Figure 36**). *I. ricinus*, commonly known as sheep tick, can transmit the three *B. burgdorferi* s.l. genospecies with a higher prevalence than any other tick species.

Ixodes ticks have four stages in their life cycle: eggs, larva, nymph and last adult stage (**Figure 36**). Males die after depositing spermatophores within the females, whereas females die after laying about 2000 eggs into the vegetation (Stanek *et al*., 2012; Steere *et al*., 2016). The length of the life cycle can vary between 2 and 6 years.

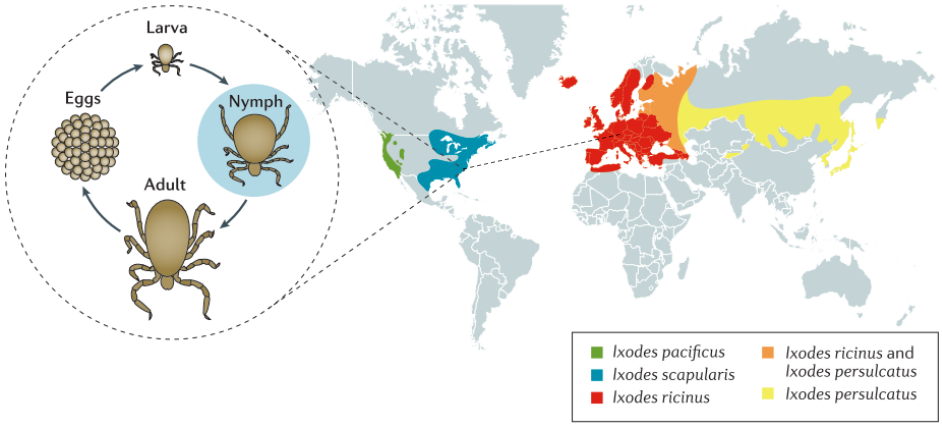

Figure 36. Distribution of *Ixodes* ticks that transmit Lyme disease causative agent to humans. In Europe, the three genospecies of *B. burgdorferi* s.l. are transmitted by *I. ricinus* (red). The principal tick vector in Asia is *I. persulcatus* (yellow), which transmits *B. afzelii* and *B. garinii*, but not *B. burgdorferi*. Both *I. ricinus* and *I. persulcatus* have been found in eastern Europe (orange). In North America, the main tick vectors that transmit *B. burgdorferi* are *Ixodes scapularis* in some areas of United States and Canada (blue) and *Ixodes pacificus* in the western United States (green). Regions with highest prevalence of *B. burgdorferi* transmission are northeastern United States and central Europe. The life cycle of ticks is illustrated inside the circle (left panel), where tick life stages are represented (eggs, larvae, nymph and adult). Nymphs (marked with a blue circle) are the main responsible for transmission of Lyme disease to humans, because they are less noticeable than adults, which are bigger in size (modified from Steere *et al.,* 2016).

Ixodes ticks can infect more than 300 animal species, ranging from small mammals, reptiles and birds to bigger hosts such as deer, sheep and wild boar, but they can only ingest blood from a single host during every life cycle stage (Gern, 2009; Stanek et al., 2012). Male ticks rarely feed, and thus, female ticks are the ones responsible for ingesting blood and infecting humans with bacteria, protozoa and viruses, such as *Anaplasma phagocytophilum*, *Babesia* spp, encephalitis virus and Powassan virus. In addition, ticks can carry more than one pathogen simultaneously (Samuels and Radolf, 2010; Eisen and Eisen, 2018). Recently, Greiman and collaborators showed that ticks can also be parasitic to other ticks (Durden et al., 2018). Transmission of the pathogens occurs during feeding through the injection into the host of tick saliva, which contains anticoagulants and local anesthetics (Halperin, 2019). The risk of transmission increases with the duration of larva (rarely) or nymph (usually) attachment to the host, which normally needs

more than 36 h-44 h of feeding (Kahl *et al.*, 1998; des Vignes, *et al*., 2001; Samuels and Radolf, 2010). Transmission to human usually occurs from late May to late September, coinciding with the activity of nymphs and with the increasing recreational use of tick habitats by the human (Stanek *et al*., 2012).

1.2. Clinical manifestations

Lyme disease often persists for long periods of time without being diagnosed because it shares common and similar manifestations with other diseases (e.g. nausea, vomiting, headache, fever, fatigue…). Therefore, it is also known as the "great imitator" (Steere *et al.,* 2016).

The early local reaction to the deposition of the bacteria in the skin is named erythema migrans (**Figure 37 A, B**), because of the expansion of the rash formed at the site of the tick bite (Azfelius *et al.,* 1910), which usually appears after 3-30 days incubation (Radolf *et al*., 2012).

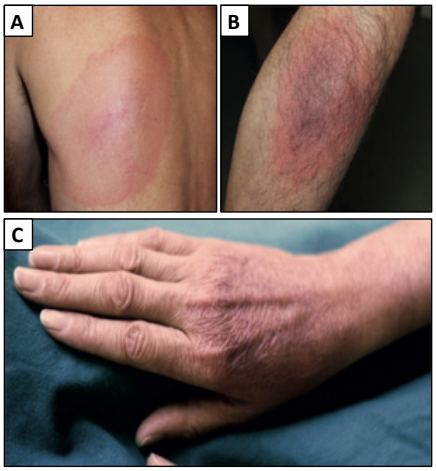

Figure 37. Dermatological manifestations of Lyme disease. A, B) Representative skin lesions known as erythema migrans, which occurs 3-30 days after a tick bite. The rash usually presents a brighter red outer border, partial central clearing and a bull's eye centre. **C)** Acrodermatitis chronica atrophicans is the most common late manifestation of Lyme borreliosis in Europe (modified from Steere *et al.,* 2016).

This skin lesion is due to host immune system activation. Dendritic cells, T cells, neutrophils, monocytes and macrophages have been observed in patient skin samples (Duray 1989; Xu *et al*., 2007; Jones *et al*., 2008; Sjöwall *et al*., 2011). It appears in 80 % of Lyme cases and is the most common and specific manifestation of Lyme disease (Steere *et al*., 2003). If the pathogen persist for long period in the human host, patient can suffer from acrodermatitis chronica atrophicans, the most common late skin manifestation of Lyme disease in Europe (**Figure 37 C**).

If not properly treated, the first contact of the pathogen with human dermis (known as the first stage of the disease) is followed by the dissemination of the spirochete via the lymphatic system or blood, which results in the colonization of different tissues and organs (known as acute Lyme disease). These include the heart, nervous system and other skin sites, causing more erythema migrans lesions, arthritis, carditis and nervous system manifestations (known as Lyme

neuroborreliosis), such as meningitis, peripheral facial palsy and encephalitis (Oschmann, 1998; Müllegger *et al*., 2000).

1.3. Diagnosis

The variability within *B. burgdorferi* genospecies and the ability of the causative agent to change surface lipoproteins leading to immune system suppression can cause false negatives, which makes the diagnosis of Lyme disease difficult. Serology is used to determine antibodies against the pathogen, including immunoglobulin M (IgM) and Immunoglobulin G (IgG), based on a two-tier system of enzyme-linked immunosorbent assay (ELISA) and confirmatory western blot. Antigens such as C6, a 26-amino-acid peptide of VlsE's (surface antigen presented in *B. burgdorferi* surface in mammal infections, explained below in "2. *Borrelia*" section) invariant region 6, are also used for rapid tests, which have been shown to be specific and highly sensitive. Difficulties in the analysis of laboratory tests make results to be interpreted in the context of patient's clinical condition and the course of the disease (Marques, 2015; Eldin *et al*., 2019).

1.4. Treatment

The wide range of symptoms of Lyme disease and the complexity of the causative agent make it difficult to find one effective treatment for all complications. However, a 14 day course of oral antibiotics (doxycycline, amoxicillin and cefuroxime) is usually enough to cure almost all of Lyme disease cases. If the pathogen is disseminated to different organs, 28 days of oral or parental antibiotic administration is normally sufficient to kill spirochetes (**Table 6**). However, 10-20 % of patients do not respond to antibiotic treatment and patients who recover from the disease are still vulnerable to reinfection (Nadelman *et al*., 2012). *B. burgdorferi* genospecies can also persist during months or years in infected niches and manifestations can return, which leads to difficulties in the treatment (Wormser *et al*., 2006; Sanchez *et al*., 2016; Schoen, 2020).

Lyme disease diagnosis and treatment costs are high. In the US, it is estimated that the medical costs per patient are about $464 for the early stages of the disease, which increases to $1380 for more acute Lyme disease manifestations. These costs are about $8200 if indirect costs (non-medical costs and productivity losses) are considered. Even without considering indirect costs, the total cost is about $700 million-$1 billion per year for the US health care system, per year in US (Zhang *et al*., 2006; Mac *et al*., 2019). Therefore, the development of an effective vaccine against *B. burgdorferi* s.l. is necessary (Barrett and Portsmouth, 2013).

Table 6. Treatment of Lyme disease. Different clinical manifestations are shown with their own specific treatments and duration (modied from Steere *et al*., 2016).

Manifestation	Antibiotic	Treatment duration (days)
Erythema migrans, borrelial lymphocytoma or acrodermatitis chronica atrophicans*	Doxycycline	10
	Amoxicillin	14
	Cefuroxime axetil	14
	Phenoxymethylpenicillin	14
	Azithromycin‡	5–10
Lyme meningitis, cranial neuropathy or radiculopathy	Doxycycline§	14
	Ceftriaxone‖	14
Lyme encephalomyelitis	Ceftriaxone	14–28
Cardiac Lyme disease	Doxycycline§	14–21
	Amoxicillin§	14–21
	Cefuroxime axetil§	14–21
	Ceftriaxone‖	14–21
Lyme arthritis	Doxycycline	28
	Amoxicillin	28
	Cefuroxime axetil	28
	Ceftriaxone¶	14–28

1.5. Prophylaxis

Nowadays, there is no human vaccine available for Lyme disease (Steere and Livey, 2012), although a vaccine named LYMErix [recombinant Outer surface protein A (OspA), which is a lipoprotein expressed in *B. burgdorferi* s.l. outer membrane when it is inside the tick environment, explained in next section] was marketed in the USA from 1998 to 2002 (Steere *et al*., 1998; Sigal *et al*., 1998; Plotkin, 2011). Although the vaccine protected 100 % of the patients in a first trial (Steere *et al*., 1998) and 98 % of patients in a second one (Sigal *et al*., 1998), and that the concerns regarding autoimmune arthritis produced by the vaccine were never confirmed, because of the vaccine poor market penetration, LYMErix was ultimately withdrawn from the market in 2002 because of poor market penetration (Steere and Livey, 2012).

Although several vaccines have been tested in animal studies for Lyme disease (Wressnigg *et al*., 2013; Comstedt *et al*., 2014), there is no commercially available human vaccine, yet. A vaccine called VLA15 has been tested since 2014, which has shown to be efficient against 3 *Borrelia* genospecies known to cause Lyme disease (Comstedt *et al*., 2017) and is now being studied for phase II clinical trial by Valneva biotech company (https://valneva.com/press-release/valneva-completes-recruitment-for-phase-2-studies-of-its-lyme-disease-vaccine-candidate-vla15/#_ftn3).

2. *Borrelia burgdorferi sensu lato*

The genus *Borrelia*, named after the French biologist Amédée Borrel, was first described in 1907 by Swellengrebel (Skerman *et al*., 1989) and is divided into 21 genospecies, sorted in two major branches: (1) *Borrelia burgdorferi* s.l., which refers to Lyme disease-associated group and (2) *Borrelia hermsii*, which represents the relapsing fever-associated branch (Margos *et al*., 2019). Members of *B. burgdorferi* s.l. are highly motile spirochetes that move due to a flagella located in the periplasmic space (between the peptidoglycan layer and the outer membrane) and attached to the cell poles (Steere *et al*., 2016) (**Figure 37 A, B**). *Borrelia* is about 300 nm wide and 5-30 µm long, with Gram negative-like structure, but without lipopolysaccharides in the outer membrane (Stübs *et al.*, 2009). The outer membrane is composed of phospholipids, glycolipids and lipoproteins, that as mentioned above, play a key role in host infectivity and survival (Fraser *et al*., 1997) (**Figure 37 C**). Lipoproteins can change depending on the environment. Previous works described not only variability in *B. burgdorferi* s.l., but also within the same species (Margos *et al*., 2011).

B. burgdorferi genome was the first analyzed from the *Borrelia* genospecies and the third microbial genome to be sequenced (Fraser *et al*., 1997). It encodes more than 1780 genes, located in a single chromosome and 21 plasmids, wherein 9 are circular and 12 linear (Casjens *et al*., 2000). The chromosome is about 1 Mb in length, and both linear and circular plasmids are in the 5-220 kbp size range (Samuel and Radolf, 2019). The chromosomes of the different genoespecies have a similar content of genes encoding metabolic enzymes, whereas plasmids carry genes encoding surface lipoproteins that are needed for host infectivity and survival (Gherardini *et al*., 2010).

Borrelia genospecies are auxotroph for all amino acids and, moreover these pathogens lack the enzymes involved in biosynthetic pathways, which makes the pathogen dependent on host nutrients (Barbour, 1984; Preac-Mursic *et al.*, 1986; Gherardini *et al*., 2010; Stanek *et al*., 2012).

2.1. Invasion, dissemination and immune evasion of *Borrelia burgdorferi*

B. burgdorferi transmission to mammalian hosts starts with the tick bite which anchors to the skin of its host by the hypostome protuberance (**Figure 35 B)**, promoting changes in the environment of the pathogen. The availability of nutrients, increase in temperature and decrease in pH, among others, stimulate changes in the gene expression of the spriochetes and promote their colonization of the tick saliva from tick midgut, where they are usually found

attached to epithelial cells, with their lipoprotein OspA bound to the tick receptor for OspA (TROSPA) (Pal *et al*., 2004), to finally invade the new host.

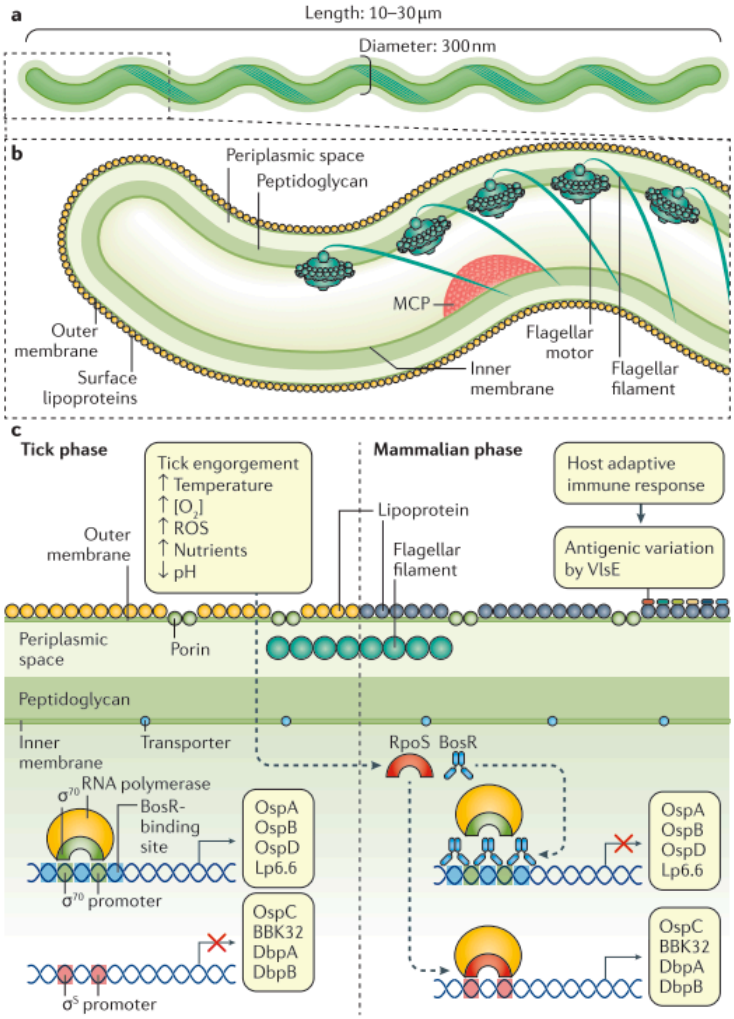

Figure 37. ***Borrelia burgdorferi* s.l. morphology. a)** *B. burgdoreferi* size is 10-30 µm in length and about 300 nm in diameter. **b)** B. burgdorferi structure, where outer membrane, surface lipoproteins, inner membrane, peptidoglycan, periplasmic space, flagellar filaments and flagellar motor are represented. **c)** Representation of the outer membrane representation, which is a lipid bilayer with several lipoproteins on the surface. These lipoproteins are modified depending on the environment. Here it is described as the tick phase and mammalian phase. These changes in lipoproteins expression are regulated by a complex regulatory network, which involves the *Borrelia* oxidative stress regulator (BosR) and the RNA polymerase alternative σ-factor RpoS are involved (modified from Steere *et al*., 2016).

In this first step of tick colonization, which is required for human invasion, the expression of the RNA polymerase alternative σ-factor RpoS and Borrelia oxidative stress regulator (BosR) play a key role (Hübner *et al*., 2001; Wang *et al*., 2013) by targeting genes that encodes surface lipoproteins (**Figure 37 C**), such as OspA, which is replaced by Outer surface protein C (OspC) (Grimm *et al*., 2004). OspC recruits SALP15, a tick immunosuppressive protein, which enables *B.*

burgdorferi delivery into the host by inhibiting T cell activation (Anguita *et al*., 2002). Moreover, tick salivary protein sialostatin L blocks neutrophil chemotaxis (Kotsyfakis *et al*., 2006).

After bacteria deposition in the skin, *B. burgdorferi* multiplies before spreading to other tissues. New surface lipoproteins interact with mammalian host molecules, such as, plasminogen for proteolysis of host tissues, extracellular matrix components [fibronectin (Seshu *et al*., 2006), integrin (Behera *et al*., 2008), collagen (Zambrano *et al*., 2004; Zhi *et al*., 2015), laminin (Brissette *et al*., 2009; Verma *et al*., 2009) and glycosaminoglycans (Guo *et al*., 1995)] for cell host adhesion and complement regulatory proteins for immune evasion, which are essential steps for colonization of host tissues. *B. burgdorferi* evades the host innate immune system by the binding of its complement regulator acquiring surface proteins (CRASPs) to host factor H, which inactivates the complement serum proteins, C3b and C4b, preventing killing of the bacteria (de Taeye *et al*., 2013). Furthermore, *B. burgdorferi* can also evade the adaptive immune system by replacing OspC with VIsE, which undergoes several antigenic variations, leading the bacteria to spread through the bloodstream and invading different tissue and organs (Zhang *et al*., 1997). Fibronectin and glycosaminoglycans-binding protein BBK32 enable the bacteria to attach to the vascular surfaces allowing transmigration across the endothelium, hence dissemination into the host (Moriarty *et al*., 2012).

B. burgdorferi can evade the immune system and persist for months and years in some patients, even though it can be recognized initially by the induction of a local inflammatory response in the host, which manifests as the Erythema migrans as explained above. The initial recognition of the bacteria is mediated by phatogen-associated molecular patterns (PAMPs) that are detected by pattern recognition receptors, such as, cytosolic nucleotide-binding oligomerization domain containing protein-like receptors and Toll-like receptors (TLRs) (Shin *et al*., 2008; Petzke *et al*., 2009; Cervantes *et al*., 2011), although the innate immune system is not enough to kill all spirochetes and inhibit dissemination and colonization.

3. Lyme neuroborreliosis and Peripheral nervous system involvement

B. burgdorferi s.l. can cross the blood brain and blood nerves barrier leading to central nervous system (CNS) and peripheral nervous system (PNS) infection, which is referred to as Lyme neuroborreliosis. PNS involvement occurs in 5 % up to 15 % of patients with Lyme disease (Halperin, 2017). Overall, Lyme neuroborreliosis is more frequent in Europe (Eldin *et al*., 2019) and it develops within 2-18 weeks following pathogen infection (early Lyme neuroborreliosis), although 2 % of the patients present neurological manifestations after months or years after *B. burgdorferi* infection, which is known as late Lyme neuroborreliosis. These differences in the

stages of the disease are also related with different clinical manifestations. In Europe, the most common manifestation of early Lyme neuroborreliosis is painful lymphocytic meningoradiculitis. In addition, about 50 % and one-third of the patients present facial palsy and radiculoneuritis (neuropathic pain in the site of one or more dermatomes, which associate with muscle weakness and atrophy), respectively (Garin and Bujadoux, 1922; Babbwarth, 1941; Halperin, 2016). The most common manifestation of late Lyme neuroborreliosis is polyneurophaty, which has been reported in 40-60 % of patients, who also present acrodermatitis chronica atrophicans (ACA, late dermatological manifestation) (**Figure 37 C**). Few polyneurophaty cases have been reported not being related with ACA. ACA-related polyneurophaty is primarily caused by axonal degeneration (Kristoferitsch et al., 1988; Halperin, 2016), which can lead to long-term motor deficits without complete recovery (Kalish *et al*., 2001).

B. burgdorferi infection in the PNS is complicated to diagnose, whereas CNS infection is often studied by cerebrospinal fluid (CSF) analysis of *B. burgdorferi* antibodies, lymphocytic or monocytic pleocytosis (Ogrinc *et al*., 2016) and CXCL13 chemokine expression (Rupprecht, 2018). Several animal models are used to study the different stages of Lyme disease, such as mice, rabbits and dogs, but only rhesus monkeys present nervous system manifestations, in addition to all the other symptoms (Roberts *et al.*, 1998). The absence of accessible laboratory animal models makes the study of the mechanisms involved in nervous system damage by *B. burgdorferi* difficult. In fact, to date, the molecular mechanisms leading to a persistent demyelination of PNS in Lyme neuroborreliosis are still not elucidated.

Aims of the study

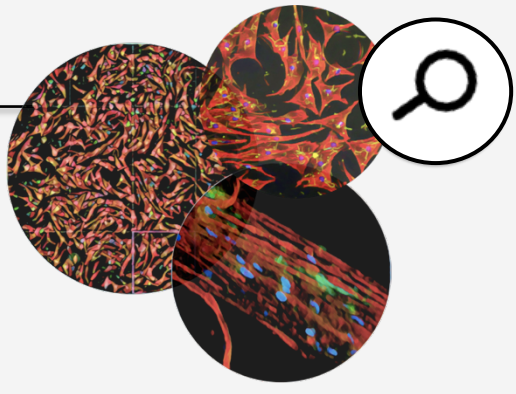

Aims of the study

The increase of Lyme disease cases (Jones *et al.*, 2018), misdiagnosis and the absence of an effective vaccine (Steere and Livey, 2012) that could prevent or halt the most common tick-borne disease, makes this infectious disease a public health concern. The nervous system involvement in Lyme disease (Lyme neuroborreliosis) remains one of the least understood of all clinical manifestations and to date, the mechanisms implicated in neural dysfunction induced by *Borrelia burgdorferi* are still unclear.

Thus, in this project, we sought to examine the direct effects of *Borrelia burgdorferi* in driving pathology in the peripheral nervous system (PNS) to fill this gap in knowledge we presently have. A particular focus of this work is on the effects of the spirochete on Schwann cells. These glial cells, as mentioned above, are highly plastic cells that can undergo a switch in their phenotypic identify in response to a range of insults, e.g. nerve injury. For example, we recently showed that Schwann cells are able to activate an adaptive response to clear their myelin debris after nerve injury, and convert themselves to repair Schwann cells that support axonal regeneration (Gomez-Sanchez *et al*., 2015). Similarly, Schwann cells can respond adaptively to various microbes, including viruses (Levine *et al*., 2003; Dhiman *et al*., 2019) and bacteria (Rambukkana *et al*., 2014; Delbaz *et al*., 2020). One of the best characterized examples is *Mycobacterium leprae* (Palmer *et al*., 1965; Serrano-Coll *et al*., 2018; Casalenovo *et al*., 2019), whose direct targets are Schwann cells and the infection with *M. leprae* can lead to demyelination in PNS.

We **hypothesize** that similar to *M. leprae*, *B. burgdorferi* could also play a direct effect on Schwann cells, inducing demyelination as it has been reported by nerve conduction studies in patients (Sterman *et al*., 1982; Tyagi *et al*., 2015) and histological examinations from the macaque model (Roberts *et al*., 1998; Ramesh *et al*., 2015a).

Therefore, the main **objectives** of this project are highlighted below:

Aim 1. To examine whether *Borrelia burgdorferi* induces demyelination directly in peripheral nerves.

Aim 2. To study whether *Borrelia* burgdorferi-induced demyelination is due to a direct effect on Schwann cells.

Aim 3. To identify the mechanisms implicated in *Borrelia burgdorferi*-induced demyelination in Schwann cells:

- **3.1.** Examine whether myelin breakdown is via contact-mediated interaction between pathogen and Schwann cells.

3.2. Characterize the molecular mechanisms involved in demyelination mediated by *B. burgdorferi*.

Overall, these objectives could improve our understanding of the effects of *Borrelia burgdorferi* on the PNS, particularly on myelination, and could generate valuable insights on potential therapeutical strategies for Lyme neuroborreliosis.

Material and methods

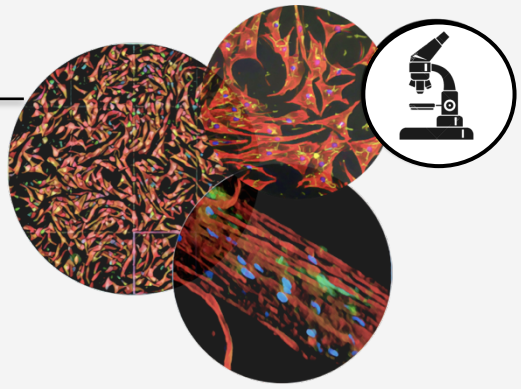

Material and Methods

1. Animals

All experiments were performed in accordance with Spanish Guide for the Care and use of Laboratory animals, and by the International Animal Care and Use Committee Standards. All procedures were performed following the ethical guidelines established by the Biosafety and Welfare Committee at CIC bioGUNE, which is an AAALAC-accredited facility (Assessment and Accreditation of Laboratory Animal Care).

Wistar rats and C57 BL6/J mice were used and were handled under conventional housing conditions (22 ± 2 °C, 55 ± 10 % humidity, 12-hour day/night cycle) and fed with a standard diet (Harlan Teklad) with *ad libitum* access to food and water. All possible efforts were made to minimize animal suffering and the number of animals used.

2. Bacteria

2.1. *Borrelia burgdorferi*

Borrelia burgdorferi 297 strain, isolated from a cerebrospinal fluid (CSF) (Steere *et al*., 1983; Hughes *et al*., 1992), B31 clone 5A15, isolated from *Ixodes dammini* tick (Burgdorfer *et al*., 1982; Barbour *et al*., 1983), and *Borrelia burgdorferi* 914, a clone derived from strain 297 that contains a constitutively expressed Green Fluorescent Protein (GFP) reporter stably inserted into cp26 (Dunham-Ems *et al*., 2009), were used for cell and tissue infection (Dunham-Ems SM, *et al.* 2009). Bacteria were grown in 15 ml tubes at 34 °C in Barbour-Stonner-Kelly (BSK-H) medium (Sigma-Aldrich) for 3 days (Veinović *et al.*, 2016). All infections were performed with multiplicity of infection (MOI) of 50 for a period of 24 h and/or 48 h, unless otherwise stated.

2.2. *Lactobacillus*

Lactobacillus plantarum strain WCFS1, *L. plantarum* WCFS1 pNZ8048-cherry and *L. plantarum* strain WCFS1 pNZ8048-GFP (isolated from human saliva), *L. casei* strain RM23 (isolated from wine), and *L. rhamnosus* strain K3 (isolated from human breastmilk) were grown statically in De Man-Rogosa-Sharpe (MRS) medium at 37 °C, 200 rpm. The estimation of bacteria numbers in culture was performed with a correlation equation, calculated specifically for all strains, by measuring the correlation between culture optical density and bacterial numbers determined by dilution plating. All infections were performed with multiplicity of infection (MOI) of 50 for a period of 48 h.

2.3. *Mycobacterium tuberculosis*

Mycobacterium tuberculosis $mc^2$6230 strain were obtained from the American Type Culture Collection (ATCC) and grown in Middlebrook 7H9 medium (M7H9) supplemented with 10 % OADC enrichment (Becton Dickinson Microbiology Systems), 0.5 % glycerol (Amresco) and with Tyloxapol 0.05 % (Sigma-Aldrich) prior to inoculation in a minimal medium (KH_2PO_4 1g/l, Na_2HPO_4 2.5 g/l, asparagine 0.5 g/l, ferric ammonium citrate 50 mg/l, $MgSO_4 \times 7\ H_2O$ 0.5 g/l, $CaCl_2$ 0.5 mg/l and $ZnSO_4$ 0.1 mg/l). The bacteria were grown for up to 14 days at 37 °C. The estimation of bacteria numbers in culture was performed with a correlation equation, calculated specifically for all strains, and measuring the correlation between culture optical density and bacterial numbers determined by dilution plating. All infections were performed with multiplicity of infection (MOI) of 50 for a period of 48 h.

3. Cell culture

3.1. Substrate coating of cell culture dishes

Autoclaved 12 mm coverslips were coated with 1 mg/ml Poly-D-lysine (PDL, Sigma-Aldrich) in double distilled water (ddH_2O) at room temperature (RT) for 4 hours. Coverslips were then washed in ddH_2O 3 times at RT on a shaker before air drying in a flow cabinet, and were then stored desiccated. Tissue culture dishes (6-well plates, 60 mm and 100 mm dishes) were coated with PDL (1 mg/ml) for 2 hours at RT. The solution was then removed and the dishes were air dried in a flow cabinet without washing. A 50 µl laminin drop (20 µg/ml in DMEM/F12; Sigma-Aldrich) was added onto PDL-coated coverslips and left for at least 1 h before removal prior to plating the cells. Alternatively, laminin was added to dishes (10 µg/ml in DMEM/F12), left for at least 1 h and removed just before plating the cells.

3.2. Dorsal Root Ganglia (DRG)

DRG culture system is the best model used to mimic Schwann cells myelination *in vitro*, whereby Schwann cells associate with neuronal axons and form myelin segments around them. DRGs were plucked off from the spinal cord of embryonic day 15 (E15) rat embryos (**Figure 38**). 1 up to 3 DRGs were deposited onto the center of each PDL-treated coverslip after 1 h of laminin treatment. Cells were cultured at 37 °C with 5 % CO_2 overnight in 200 µl C media [MEM (Gibco), containing, 10 % fetal bovine serum (FBS, Gibco), 0.4 % D–glucose, 2 mM L-glutamine (Gibco), and 50 ng/ml of 2.5S nerve growth factor (NGF; Gibco)]. Fresh medium was added once more before replacing with NB medium [Neurobasal medium (Gibco) containing 10 % FBS, 0,4 % D-

glucose, 2 mM L-glutamine, 1X B-27 (Gibco) and 50 ng/ml 2.5S NGF],which was replaced 2 days later with fresh NB media. At this stage, neurites grow and occupy 2/3 of the area of the coverslip and Schwann cells are typically seen elongated along axons.

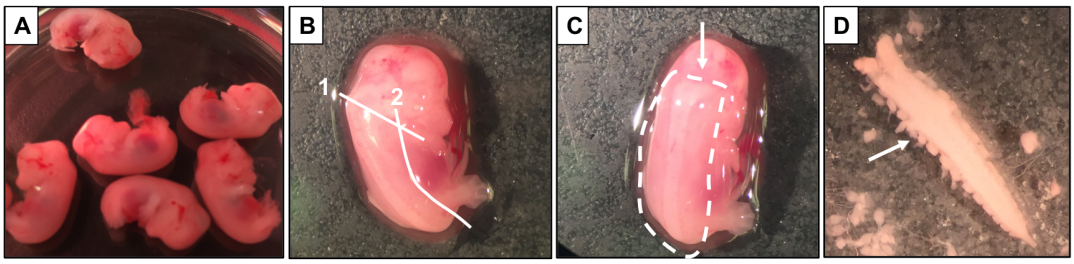

Figure 38. Representative steps of DRGs dissection. A) E16 rat embryos recently isolated. **B)** Lateral part of an embryo is shown, in which lines 1 and 2 represent cuts that are to be made for spinal cord removal. **C**) The dorsal part of the embryo. Spinal cord is pointed with the arrow. **D)** An isolated spinal cord with DRGs (arrow).

In Schwann cell cultures myelination is triggered by switching to C medium (200-300 µl C media per coverslip) supplemented with 50 µg/ml ascorbic acid. Ascorbic acid triggers the formation of a basal lamina around the Schwann cells and subsequent myelination. C medium containing freshly prepared ascorbic acid was added every 2 days for up to 7-21 days (Taveggia and Bolino, 2018). Myelin basic protein (MBP) antibody was used to label myelin segments by immunocytochemistry (ICC) to monitor myelination. 3 independent experiments were carried out, each with 4 coverslips per condition.

3.3. OX-7 hybridoma

The OX-7 hybridoma produces a mouse IgG1 antibody that reacts with rat CD90 (Thy-1) and mouse CD90.1 (Thy-1.1). OX-7 cells were defrosted at 37 °C and centrifuged at 200 *g* for 5 min. The pellet was resuspended in 7 ml hybridoma medium [RPMI medium (Gibco) supplemented with 10 % FBS, 1 % antibiotic and antimycotic (A/A; Gibco), 2 mM L-glutamine (Gibco), 1 mM sodium pyruvate (Hyclone), and 50 µM β-mercaptoethanol (Bio-Rad)] and plated onto 100 mm tissue culture dishes. When the plate was about 70-80 % confluent (after about 3-4 days), the medium was replaced with 5 ml of fresh hybridoma medium. Supernatant was collected 2 days later, filtered with 0.02 µm filters and sodium azide was added to a final concentration of 0.01% (1:1000 dilution of 10 % stock solution, Sigma-Aldrich) before storage at 4 °C. The supernatant was used for immunopanning of Schwann cell cultures (see below, section 3.4.1.).

3.4. Primary rat Schwann cells culture

3.4.1. Schwann cells isolation and purification by immunopanning

Schwann cells were isolated from Wistar rat sciatic nerves and brachial plexus at postnatal day 3-5 (P3-5) (**Figure 39**). The sciatic nerves were dissected, placed in ice cold Leibovitz's L15 medium (Gibco) complemented with A/A.

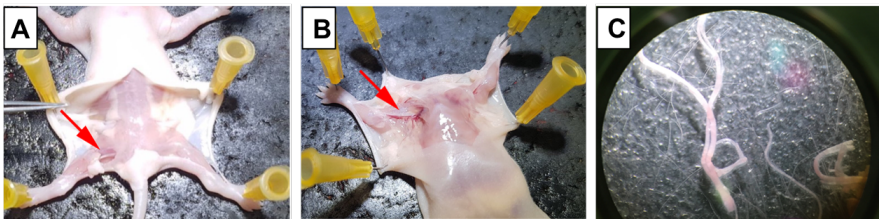

Figure 39. Dissection of sciatic nerves and brachial plexus. A) Sciatic nerves removal. Rat P5 pup body pinned with the dorsal face up and skin removed from lower part of the body. A small cut in the muscle reveals the underlying sciatic nerve (red arrow). **B**) Brachial plexus removal. Rat P5 pup body pinned with the ventral face up and skin removed from upper part of the body. Arrow shows the brachial plexus underneath the muscle layer. **C)** Sciatic nerves isolated after dissection

The epineural sheath was removed and the nerves were dissociated by digestion in an enzymatic mix consisting of 100 µl of 0.25 % trypsin and 100 µl of 0.4 % collagenase mix per rat at 37 °C, 5 % CO_2 and 95 % humidity for 35 minutes with trituration at the end to further break up the tissue structure. An equal volume of DMEM with 10 % FBS was added to the cell suspension and this was centrifuged for 10 minutes at 1,000 rpm and 4 °C. The cell pellet was resuspended in DMEM with 10 % FBS supplemented with 10^{-3} M AraC and cultured onto PDL- and laminin-coated 35 mm tissue culture dishes for 3 days. The serum in the medium promotes the proliferation of the fibroblasts present in the cultures, which are then subsequently killed by the anti-mitotic compound AraC, leaving relatively pure Schwann cell cultures.

Reverse immunopanning, which is a further purification step, is then carried out to remove the few remaining contaminating fibroblasts. In brief, petri dishes are coated with Thy1.1 antibodies (OX-7 supernatant above), and Schwann cells are added to them. The fibroblasts attach to the antibodies found on the surface of the dish, whereas the Schwann cells remain floating in the culture medium, and are then recovered for further expansion. For the antibody coating, first the 90 mm Petri dish (Falcon) is coated with rabbit anti-mouse IgG (Dako) (7ml 50 mM Tris pH 9.5 and 50 µl IgG per dish) and then with Thy 1.1 antibody (4 ml OX-7 supernatant, 2 ml L15 medium and 400 µl 35 % BSA per dish). Schwann cells, after 3 days of treatment with AraC (see above) were detached from the dishes by treatment with 0.25 % trypsin-EDTA (2,2',2'',2'''-Ethane-1,2-diyldinitrilo-tetraacetic acid; Gibco), centrifuged and resuspended in 10 ml DMEM containing 10% FBS. The cell suspension was then added to the Thy1.1-coated dishes and

cultured at 37 °C, 5% CO_2 and 95 % humidity for 20 min, with a gentle shaking of the dish midway through. The fibroblasts remain attached to the dishes, and the cell suspension containing Schwann cells was then recovered, pelleted by centrifugation and resuspended in expansion medium (see below*) and cultured onto PDL- and laminin-coated dishes (**Figure 40**). The medium was replaced every 3 days until the cells were confluent.

*Schwann cells expansion medium:

1. Defined medium: DMEM/F12 (Gibco) supplemented with SATO [(100 µg/ml bovine serum albumin (BSA; Sigma-Aldrich), 100 µg/ml transferrin powder (Sigma-Aldrich), 16 µg/ml Putrescine; 60 ng/ml progesterone (Sigma-Aldrich) and 40 ng/ml sodium selenite (Sigma-Aldrich) in Neurobasal medium (Gibco)], 1X B27 supplement; 0.101 mg/ml of 3,3',5-Triiodo-L-thyronine sodium salt (T3, Sigma-Aldrich), 10 mM Insulin, 1 % L-glutamine and 1 % A/A.

2. Expansion medium: Defined medium complemented with 0,5 % FBS, 10 ng/ml neuregulin (NRG1, R&D Systems) and 2 µM forskolin (Calbiochem).

3.4.2. *In vitro* Schwann cells myelination assay by db cAMP treatment

Elevation of intracellular cAMP has been shown to induce myelin-associated gene expression, such as *P0*, *Krox20* and *Galc* in rat and human Schwann cell cultures and decreases expression of proteins expressed in immature or Remak Schwann cells, including $p75^{NTR}$, GFAP, growth associated protein 43 (Gap43) and c-Jun (Schmid *et al.,* 2014). Upon ligand binding, the G protein coupled receptor activates adenylyl cyclase, converting ATP into the second messenger cAMP. cAMP activates the protein kinase A (PKA), which in turn stimulates the cAMP response element (CREB) signal transduction pathway. The G protein-coupled receptor 126 (Gpr126) is the only receptor identified to drive Schwann cell differentiation by elevating cAMP levels (Monk *et al.,* 2009).

Purified and expanded Schwann cells (see section 3.4.1) were counted to seed for the correspondent experiments and cultured overnight in starvation medium [defined medium (see section 3.4.1*) supplemented with 0.5 % FBS] following treatment with 4 mM N^6,2'-O-Dibutyryladenosine 3',5'-cyclic monophosphate sodium salt (db cAMP), a cell-permeable and non-hydrolysable cAMP analogue, for 48 h to induce upregulation of myelin differentiation markers.

Myelin was monitored by immunocytochemistry (ICC) in DRG cultures and *in vitro* myelinated Schwann cells were used for all the assays described in this section. A schematic diagram of myelination assay timeline is shown below (**Figure 40**).

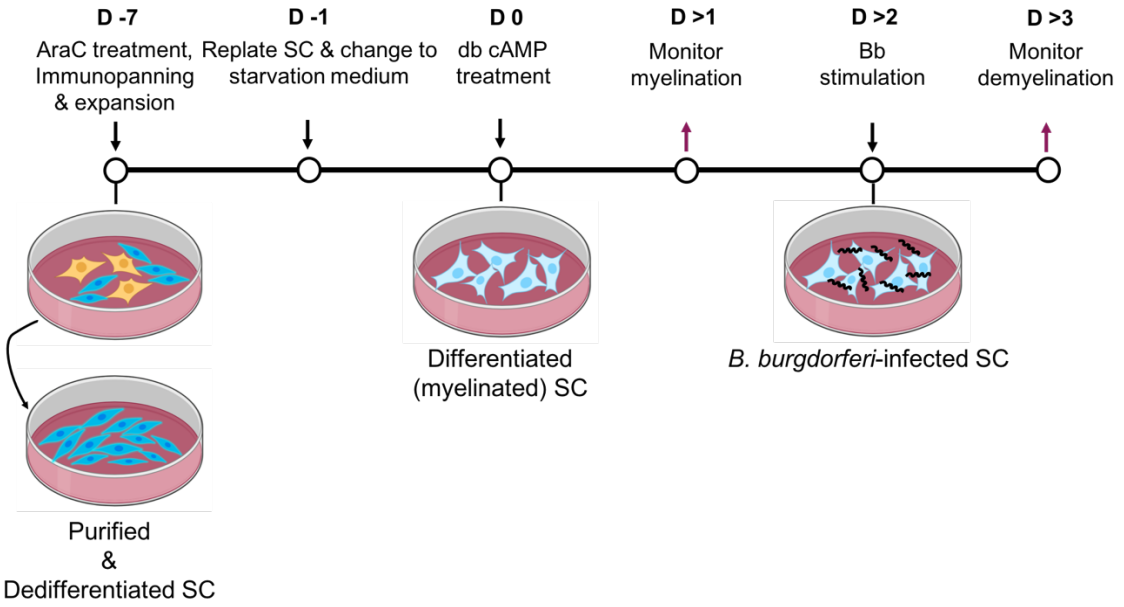

Figure 40. Timeline of Schwann cells *in vitro* myelination assay. After killing fibroblasts (here in yellow) Schwann cells (here in blue) are immunopanned and expanded in expansion medium for several days, after which the cells are replated at an appropriate density and cultured overnight in starvation medium. The next day, cells are treated with db cAMP, and myelination monitored afterwards. *B. burgdorferi* infection is done after 2 days of db cAMP treatment and demyelination is observed afterwards by different techniques.

3.5. RAW 264.7 cell line

RAW 264.7 macrophage cell line was used as positive control of *B. burgdorferi* binding assays, as analyzed by flow cytometry and ICC. Cells were maintained in DMEM supplemented with 10 % FBS and 1 % A/A and plated onto 6-well plates (for flow cytometry) and 12 mm coverslips (for ICC) the day before the experiment.

3.6. HEK293FT cell line

HEK293FT cells were maintained in complete growth medium [DMEM, 10 % FBS, 0.1 mM non-essential amino acids (Gibco), 1 mM sodium pyruvate (Gibco), 2 mM L-glutamine (Gibco) and 1% A/A] under standard culture conditions at 37 °C and 5 % CO_2.

4. *In vitro* experimental procedures

4.1. *B. burgdorferi* infection

4.1.1. *B. burgdorferi* binding assay

4.1.1.1. Immunocytochemistry

Schwann cells, seeded at a density of 5,000 cells per PDL- and laminin-coated 12 mm coverslips in medium without antibiotics, were used for *B. burgdorferi* binding assay. Thus, spirochetes

were counted using phase contrast microscope and the required number of bacteria was calculated to give an MOI of 50, unless otherwise is specified. The correspondent volume of bacteria was centrifuged at 10,000 rpm for 10 min and pellet was resuspend in Schwann cells medium. GFP expressing *B. burgdorferi* was then added to the cells for 3 h, 6 h, 24 h and 48 h. Cells were then washed with 1X PBS to eliminate excess bacteria and analyzed by ICC. In brief, cells were fixed in 4 % paraformaldehyde for 10 minutes. Schwann cells were permeabilized with 1X PBS containing 0.3 % Triton X-100 and stained with rhodamine phalloidin (1:300 dilution, Thermo Fisher Scientific) and 50 ng/ml DAPI for 30 min at RT. Samples were washed in 1X PBS and coverslips were mounted in Dako fluorescence mounting medium and analyzed using AxioImager.D1 fluorescent microscope or Zeiss LSM 880 Confocal System.

Heat inactivation of *B. burgdorferi* was done after culturing the corresponding amount of spirochetes at 56 °C for 30 min and washing them with 1X PBS. Sonication of the pathogen by ultrasonic disintegration was done in Soniprep 150 sonicator (MSE) with 2 pulses of 10 microns amplitude for 1 min.

Number of infected cells and the average of bacteria per cell were calculated using a CellInsight CX7 LZR High-Content Screening (HCS) Platform (Thermo Fisher Scientific). RAW 264.7 cells were used as binding positive control, as explained above. At 4 h before *B. burgdorferi* stimulation, RAW 264.7 cells were plated at a 1 x 10^5 density per coverslip or 7 x 10^5 in 6-well plates with medium without A/A.

DRGs were infected with 3 × 10^7 *B. burgdorferi* for 6 days. Cells were then washed with 1X PBS to eliminate excess bacteria and cold methanol (-20 °C) was added to samples for 10 minutes and blocked in antibody diluent solution (ADS; PBS containing 5 % goat serum and 1 % BSA) with 0.3 % Triton X-100 (Sigma-Aldrich) followed by MBP antibody incubation (1:100 dilution in ADS; Abcam) overnight at 4 °C. Next day, cells were incubated with anti-mouse Cy3 secondary antibody (1:100 dilution; Jackson ImmunoResearch Laboratories) and nuclear stained with 50 ng/ml DAPI (Merck) for 30 minutes at RT, covered from the light. Samples were mounted in Dako fluorescence mounting medium (Dako) and analyzed using an AxioImager.D1 fluorescent microscope.

4.1.1.2. Flow cytometry

Schwann cells were seeded at a density of 2 × 10^5 cells per 1.5 ml in 6-well culture dishes for *B. burgdorferi* binding assay. MOI of 50 were used for infection of myelinated Schwann cells with GFP expressing *B. burgdorferi*. After 48 h of bacteria infection, cells were washed with 1X PBS to

eliminate excess bacteria and samples then were fixed in 4 % paraformaldehyde for 10 minutes for further analysis in FACS CANTO flow cytometer.

4.1.1.3. Scanning electron microscopy

Schwann cells plated onto 12 mm coverslips were fixed in 2 % glutaraldehyde solution [25 % stock solution (TAAB Laboratories) diluted in 0.1 M phosphate (from 0.24 M phosphate buffer stock solution: 900 ml 0.34 % $NaHPO_4$ in H_2O and add 0.288 % NaH_2PO_4 in H_2O until reaching pH 7.4) and 0.4 % H_2O] for 2 h. The samples were washed in 0.1 M phosphate buffer, followed by osmication in 1 % osmium tetroxide (Electron Microscopy Sciences) for 1 h at 4 °C in the dark. The samples were dehydrated in a graded ethanol series of 30 % ethanol, 50 %, 70 %, 90% and 96 % ethanol for 10 min each time, and 100 % ethanol addition twice for 10 min each. The samples were then chemically dried with hexamethyldisilazane twice for 10 min each time and allowed to air dry. The next steps were then processed at the Analytical and High-resolution Microscopy department of the UPV/EHU. In brief, dried samples were mounted in an argon atmosphere, coated with gold (**Figure 41**) in an Emitech K550X metalizer and visualized in Hitachi S4800 Scanning Electron Microscopy (SEM). A minimum of 5 photos per coverslip were taken at different magnifications.

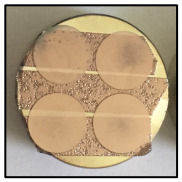

Figure 41. Gold-coated covers for scanning electron microscopy (SEM). 4 gold-coated 12 mm coverslips with Schwann cells are shown, ready to be visualized by SEM.

4.1.2. Immunohistochemistry

Peripheral nerves (sciatic nerves, brachial plexus or, its corresponding 5 mm segments for western blots) from rat and mice of 1-7 months of age were infected with 1 x 10^6 and 30 × 10^6 *B. burgdorferi* for 7-14 days. Nerves were then washed with 1X PBS to eliminate excess bacteria and analyzed by immunohistochemistry (IHC). In brief, nerves were added onto microscope slides, stretched out and fixed in 2 % paraformaldehyde for 10 minutes. Then, cold methanol (-20 °C) was added to samples for 10 minutes and blocked in antibody diluent solution (ADS; PBS containing 5 % goat serum and 1 % BSA) with 0.3 % Triton X-100 (Sigma-Aldrich) followed by MBP antibody incubation (1:100 dilution in ADS; Abcam) overnight at 4 °C. Next day, samples were incubated with anti-mouse Cy3 secondary antibody (1:100 dilution; Jackson ImmunoResearch Laboratories) and nuclear stained with 50 ng/ml DAPI (Merck) for 30 minutes at RT, covered from the light. Samples were mounted in Dako fluorescence mounting medium (Dako) and analyzed using an AxioImager.D1 fluorescent microscope.

4.2. *Lactobacillus* binding assay by flow cytometry

Schwann cells were seeded at a density of 2×10^5 cells per 1.5 ml, in 6-well culture dishes for binding assays of different *Lactobacillus*. MOI of 50 was used for infection of myelinated Schwann cells with Cherry-expressing *L. plantarum* (*L. plantarum*-cherry) and GFP-expressing *L. plantarum* (*L. plantarum*-GFP). After 48 h of bacteria infection, cells were washed with 1X PBS to eliminate excess bacteria and samples then were fixed in 4 % paraformaldehyde for 10 minutes for further analysis in FACS CANTO flow cytometer.

4.3. Genes overexpression by lentivirus

4.3.1. Production and concentration of lentivirus in HEK293FT cells

HEK 293FT cells were plated in their complete growth medium [DMEM, 10 % FBS, 0.1 mM non-essential amino acids (Gibco), 1 mM sodium pyruvate, 2 mM L-glutamine and 1% A/A] three days before transfections.

For each transfection, DNA-Lipofectamine 2000 (Invitrogen) complexes were prepared as follows: 36 µl of Lipofectamine 2000 were diluted in 1.5 ml Opti-MEM (Gibco) in a sterile 5 ml tube and incubated for 5 minutes at room temperature (RT). During those 5 minutes, packaging mix (PSPAX2 and VSVG) with β-*Catenin* 4A (pcw107.puroBETA-CATENIN, which harbours alanine substitutions in S33, S37, T41 and S45; Addgene) or β-*Catenin* S33Y (pcw107.puroBETA-CATENIN, which harbours a thyrosine substitution in S33; Addgene) and their respective control, the empty vector (pcw107.puro.empty; Addgene) plasmid DNA were diluted in 1.5 ml of Opti-MEM in a separate sterile 5 ml tube. After the 5 minutes of incubation, diluted DNA was combined with the diluted Lipofectamine 2000 and incubated for about 20-30 minutes at RT to allow the DNA-Lipofectamine complexes to form. After the incubation, suspension mix was added to a 100 mm culture dish containing 5 ml Opti-MEM with 10 % FBS. 6 x 10^6 HEK293FT cells were used for each Lentivirus. Cells were incubated overnight in normal cell culture conditions (95 % humidity, 5 % CO_2 and 37 °C). Next day, transfection mix was replaced with 10 ml complete growth medium, without antibiotics and cells were incubated overnight in same culture conditions. Virus-containing supernatants were harvested 72 h post-transfection by removing medium into a 15 ml sterile tube. Supernatants were centrifuged and filtered through a Millex-HV 0.45 µm PVDF filter (Millipore). Three volumes of centrifuged supernatants were combined with 1 volume of Lenti-X concentrator (Millipore) and the mixture was incubated overnight at 4 °C in a rotator. Next day, samples were centrifuged, supernatants discarded and pellet containing the viral particles resuspended in 1 ml PBS. Viruses were kept in 250 µl aliquots into single-use microtubes and stored at -80 °C.

4.3.2 Infection of Schwann cells with lentiviral particles

For lentiviral infections, Schwann cells were treated with lentiviral particles against β-*Catenin* or its respective control (empty vector) in the presence of hexadimethrine bromide (8 µg/ml, commercial name Polybrene; Merck) for enhancing infection efficiency. After 48 h of transduction, medium was replaced with fresh expansion medium and the cells infected with lentiviral particles harboring puromycin resistance were selected using 0,25 µg/ml puromycin. Puromycin-resistant cells were grown for the experiments or frozen for future use.

4.4. Ribonucleic acid (RNA) extraction and processing

4.4.1. RNA isolation

Total RNA from tissue (sciatic nerves and brachial plexus) and cells (600,000 Schwann cells/ 60 mm culture dish) was isolated using QIAshredder homogenizer (Qiagen) and AllPrep DNA/RNA Mini Kit (Qiagen) according to the manufacturer's instructions. RNA concentration was determined using RNA BR Qubit® assay kit (Life Technologies) in a Qubit® 2.0 Fluorometer (Life Technologies) according to the manufacturer´s instructions. RNA integrity was assessed by electrophoresis in an 1 % agarose gel.

4.4.2. Retrotranscription and Real Time-Polymerase Chain Reaction (RT-PCR)

Total RNA was reversed transcribed in a 20 µl reaction containing dNTPs (Invitrogen), random primers (Invitrogen), 0.1 M DTT (Invitrogen), RNAseOUT (Invitrogen), 5X Buffer (Invitrogen) and Superscript II retrotranscriptase (Invitrogen) according to the manufacturer's instructions. Reactions were carried out in a Thermocycler (Biometra). Resulting cDNA was diluted in RNAse-free H_2O (Sigma-Aldrich). RT-PCR was performed in a 20 µl reaction containing 10 µl SYBR Green Super Mix (Bio Rad), 6 µl RNase free H_2O, 2 µl properly diluted primers (10 µM) and 2 µl cDNA in BioRad iCycler iQ5 Thermal Cycler. PCR conditions for the primers were optimized, and 40 cycles with a melting temperature of 60 °C, and 30 sec of each step were used. Specific primers were designed in Primer Blast database and synthesized by Sigma-Aldrich (**Table 7, Table 8, Table 9**). Quantification was performed using the ΔΔCT method and data was normalized using *Gapdh* mRNA as a standard.

Table 7. Rat primers used for qPCR.

Target gene	Forward (5'->3')	Reverse (5'->3')
c-Jun	GCCACCGAGACCGTAAAGAA	TAGCACTCGCCCAACTTCAG
Gapdh	GTGCAGTGCCAGCCTCGTCTCATAG	TTTGTCACAAGAGAAGGCAGCCCT
Il-1β	AGCCTTTGTCCTCTGCCAAGTCAGGT	TCGACAATGCTGCCTCGTGACCC
Il-6	CCACTGCCTTCCCTACTTCACA	TTGTTTTCTGACAGTGCATCATCG

Table 7. Rat primers used for qPCR.

Target gene	Forward (5'->3')	Reverse (5'->3')
Krox20	TGGGCGAGGGGACACACTGA	GCCTGGGATCCGGCTGTTGG
Mbp	GGGGCTCTGGCAAGGACTCAC	GGGATGGAGGGGGTGTACGAGG
Mpz	AGGACTCCTCGAAGCGCGGG	GGCAGCTTTGGTGCTTCGGC
Pmp22	CACTCTCACCAAAGGCGGCCG	ATGGCCGCTGCACTCATCACAC
TNF	CTACCCAGCCCCTGTCCCCGACTC	TCCAGGCCACTACTTCAGCGTCTCGT

Table 8. Mouse primers used for qPCR.

Target gene	Forward (5'->3')	Reverse (5'->3')
Mbp	ACACAAGAACTACCCACTACGG	GGGTGTACGAGGTGTCACAA
Mpz	CTGGTCCAGTGAATGGGTCT	CATGTGAAAGTGCCGTTGTC

Table 9. Bacterial primer used for qPCR.

Target gene	Forward (5'->3')	Reverse (5'->3')
RecA	GTGGATCTATTGTATTAGATGAGGCT	GCCAAAGTTCTGCAACATTAACACCT

4.5. RNA Sequencing and Data Analysis

RNA-Seq analysis was performed for control Schwann cells (treated with db cAMP for 48 h) and *B. burgdorferi*-stimulated Schwann cells (treated with db cAMP for 48 h followed by a 48 h infection with *B. burgdorferi*). RNA was extracted from these cultures, as explained above using the AllPrep DNA/RNA Mini Kit (Qiagen) according to the manufacturer's instructions. The quantity and quality of the RNAs were evaluated using Qubit dsDNA Assay Kit (Thermo Fisher Scientific) in a Qubit® 2.0 Fluorometer (Life Technologies) and Agilent RNA Nano Chips (Agilent Technologies) respectively.

RNA samples were then processed at the Genome Analysis Platform at CIC bioGUNE for preparation of sequencing libraries using the TruSeq RNA Sample Preparation v2 kit (Illumina Inc.) was used following the TruSeq® RNA Sample Preparation v2 Guide (Part #15026495 Rev. F). In brief, starting from 500 ng of total RNA, mRNA was purified, fragmented and primed for cDNA synthesis. cDNA first strand was synthesized with SuperScript-II Reverse Transcriptase (Thermo Fisher Scientific) for 10 min at 25 °C, 15 min at 42 °C, 15 min at 72 °C and pause at 4 °C. The cDNA second strand was synthesized with Illumina reagents at 16 °C for 1 hour. Then, A-tailing and adaptor ligation were performed. Finally, enrichment of libraries was achieved by PCR (30 sec at 98 °C; 15 cycles of 10 sec at 98 °C, 30 sec at 60 °C, 30 sec at 72 °C; 5 min at 72 °C and pause at 10 °C). The libraries were visualized on an Agilent 2100 Bioanalyzer using Agilent High Sensitivity DNA kit (Agilent Technologies) and quantified by quantitative PCR with the Kapa Library Quantification Kit (Master Mix and DNA Standards, KAPA–Biosystems) and Qubit dsDNA HS DNA Kit (Thermo Fisher Scientific). Paired-end (50 nucleotides) of the RNA-seq-libraries was

then carried out in a HiSeq400 platform (Illumina Inc.). All libraries were divided in 2 pools, and each pool was sequenced in 2 lanes at a final concentration of 4.3 pM (each library was intended to be sequenced at 0.473 and 4.3 pM per lane, respectively). Reads were trimmed for adapters using cutadapt (Martin, 2011) and aligned to mm10 genome using STAR (Dobin *et al.*, 2013). Quantification in expected counts from genes and isoforms were computed by RSEM (Li and Dewey, 2011) using genecode annotation v.26 [*https://www.gencodegenes.org/*]. We use TMM method to estimate scale factors between samples followed by the voom function in *limma* to convert them into log_2counts per million (logCPM). Finally, differential expression between control and *B. burgdorferi*-infected Schwann cells were evaluated by LIMMA bioconductor package (Ritchie *et al.*, 2015). Genes with a fold change of 2 (absolute value of Log2 ratio 1) and FDR< 0.05 were considered as significantly different. (Data analysis was performed by Dr José Luis Lavín).

4.6. Protein analysis

4.6.1. Total protein extraction and quantification

Frozen sciatic nerve segments (5 mm) were chopped on dry ice using a scalpel (Swann-Morton) and resuspended in 150 µl RIPA lysis buffer [500 ml stock solution: 1.6 mM NaH_2PO_4 (Merck), 8.4 mM Na_2HPO_4 (Merck), 0.1 % Triton X-100 (VWR), 0.1 M NaCl (Ambion), 0.1 % sodium dodecyl sulfate (SDS; Fisher Scientific) and ddH_2O] supplemented with sodium deoxycholate (Merck), 1 mM sodium fluoride and 1X protease and phosphatase inhibitor cocktails (Roche), and then homogenized in a Precellys 24 tissue grinder (Bertin Technologies). Schwann cells plated in 6 well-culture dishes were washed twice with 1X PBS and were scraped in 200 µl RIPA lysis buffer using a scraper. In both cases, lysates were snap frozen, defrosted, vortexed and incubated on ice in order to enhance the lysis process. After that, lysates were centrifuged for 30 minutes at 13000 rpm and 4 ^{o}C). Supernatants were collected and quantified through the Bicinchoninic acid (BCA) protein assay (Bio-Rad) in a SpectraMax microplate reader (bioNova científica). Bovine serum albumin (BSA) was used as protein standard.

4.6.2. Western blotting

Protein extracts were boiled at 95 °C for 5 minutes in 5X loading buffer [250 mM Tris-HCl (Sigma-Aldrich) pH 6.8, 500 mM β-mercaptoethanol (Sigma-Aldrich), 50 % glycerol (Sigma Aldrich), 10 % SDS (Sigma-Aldrich), and bromophenol blue (Sigma-Aldrich) in H_2O]. Proteins (between 2 µg and 20 µg) were separated by SDS-PAGE in 8 %, 11 % or 15 % acrylamide gels (according to the size of the protein) using Mini-PROTEAN Electrophoresis System (Bio-Rad).

Gels were transferred onto nitrocellulose membranes by electroblotting using Mini Trans-Blot cell (Bio-Rad).

Membranes were blocked with 5 % nonfat dry milk in 1X Tris Buffer Saline (TBS) [50 mM Tris, 150 mM NaCl (Sigma-Aldrich), pH 8.0) containing 0.1 % Tween-20 (Sigma-Aldrich) (TBST-0.1 %)] and incubated with primary antibodies overnight at 4 °C (**Table 10**).

Table 10. Primary antibodies used for protein detection. Target proteins of the antibodies, used dilution, host and company are specified.

Target protein	Dilution	Host	Company
β-Actin	1:5000	Mouse	Sigma-Aldrich
β-Catenin	1:1000	Rabbit	Santa Cruz Biotechnology
c-Jun	1:1000	Rabbit	Cell Signaling
Cleaved Caspase-3	1:1000	Rabbit	Cell Signaling
Gapdh	1:5000	Mouse	Cell Signaling
HuR	1:1000	Mouse	Santa Cruz Biotechnology
Krox20	1:500-1:1000	Rabbit	Cell Signaling
MBP	1:1000	Mouse	Cell Signaling
MPZ	1:1000	Rabbit	Cell Signaling
PARP (and Cleaved-PARP)	1:1000	Rabbit	Cell Signaling
Periaxin	1:20000	Rabbit	Gift from P. Brophy
SOX2	1:1000	Mouse	Santa Cruz Biotechnology
SOX10	1:1000	Mouse	Santa Cruz Biotechnology
Mouse IgG-HRP linked	1:5000	-	Cell Signaling
Rabbit IgG-HRP linked	1:5000	-	Cell Signaling

Membranes were then washed three times with TBST-0.1 % and incubated for 1 hour at RT in blocking solution containing secondary anti-mouse or anti-rabbit conjugated to horseradish peroxidase (HRP). Immunoreactive proteins were detected by Western lightning Enhanced Chemiluminiscence (ECL) Reagent (PerkinElmer) and exposed to X-ray films (Fujifilm) in a Curix 60 Developer (Agfa).

4.6.3. Nascent protein synthesis analysis by flow citometry

To measure protein synthesis rate, Schwann cells were cultured for 1h with 15 µM of O-propargy-lpuromycin (OP-puro; Medchem Source LLP; prepared in PBS for a final concentration of 10 mM at pH 6.4–6.6) in cell incubator, at 37 °C and 5 % CO_2. Then, cells were fixed in 1% paraformaldehyde in PBS for 15 min on ice, followed by 3 washes of PBS. After cell permeabilization with 0.1 % Saponin (Sigma-Aldrich) supplemented with 3 % FBS, OP-Puro conjugation to a fluorochrome was performed with an azide-alkyne cycloaddition using a CuAAC Reaction Ligand test kit (THPTA and BTTAA) (Jena Bioscience) and 25 µM of Alexa Fluor 488

conjugated to azide following manufacturer instructions. After 30 min of incubation in darkness, samples were processed in FACS CANTO flow cytometer.

4.6.4. Proteomics

4.6.4.1. Protein digestion

Control Schwann cells (without bacteria) and Schwann cells stimulated with *B. burgdorferi* were used for protein extraction with a lysis buffer containing 7 M Urea, 2 M Thiourea and 4 % CHAPS. Samples were then processed for proteomic and bioinformatic analysis at the Proteomics platform at CIC bioGUNE. Samples were incubated for 30 min at RT under agitation and digested following the filter-aided FASP protocol described by (Wiśniewski *et al.*, 2009) with minor modifications. In brief, protein was reduced and alkylated by incubation in 5 mM DTT for 45 min, followed by incubation in 20 mM Iodoacetamide (IA) for another 45 min. Excess of IA was depleted by an additional incubation in 5 mM DTT for another 45 min. All incubations were carried out at 25 °C. Then, samples were diluted to a final concentration of 0.66 M Urea, 0.18 M thiourea, 0.37 % CHAPS, and trypsin (Trypsin Gold, Promega Corporation) was added to a final trypsin/protein ratio of 1:10. The sample was vortexed and incubated overnight at 37 ^{o}C, dried out in a RVC2 25 SpeedVac concentrator (Christ) and resuspended in 0.1 % Formic Acid (FA).

4.6.4.2. Mass spectrometry analysis

Peptide separation was performed on a nanoACQUITY UPLC system (Waters) connected to an LTQ Orbitrap XL mass spectrometer (Thermo Electron). Approximately 500 ng of each sample were loaded onto a Symmetry 300 C18 UPLC Trap column (180 µm x 20 mm, 5 µm; Waters). The precolumn was connected to a BEH130 C18 column (75 µm x 200 mm, 1.7 µm; Waters) analytical column, equilibrated in 3 % acetonitrile and 0.1 % FA. Peptides were eluted directly into an LTQ Orbitrap XL mass spectrometer (Thermo Finnigan) through a nanoelectrospray capillary source (Proxeon Biosystems) at 300 nl/min and using a 120 min linear gradient of 3–50% acetonitrile. The mass spectrometer automatically switched between MS and MS/MS acquisition in DDA mode. Full MS scan survey spectra (m/z 400–2000) were acquired in the orbitrap with mass resolution of 30000 at m/z 400. After each survey scan, the six most intense ions above 1000 counts were sequentially subjected to collision-induced dissociation (CID) in the linear ion trap. Precursors with charge states of 2 and 3 were specifically selected for CID. Peptides were excluded from further analysis during 60 s using the dynamic exclusion feature.

4.6.4.3. Progenesis Liquid chromatography–mass spectrometry (LC-MS) software analysis

Progenesis LC-MS (version 2.0.5556.29015, Nonlinear Dynamics) was used for the label-free differential protein expression analysis. One of the runs was used as the reference to which the precursor masses in all other samples were aligned to. Only features comprising charges of 2+ and 3+ were selected. The raw abundances of each feature were automatically normalized and logarithmized against the reference run. Samples were grouped in accordance to the comparison being performed, and an ANOVA analysis was performed. A peak list containing the information of all the features was generated and exported to the Mascot search engine (Matrix Science Ltd.). This file was searched against a Uniprot/Swissprot database containing both *Borrelia burgdorferi* and *Rattus norvegicus* entries, and the list of identified peptides was imported back to Progenesis LC-MS. Protein quantitation was performed based on the three most intense non-conflicting peptides (peptides occurring in only one protein), except for proteins with only two non-conflicting peptides. The significance of expression changes was tested at protein level, and proteins with an ANOVA p-value ≤ 0.05 were selected for further analyses.

4.6.5. Enzyme-Linked Immunosorbent Assay (ELISA)

The levels of Tumour Necrosis Factor (TNF) in control and *B.* burgdorferi-stimulated Schwann cells were determined by capture ELISA using the Legend Max™ Rat TNF ELISA kit (BioLegend) according to the manufacturer's recommendations. In brief, anti-rat TNF pre-coated 96-well strip microplate was incubated with blocking buffer (10 % FBS in PBS) at RT for 1 h. Six two-fold dilutions from the 500 pg/ml standard and 50 µl of each sample were incubated for at least 2 h at 37 °C. After several washes, 100 µl of rat TNF detection antibody was added onto each well at a dilution of 1/500 and incubated for 1 h at RT. Once plate was washed and dried, 100 µl of Adivin-HRP D solution was added onto each well at 1/1000 dilution and samples were incubated for 45 min at RT. Substrate solution F was added and reaction was stopped after 30 min with equal amount of stop solution (2 M Sulfuric acid). Absorbance was read at 450 nm within 30 min of incubation.

4.6.6. Surface receptors analysis

Schwann cells were seeded at a density of 2-2.5 × 10^5 cells per 1.5 ml, in 6-well culture dishes. Cells were detached with trypsin and washed twice in PBS. The cells were then resuspended in 100 µl of 1X PBS (with 10 % FBS) and 1 µl of corresponding antibody (**Table 11**) was added for 30 min on ice. After incubation time, 900 µl of 1X PBS was added and mixed. The samples were

washed twice and the pellet was resuspended in 1 ml of 1X PBS (with 10 % FBS) for analysis in FACS CANTO flow cytometer.

Table 11. Antibodies used for the analysis of Schwann cells' surface receptors. Antibodies, host and the company are specified.

Antibody	Host	Company
CD11b-APC	Rat	Miltenyi Biotec
CD14-FITC	Rat	Thermo Fisher Scientific
CD204-FITC (MSR1)	Human	Miltenyi Biotec
CD45-PerCP	Mouse	Miltenyi Biotec
CD64-PE	Human	Miltenyi Biotec
DCAR1-PE	Rat	Miltenyi Biotec
MARCO-FITC	Rat	Invitrogen
MR-FITC (CD206)	Rat	Thermo Fisher Scientific

4.6.7. Protein degradation

In order to analyze the pathways implicated in myelin proteins degradation after exposure to *B. burgdorferi*, we examined the role of autophagy and proteasomal degradation pathways.

4.6.7.1. Autophagy

Induction of autophagy was determined by examining microtubule-associated protein 1A/1B-light chain 3 (LC3 II) levels by Western blotting in the presence or absence of the following lysosomal inhibitors [20 mM of ammonium chloride (NH_4Cl; Sigma-Aldrich) and 100 µM of Leupeptin (Sigma-Aldrich) protease inhibitor (Gomez-Sanchez *et al*., 2015)], added at 4 h or 24 h before sample extraction.

4.6.7.2. Proteasome

To examine proteasomal degradation of myelin-related proteins, Schwann cells were treated with 10 or 20 µM MG132 (Sigma-Aldrich) for 4 h or 16 h before protein extraction. As a control, vehicle (DImethyl Sulfoxide, DMSO; VWR) was used.

4.7. Proliferation assay: 5-ethynyl-2'-deoxyuridine (EdU) incorporation

In order to measure cells proliferation, we analyzed DNA synthesis using Click-iT™ EdU Proliferation assay for imaging (Thermo Fisher Scientific), which is based on a click reaction, which a copper-catalyzed covalent reaction between an azide (Alexa Fluor dye) and an alkyne (EdU). The small size of the dye azide allows the efficient detection of the incorporated EdU using a standard aldehyde-based fixation and detergent permeabilization. Thus, 10 µM EdU was added to the cultures for 4 h at 37 °C and 5 % CO_2. The coverslips were then fixed in 3.7 % formaldehyde in PBS followed by permeabilization for 20 min with 0.5 % Triton X-100. The

samples were incubated for 30 min at RT with 0.5 ml of Click-iT reaction cocktail per coverslip, prepared following manufacturer's instructions. 50 ng/ml of DAPI was used for 30 min at RT in order to stain DNA. 4 pictures from different fields of each coverslip were acquired using a 20x AxioImager.D1 fluorescent microscope objective (Zeiss).

4.8. Transmission electron microscopy

Nerve segments were fixed in 2.5 % glutaraldehyde overnight at 4 °C and then washed in 0.1 M phosphate buffer and stained in 1 % osmium tetroxide overnight at 4 °C. The next day, the nerves were washed 3 times in 0,1 M phosphate buffer and dehydrated in 25 % ethanol (5 min), 50 % ethanol (5 min), 70 % ethanol (5 min), 90 % ethanol (10 min) and 100 % ethanol (4 times, 10 min each) followed by 3 incubations with 1,2-epoxypropane (10 min each; VWR). The samples were then embedded in Agar 100 resin (12 g resin, 8 g DDSA, 5 g MNA, and 400 ml BDMA; Agar Scientific) with 1,2-epoxypropane in a 1:1 mixture, and then replaced with resin for an overnight incubation. The next morning, the resin was replaced with fresh resin solution and 6 h later, the nerve samples were placed inside rubber moulds with fresh resin solution and kept at 65 °C overnight. 1 µm semi-thin sections were cut with a diamond knife in a Diatome (Leica). Semi-thin sections were stained with 0.1 % toluidine blue in ethanol, washed with ddH_2O and allowed to dry. Photos were taken with a light microscope and sent for ultrathin sections processing.

4.9. Apoptosis

4.9.1. Annexin V-FITC by Flow cytometry

For apoptosis analysis, triplicate cultures of 6 x 10^5 control or Bb-stimulated Schwann cells per 60 mm dish were used. Adherent and non-adherent cells were collected and stained with Annexin V–FITC (Immunostep) following the manufacturer's instructions. Cells were fixed with 1 % formaldehyde before analysis using a FACS CANTO (BD Biosciences) flow cytometer. Data were analyzed using FACSDiva software (BD Biosciences).

4.9.2. TdT-mediated dUTP nick end labeling (TUNEL) assay

Control or *B. burgdorferi*-stimulated Schwann cells were plated onto coverslips and fixed in 4 % paraformaldehyde. Apoptosis was analyzed using *in situ* Cell Death detection kit (Roche) according to the manufacturer's instructions. Cells were fixed in 4 % paraformaldehyde, permeabilized in 1X PBS with 0.1% Triton X-100 and incubated with FITC-conjugated primary antibody diluted in TUNEL diluent buffer (1:10) for 2 h at 37 °C. 50 ng/ml of DAPI was used for nuclear staining (30 min, RT) and coverslips were mounted in DAKO fluorescent mounting medium. TUNEL positive cells were examined on a fluorescence microscope Axio Imager.D1

(Zeiss). As a positive control, cells were treated with DNase I recombinant (3,000 U/ml – 3 U/ml in 50 mM Tris-HCl, pH 7.5, 1 mg/ml BSA) for 10 min at 25 °C to induce DNA strand breaks.

4.9.3. Caspase-3 ICC

5,000 Schwann cells, seeded onto 12 mm coverslips in 24-well-culture dishes, were washed twice in 1X PBS and fixed in 4 % paraformaldehyde for 10 minutes. Cells were permeabilized with 1X PBS containing 0.3 % Triton X-100 and incubated with Caspase-3 antibody (Cell Signaling) at 1:500 dilution overnight at 4 °C. The next day, the samples were incubated with anti-rabbit FITC secondary antibody (1:100 dilution; Jackson ImmunoResearch Laboratories) and 50 ng/ml of DAPI was used for nuclear staining (30 min, RT). The coverslips were washed in 1X PBS and fixed in 4 % paraformaldehyde for 10 minutes. Samples were washed in 1X PBS and coverslips were mounted in Dako fluorescence mounting medium, and analyzed using AxioImager.D1 fluorescent microscope or Zeiss LSM 880.

5. Statistics

All analyses were done using Microsoft Excel or GraphPad Prism 6.00 (San Diego California, www.graphpad.com). Data are shown in histograms as mean ± SEM, $p < 0.05$ is deemed statistically significant. Statistical analysis was performed by two-tailed unpaired Student's t tests. Quantifications were performed from a minimum of three experimental groups.

Results

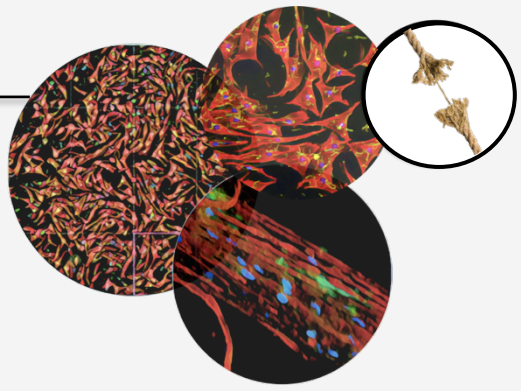

Results

1. Borrelia burgdorferi induces demyelination in Peripheral Nervous System

Myelin breakdown, demyelination, is the result of a wide range of conditions causing nerve damage, including pathogens infection, e.g. *Mycobacterium leprae* (Masaki *et al*., 2013). Peripheral nerves damage is observed in Lyme neuroborreliosis, which perhaps is one of the most dangerous and poorly understood of Lyme disease manifestations (Rupprecht *et al*., 2008). Thus, we wanted to examine whether nerve damage observed in patients could be due to a direct effect of the main causative agent of Lyme disease, *B. burgdorferi* (Bb), on myelin sheaths. For this purpose, we established Schwann cells-Dorsal Root Ganglia (DRG) axon co-culture systems and induced myelin sheath formation using ascorbic acid (Taveggia and Bolino, 2018). We then infected these co-cultures with Bb. Using the myelin marker Myelin Basic Protein (MBP), we found that control cultures showed the presence of normal myelin sheaths, whereas Bb induced myelin breakdown, as shown by presence of myelin ovoids, 6 days after infection (**arrows in Figure 42 A**).

To further explore response this effect on myelination mice sciatic nerve segments were cultured in the presence or absence of Bb (Bb-GFP or Bb-WT). 7 days after either Bb stimulation, semi-thin sections of sciatic nerves revealed fewer myelinated axons in Bb-cultured nerve segments than in unstimulated ones, as observed by light microscope (**Figure 42 B**). Bb-GFP was clearly observed surrounding a sciatic nerve by phase contrast microscopy (before fixing samples for MBP analysis by ICC) (**Figure 42 C**). Notably, fewer MBP+ segments were observed (in red) in nerves infected with 3 x 10^7 Bb-WT or 1.5 x 10^6 Bb-GFP for 7 days (**Figure 42 D**), suggesting an increase in myelin breakdown.

Similarly, we found downregulation of the myelin proteins MBP, MPZ and Periaxin induced by Bb in cultured segments of sciatic nerves (**Figure 43 A**) and brachial plexus (**Figure 43 B**).

Moreover, RT-qPCR analysis showed a strong reduction in expression of myelin genes *Mbp* and *Mpz* in rat sciatic nerves, which indicated a downregulation in transcription of myelin genes *Mbp* and *Mpz*, induced by Bb as detected by expression of the Bb gene *RecA* (**Figure 43 C**).

Collectively, these experiments show that *B. burgdorferi* can promote Schwann cells demyelination, suggesting a direct role of *B. burgdorferi* in nerve pathology.

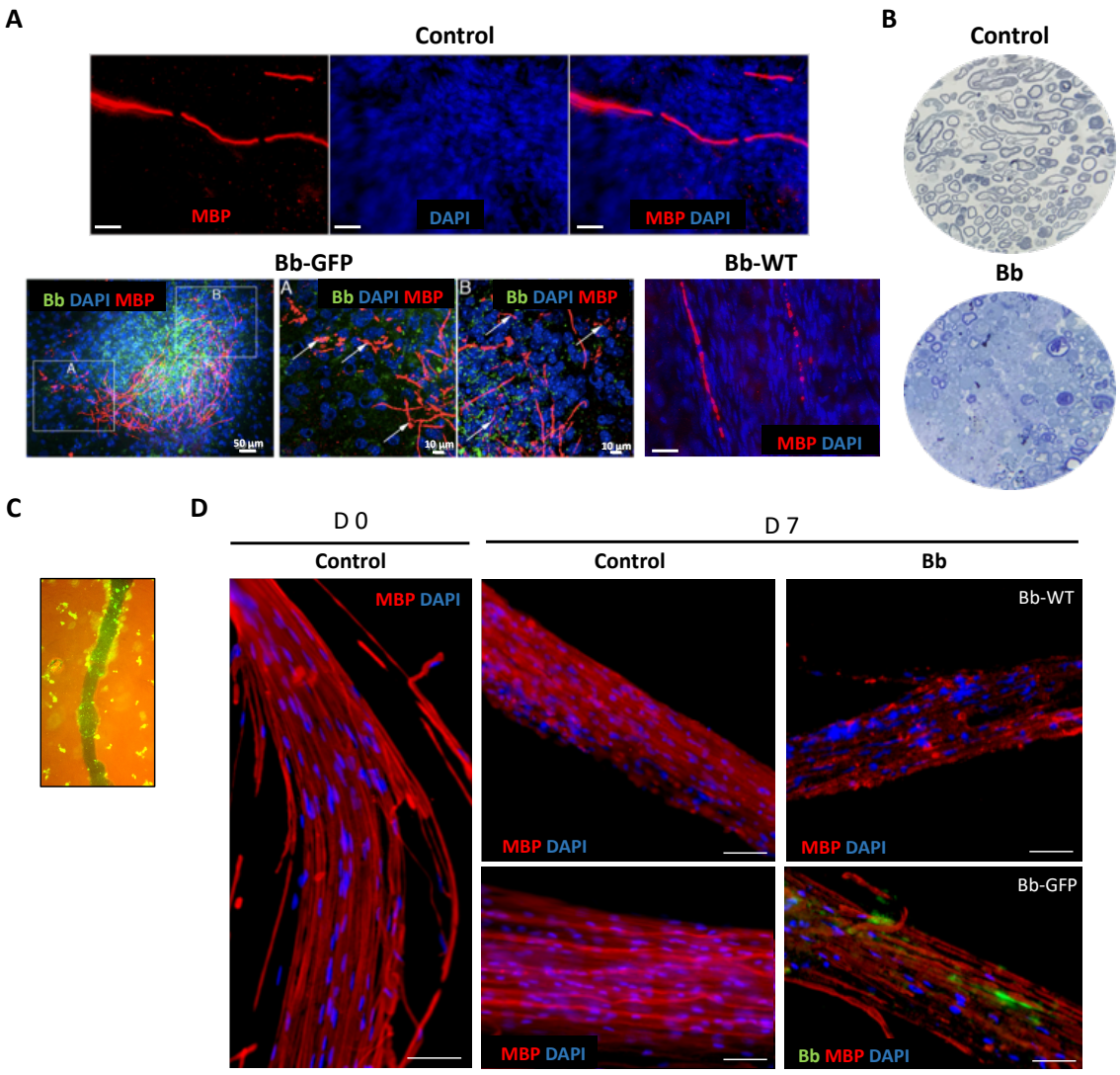

Figure 42. *B. burgdorferi* induces demyelination in DRG and sciatic nerves. A) Fluorescent microscopy images showing DRG-Schwann cells co-culture labeled with the myelin marker MBP (and DAPI for DNA staining) in control conditions or in the presence of *B. burgdorferi* (Bb-GFP or Bb-WT) for 6 days. **B)** Representative images of semi-thin sections of control or Bb-treated sciatic nerves stained with toluidine blue. **C)** A sciatic nerve segment surrounded by Bb-GFP seen by phase contrast microscopy (before fixing the sample for fluorescent microscopy). **D)** Sciatic nerves cultured in the absence or presence of Bb for 7 days are shown in representative images. Samples are labeled with MBP (and DAPI for DNA Staining). Scale bar, 50 µm.

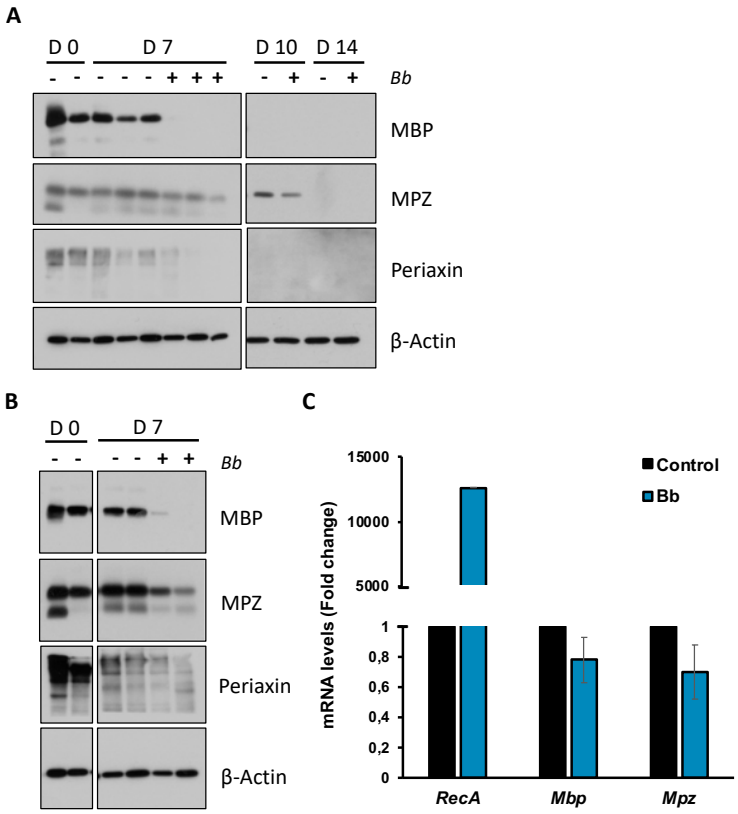

Figure 43. *B. burgdorferi* induces myelin proteins downregulation in sciatic nerves and brachial plexus. A) Western blot analysis showing downregulation of myelin structural proteins (MBP, MPZ and Periaxin) downregulation in *B. burgdorferi* (Bb)-infected sciatic nerves, compared to control samples (without pathogen) after 7, 10 and 14 days, shown in a representative Western blot. **B)** A representative western blot showing downregulation of myelin structural proteins (MBP, MPZ and Periaxin) after 7 days of Bb stimulation in brachial plexus, compared to unstimulated samples. **C)** RT-qPCR showing expression of *Mbp*, *Mpz* and Bb gene *RecA.* Graph data are presented as mean ± SEM.

2. Borrelia burgdorferi induces demyelination in myelinated Schwann cells

2.1. In vitro Schwann cell myelination assay

To study the molecular mechanisms implicated in Bb-induced demyelination, we optimized an *in vitro* Schwann cell myelination assay that mimics Schwann cells myelin differentiation *in vitro*. Thus, after Schwann cells isolation from nerves and their purification, Schwann cells were treated with db cAMP, a cell-permeable and non-hydrolyzable cAMP analogue, for 48 h. This treatment induces a drastical change to a bigger flattened cell morphology and cytoplasm vacuolization, as observed by phase contract microscopy and phalloidin staining by fluorescent microcopy (DAPI was used to stain DNA) (**Figure 44 A**).

In this myelination model, levels of the transcription factor Krox20, a positive regulator of myelination, increased rapidly after db cAMP addition, while levels of the structural myelin proteins MPZ and Periaxin increased after 24 h with a peak at 48 h (**Figure 44 B**). In this model,

a switch to a starvation medium (without cAMP), after an initial induction of myelination with db cAMP for 48 h, led to a clear decrease in myelin marker levels (**Figure 44 C**), showing that this model could also be used to mimic demyelination.

Thus, we propose this model for studying not only direct Schwann cells myelination, but also molecular mechanisms implicated in *B. burgdorferi*-induced demyelination.

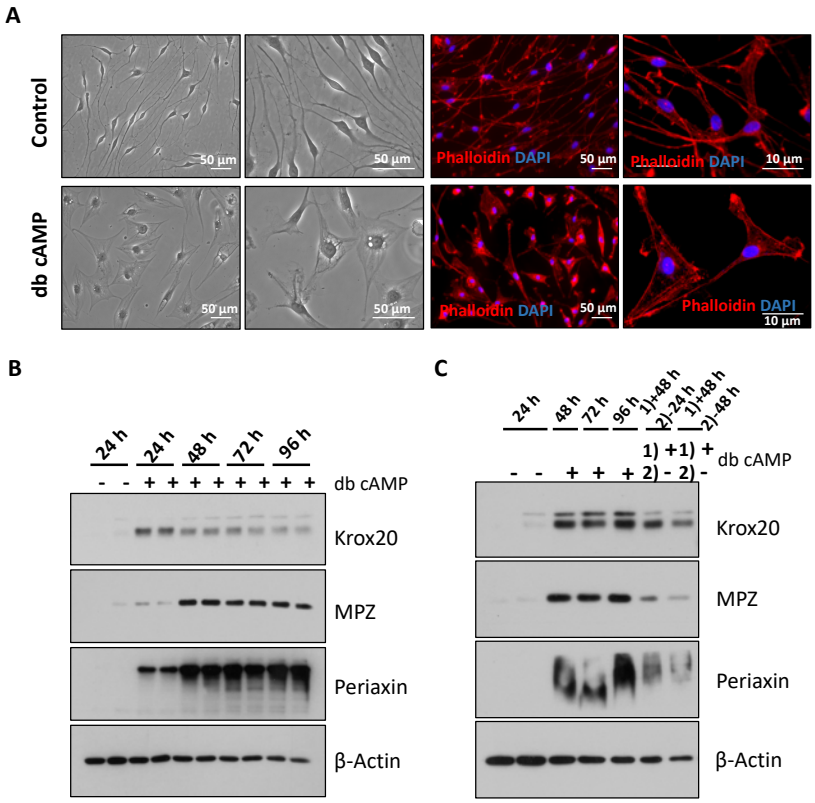

Figure 44. Schwann cell *in vitro* myelination assay. A) Differences in Schwann cells morphology before and after myelin differentiation by phase contrast microscopy (left panel) and fluorescent microscopy (right panel). **B)** Myelin related protein (Krox20, MPZ and Periaxin) levels after db cAMP stimulation for 24 h to 96 h. **C)** Krox20, MPZ and Periaxin levels after db cAMP removal for 24 h and 48 h. Schwann cells treated with db cAMP for 24 h to 96 h are shown as positive controls of myelin proteins.

2.2. Borrelia burgdorferi induces demyelination in Schwann cells myelinated *in vitro*

To examine whether Bb could induce demyelination in *in vitro*-myelinated Schwann cells in the absence of other type of cells, such as immune cells, we analyzed myelin protein levels (Krox20, MPZ and Periaxin) by western blot after 6 h to 48 h of Bb infection following 48 h of db cAMP stimulation. There was a clear decrease in myelin-related proteins in cells cultured with Bb (**Figure 45 A**).

Furthermore, we showed a global decrease in the transcription of myelin genes at 24 h and 48 h, where genes encoding Krox20 transcription factor and Pmp22 myelin structural protein were

significantly downregulated at 24 h, while at 48 h *Mbp*, *Mpz*, *Periaxin* and *Pmp22* were significantly downregulated in Bb-treated Schwann cells (**Figure 45 B**).

These results show that *B. burgdorferi* can directly induce Schwann cells demyelination, in the absence of other type of cells, including immune cells.

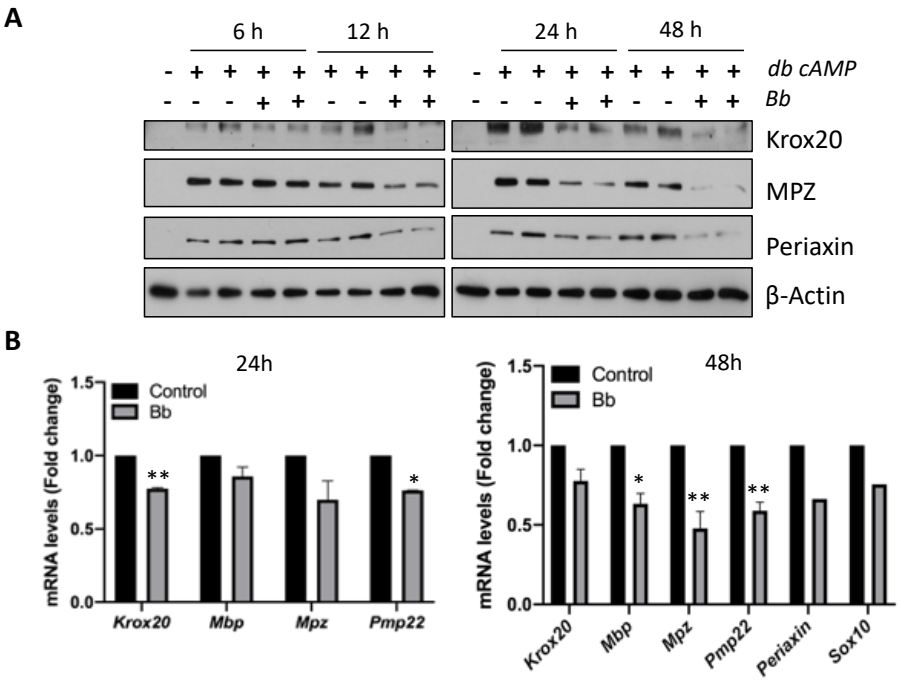

Figure 45. *B. burgdorferi* induces demyelination in myelinated Schwann cells. A) Western blots showing a decrease in the levels of myelin proteins (Krox20, MPZ, Periaxin) in Schwann cells upon *B. burgdorferi* (Bb) stimuli for 6 h to 48 h, compared to control samples (without bacteria). Technical duplicates are shown in the western blot. **B)** RT-qPCR analysis showing expression of myelin genes in control (black) or Schwann cells cultured with Bb (grey) for 24 h and 48 h. Data are presented as mean ± SEM; n=3-4 independent experiments; Two-tailed unpaired Student's t-test was used for statistics. *p<0.05; **p<0.01.

2.3. Direct contact between *Borrelia burgdorferi* and Schwann cells leads to demyelination

2.3.1. *Borrelia burgdorferi* binds to but cannot internalize in Schwann cells

We next sought to determine whether the observed demyelination in primary Schwann cells could be due to a direct contact of Bb with these glial cells. For that purpose, we immunolabeled Schwann cells with phalloidin and DAPI DNA staining after Bb-GFP infection at different time-points. Strikingly, we found that Bb was bound to Schwann cells after 6 h of the incubation with the pathogen. The binding is represented in a mosaic image done with 16 photos of different fields of the same cover (**Figure 46 A).** Next, we wanted to study if Bb not only can bind to Schwann cells' surface, but can also internalize as it has been described for the *Mycobacterium leprae* bacterium, which allows the bacterium to evade immune system and disseminate and reach other tissue and organs (Masaki *et al.*, 2013). For this aim, we compared myelinated

Schwann cells with a macrophage cell line, RAW 264.7, that it is well known to phagocytize Bb in normal culture conditions, at 37 °C (in contrast to 4 °C, where only binding is observed) (Hovius *et al.,* 2009). Bb binding to macrophages reached a peak after 2.30 h of stimulation, as shown by flow cytometry assay.

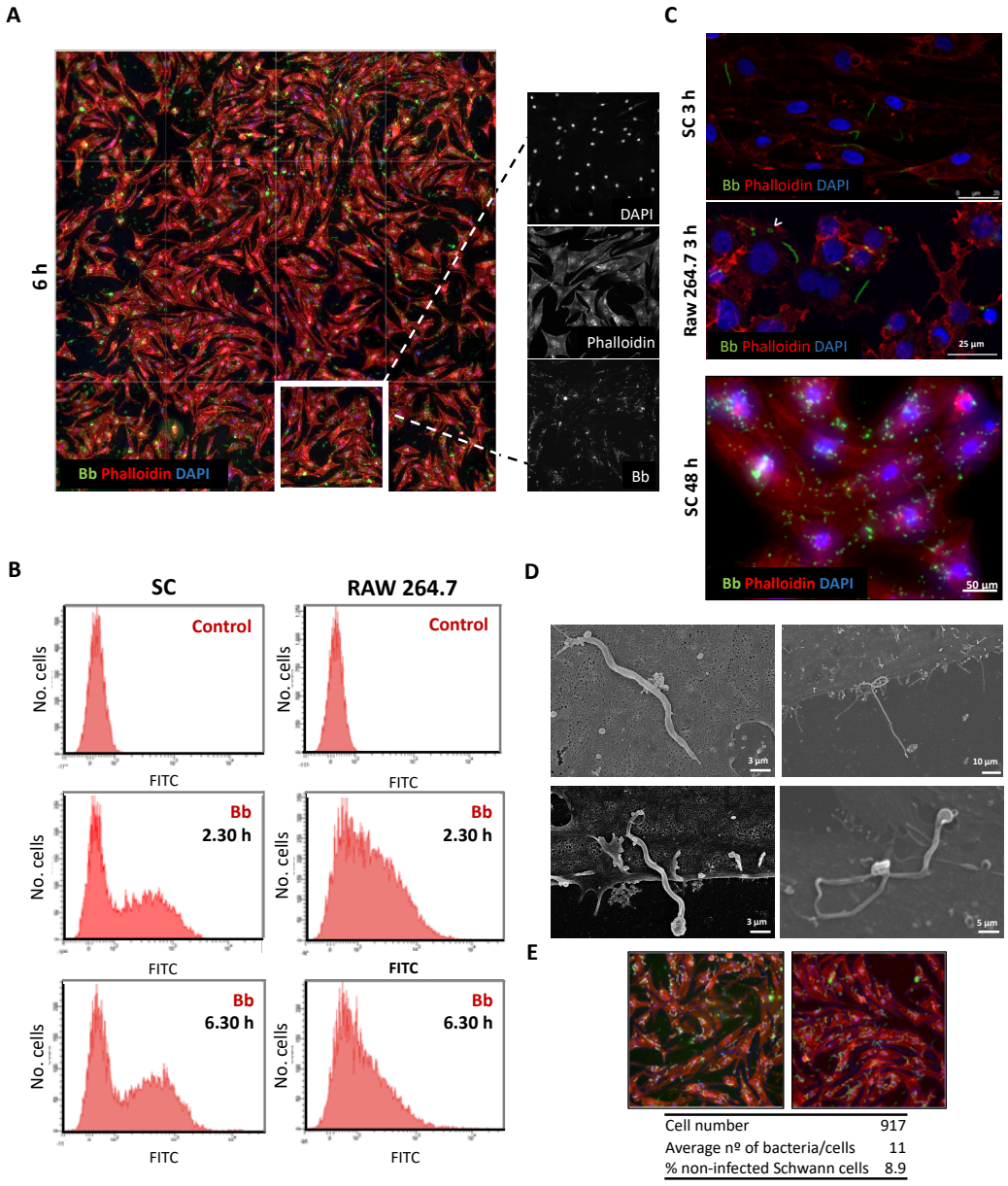

Figure 46. *B. burgdorferi* binds to Schwann cells surface but cannot internalize. A) A mosaic image of 16 different fields of a unique cover showing binding of *B. burgdorferi* (Bb) to Schwann cells' surface upon 6 h of bacteria addition to the culture. **B)** Flow cytometry assay confirming Bb and Schwann cells binding, in a time-dependent manner from 2.30 h to 6 h, and binding and phagocytosis of Bb in RAW 264.7 macrophage cell line. **C)** Confocal images showing Bb bound to Schwann cells at 3h and fluorescent microscopy confirming binding between Bb and Schwann cells but not internalization of the pathogen after 48 h of infection. Internalized spirochetes were observed in RAW 264.7 upon 3 h of stimulation. Arrowhead in RAW 264.7 image points a Bb circle indicating an internalized Bb. **D**) Scanning electron microscopy images show clear spirochetes on the surface of Schwann cells. **E)** Counts of number of infected Schwann cells and average number of bacteria per Schwann cells.

After RAW 264.7 cells continue phagocyting bacteria, there was a decrease in Bb and RAW 264.7 binding, which was observed after 6.30 h of pathogen stimulation, while Bb binding to Schwann cells took place in a time dependent manner (**Figure 46 B**). In addition to this observation, we did not observe the characteristic Bb-GFP circles, which indicate internalized Bb, inside Schwann cells in contrast to Raw 264.7 cells at 3 h of Bb stimulation, as shown by representative confocal microscopy images. Moreover, a representative image of fluorescent microscopy of Schwann cells cultured in the presence of Bb for 48 h, confirmed that there was no internalization of Bb into Schwann cells, even later. However, as expected, a greater number of Bb-GFP were bound to the surface of Schwann cells (**Figure 46 C**). High-resolution images by scanning electron microscopy (SEM) confirmed the presence of the spirochete on the surface of Schwann cells (**Figure 46 D**). To gain a better insight of the binding of Bb to Schwann cells, the percentage of infected cells after 6 h of Bb infection was calculated. Only 8.9 % of Schwann cells shoed no bacterial binding and there was an average of 11 spirochetes bound to each Schwann cell at 6 h after pathogen infection (**Figure 46 E**).

Overall, our data indicate direct contact between *B. burgdorferi* spirochete and Schwann cells.

2.3.2. Borrelia burgdorferi recognition by Schwann cells induces demyelination

Next, we wanted to determine whether this direct contact between Bb and Schwann cells was responsible for the demyelination, or whether this effect was contact-independent. To address this, we compared the effects of live spirochetes, metabolically inactive Bb (heat-inactivated by pathogen incubation at 56 ^{o}C for 30 min) and sonicated Bb (3 times sonicated Bb, 1 min each time) on Schwann cell myelination after 48 h of stimulation. Interestingly, representative fluorescent images at 6 h of pathogen stimulation showed a direct binding of heat-inactivated Bb to Schwann cells, similar to that observed with live Bb, but as expected, no bacteria pieces (after sonication) were observed in the surface of Schwann cells (**Figure 47 A**). Western blot analysis showed that either live Bb or heat-inactivated Bb led to a decrease in myelin protein levels. Stimulation with sonicated Bb induced demyelination only at higher MOIs (**Figure 47 B**). Although, spirochetes did not need to be metabolically active for direct binding to Schwann cells, the cells need to recognize Bb intracellular compounds of Bb to promote demyelination, we did not know if Bb cultured with Schwann cells for 48 h remain alive at the end of the experiment. To asses this, first, we optimized a generic bacterial viability kit. Pathogens were grown in the presence of more oxygen, in 5 ml BSK-H medium in a 15 ml centrifuge tube, or with less oxygen as bacteria optimal condition (De Martino *et al*., 2006), in 14 ml BSK-H medium in a 15 ml centrifuge tube, and checked if there were differences in the spirochetes viability. As expected,

there were less live Bb (green) and more dead spirochetes (red) when Bb was grown in the presence of higher oxygen concentrations. This viability reduction was clearly observed by fluorescent microscopy images of aliquots taken from the medium of both conditions (**Figure 47 C**). Once we checked the bacteria viability kit works with Bb bacterium, which we confirmed by the bacteria susceptibility to the oxygen, we took Bb-WT-infected Schwann cells' supernatant after 48 h of incubation and tested bacteria viability. Almost all bacteria in the supernatant (without binding to the cells) were dead after 48 h in Schwann cells culture conditions, as it is shown in a representative fluorescent microcopy image (**Figure 47 D**). Nevertheless, it is still unclear whether *B. burgdorferi* bound to Schwann cells remain alive after 48 h and if blocking *B. burgdorferi* ability to bind to Schwann cells surface could lead to bacteria dead and a decrease in demyelination induction. This needs to be addressed.

These data suggest that recognition by Schwann cells of live or just *B. burgdorferi* pieces is enough to trigger demyelination.

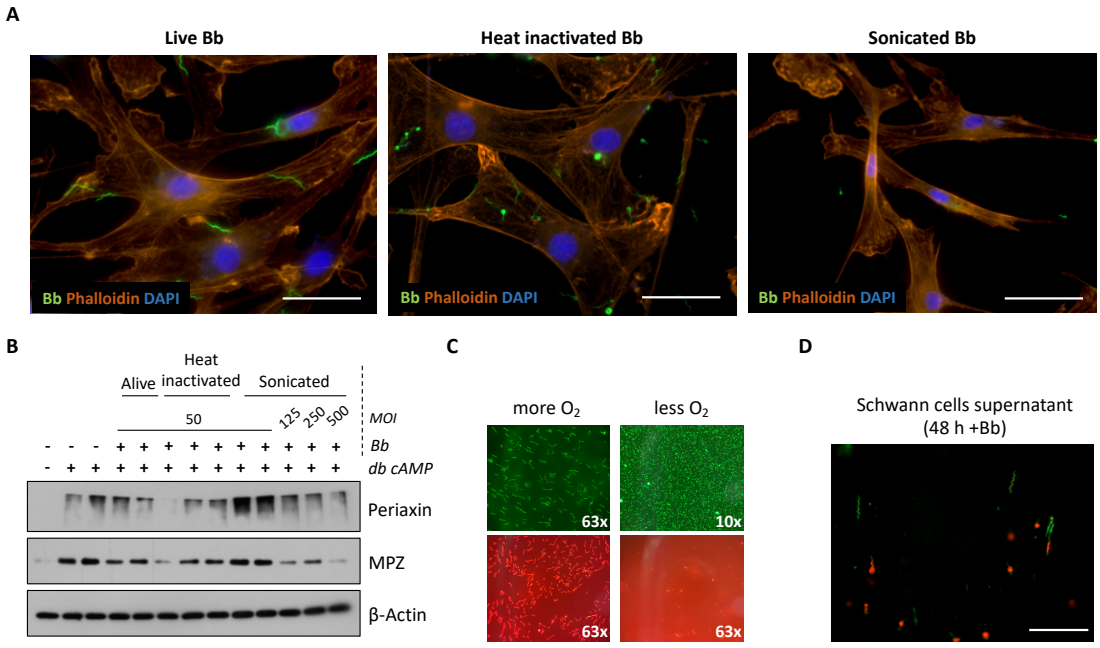

Figure 47. *B. burgdorferi* needs direct contact with Schwann cells to induce demyelination. A) Fluorescent microscopy images show live, heat inactivated and sonicated *B. burgdorferi* (Bb) cultured with Schwann cells for 6 h. **B)** Western blot showing MPZ and Periaxin protein levels after 24 h of live, heat inactivated or sonicated Bb stimulation. **C)** Bacteria viability assay showing live Bb (green) and dead Bb (red) cultured in 5 ml of medium in a 15 ml centrifuge tube (left panel) or in 13 ml of medium (right panel). **D)** Live Bb (green) and dead Bb (red) from Schwann cells' supernatant, after 48 h of pathogen addition to cell culture, are shown in a fluorescent microscopy image. Scale bar, 10 µm.

2.3.3. Surface receptors of Schwann cells associated with microorganisms recognition

A plethora of surface receptors are involved in microorganisms recognition and binding, such as integrins, C-type lectins and scavenger receptors. Several of these receptors have been

implicated in *B. burgdorferi* recognition, including macrophage-1 antigen Mac-1 (CD11b), cluster of differentiation 14 (CD14), scavenger receptor-A (CD204), protein tyrosine phosphatase receptor type C (CD45), cluster of differentiation 64 (CD64), dendritic cell activating receptor (DCAR1), macrophage receptor with collagenous structure (MARCO) and mannose receptor (MR) (Cinco *et al*., 2001; Hawley *et al*., 2013). We aimed to determine whether those proteins could be implicated in Bb recognition of Schwann cells, and thus we analyzed their expression by flow cytometry in control and 48 h db cAMP-treated Schwann cells (**Figure 48 A**).

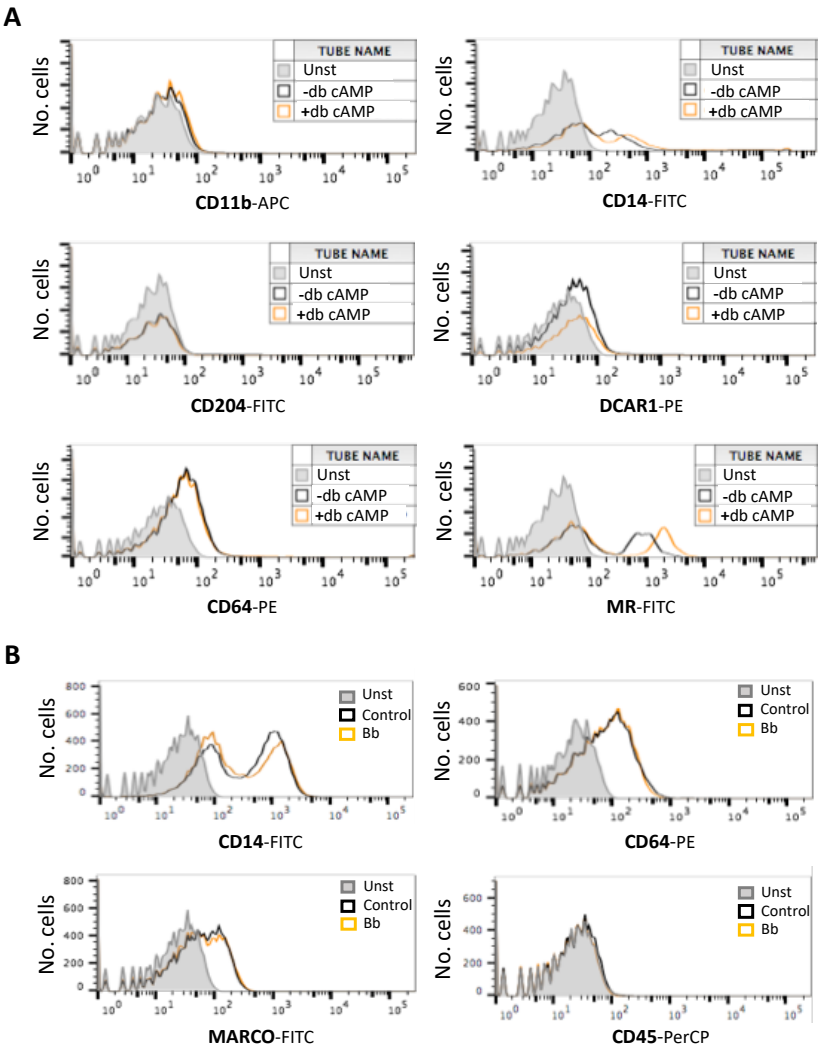

Figure 48. Microorganisms-and *B. burgdorferi*-associated surface receptors in Schwann cells. A) Representative flow cytometry histograms of CD11b, CD204, CD64, DCAR1 and MR surface receptors in untreated Schwann cells (grey, not filled) and 48 h db cAMP-treated myelinated Schwann cells (orange). Unstained (Unst) control is represented in grey (filled in grey). **B)** Most positive stained receptors of A) (CD14 and CD64) and other *B.burgdorferi* (Bb) recognition-associated proteins (CD45 and MARCO) expression in the absence (control, black) or presence of Bb (orange) for 48 h. Unstained (Unst) control is represented in grey (filled in grey).

There was a clear evidence of CD64, CD14 and MR expression on the Schwann cells' surface, in line with previous works (Vedeler *et al*., 1991; Baetas-da-Cruz *et al*., 2009), both at basal conditions and after db cAMP treatment (-/+ db cAMP). We did not observe a detectable levels of CD11b, CD204 and DCAR1 receptors in either condition (-/+ db cAMP).

Next, we determined whether Bb could regulate levels of some surface receptos that we detected previously in Schwann cells (CD64 and CD14) (**Figure 48 A**), as well as the expression of MARCO and CD45 receptors which have previously been implicated in Bb recognition by macrophages (**Figure 48 B**) (Petnicki-Ocwieja *et al*., 2013; Carreras-González *et al*., 2018). Although these receptors (except CD45) were clearly expressed on the surface of Schwann cells, Bb did not induce upregulation of any of the receptors after 48 h of stimulation.

Together, these data point the possible recognition of *B. burgdorferi* by Schwann cells, via interaction of these specific receptors and Pathogen-associated molecular patterns (PAMPs), although further studies are required to determine how this drives the demyelination phenotype observed in the presence of the pathogen.

3. Molecular mechanisms involved in *B.burgdorferi*-induced Schwann cells demyelination

3.1. B. burgdorferi does not induce cytokine expression in Schwann cells

Pro-inflammatory cytokines can be expressed in Schwann cells and DRG-Schwann cell cultures after being in contact with pathogens (Masaki *et al*., 2013; Ramesh *et al*., 2013). Furthermore, Bb can lead to host immune activation and a systemic inflammatory response (Duray, 1989; Salazar *et al*., 2003; Jones *et al*., 2008; Strle *et al*., 2009), which is thought to be the resposible for Lyme disease clinical manifestations. Therefore, immune system activation could induce a damage response leading to demyelination in nervous system. Thus, we wanted to examine whether Bb could directly enhance the expression of pro-inflammatory cytokines in Schwann cells, in the absence of immune cells. For that purpose, we analyzed TNF levels in supernatant of Bb-infected Schwann cells after 6 h to 48 h by ELISA. We did not observe significant differences in Bb-stimulated or unstimulated cells (**Figure 49 A**). Notably, we still did not observe any differences in TNF levels when the supernatants of Bb-infected Schwann cells at 24 h were concentrated (**Figure 49 B**). We also analyzed mRNA levels of different cytokines, which have been previously observed to be induced in the presence of Bb in DRG cultures in the animal model of Lyme neuroborreliosis, rhesus macaque, and human Schwann cell lines (Ramesh *et al*., 2015a,b). RT-qPCR confirmed no induction of *IL-1β*, *IL-6* and *TNF* cytokines expression in the presence of Bb (**Figure 49 C**). Strikingly, MPZ levels did not decrease after TNF addition to

purified, myelinated Schwann cell cultures, further showing that TNF cannot induce demyelination (**Figure 49 D**).

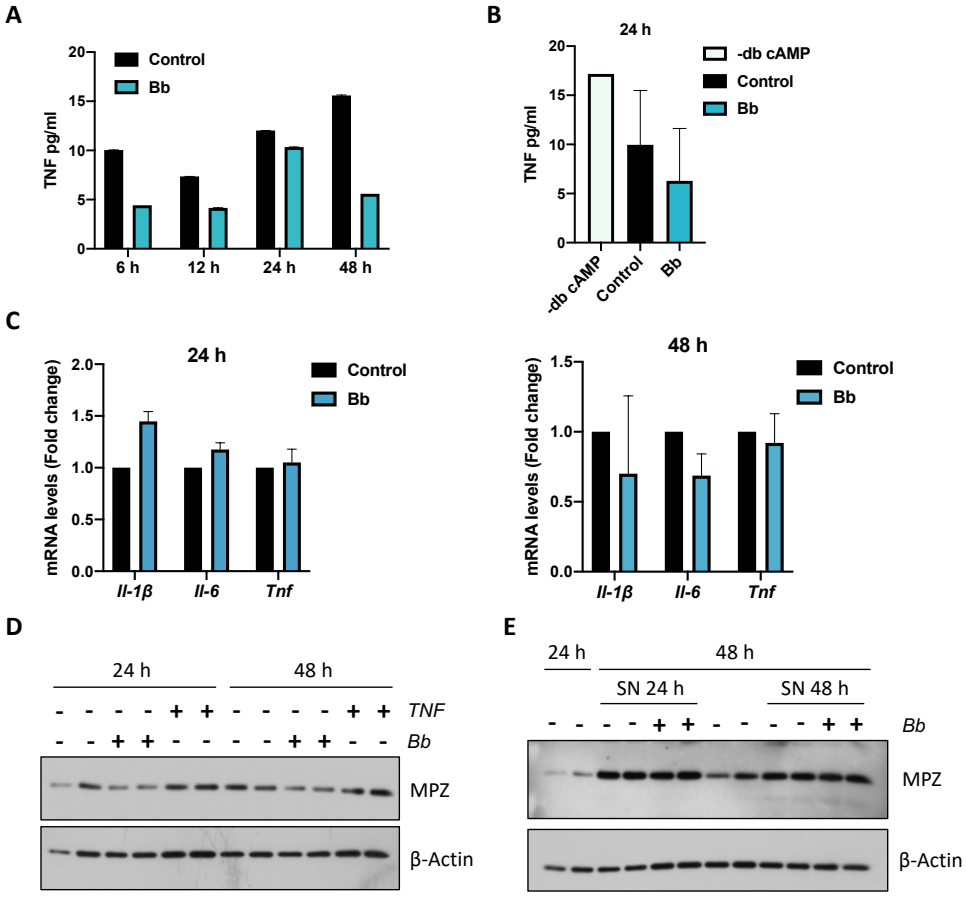

Figure 49. *B. burgdorferi* does not induce cytokine-mediated demyelination in Schwann cells. A) TNF expression analyzed by ELISA in control (black) and Schwann cells after 6 h to 48 h of *B. burgdorferi* (Bb) infection (blue). **B)** TNF expression analysis in Schwann cells cultured without db cAMP (green), control Schwann cells without Bb (black) or Bb-treated Schwann cells (blue), cultured in half of the volume of A) for 24 h since Bb addition. **C)** *IL-1ß, IL-6 and Tnf* expression in control Schwann cells (black) and Bb-stimulated Schwann cells (blue) after 24 h and 48 h of Bb addition. **D)** MPZ levels are shown in a representative Western blot of Schwann cells cultured in the absence or presence of TNF or with Bb, as a positive control of demyelination. **E)** Western blot showing MPZ levels in Schwann cells cultured in normal myelinated conditions, with supernatant from Bb-infected Schwann cell cultures, after bacterial removal from supernatant, or with supernatant from Schwann cells cultured without Bb 48 h before. Technical duplicates are shown in western blots. Data are presented as mean ± SEM; n=3 independent experiments.

Although Bb does not produce toxins (Strle *et al*., 2009) that could, in part, promote the observed demyelination, we wanted to further confirm that the demyelination was not due to the secretion of factors by Schwann cells induced by Bb, we next treated *in vitro* myelinated Schwann cells for 24 h and 48 h with supernatant of unstimulated or Bb-stimulated Schwann cells for 48 h. We did not find any decrease in MPZ levels in Schwann cells cultured with previously Bb-infected Schwann cells' supernatant, even after 48 h of incubation (**Figure 49 E**), which suggests demyelination observed in Schwann cells after Bb stimulation is due to a direct

recognition of the bacteria by Schwann cells rather than the production of compounds in the medium.

Overall, our results show that *B. burgdorferi*-induced demyelination in Schwann cells is not mediated neither by an immune response nor by the production of demyelination-inducing factors in the medium by the pathogen or Schwann cells, supporting the suggestion that a direct recognition of *B. burgdorferi* by Schwann cells (and direct binding of the membrane lipoproteins or intracelluar pieces of the bacteria to the surface of Schwann cells) induces demyelination.

3.2. *Borrelia burgdorferi* does not induce apoptosis in Schwann cells

Cell death, such as apoptosis or programmed cell death, is an intrinsic response used as a defense mechanism against microbial infections (Zitvogel *et al.,* 2010). In this sense, Bb can induce apoptosis in DRG cultures (Ramesh *et al*., 2013). So, we next wanted to determine whether Bb might induce apoptosis in Schwann cells. We did not find neither Tunel+ cells (**Figure 50 A**) nor Caspase-3+ cells (**Figure 50 B**) after Bb treatment of Schwann cells.

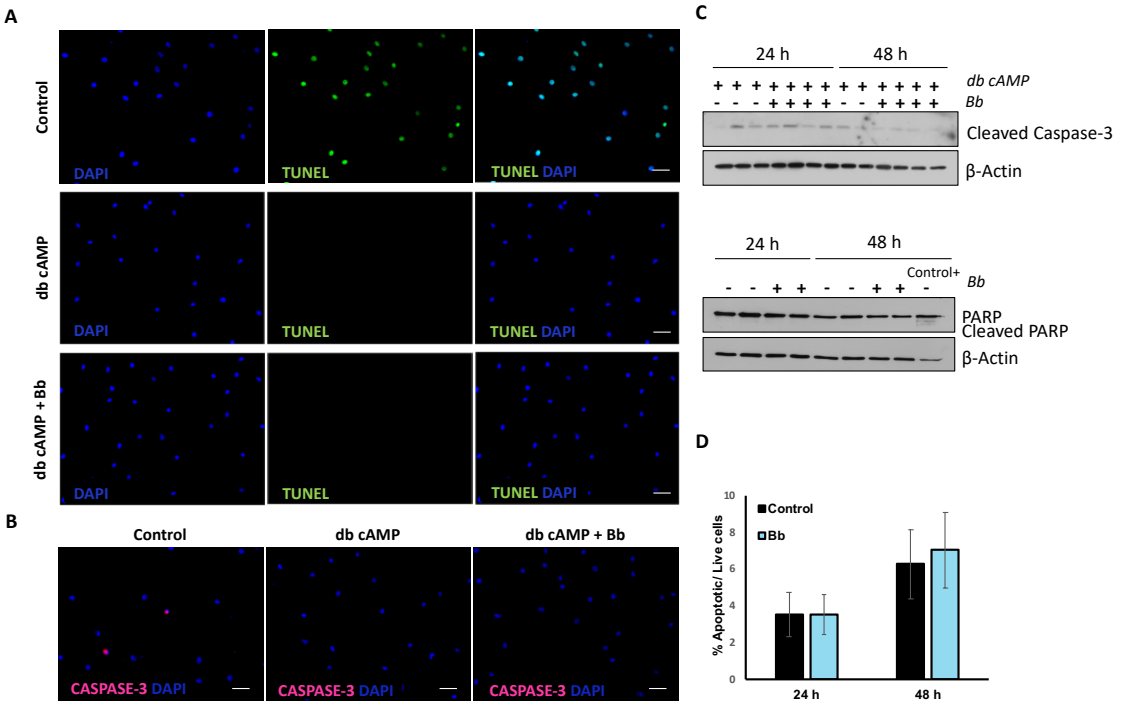

Figure 50. *B. burgdorferi* does not induce apoptosis in Schwann cells. A) TUNEL assay confirming DNA strand breaks (green) in DNase treated control Schwann cells, compared to Schwann cells cultured with or without *B. burgdorferi* (Bb) after 48 h. **B)** Caspase-3 expression is shown by ICC represented in pink in control Schwann cells, treated for 3 min at 65 °C. Caspase-3, compared to Schwann cells with or without Bb after 48 h. **C)** Western blot showing apoptosis markers Cleaved-Caspase3 and Cleaved-PARP, in control Schwann cells (without Bb) and Bb-stimulated Schwann cells, with no differences in proteins levels at 24 h and 48 h of pathogen exposition. **D)** Annexin-V showing percentage of apoptotic cells in control Schwann cells (black) or upon Bb stimulation (blue). Scale bar, 50 µm. Data are presented as mean ± SEM; n=3-4 independent experiments.

Accordingly, Western blot nalysis did not show any increase in the apoptosis markers Cleaved-PARP and Cleaved Caspase-3 showed upon Bb stimulus (**Figure 50 C**). In line with this, there were no differences in Annexin-V+ cells, as shown by flow cytometry assay, in control and Bb-treated Schwann cells at 24 h and 48 h after infection (**Figure 50 D**).

These results show that Bb cannot induce apoptosis in Schwann cells, which suggest that apoptosis cannot be the responsible mechanism for the observed demyelination.

3.3. *Borrelia burgdorferi* does not induce dedifferentiation of myelinated Schwann cells

Schwann cells are highly plastic cells that can undergo a switch in their phenotypic identity in response to a number of insults, including nerve injury or bacterial infection, which leads to a transdifferentiation of mature Schwann cells into repair Schwann cells (see chapter 1, section 2.4). This change includes loss of the myelinating phenotype and increase in proliferation rate (Jessen and Mirsky, 2019b). Thus, we analyzed Schwann cells proliferation after Bb infection and supresingly, Bb had no effect on proliferation of Schwann cells, as shown by EdU incorporation assay (**Figure 51 A**).

A number of key regulators drive Schwann cells transdifferentiation after a nerve insult, including the transcription factors c-Jun (Arthur-Farraj *et al.* 2012) and SOX2 (Roberts *et al*., 2017) have been identified. Surprisingly, we did not find any effect of Bb on the expression of c-Jun and SOX2 proteins while, as expected, MPZ levels were decreased upon Bb stimulation in db-cAMP-treated Schwann cells after 24 h and 48 h of Bb infection (**Figure 51 B**). Furthermore, RT-qPCR analysis showed no induction of *c-Jun* mRNA levels in the presence of Bb, which is the initial transcription factor engaged and activated after an insult to the nerve. (**Figure 51 C**). Similarly, we did not find any effect of Bb on expression of HuR, a marker of immature Schwann cells (Iruarrizaga-Lejarreta *et al*., 2012) (see chapter2) (**Figure 51 D**).

These results remark *B. burgdorferi* induced demyelination as specific and active response affecting myelinated Schwann cells, but without any effect on Schwann cells dedifferentiation.

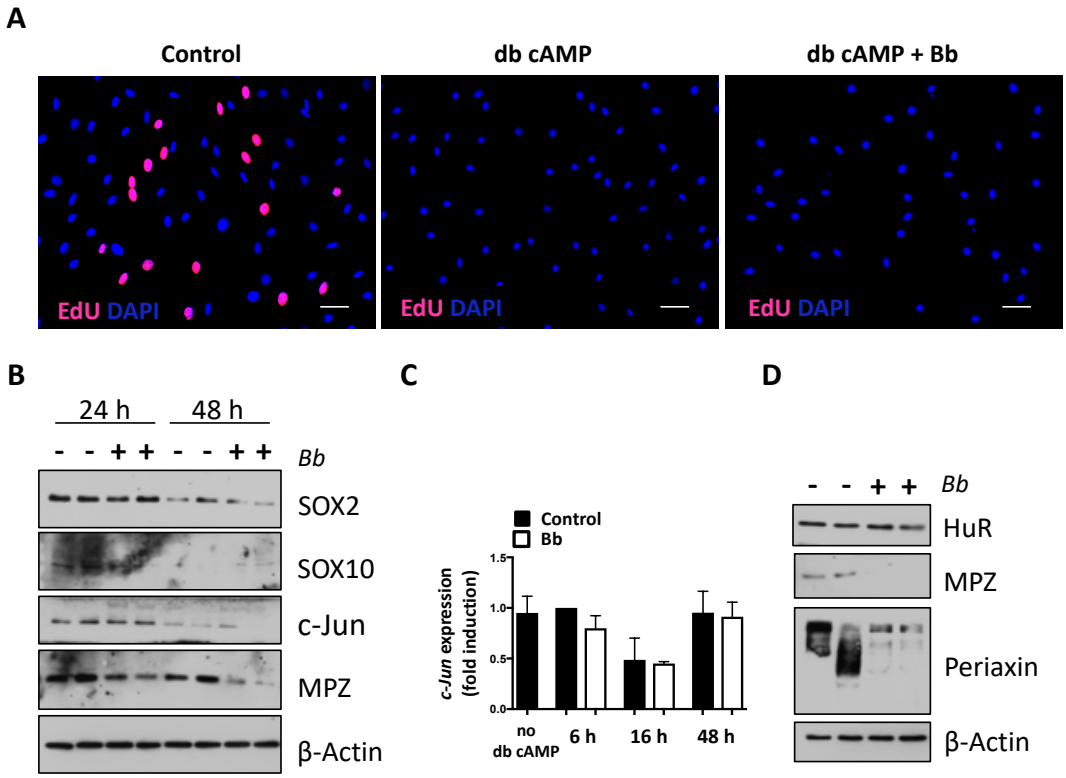

Figure 51. *B. burgdorferi* does not induce dedifferentiation in Schwann cells. A) Proliferation is shown by EdU incorporation into DNA (pink) in control Schwann cells, cultured in expansion medium and db cAMP-treated Schwann cells with or without *B. burgdorferi* (Bb) for 48 h. DAPI was used for DNA staining. Scale bar, 50 µm. **B)** Representative Western blot showing no change in expression of the negative regulators of myelination SOX2 and c-Jun by Bb at 24 h and 48 h. Technical duplicates are shown. **C)** *c-Jun* expression (one of the initial activators of demyelination response) in control Schwann cells and after 6h - 48h of Bb stimulation, shown by RT-qPCR. **D)** Representative Western blot of the immature Schwann cell marker, HuR, and downregulation of myelin structural proteins, MPZ and Periaxin, in Schwann cells cultured in the absence or presence of Bb for 48 h. technical duplicates are pointed out in the western blot. Representative results of at least 3 independent experiments are shown. Data are presented as mean ± SEM; n=3-4 independent experiments.

3.4. *Borrelia burgdorferi* leads to Wnt/β-Catenin deregulation in Schwann cells

3.4.1. Proteomics analysis identifies deregulation of cell-adhesion and WNT/β-Catenin pathway in *Borrelia burgdorferi*-infected Schwann cells

To get better insight of the downstream pathways regulated by Bb, we perfomed a proteomics analysis of control and Bb-infected Schwann cells, and identified 103 downregulated proteins and 90 upregulated proteins (**Figure 52 A**) by Bb treatment. Gene Ontology analysis show that categories related to ribosomes and cell-adhesion were the most deregulated categories (**Figure 52 B**), with almost all proteins implicated in these categories were downregulated after Bb-stimulation. This suggested that translation could be affected by Bb, and we confirmed this by showing decreased nascent proteins production using OP-puro incorporation (**Figure 52 C**).

Interestingly, β-Catenin and N-Myc downstream regulated gene (NDRG1) were the most downregulated proteins in the presence of the pathogen (**Figure 52 B**).

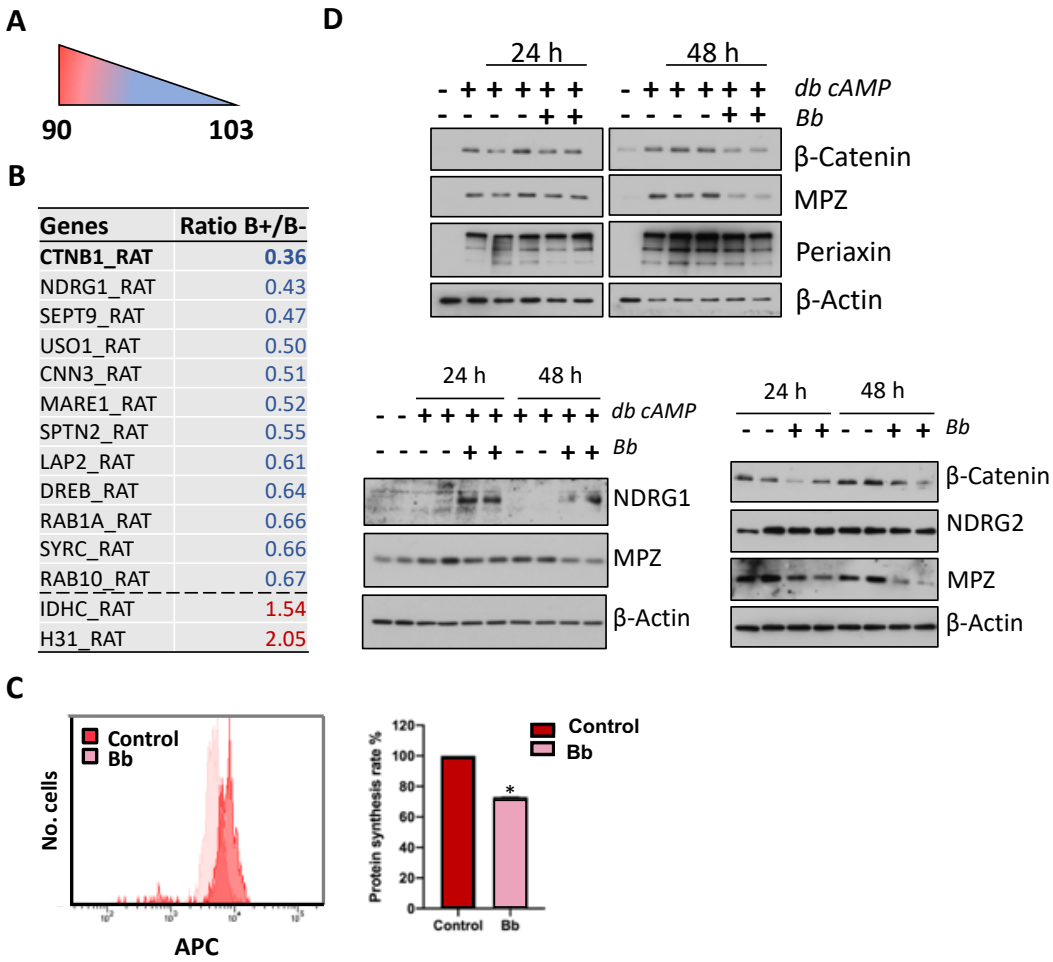

Figure 52. *B. burgdorferi* induces demyelination by regulating β-Catenin in Schwann cells. A) Proteomic analysis reveals 90 upregulated and 103 downregulated rat proteins (FC >1.5, P <0.05) after *B. burgdorferi* (Bb)-stimulation in Schwann cells. **B)** Gene Ontology Biological Processes identifies cell-adhesion as the most deregulated category in Bb-stimulated Schwann cells (FC >1.5, P <0.05). **C)** Representative image of a decrease in nascent protein synthesis after Bb-stimulation (pink) compared to control Schwann cells (red). **D)** Representative western blots showing a decrease in β-Catenin levels but not of the levels of other deregulated proteins observed in proteomic analysis (NDRG1 and NDRG2) after Bb infection at 24 h and 48 h, following 48 h of db cAMP treatment. Technical duplicates are shown. MPZ and PERIAXIN levels are used as confirmation of Bb induced demyelination. SEM is represented as error bar. Two-tailed unpaired Student's t-test was used for statistics, *p< 0.05.

In line with this, both β-Catenin and NDRG1, have been linked to myelin development, since Ndrg1-deficient mice show demyelination in peripheral nerves (King *et al*., 2011) and mutations in *Ndrg1* gene cause Charcot-Marie-tooth disease type 4D (CMT4D) demyelinating neuropathy (Okuda *et al.,* 2004) and β-Catenin has been in turn, implicated in axonal sorting (Gregoryan *et al*., 2013). We confirmed by western blot a decrease in β-Catenin levels after Bb-infection in Schwann cells, but we did not observe any major effect in other deregulated proteins such as

NDRG1 and its family member NDRG2, which in fact, is a negative regulator of β-Catenin (**Figure 52 D**).

Our results suggest *B. burgdorferi*-induced demyelination in Schwann cells could be due to a deregulation of the β-Catenin signaling pathway.

3.4.2. RNA-seq identifies Wnt/β-Catenin deregulation in *Borrelia burgdorferi*-infected Schwann cells

We next used RNA sequencing (RNA-seq) to examine how Bb infection influenced the transcriptional landscape of Schwann cells, and determine whether translational changes observed in proteomics analyses was the result of a direct deregulation in transcription. Principal component analysis (PCA) (**Figure 53 A**) and sample distance matrix (**Figure 53 B**) showed a clear transcriptional signature derived from Schwann cells exposure to the spirochete. A total of 37 genes were upregulated and 31 were downregulated when applying cut-off values of 2 fold induction (absolute value of Log2 ratio 1) and a p value of 0.05 (**Figure 53 C**). We observed a significant overlap between the Bb-induced deregulated targets previously identified by proteomics and the RNA-seq analysis. Heatmap of 50 most deregulated genes after Bb-stimulation in Schwann cells, showed downregulation of genes encoding myelin structural proteins (*Periaxin*, *Pmp22*, *MPZ* and *Mag*) and enzymes involved in biosynthesis of myelin lipids (*Utg8*) and fatty acids (*Fasn, Scd4*), gene products related with formation of nodes of Ranvier (*Gldn*) and genes linked to immune system activation (*Il-16*, *Il-34*). In line with proteomics analysis, downregulation of cell-adhesion related genes (*Cadm3*, *Cldn19* and *Thbs4*) was observed (**Figure 53 D**). Overall, among 1376 downregulated genes after Bb exposition, a large number of genes were involved in cell communication (229), axon escheatment (34), myelination (34), myelin assembly (10), among others. On the other hand, among 1139 upregulated genes in the presence of the pathogen in Schwann cells, 80 genes were related with cell migration, 50 were linked to regulation of cytokine production [e.g. NF-kappa-B (*NF-κB*) inhibitor-like protein 1, macrophage migration inhibitory factor (*Mif*)], among others [Panther database (http://www.pantherdb.org). Interestingly, RNA-seq showed *Wnt-5a* upregulation after Bb-stimulation in Schwann cells (**Figure 53 D**). Depending on the receptor context, Wnt-5a could act as an inducer or repressor of canonical Wnt pathway. In the presence of FZD4 Wnt5a activates β-catenin signaling, while Wnt5a acts as inhibitor of β-Catenin with ROR2 receptor, promoting β-Catenin degradation. It has also been shown that Wnt5a inhibits myelin formation in DRG-Schwann cell cocultures and delays remyelination in the subventricular zone of the adult

brain (Chavali *et al.,* 2018). So, this observation suggests that *Wnt-5a* could be inducing β-Catenin degradation in a Bb scenario.

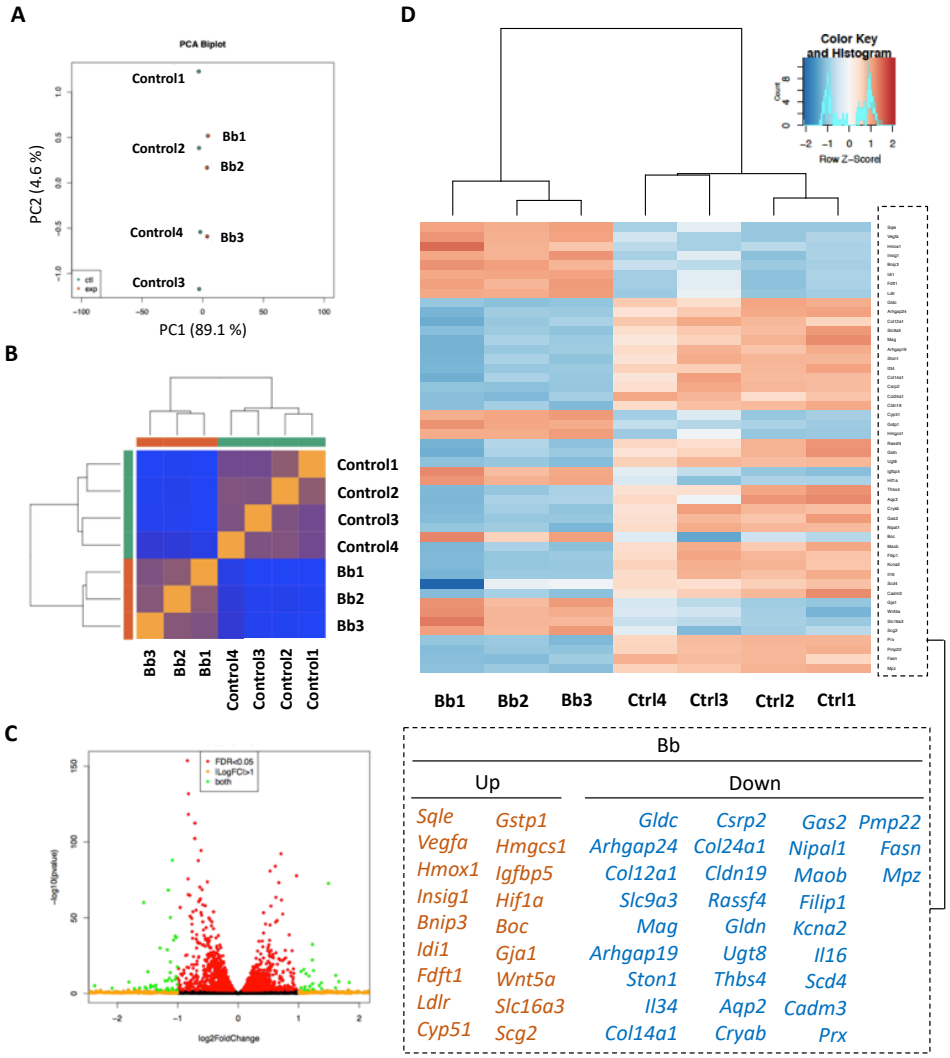

Figure 53. RNA-seq analysis shows altered transcriptomic profile of Schwann cells after *B. burgdorferi* stimulation. A) Principal component analysis of control Schwann cells (green circles) and Schwann cells stimulated with *B. burgdorferi* (Bb) (orange circles). **B)** Sample distance matrix of control and Bb-stimulated Schwann cells. **C)** Volcano plot showing downregulated genes (left red circles) and upregulated genes (right red circles), p <0.05. Green circles represent genes both p <0.05 and FC <1. Orange circles only represent genes FC <1 and black genes do not pass any cutting range. **D)** Heat map showing the most 50 deregulated genes (most of them linked to cell-adhesion, myelin lipid biosynthesis, myelin structural proteins) in response to Bb-stimulation of Schwann cells after 48 h, compared to unstimulated Schwann cells.

These results strongly suggest a downregulation of cell-adhesion related genes after *B. burgdorferi* infection and links the Wnt/β-Catenin pathway to *B. burgdorferi*-induced demyelination, involving β-Catenin degradation by *Wnt-5a* upregulation. Further work is required to confirm these results.

3.5. *Borrelia burgdorferi* induces proteasomal and autophagy-mediated degradation of myelin proteins in Schwann cells

As mentioned above, myelin breakdown is a universal response to several conditions, such as microbial infections or nerve injury. We previously described that after nerve injury, Schwann cells initially digest their myelin by a novel form of selective autophagy, a process we termed myelinophagy (Gomez-Sanchez *et al*., 2015). Thus, we wanted to examine whether autophagy was also involved in Bb-induced myelin breakdown.

To monitor autophagy activation in vitro, we used a simple culture system, called the autophagy flux assay (REF: Miguel book chapter) that we previously employed to demonstrate myelinophagy (Gomez-Sanchez *et al*., 2015). Autophagic flux is inferred on the basis of turnover of a key autophagosomal protein, called LC3 II in the presence and absence of lysosomal degradation. Thus, we analyzed levels of LC3II levels in the absence or presence of 20 mM of autophagy inhibitor ammonium chloride (NH_4Cl) and 100 µM of the protease inhibitor Leupeptin at different time exposures (4 h, 24 h or 48 h before protein extraction). Surprisingly, autophagy was not seem to be hyperactivated after Bb-stimulation in Schwann cells, compared to their unstimulated counterparts. Furthermore, MPZ and Krox20 levels did not increase after 4 h of autophagy inhibition at 24 h or 48 h of Bb infection. However, MPZ levels slightly recovered when inhibitor addition and pathogen were simultaneously added. In contrast, Periaxin levels were recovered in the presence of autophagy inhibitor just at 4 h before protein extraction, after 24 h and 48 h of Bb infection (**Figure 54 A**).

We next examined whether the decrease of MPZ levels by Bb could be also mediated by proteasomal degradation. For this, we compared Bb-stimulated Schwann cells to the control samples (without pathogen) in the absence or presence of the proteasomal inhibitor MG132 at different time exposures (4 h or 16 h before protein extraction) and analyzed MPZ levels after 24 h and 48 h, as well as general ubiquitination smear, in order to confirm drug effectiveness. We could observe a slight recovery in MPZ levels after 16 h of MG132 treatment in d Schwann cells infected with Bb (**Figure 54 B**).

Overall, these data suggest degradation of myelin proteins in the presence of *B. burgdorferi* could be indeed mediated by proteasomal pathway either by autophagy, depending on the myelin protein.

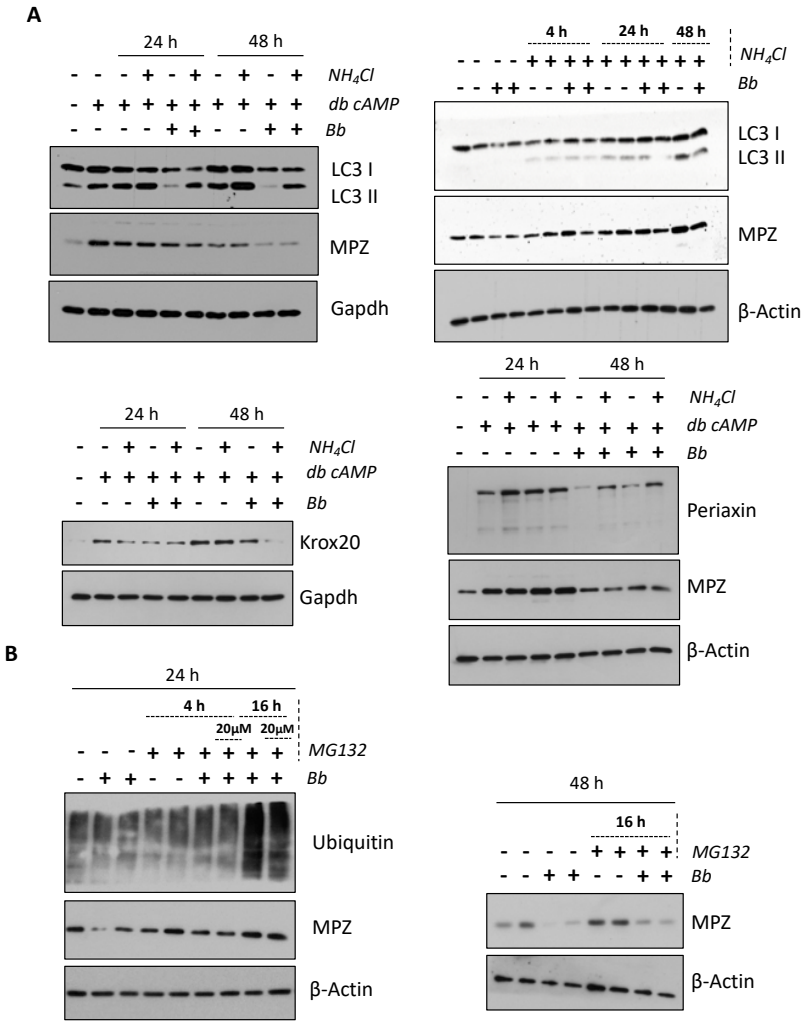

Figure 54. Proteasomal and autophagy-induced degradation of myelin proteins after *B. burgdorferi* infection. A) Autophagy activation, shown by western blot of LC3II levels, as well as MPZ, Krox20 and Periaxin myelin protein levels, after vehicle (H_2O) or 20 mM NH_4Cl (+100 μM Leupeptin) addition for 4 h (24 h or 48 h of inhibitor exposure is specified), before 24 h or 48 h of protein extraction in control and *B. burgdorferi* (Bb)-stimulated Schwann cells. **B)** Myelin structural protein MPZ levels after 24 h and 48 h of Bb-stimulation, compared to control Schwann cells (without bacteria) after vehicle (DMSO) or 10 μM of MG132 (samples with 20 μM are specified) proteasomal inhibitor addition for 4 h or 16 h.

4. β-Catenin overexpression rescues MPZ levels

Our data indicate that Bb-induced downregulation of β-Catenin could be mediating myelin-related proteins degradation. To confirm these results, we examined the capacity of ectopically expressing a degradation-resistant form of β-Catenin to abrogate the effects of Bb on Schwann cells demyelination. We found that constitutive expression of the β-Catenin mutants was able to block the downregulation of MPZ induced by Bb. Interestingly, MPZ levels were highly increased after *β-Catenin* overexpression in both control (without pathogen) and in the presence of Bb compared to their respective empty vector (pcw107-EV), as shown in a representative western blot (**Figure 55**).

This result suggests that β-Catenin is a key downstream node that mediates the effects of Bb on Schwann cell demyelination.

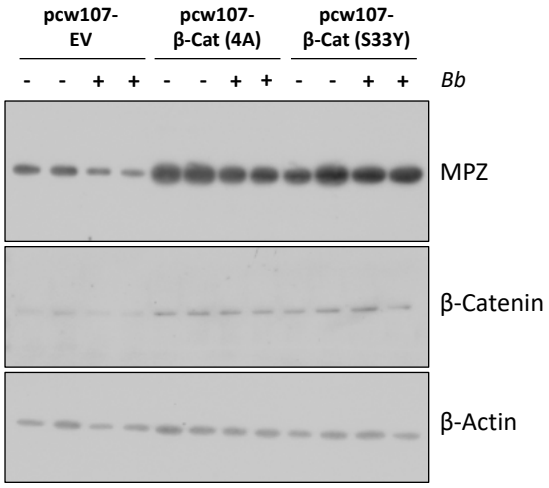

Figure 55. Ectopic expression of β-Catenin rescues demyelination induced by *B.burgdorferi*. Western blot showing MPZ and β-Catenin protein levels in lentivirus-based expression of constitutively active β-Catenin 4A and β-Catenin S33Y mutants or their respective control, the empty vector (pcw107-EV), in the presence of *B. burgdorferi* (Bb) or in the absence of pathogen for 48 h. Similar results were obtained in Schwann cells transduced 3 different times, and representative western blot is showing.

5. *Borrelia burgdorferi* inhibits myelin formation in Schwann cells

Next, we examined the role of Bb in myelination, and for this we compared db cAMP-treated Schwann cells (control samples) with Schwann cells treated with db cAMP and pathogen simultaneously and analyzed the expression of myelin related genes and induction of the corresponding proteins by RT-qPCR and Western blot, respectively (**Figure 56**). Notably, we found that Bb also inhibited myelination *in vitro*, in addition to myelin degradation as shown above. We found that Bb suppressed the increase in levels of the myelin structural proteins MPZ and Periaxin, and the Krox20 transcription factor, typically seen with db cAMP treatment (**Figure 56 A**). Furthermore, Bb did not affect c-Jun levels, shown by protein levels and gene expression (**Figure 56 A, B)**, again showing that Bb-mediated effects were irrespective of c-Jun. Genes encoding myelin structural proteins (*Mbp, Mpz, Pmp22*) and Krox20 transcription factor were downregulated in Bb-infected Schwann cells (**Figure 56 B**).

These results demostrate that *B. burgdorferi* can prevent upregulation of myelin-related genes in the *in vitro* myelination assay, in addition to inducing myelin breakdown, which could have a role in suppressing nerves regeneration and recovery of nervous system observed in patients.

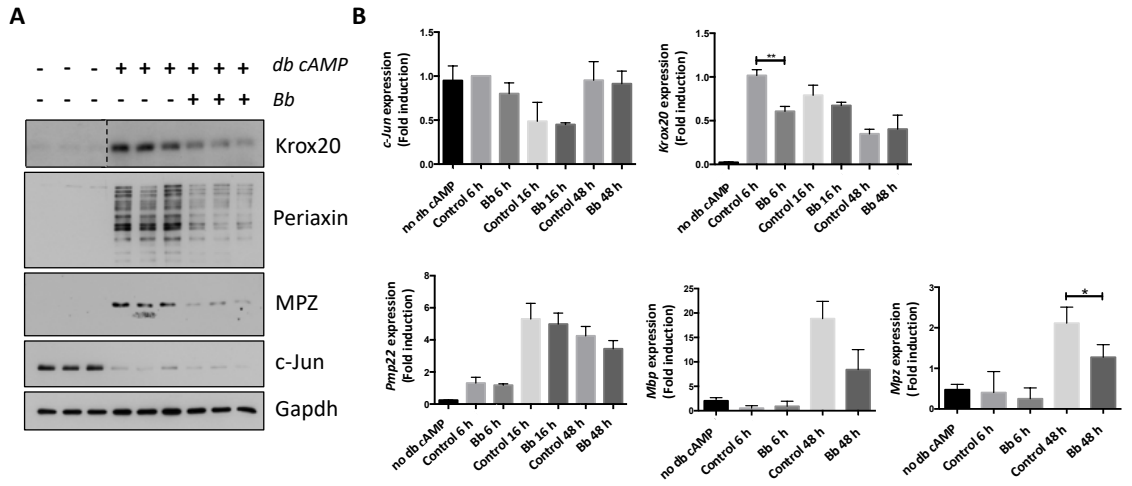

Figure 56. *B. burgdorferi* inhibits myelin formation in Schwann cells. A) Representative Western blots showing myelin related protein levels at 48 h in myelinated Schwann cells (after db cAMP treatment) or Schwann cells treated with *B. burgdorferi* (Bb) and db cAMP at the same time. **B)** Expression of myelin related transcription factors (negative regulator *c-Jun* and positive regulator *Krox20*) and genes encoding structural proteins (*Pmp22*, *Mbp* and *Mpz*) in control Schwann cells (treated with db cAMP) and Schwann cells treated with db cAMP together with Bb pathogen from 6 h to 48 h. SEM is represented as error bars. *p< 0.05, **p< 0.01.

6. Demyelination in Schwann cells cannot be induced by all type of microorganisms

We next wanted to ascertain whether Schwann cell demyelination was specific to Bb infection or whether other types of bacteria could also promote similar responses. For that purpose, we cultured Schwann cells with different symbiotic bacteria (bacilli shaped *Lactobacillus plantarum*-WT, *L. plantarum*-GFP, *L. plantarum*-Cherry, *L. casei* and *L. rhamnosus*) and pathogenic bacteria (bacilli shaped intracellular *Mycobacterium tuberculosis)* for 48 h and compared their effect with different Bb strains previously described (Bb297 used for all other assays and Bb clone B31, named as Bb31). Interestingly, we did not observe any decrease in MPZ levels in the presence of these other bacteria, whereas Bb297 lead to a remarkable decrease in MPZ levels, as observed previously. A minor effect was observed in the presence of Bb31, likely due to variation in the expression of the major virulence factor OspC, expression (Xiang *et al*., 2017) (**Figure 57 A**). We could not test the effect of other pathogens in Schwann cells, such as Gram-negative *Acinetobacter baumannii* and Gram-positive *Rhodococcus equi*, because we could not grow them for more than 6 h in Schwann cell cultures, even with a MOI of 0.5, because of the fast growth of the pathogens (data not shown).

Once we observed that these bacteria could not trigger demyelination in Schwann cells (cultures depleted of immune cells), we checked the viability to analyze if the result showed here could be due to death of bacteria. For that, we took 100 µl directly from the supernatant of Schwann cells cultured in the presence of *L. plantarum*-WT and *L. plantarum*-GFP for 48 h,

the bacteria taxa initially used. Interestingly, *L. plantarum* cultures in optimal medium MRS, showed live bacteria at the end of the assay (**Figure 57 B**), that the lack of effect on Schwann cells was not due to the death of the bacteria. We reasoned that the absence of demyelination after Schwann cells stimulation with different type of bacteria might be related to the incapacity of these bacteria to bind to Schwann cells. To further analyze bacteria binding, we used flow cytometry assay of Schwann cells stimulated with *L. plantarum*-GFP or *L. plantarum*-Cherry. Representative flow cytometry images showed no detectable binding of these bacteria to Schwann cells (**Figure 57 C**).

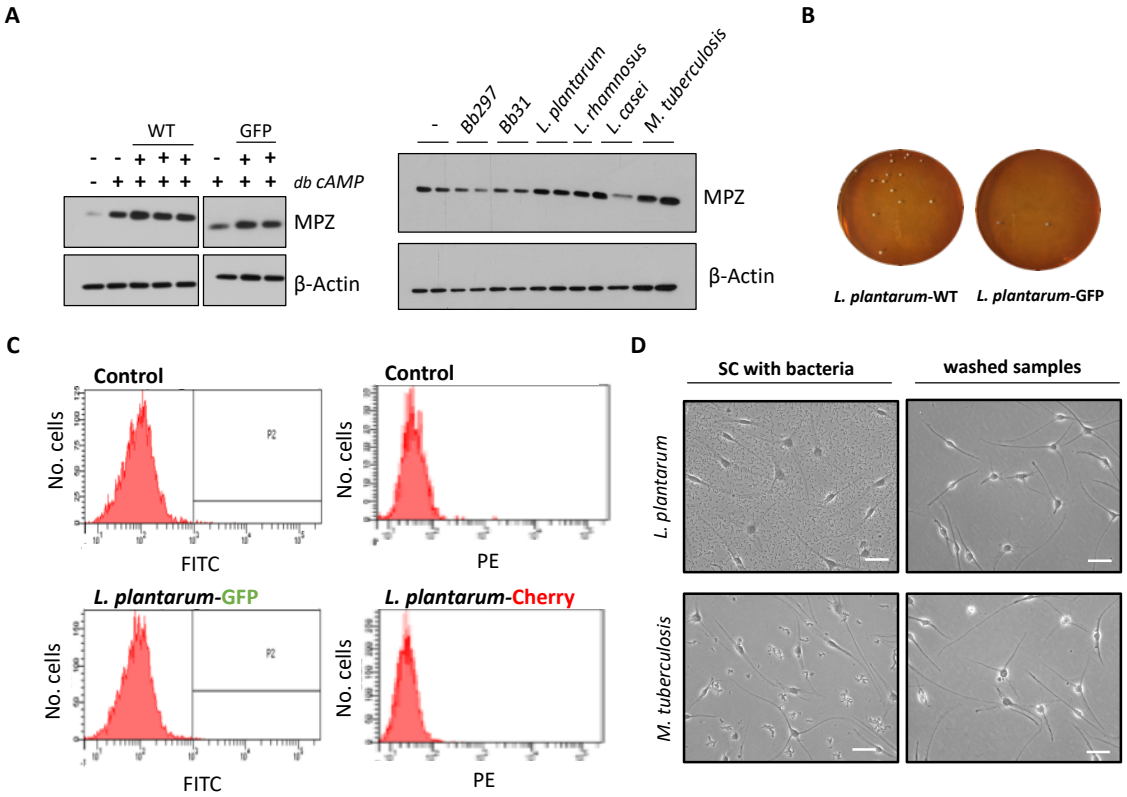

Figure 57. Schwann cells demyelination is specific to *B. burgdorferi*. A) MPZ levels are shown in representative western blots at 48 h of absence or presence of different bateria (*L. plantarum*-WT and -GFP, *L. rhamnosus*, *L. casei* and *M. tuberculosis*, and demyelination positive controls with *B. burgdorferi* (Bb297 and Bb31). **B)** WT- and GFP-*L. plantarum* were cultured to study viability after growing for 48 h with Schwann cells, taken from the culture supernatant. **C)** Flow cytometry analysis is shown of Schwann cells, cultured in the absence or presence of GFP- and Cherry- *L. plantarum.* **D)** Phase contrast images showing Schwann cells, cultured with *L. plantarum* or *M. tuberculosis* (left panel) and after washing samples (right panel). Scale bar, 50 µm.

Furthermore, we could not see any bacteria remaining in the culture dishes of Schwann cells stimulated with *L. plantarum* or *M. tuberculosis*, after several washes (before protein extraction for western blot) with phase contract microscopy (**Figure 57 D**).

These results show the remarkable potential role of *B. burgdorferi* to induce Schwann cells demyelination, an effect that seems specific to this bacterium.

Discussion

Discussion

Myelinating Schwann cells, the main glial cells of peripheral nervous system (PNS), can be easily destabilized in response to several pathological conditions, which can lead to myelin breakdown. One of the most fascinating examples is microbial infection, including *Mycobacterium leprae,* whereby the bacteria adhere to Schwann cells and are subsequently internalized, inducing demyelination (Rambukkana *et al*., 2002). Myelin digestion can also be induced indirectly by an immune attack promoted by viral particles as it has been observed in HIV infected patients (Parry, 1988; Morgello, 2018). Myelin disturbances are the consequences of peripheral neuropathies which result in muscle weakness, numbness and paralysis, among others (Kamil *et al*., 2019). These clinical manifestations have been observed in up to 15 % of Lyme disease cases. Although research in the last decades has shed some light on the pathophysiology of the disease, PNS involvement is still the most intriguing feature of Lyme neuroborreliosis. Moreover, nervous system damage, as well as the rest of the clinical manifestations of Lyme disease are widely thought to be an indirect response of the host immune system activation against the pathogen. Even so, peripheral demyelination in Lyme disease is still poorly defined.

In this chapter of the thesis, we present evidence that Schwann cells are direct targets of *Borrelia burgdorferi* (Bb), the causative agent of Lyme disease. Here, we optimized an *in vitro* Schwann cell myelination assay (Sobue and Pleasure, 1984) by addition of N^6,2′-O-dibutyryladenosine 3′,5′-cyclic monophosphate sodium salt, cell-permeable and non-hydrolyzable cAMP analogue (db cAMP) in purified Schwann cells, which enabled us study direct interaction of the pathogen with myelinated Schwann cells. We find that live Bb binds directly to Schwann cells' surface leading to myelin breakdown. Moreover, pathogen binding to Schwann cells increases in a time-dependent manner, but it cannot be internalized, in line with previous works concerning extracellular Bb infection of non-phagocytic cells (Schwarzova *et al*., 2019). Live Bb, as well as non-viable bacteria, can induce similar response in oligodendrocytes, the Schwann cells counterparts of central nervous system (Parthasarathy *et al*., 2013). We show here that metabolically inactive Bb (heat-inactivated), as well as pathogen residues obtained from sonication are recognized by Schwann cells, which also induces demyelination, similar to thus seen in the presence of live bacteria. However, a higher number of sonicated spirochetes is needed to induce a similar effect as live Bb on expression of MPZ, likely because of a breakdown of virulence factors induced by fragmentation of the pathogen after sonication (**Figure 58**). Overall, these facts show that Schwann cells can recognize not only Bb surface lipoproteins, but also intracellular components or membrane pieces of Bb (obtained after

sonication), leading, in turn, to demyelination. Even though we found a similar response leading to demyelination in the presence of metabolically inactive or sonicated bacteria, a mayor effect is seen after the addition of live Bb. Furthermore, it is known that Bb is auxotroph for all the amino acids, which makes bacteria dependent on host nutrients (Gherardini *et al*., 2010; Stanek *et al*., 2012). Nonetheless, we have confirmed that demyelination in the presence of Bb is due to a direct recognition of the pathogen by the cells and it is not, in part, due to a possible digestion by Bb of Schwann cells' nutrients or essential components of myelination medium. Normal levels of MPZ structural protein are seen when Schwann cells are infected with supernatant of previously infected Schwann cells, following pathogen removal. So, the mayor effect observed in the presence of live Bb is likely due to a higher number of accessible surface lipoproteins, when bacteria is not fragmented, making easier the binding of several receptors (**Figure 58**).

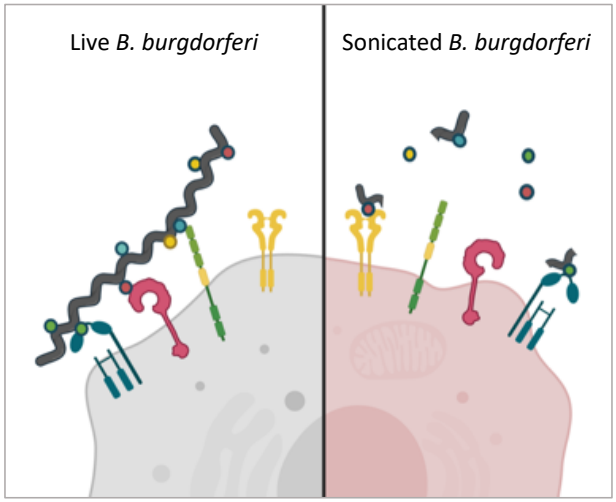

Figure 58. Recognition of live and sonicated *B. burgdorferi* by Schwann cells. Schwann cells can recognize live spirochetes, as well as *B. burgdorferi* fractions obtained after sonication. Nonetheless adherence of live bacteria induces a mayor decrease in MPZ levels, likely because of its surface lipoproteins accessibility; once pathogen is recognized by a receptor, it enables binding to neighbor receptors.

Additionally, similar to the demyelination observed in primary Schwann cells, we find a similar damage response in Dorsal root ganglia (DRG) cells and peripheral nerves (sciatic nerves and brachial plexus) in the presence of live Bb, as shown by appearance of myelin ovoids and downregulation of myelin genes, indicating myelin breakdown.

Moreover, here we show Bb also inhibits myelination in non-differentiated Schwann cells, when db cAMP and pathogen are added simultaneously to the cell culture. These observations likely could have a role in the axonal degeneration seen in Lyme neuroborreliosis after years of the disease detection and even after treatment, when spirochetes are undetectable, which in fact, could be the reason of an axonal regenerative failure. We find that Bb also inhibits

myelination in non-differentiated Schwann cells, when db cAMP and pathogen are added simultaneously to the cell culture. These observations clearly show that Bb have a general negative effect on Schwann cell myelination.

Nerve damage leads to dramatic alterations in the architecture and signaling environment of peripheral nerves. Remak (non-myelin) or myelinated Schwann cells, from the distal part of the damage site lose axonal contact and transdifferentiate to a repair phenotype, a process regulated by several key regulators, including c-Jun and SOX2 (Arthur-Farraj *et al*., 2012; Roberts *et al*., 2017). Genes involved in myelin synthesis and maintenance [Krox20 transcription factor, MPZ, MBP and Periaxin structural proteins, myelin associated glycoprotein (MAG)…] are downregulated (Morris *et al*., 1972), among other changes (Jessen and Mirsky, 2019a). We have observed a decrease in myelin-related genes and its corresponding proteins in the presence of Bb, whereas proteins levels of SOX2, c-Jun, are not affected by Bb stimulation. Furthermore, the levels of SOX10 protein, which is expressed in all different Schwann cell phenotypes, do not change in the presence of Bb. After nerve injury, c-Jun is one of the first transcription factors been activated, with an increase in expression within hours of the damage (Gomez-Sanchez *et al*., 2017). Strikingly, we have shown that *c-Jun* mRNA levels are not upregulated even at 6 h of Bb infection up to 48 h of stimulation, suggesting a different molecular pathway might be mediating myelin-associated markers downregulation. Interestingly, we investigated if RNA binding protein (RBP) Human antigen R (HuR) could be dysregulated after Bb stimulus, because RBP are emerging as master regulators in different physiological scenarios, due to the ability to simultaneously control a broad range of pathways. HuR can bind to several mRNA targets and control positively or repressing translation of key components of essential oncogenic and developmental pathways, among others (more information on chapter 2 of this thesis). Previous work from this laboratory identified HuR highly expressed in immature Schwann cells (iSC), a highly proliferative stage, regulating a plethora of mRNA targets implicated in proliferation (Iruarrizaga-Lejarreta et al., 2012). Notably, in denervated axons, Schwann cells proliferate and promote support for axonal growth and next regeneration (Jessen and Mirsky, 2019b). Furthermore, direct microbial infections of Schwann cells may increase proliferation rate (Rambukkana *et al*., 2002; Masaki *et al*., 2013). However, we did not see changes in HuR protein levels upon Bb infection of Schwann cells, as demostratred by western blotting. In line with this, the presence of the pathogen does not lead to an induction in proliferation, as observed by Edu incorporation. So, overall, suggest that the molecular mechanisms involved in injury-induced demyelination are different from Bb-induced demyelination.

In the early stages of the Lyme disease, there is a prompt activation of innate immune system, followed by the activation of the adaptive immune system, leading to a generalized inflammatory response (Duray, 1989; Salazar *et al*., 2003; Jones *et al*., 2008; Strle *et al*., 2009). Furthermore, pro-inflammatory cytokines can be expressed in Schwann cells and DRG-Schwann cell cocultures after contact with pathogens, such as *M. leprae* and Bb (Masaki *et al*., 2013; Ramesh *et al*., 2013). Immune system activation, in turn, can cause axonal damage promoting nervous system demyelination. Unexpectedly, we did not find neither upregulation of *IL-1β*, *IL-6* and *TNF* cytokines transcription upon Bb addition, nor TNF secretion in supernatants of Schwann cells cultured with the spirochetes. These results suggest that the activation of Schwann cells or recognition of the pathogen in the absence of communication or interaction with other activated cells (neurons, macrophages) in a Bb scenario, is not sufficient to trigger expression of immune mediators by Schwann cells. Programmed cell death, apoptosis, is used as a defense mechanism against microbial infections (Zitvogel *et al*., 2010), and could be promoting the observed demyelination. Notably, we did not find activation of apoptosis after Bb stimulus, as shown by an absence of DNA strand breaks, a marker of late apoptosis and, in line with this, there was no increase of apoptosis markers cleaved Caspase-3 and cleaved PARP levels 48 h after Bb infection. This absence of the apoptosis could be a mechanism used by the pathogen to persist in the host, leading to its dissemination and colonization of different tissues observed in mammal's infection. This lack of apoptosis might be due to the absence of immune cells and cytokines expression, as shown by previous work of Ramesh and collaborators, which linked apoptosis of glial and neuronal cells in Lyme disease with the immune activation and cytokines expression observed in the presence of bacteria (Ramesh *et al*., 2013).

Our results show evidence that Schwann cells are a direct target of Bb and the recognition of the pathogen lead to demyelination. Importantly, this is an effect specific to Bb, since other taxonomic bacteria, including *Mycobacterium tuberculosis*, *Lactobacillus platarum*, *L. casei* and L. *rhamnosus* cannot bind to Schwann cells. There was also a distint infection capacity of Bb strains in Schwann cells, both BbB31 (Bb31 hereafter) and Bb297 (Bb, the strain used in all the experiments) promote a decrease in MPZ levels, but Bb31 induces a minor effect compared to the remarkable demyelination observed with Bb297 strain. This difference in Schwann cell response could be due to a variation in the major virulence factor OspC expression or a loss of plasmids between different Bb strains and clones (Xiang *et al.*, 2017). Bb was originally isolated from a Cerebrospinal fluid (CSF) of a patient with Lyme disease, which it means Bb is able to cross blood-brain barrier and may adapt to local and host environment promoting gene expression changes, such as OspC expression, whereas Bb31 was isolated from an *Ixodes* tick, which makes B31 strain less pathogenic for human host and more favorable for tick

environment, as well as, for *in vivo* experiments mimicking natural transmission of the pathogen by a tick.

We find here non-myelinated and db cAMP-myelinated Schwann cells present a similar patron of immune-related surface receptors that have been previously implicated in Bb-adherence, such as, CD64, MR (CD206) and CD14 (Cinco et al., 2001). Additionally, the presence of Bb does not induce an upregulation of CD14, CD64 and MARCO levels, which are present in normal Schwann cells culture conditions. Thus, in addition to Tool like receptors (TLRs), Schwann cells also contain Scavenger receptors (MARCO), c-type lectins (MR), Fc gamma receptors (CD64) and glycosylphosphatidylinositol (GPI)-anchored receptors (CD14), that could play a role in Bb recognition by Schwann cells and subsequent molecular changes inducing demyelination.

Overall, there is a slightly decrease of general transcription in Schwann cells after Bb stimulation, as observed by RNA-seq (1139 upregulated genes against 1375 downregulated genes), in addition to a translational decrease that was confirmed by a decrease in protein synthesis rate, using OP-puro incorporation into nascent proteins. Nonetheless, we show there is also an increase in degradation of myelin-related proteins in the presence of Bb that can be slightly blocked with proteasomal or autophagy inhibitors (depending on the myelin-related protein), which is the mechanism used by Schwann cells to initially digest their own myelin after nerve injury (Gomez-Sanchez *et al*., 2015).

Mechanistically, RNA-seq and proteomics analysis show a dysregulation of Wnt/β-Catenin pathway after Bb infection, wherein Wnt5a is upregulated and β-Catenin transcription factor is downregulated in the presence of the pathogen, and which was confirmed by western blotting. Lentivirus-mediated overexpression lighthly rescue Bb-induced demyelination by increasing MPZ levels in primary Schwann cells. Moreover, Wnt5a can act as an inducer or repressor of canonical Wnt pathway, depending on the receptor context, promoting β-Catenin signaling or degradation. It has also been shown that Wnt5a is upregulated after nerve injury (Wang *et al*., 2015) and moreover, it can inhibit myelin formation in DRG-Schwann cells cocultures and delays remyelination in the subventricular zone of the adult brain (Chavali *et al*., 2018). Hence, it appears *Wnt5a* upregulation could promote β-Catenin downregulation, leading to demyelination in the presence of Bb. Nevertheless, major effort is needed for addressing this hypothesis.

Thus, we propose the following future perspectives to cover unanswered questions and gain a better insight into PNS involvement in Lyme neuroborreliosis.

Future perspectives

 Wnt5a knockdown or antagonists-mediated blocking of Wnt5a [e.g. BOX5 peptide (Jenei *et al*., 2009)] in primary, purified and myelinated Schwann cells before and simultaneously with *B. burgdorferi* addition to try to recover β-Catenin levels and rescue demyelination.

 Search for Schwann cells' receptors implicated in *B. burgdorferi* recognition that would be useful for silencing or pharmacologically blocking them to rescue myelinating Schwann cells phenotype.

 Study proteasomal and autophagic inhibitors in β-Catenin degradation in order to recognize specific protein degradation inhibitors as prospective therapeutic treatments for *B. burgdorferi sensu stricto*-induced PNS-involved Lyme neuroborreliosis.

 Investigate if metabolically inactive, dead or live *B. burgdorferi* recognition by Schwann cells and subsequent demyelination occur through similar molecular mechanisms.

 Analyze Schwann cells migration capacity after *B. burgdorferi* infection, because Wnt5a knockdown reduces migration rate (Linnskog *et al*., 2014; Shimamoto *et al*., 2020) and Wnt5a overexpression leads to Schwann cells migration, which could enable pathogen dissemination and invasion of surrounding cells *in vivo* and evasion of immune system, similar to that observed in the presence of *Mycobacterium leprae* (Masaki *et al*., 2013).

 Investigate whether other *Borrelia* genospecies-induced peripheral nervous system infection is promoted by similar molecular mechanisms.

Conclusions

☑ Direct binding of live *Borrelia burgdorferi* as well as recognition of pathogen fractions by db cAMP-myelinated Schwann cells triggers demyelination in the absence of immune cells and immune inflammation.

☑ Demyelination of Schwann cells in *B. burgdorferi* scenario is due to a downregulation of myelin-related genes expression and degradation of myelin proteins by either proteasome or autophagy.

☑ *B. burgdorferi* infection promotes Wnt/β-Catenin pathway-mediated demyelination.

☑ Schwann cells does not recognize all taxonomic groups of bacteria, and consequently these cannot induce demyelination.

REFERENCES

Abdelmohsen, K., Pullmann, P.Jr., Lal, A., Kim, H.H., Galban, S., Yang, X., Blethrow, J.D., Walker, M., Shubert, J., Gillespie, D.A., Furneaux, H., and Gorospe, M. (2007). Phosphorylation of HuR by Chk2 regulates SIRT1 expression. *Mol Cell*, 25, 543–557.

Abdelmohsen, K., Srikantan, S., Yang, X., Lal, A., Kim, H.H., Kuwano, Y., Galban, S., Becker, K.G., Kamara, D., de Cabo, R., and Gorospe, M. (2009). Ubiquitin-mediated proteolysis of HuR by heat shock. *EMBO J*, 28, 1271–1282.

Abdelmohsen, K., and Gorospe, M. (2010). Posttranscriptional regulation of cancer traits by HuR. *Wiley Interdiscip Rev RNA*, 1, 214–229.

Adameyko, I., Lallemend, F., Aquino, J. B., Pereira, J. A., Topilko, P., Müller, T., Fritz, N., Beljajeva, A., Mochii, M., Liste, I., Usoskin, D., Suter, U., Birchmeier, C., and Ernfors, P. (2009). Schwann cell precursors from nerve innervation are a cellular origin of melanocytes in skin. *Cell*, 139, 366–379.

Alaggio, R., Turrini, R., Boldrin, D., Merlo, A., Gambini, C., Ferrari, A., Dall'igna, P., Coffin, C.M., Martines, A., Bonaldi, L., De Salvo, G.L., Zanovello, P., and Rosato, A. (2013). Survivin expression and prognostic significance in pediatric malignant peripheral nerve sheath tumors (MPNST). *PloS One*, 8, e80456.

Anastas, J.N., and Moon, R.T. (2013). WNT signalling pathways as therapeutic targets in cancer. *Nat Rev Cancer*, 13, 11–26.

Anastasaki, C., and Gutmann, D.H. (2014). Neuronal NF1/RAS regulation of cyclic AMP requires atypical PKC activation. *Hum Mol Genet*, 23, 6712–6721.

Anguita, J., Ramamoorthi, N., Hovius, J. W. R., Das, S., Thomas, V., Persinski, R., Conze, D., Askenase, PW., Rincón, M., Kantor, F. S., Fikrig, E. (2002). Salp15, an *Ixodes scapularis* salivary protein, inhibits $CD4^{+}$T cell activation. *Immunity*, 16, 849–859.

Arthur-Farraj, P., Wanek, K., Hantke, J., Davis, C.M., Jayakar, A., Parkinson, D.B., Mirsky, R., and Jessen, K.R. (2011). Mouse Schwann cells need both NRG1 and cyclic AMP to myelinate. *Glia*, 59, 720–733.

Arthur-Farraj, P.J., Latouche, M., Wilton, D.K., Quintes, S., Chabrol, E., Banerjee, A., Woodhoo, A., Jenkins, B., Rahman, M., Turmaine, M., Wicher, G.K., Mitter, R., Greensmith, L., Behrens, A., Raivich, G., Mirsky, R., and Jessen, K.R. (2012). c-Jun reprograms Schwann cells of injured nerves to generate a repair cell essential for regeneration. *Neuron*, 75, 633–647.

Arthur-Farraj, P.J., Morgan, C.C., Adamowicz, M., Gomez-Sanchez, J.A., Fazal, S.V., Beucher, A., Razzaghi, B., Mirsky, R., Jessen, K.R., and Aitman, T.J. (2017). Changes in the coding and non-coding transcriptome and DNA methylome that define the Schwann cell repair phenotype after nerve injury. *Cell Rep*, 20, 2719–2734.

Asbrink, E., Hederstedt, B., and Hovmark, A. (1984). The spirochetal etiology of erythema chronicum migrans Afzelius. *Acta Derm. Venereol*, 64, 291–295.

Ascension, A.M., Arrospide-Elgarresta, M., Izeta, A., and Arauzo-Bravo, M.J. (2017). NaviSE: superenhancer navigator integrating epigenomics signal algebra. *BMC Bioinformatics*, 18, 296.

Auld, D.S, and Robitaille, R. (2003). Glial cells and neurotransmission: an inclusive view of synaptic function. *Neuron*, 40, 389–400.

Azfelius, A. (1910). Verhandlungen der dermatologischen gesellschaft zu Stockholm, 28 October 1909. *Arch. Derm. Syph*, 101, 404.

Baetas-da-Cruz, W., Alves, L., Pessolani, M.C., Barbosa, H.S., Regnier-Vigouroux, A., Corte-Real, S., and Cavalcante, L.A. (2009). Schwann cells express the macrophage mannose receptor and MHC class II. Do they have a role in antigen presentation? *J Peripher Nerv Syst*, 14, 84–92.

Bannwarth, A. (1941). Chronische lymphocytare meningitis, entzundliche polyneuritis und "rheumatismus". *Arch Psychiatr Nervenkr*, 113, 284–376.

Barbour, A.G., Burgdorfer, W., Hayes, S.F., Péter, O., and Aeschlimann, A. (1983). Isolation of a cultivable spirochete from Ixodes ricinus ticks of Switzerland. *Curr Microbiol*, 8, 123–126.

Barbour, A.G. (1984). Isolation and cultivation of Lyme disease spirochetes. *Yale J Biol Med*, 57, 521–25.

Barbour, A.G and Benach, J.L. (2019). Discovery of the Lyme Disease Agent. *mBio*, 10:e02166–19.

Barrett, P.N., and Portsmouth, D. (2013). The need for a new vaccine against lyme borreliosis. *Expert Rev Vaccines*, 12, 101–3.

Barrette, B., Hébert, M.A., Filali, M., Lafortune, K., Vallières, N., Gowing, G., Julien, J.P., Lacroix, S. (2008). Requirement of myeloid cells for axon regeneration. *J Neurosci*, 28, 9363–9376.

Behera, A.K., Durand, E., Cugini, C., Antonara, S., Bourassa, L., Hildebrand, E., Hu, L.T., and Coburn, J. (2008). *Borrelia burgdorferi* BBB07 interaction with integrin alpha3beta1 stimulates production of pro-inflammatory mediators in primary human chondrocytes. *Cell Microbiol*, 10, 320-31.

Berger, P., Niemann, A., and Suter, U. (2006). Schwann cells and the pathogenesis of inherited motor and sensory neuropathies (Charcot-Marie-Tooth disease). *Glia*, 54, 243–257.

Beuche, W., and Friede, R.L. (1985). A new approach toward analyzing peripheral nerve fiber populations. II. Foreshortening of regenerated internodes corresponds to reduced sheath thickness. *J Neuropathol Exp Neurol*, 44, 73–84.

Birchmeier, C., and Nave, K.A. (2008). Neuregulin-1, a key axonal signal that drives Schwann cell growth and differentiation. *Glia*, 56, 1491–1497.

Bisogno, L.S., and Keene, J.D. (2018). RNA regulons in cancer and inflammation. *Curr Opin Genet Dev*, 48, 97–103.

Blache, P., van de Wetering, M., Duluc, I., Domon, C., Berta, P., Freund, J.N., Clevers, H., and Jay, P. (2004). SOX9 is an intestine crypt transcription factor, is regulated by the Wnt pathway, and represses the CDX2 and MUC2 genes. *J Cell Biol*, 166, 37–47.

Boullerne, A.I. (2011). Neurophysiology to neuroanatomy: The transition from Claude Bernard to Louis-Antoine Ranvier. *Arch Ital Biol*, 149, 38–46.

Boullerne, A.I. (2016). The history of myelin. *Exp Neurol*, 283, 431–445.

Bradner, J.E., Hnisz, D., and Young, R.A. (2017). Transcriptional Addiction in Cancer. *Cell*, 168, 629–643.

Brennan, A., Dean, C.H., Zhang, A.L., Cass, D.T., Mirsky, R., and Jessen, K.R. 2000. Endothelins control the timing of Schwann cell generation *in vitro* and *in vivo*. *Dev Biol*, 227, 545–557.

Brissette, C.A., Verma, A., Bowman, A., Cooley, A.E., and Stevenson, B. (2009). The *Borrelia burgdorferi* outer-surface protein ErpX binds mammalian laminin. *Microbiology*, 155, 863–872.

Brushart, T.M., Aspalter, M., Griffin, J.W., Redett, R., Hameed, H., Zhou, C., Wright, M., Vyas, A., and Ho¨ke, A. (2013). Schwann cell phenotype is regulated by axon modality and central-peripheral location, and persists in vitro. *Exp Neurol*, 247, 272–281.

Bunge, R.P., Bunge, M.B., and Bates, M. (1989). Movements of the Schwann cell nucleus implicate progression of the inner (axon-related) Schwann cell process during myelination. *J Cell Biol,* 109, 273–284.

Burgdorfer, W., Barbour, A.G., Hayes, S.F., Benach, J.L., Grunwaldt, E., and Davis, J.P. (1982). Lyme disease—a tick-borne spirochetosis? *Science*, 216, 1317–1319.

Carreras-González, A., Navasa, N., Martín-Ruiz, I., Lavín, J.L., Azkargorta, M., Atondo, E., Barriales, D., Macías-Cámara, N., Pascual-Itoiz, M.A., Sampedro, L., Tomás-Cortázar, J., Peña-Cearra, A.,, Pellón, A., Prados-Rosales, R., Abecia, L., Elortza, F., Aransay, A.M., Rodríguez, H., and Anguita, J. (2018). A multi-omic analysis reveals the regulatory role of CD180 during the response of macrophages to *Borrelia burgdorferi*. *Emerg Microbes Infect*, 7, 19.

Carroll, S.L. (2016). The Challenge of Cancer Genomics in Rare Nervous System Neoplasms: Malignant Peripheral Nerve Sheath Tumors as a Paradigm for Cross- Species Comparative Oncogenomics. *Am J Pathol*, 186, 464–477.

Casalenovo, M.B., Rosa, P.S., de Faria Bertoluci, D.F., Barbosa, A.S.A.A., Nascimento, D.C.D., de Souza, V.N.B., and Nogueira, M.R.S. (2919). Myelination key factor krox-20 is downregulated in Schwann cells and murine sciatic nerves infected by Mycobacterium leprae. *Int J Exp Pathol*, 100, 83–93.

Casjens, S., Palmer, N., van Vugt, R., Huang, W.M., Stevenson, B., Rosa, P., Lathigra, R., Sutton, G., Peterson, J., Dodson, R.J., Haft, D,, Hickey, E., Gwinn, M., White, O., and Fraser, C.M. (2000). A bacterial genome in flux: the twelve linear and nine circular ex- trachromosomal DNAs in an infectious isolate of the Lyme disease spirochete. *Borrelia burgdorferi*. *Mol. Microbiol,* 35, 490–516.

Cervantes, J.L., Dunham-Ems, S.M., La Vake, C.J., Petzke, M.M., Sahay, B., Sellati, T.J., Radolf, J.D. and Salazara, J.C. (2011). Phagosomal signaling by *Borrelia burgdorferi* in human monocytes involves Toll-like receptor (TLR) 2 and TLR8 cooperativity and TLR8-mediated induction of IFN-β. *Proc Natl Acad Sci*, 108, 3683–3688.

Chapuy, B., McKeown, M.R., Lin, C.Y., Monti, S., Roemer, M.G., Qi, J., Rahl, P.B., Sun, H.H., Yeda, K.T., Doench, J.G., Reichert, E., Kung, A.L., Rodig, S.J., Young, R.A., Shipp, M.A., and Bradner, J.E. (2013). Discovery and characterization of super-enhancer-associated dependencies in diffuse large B cell lymphoma. *Cancer Cell*, 24, 777–790.

Chavali, M., Klingener, M., Kokkosis, A.G., Garkun, Y., Felong, S., Maffei, A., and Aguirre, A. (2018). Non-canonical Wnt signaling regulates neural stem cell quiescence during homeostasis and after demyelination. *Nat commun,* 9, 36.

Chen, Z.L., Yu, W.M., and Strickland, S. (2007). Peripheral regeneration. *Annu Rev Neurosci*, 30, 209–233.

Chen, J., Bardes, E.E., Aronow, B.J., and Jegga, A.G. (2009a). ToppGene Suite for gene list enrichment analysis and candidate gene prioritization. *Nucleic Acids Res*, 37 (Web Server issue), W305–311.

Chen HZ, Tsai SY, Leone G. (2009b). Emerging roles of E2Fs in cancer: an exit from cell cycle control. *Nat Rev Cancer*, 9, 785–797.

Chin, R.L., Sander, H.W., Brannagan, T.H., De Sousa, E., and Latov, N. (2010). Demyelinating neuropathy in patients with hepatitis C virus infection. *J Clin Neuromuscul Dis*, 11, 209–12.

Chuah, M.I., and West, A.K. (2002). Cellular and molecular biology of ensheathing cells. *Microsc Res Tech*, 58, 216–227.

Cinco, M., Cini, B., Murgia, R., Presani, G., Prodan, M., and Perticarari, S. (2001). Evidence of involvement of the mannose receptor in adhesion of Borrelia burgdorferi to monocyte/macrophages. *Infection and Immunity*, 69, 2743–2747.

Comstedt, P., Hanner, M., Schu¨ler, W., Meinke, A., and Lundberg, U. (2014). Design and Development of a Novel Vaccine for Protection against Lyme Borreliosis. *PLoS ONE,* 9, e113294.

Comstedt, P., Schu¨ler, W., Meinke, A., and Lundberg, U. (2017). The novel Lyme borreliosis vaccine VLA15 shows broad protection against Borrelia species expressing six different OspA serotypes. *PLoS ONE*, 12, e0184357.

Cordenonsi, M., Zanconato, F., Azzolin, L., Forcato, M., Rosato, A., Frasson, C., Inui, M., Montagner, M., Parenti, A.R., Poletti, A., Daidone, M.G., Dupont, S., Basso, G., Bicciato, S., and Piccolo, S. (2011). The Hippo transducer TAZ confers cancer stem cell-related traits on breast cancer cells. *Cell*, 147, 759–772.

Costa, R.M., Federov, N.B., Kogan, J.H., Murphy, G.G., Stern, J., Ohno, M., Kucherlapati, R., Jacks, T., and Silva, A.J. (2002). Mechanism for the learning deficits in a mouse model of neurofibromatosis type 1. *Nature*, 415, 526–530.

Court, F.A., Sherman, D.L., Pratt, T., Garry, E.M., Ribchester, R.R., Cottrell, D.F., Fleetwood-Walker, S.M., and Brophy, P.J. (2004). Restricted growth of Schwann cells lacking Cajal bands slows conduction in myelinated nerves. *Nature*, 431, 191–195.

Crespo, I., Krishna, A., Le Bechec, A., and del Sol, A. (2013). Predicting missing expression values in gene regulatory networks using a discrete logic modeling optimization guided by network stable states. *Nucleic Acids Res*, 41, e8.

D'Antonio, M., Droggiti, A., Feltri, M.L., Roes, J., Wrabetz, L., Mirsky, R., and Jessen, K.R. (2006a). TGFβ type II receptor signaling controls Schwann cell death and proliferation in developing nerves. *J Neurosci*, 26, 8417–8427.

Datta, G., Miller, N.M., Afghah, Z., Geiger, J.D., Chen, X. (2019). HIV-1 gp120 Promotes Lysosomal Exocytosis in Human Schwann Cells. *Front Cell Neurosci*, 13, 329.

Dauch, D., Rudalska, R., Cossa, G., Nault, J.C., Kang, T.W., Wuestefeld, T., Hohmeyer, A., Imbeaud, S., Yevsa, T., Hoenicke, L., Pantsar, T., Bozko, P., Malek, N.P., Longerich, T., Laufer, S., Poso, A., Zucman-Rossi, J., Eilers, M., and Zender, L. (2016). A MYC-aurora kinase A protein complex represents an actionable drug target in p53-altered liver cancer. *Nat Med*, 22, 744–753.

Delbaz, A., Chen, M., Jen, F.E., Schulz, B.L., Gorse, A.D., Jennings, M.P., St John, J.A., and Ekberg, J.A.K. (2020). Neisseria meningitidis Induces Pathology-Associated Cellular and Molecular Changes in Trigeminal Schwann Cells. *Infect Immun*, 88, pii: e00955-19.

De Martino, S.J., Sordet, C., Piémont, Y., Ruzic-Sabljic, E., Thaddée Vetter, M., Monteil, H., Sibilia, J., and Jaulhac B. (2006). Enhanced culture of Borrelia garinii and Borrelia afzelii strains on a solid BSK-based medium in anaerobic conditions. *Res Microbio*, 157, 726–9.

De Raedt, T., Beert, E., Pasmant, E., Luscan, A., Brems, H., Ortonne, N., Helin, K., Hornick, J.L., Mautner, V., Kehrer-Sawatzki, H., Clapp, W., Bradner, J., Vidaud, M., Upadhyaya, M., Legius, E., and Cichowski, K. (2014). PRC2 loss amplifies Ras-driven transcription and confers sensitivity to BRD4-based therapies. *Nature*, 514, 247–251.

de Taeye, S.W., Kreuk, L., van Dam, A.P., Hovius, J.W., and Schuijt, T.J. (2013). Complement evasion by Borrelia burgdorferi: it takes three to tango. *Trends Parasitol*, 29, 119–128.

des Vignes, F., Piesman, J., Heffernan, R., Schulze, T.L., Stafford, K.C., and Fish, D. (2001). Effect of tick removal on transmission of *Borrelia burgdorferi* and *Ehrlichia phagocytophila* by *Ixodes scapularis* nymphs. *J Infect Dis*; 183, 773–78.

Deschênes-Furry, J., Perrone-Bizzozero, N., and Jasmin, B.J. (2006). The RNA-binding protein HuD: a regulator of neuronal differentiation, maintenance and plasticity. *Bioessays*, 28, 822–833.

Dhiman, G., Abraham, R., and Griffin, D.E. (2019). Human Schwann cells are susceptible to infection with Zika and yellow fever viruses, but not dengue virus. *Sci Rep*, 9, 9951.

Dickson, A.M., Anderson, J.R., Barnhart, M.D., Sokoloski, K.J., Oko, L.; Opyrchal, M., Galanis, E., Wilusz, C.J., Morrison, T.E., and Wilusz, J. (2012). Dephosphorylation of HuR Protein during alphavirus infection is associated with HuR relocalization to the cytoplasm. *J Biol Chem*, 287, 36229–36238.

Dobin, A., Davis, C.A., Schlesinger, F., Drenkow, J., Zaleski, C., Jha, S., Batut, P., Chaisson, M., and Gingeras, T.R. (2013). STAR: ultrafast universal RNA-seq aligner. *Bioinformatics*, 29, 15–21.

Doller, A., Akool, el-S., Huwiler, A., Müller, R., Radeke, H.H., Pfeilschifter, J., and Eberhardt, W. (2008). Posttranslational modification of the AU-rich element binding protein HuR by protein kinase Cδ elicits angiotensin II-induced stabilization and nuclear export of cyclooxygenase 2 mRNA. *Mol Cell Biol*, 28, 2608–2625.

Dunham-Ems, S.M., Caimano, M.J., Pal, U., Wolgemuth, C.W., Eggers, C.H., Balic, A., and Radolf, J.D. (2009). Live imaging reveals a biphasic mode of dissemination of Borrelia burgdorferi within ticks. *J Clin Invest*, 119, 3652–3665.

Duray, P.H. (1989). Histopathology of clinical phases of human Lyme disease. *Rheum Dis Clin North Am*, 15, 691–710.

Durdern, L.A., Gerlach, R.F., Beckmen, K.B., and Greiman, S.E. (2018). Hyperparasitism and Non-Nidicolous Mating by Male *Ixodes angustus* Ticks (Acari: Ixodidae). *J Med Entomol,* 55, 766–768.

Durie, D., Lewis, S.M., Liwak, U., Kisilewicz, M., Gorospe, M., and Holcik, M. (2011). RNA-binding protein HuR mediates cytoprotection through stimulation of XIAP translation. *Oncogen*e, 30, 1460–1469.

Dutta-Simmons, J., Zhang, Y., Gorgun, G., Gatt, M., Mani, M., Hideshima, T., Takada, K., Carlson, N.E., Carrasco, D.E., Tai, Y.T., Raje, N., Letai, A.G., Anderson, K.C., and Carrasco, D.R. (2009). Aurora kinase A is a target of Wnt/beta-catenin involved in multiple myeloma disease progression. *Blood*, 114, 2699–2708.

Eisen, R.J., and Eisen, L. (2018). The Blacklegged Tick, *Ixodes scapularis*: An Increasing Public Health Concern. *Trends Parasithol*, 34, 295–309.

Eldin, C., Raffetin, A., Bouiller K., Hansmann, Y., Roblot, F., Raoult, D., and Parola, P. (2019). Review of European and American guidelines for the diagnosis of Lyme borreliosis. *Med Mal Infect*, 49, 121–132.

Espinosa-Medina, I., Jevans, B., Boismoreau, F., Chettouh, Z., Enomoto, H., Müller, T., Birchmeier, C., Burns, A.J., and Brunet, J.F. (2017). Dual origin of enteric neurons in vagal Schwann cell precursors and the sympathetic neural crest. *Proc Natl Acad Sci USA*, 114, 11980–11985.

Estrada-Peña, A. (2015). Ticks as vectors: taxonomy, biology and ecology. *Rev Sci Tech*, 34, 53–65.

Farid, M., Demico, E.G., Garcia, R., Ahn, L., Merola, P.R., Cioffi, A., and Maki, R.G. (2014). Malignant Peripheral Nerve Sheath Tumors. *Oncologist*, 19, 193–201.

Feltri, M.L., Poitelon, Y., and Previtali, S.C. (2016). How Schwann cells sort axons: new concepts. *Neuroscientist*, 22, 252–265.

Ferner, R.E. (2007). Neurofibromatosis 1 and neurofibromatosis 2: a twenty first century perspective. *Lancet Neurol*, 6, 340–351.

Ferner, R.E. (2010). The neurofibromatosis. *Pract Neurol*, 10, 82–93.

Ferner, R.E., Listernick, R.H., Korf, B.R., Wolters, P.L., and Johnson, K.J. (2017). Neurofibromatosis type 1. *Nat Rev Dis Primers*, 3, 17004.

Fishilevich, S., Nudel, R., Rappaport, N., Hadar, R., Plaschkes, I., Iny Stein, T., Rosen, N., Kohn, A., Twik, M., Safran, M., Lancet, D., and Cohen, D. (2017). GeneHancer: genome-wide integration of enhancers and target genes in GeneCards. *Database (Oxford)*, 2017.

Fleming, M.S., and Luo, W. (2013). The anatomy, function, and development of mammalian Aβ low-threshold mechanoreceptors. *Front Biol (Beijing)*, 8.

Fontana, X., Hristova, M., Da Costa, C., Patodia, S., Thei, L., Makwana, M., Spencer-Dene, B., Latouche, M., Mirsky, R., Jessen, K.R, Klein, R., Raivich, G., and Behrens, A. (2012). c-Jun in Schwann cells promotes axonal regeneration and motoneuron survival via paracrine signaling. *J Cell Biol*, 198, 127–141.

Fontanals-Cirera, B., Hasson, D., Vardabasso, C., Di Micco, R., Agrawal, P., Chowdhury, A., Gantz, M., de Pablos-Aragoneses, A., Morgenstern, A., Wu, P., Filipescu, D., Valle-Garcia, D., Darvishian, F., Roe, J.S., Davies, M.A., Vakoc, C.R., Hernando, E., and Bernstein, E. (2017). Harnessing BET Inhibitor Sensitivity Reveals AMIGO2 as a Melanoma Survival Gene. *Mol Cell*, 68, 731–744 e739.

Fraser, C.M., Casjens, S., Huang, W.M., Sutton, G.G., Clayton, R., Lathigra, R., White, O., Ketchum, K.A., Dodson, R., Hickey, E.K., Gwinn, M., Dougherty, B., Tomb, J.F., Fleischmann, R.D., Richardson, D., Peterson, J., Kerlavage, A.R., Quackenbush, J., Salzberg, S., Hanson, M., van Vugt, R., Palmer, N., Adams, M.D., Gocayne, J., Weidman, J., Utterback, T., Watthey, L., McDonald, L., Artiach, P., Bowman, C., Garland, S., Fuji, C., Cotton, M.D., Horst, K., Roberts, K., Hatch, B., Smith, H.O., and Venter, J.C. (1997). Genomic sequence of a Lyme disease spirochaete, *Borrelia burgdorferi*. *Nature*, 390, 580–586.

Fricker, F.R., Antunes-Martins, A., Galino, J., Paramsothy, R., La Russa, F., Perkins, J., Goldberg, R., Brelstaff, J., Zhu, N., McMahon, S.B., Orengo, C., Garratt, A.N., Birchmeier, C., and Bennett, D.L. (2013). Axonal neuregulin 1 is a rate limiting but not essential factor for nerve remyelination. *Brain*, 136, 2279–2297.

Furlan, A., Dyachuk, V., Kastriti, M. E., Calvo-Enrique, L., Abdo, H., Hadjab, S., Chontorotzea, T., Akkuratova, N., Usoskin, D., Kamenev, D., Petersen, J., Sunadome, K., Memic, F., Marklund, U., Fried, K., Topilko, P., Lallemend, F., Kharchenko, P.V., Ernfors, P., and Adameyko, I. (2017). Multipotent peripheral glial cells generate neuroendocrine cells of the adrenal medulla. *Science*, 357, eaal3753.

Gabella, G. (1981). Ultrastructure of the nerve plexuses of the mammalian intestine: the enteric glial cells. *Neuroscience*, 6, 425–436.

Garbay, B., Heape, A.M., Sargueil, F., and Cassagne, C. (2000). Myelin synthesis in the peripheral nervous system. *Prog Neurobiol*, 61, 267–304.

Garin, C., and Bujadoux, A. Paralysie par les tiques. (1922). *J Med Lyon*, 71,765–767.

Garratt, A.N., Voiculescu, O., Topilko, P., Charnay, P., and Birchmeier, C. (2000). A dual role of erbB2 in myelination and in ex- pansion of the Schwann cell precursor pool. *J Cell Biol*, 148, 1035–1046.

Geren, B.B. (1954). The formation from the Schwann cell surface of myelin in the peripheral nerves of chick embryos. *Exp Cell Res,* 7, 558–562.

Gern, L. (2009). Life cycle of *Borrelia burgdorferi* sensu lato and transmission to humans. *Curr Probl Dermatol*, 37, 18–30.

Ghadimi, M.P., Young, E.D., Belousov, R., Zhang, Y., Lopez, G., Lusby, K., Kivlin, C., Demicco, E.G., Creighton, C.J., Lazar, A.J., Pollock, R.E., and Lev, D. (2012). Survivin is a viable target for the treatment of malignant peripheral nerve sheath tumors. *Clin Cancer Res*, 18, 2545–2557.

Gherardini, F., Boylan, J., Lawrence, K., and Skare, J. (2010). Metabolism and Physiology of *Borrelia*. In *Borrelia*: Molecular Biology, Host Interaction, and Pathogenesis. *Caister Academic*, 103–138.

Glenn, T.D., and Talbot, W.S. (2013). Signals regulating myelination in peripheral nerves and the Schwann cell response to injury. *Curr Opin Neurobiol*, 23, 1041–1048.

Gomez-Sanchez, J.A., Carty, L., Iruarrizaga-Lejarreta, M., Palomo-Irigoyen, M., Varela-Rey, M., Griffith, M., Hantke, J., Macias-Camara, N., Azkargorta, Mikel Aurrekoetxea, I., De Juan, V.G., et al. (2015). Schwann cell autophagy, myelinophagy, initiates myelin clearance from injured nerves. *J Cell Biol*, 210, 153–168.

Gomez-Sanchez, J.A., Pilch, K.S., van der Lans, M., Fazal, S.V., Benito, C., Wagstaff, L.J., Mirsky, R., and Jessen, K,R. (2017). After nerve injury, lineage tracing shows that myelin and remak schwann cells elongate extensively and branch to form repair schwann cells, which shorten radically on remyelination. *J Neurosci*, 37, 9086–9099.

Gonda, T.J., and Ramsay, R.G. (2015). Directly targeting transcriptional dysregulation in cancer. *Nat Rev Cancer*, 15, 686–694.

Gregoryan, T., Steina, S., Qia, J., Wendeb, H., Garrattc, A.N., Naved, K.A., Birchmeierb, C., and Birchmeiera, W. (2013). Wnt/Rspondin/β-catenin signals control axonal sorting and lineage progression in Schwann cell development. *PNAS,* 110, 18174–18179.

Griffiths, S., and Thompson, P., Frayling, I., and Upadhyaya, M. (2007). Molecular diagnosis of neurofibromatosis type 1: 2 years experience. *Fam Cancer*, 6, 21–34.

Grimm, D., Tilly, K., Byram, R., Stewart, P.E., Krum, J.G., Bueschel, D.M., Schwan, T.G., Policastro, P.F., Elias, A.F., and Rosa, P.A. (2004). Outer-surface protein C of the Lyme disease spirochete: a protein induced in ticks for infection of mammals*. Proc Natl Acad Sci,* 101, 3142–7.

Grinspan, J.B., Marchionni, M.A., Reeves, M., Coulaloglou, M., and Scherer, S.S. (1996). Axonal interactions regulate Schwann cell apoptosis in developing peripheral nerve: neuregulin receptors and the role of neuregulins. *J Neurosci*, 16, 6107–6118.

Gu, Z., Jiang, Q., Fu, A.K., Ip, N.Y., and Yan, Z. (2005). Regulation of NMDA receptors by neuregulin signalling in PFC. *J Neurosci*, 25, 4974–4984.

Guglielmone, A.A., Robbins, R.G., Apanaskevich, D.A., Petney, T.N., Estrada-Peña, A., Horak, I.G., Shao, R., and Barker, S.C. (2010). The Argasidae, Ixodidae and Nuttalliellidae (Acari: Ixodida) of the world: a list of valid species names. *Zootaxa*, 2528, 1–28.

Guo, B.P., Norris, S.J., Rosenberg, L.C., Höök, M. (1995). Adherence of *Borrelia burgdorferi* to the proteoglycan decorin. *Infect Immun*, 63, 3467–72.

Guo, J., Lv, J., Chang, S., Chen, Z., Lu, W., Xu, C., Liu, M., and Pang, X. (2016). Inhibiting cytoplasmic accumulation of HuR synergizes genotoxic agents in urothelial carcinoma of the bladder. *Oncotarget*, 7, 45249–45262.

Gutmann, D.H., Wood, D.L., and Collins, F.S. (1991). Identification of the neurofibromatosis type 1 gene product. Proc. *Natl Acad Sci U S A*, 88, 9658–9662.

Gutmann, D.H., Blakeley, J.O., Korf, B.R., and Packer, R.J. (2013). Optimizing biologically targeted clinical trials for neurofibromatosis. *Expert Opin Investig Drugs*, 22, 443–462.

Gutmann, D.H., Ferner, R.E., Listernick, R.H., Korf, B.R., Wolters, P.L., and Johnson, K.J. (2017). Neurofibromatosis type 1. *Nat Rev Dis Primers*, 23, 17004.

Güttinger, S., Mühlhäusser, P., Koller-Eichhorn, R., Brennecke, J., and Kutay, U. (2004). Transportin2 functions as importin and mediates nuclear import of HuR. *Proc Natl Acad Sci U S A*, 101, 2918–2923.

Hall, S.M., and Williams, P.L. (1970). Studies on the 'Incisures' of Schmidt and Lanterman. *J Cell Sci*, 6, 767–791.

Halperin, J.J. (2016). Nervous system Lyme disease, chronic Lyme disease, and none of the above. *Acta Neurol Belg,* 116,1–6.

Halperin, J.J. (2017). Neuroborreliosis. *J Neurol*, 264, 1292–1297.

Halperin, J.J. (2019). Neuroborreliosis. *Curr Opin Infect Dis,* 32, 259–264.

Hanahan, D., and Weinberg, R.A. (2011). Hallmarks of cancer: the next generation. *Cell*, 144, 646–674.

Hannan, F., Ho, I., Tong, J.J., Zhu, Y., Nurnberg, P., and Zhong, Y. (2006). Effect of neurofibromatosis type I mutations on a novel pathway for adenylyl cyclase activation requiring neurofibromin and Ras. *Hum Mol Genet*, 15, 1087–1098.

Harrisingh, M.C., Perez-Nadales, E., Parkinson, D.B., Malcolm, D.S., Mudge, A.W., and Lloyd AC. (2004). The Ras/Raf/ERK signalling pathway drives Schwann cell dedifferentiation. *EMBO J*, 23, 3061–3071.

Hawley, K.L., Martin-Ruiz, I., Iglesias-Pedraz, J.M., Berwin, B., and Anguita, J. (2013). CD14 targets complement receptor 3 to lipid rafts during phagocytosis of Borrelia burgdorferi. *Int J Biol Sci*, 9, 803–10.

He, T.C., Sparks, A.B., Rago, C., Hermeking, H., Zawel, L., da Costa, L..T, Morin, P.J., Vogelstein, B., and Kinzler, K.W. (1998). Identification of c-MYC as a target of the APC pathway. *Science*, 281, 1509–1512.

Hildebrand, C., Bowe, C.M., and Remahl, I.N. (1994). Myelination and myelin sheath remodelling in normal and pathological PNS nerve fibres. *Prog Neurobiol*, 43, 85–141.

Hinckley, A.F, Connally, N.P, Meek, J.I., Johnson, B.J., Kemperman, M.M., Feldman, K.A., White, J.L., and Mead, P.S. (2014). Lyme disease testing by large commercial laboratories in the United States. *Clin Infect Dis*, 59, 676–681.

Hinman, M.N, and Lou, H. (2008). Diverse molecular functions of Hu proteins. *Cell Mol Life Sci*, 65, 3168–3181.

Hovius, J.W.R., et al. (2009). The Urokinase Receptor (uPAR) Facilitates Clearance of Borrelia burgdorferi. *PLoS Pathog,* 5, e1000447.

Hübner, A., Yang, X., Nolen, D.M., Popova, T.G., Cabello, F.C., and Norgard, M.V. (2001). Expression of *Borrelia burgdorferi* OspC and DbpA is controlled by a RpoN-RpoS regulatory pathway. *Proc Natl Acad Sci*, 98, 12724–12729.

Hughes, C.N., Kodner, C.B., and Johnson, R.C. (1992). DNA analysis of Borrelia burgdorferi NCH-1, the first northcentral U.S. human Lyme disease isolate. *J Clin Microbiol*, 30, 698–703.

Hulsebos, T.J.M, Plomp, A.S., Wolterman, R.A., Robanus-Maandag, E.C., Baas, F., and Wesseling, P. (2007). Germline mutation of *INI1/SMARCB1* in familial schwannomatosis. *Am J Hum Genet*, 80, 805–810.

Iruarrizaga-Lejarreta, M., Varela-Rey, M., Lozano, J.J., Fernández-Ramos, D., Rodríguez-Ezpeleta, N., Embade, Lu, S.C., van der Kraan, P.M., Blaney Davidson, E.N., Gorospe, M., Mirsky, R., Jessen, K.R., Aransay, A.M., Mato, J.M., Martínez-Chantar, M.L., and Woodhoo, A. (2012). The RNA-binding protein human antigen R controls global changes in gene expression during Schwann cell development. *J Neurosci*, 32, 4944–4958.

Iruarrizaga-Lejarreta, M. (2014). Molecular Mechanisms Regulating Schwann Cell Myelination During Development and in Pathological Conditions. Director of the thesis: Ashwin Woodhoo. Universidad del País Vasco/Euskal Herriko Unibertsitatea.

Jayaseelan, S., Doyle, F., and Tenenbaum, S.A. (2014). Profiling post-transcriptionally networked mRNA subsets using RIP-Chip and RIP-Seq. *Methods*, 67, 13–19.

Jenei, V., Sherwood, V., Howlin, J., Linnskog, R., Säfholm, A., Axelsson, L., and Andersson, T. (2009). A t-butyloxycarbonyl-modified Wnt5a-derived hexapeptide functions as a potent antagonist of Wnt5a-dependent melanoma cell invasion. *Proc Natl Acad Sci USA*, 106, 19473–19478.

Jessen, K.R., and Mirsky, R. (1983). Astrocyte-like glia in the peripheral nervous system: an immunohistochemical study of enteric glia. *J Neurosci Off J Soc Neurosci*, 3, 2206–2218.

Jessen, K.R. (2004). Glial cells. *Int J Biochem Cell Biol*, 36, 1861–1867.

Jessen, K.R., Morgan, L., Brammer, M., and Mirsky, R. (1985). Galactocerebroside is expressed by non-myelin-forming Schwann cells in situ. *J Cell Biol*, 101, 1135–1143.

Jessen, K.R., and Mirsky, R. (2003). Embryonic Schwann cell develop- ment and the initiation of myelination. In: Myelin and Its Diseases. Lazzarini RA (Ed). *Academic Press*, 329–370.

Jessen, W.J., Miller, S.J., Jousma, E., Wu, J., Rizvi, T.A., Brundage, M.E., Eaves, D., Widemann, B., Kim. M.O., Dombi, E., Sabo, J., Hardiman Dudley, A., Niwa-Kawakita, M., Page, G.P., Giovannini, M., Aronow, B.J., Cripe, T.P., and Ratner, N. (2013). MEK inhibition exhibits efficacy in human and mouse neurofibromatosis tumors. *J Clin Invest*, 123, 340–347.

Jessen, K.R., Mirsky, R. and Lloyd, A.C. (2015). Schwann Cells: Development and Role in Nerve Repair. *Cold Spring Harb Perspect Bio,* 7, a020487.

Jessen, K.R., and Mirsky, R. (2019a). Schwann Cell Precursors; Multipotent Glial Cells in Embryonic Nerves. *Front Mol Neurosci*, 12:69.

Jessen, K.R., and Mirsky, R. (2019b). The Success and Failure of the Schwann Cell Response to Nerve Injury. *Front Cell Neurosci*, 11, 13–33.

Johnson, R.C., Schmid, G.P., Hyde, F.W., Steigerwalt, A.G., and Brenner, D.J. (1984). Borrelia burgdorferi sp.nov.: etiological agent of Lyme disease. *Int. J. Syst. Bacterio,* 34, 496–497.

Jones, G., Zhu, Y., Silva, C., Tsutsui, S., Pardo, C.A., Keppler, O.T., McArthur, J.C., and Power, C. (2005). Peripheral nerve-derived HIV-1 is predominantly CCR5-dependent and causes neuronal degeneration and neuroinflammation. Virology, 334, 178–93.

Jones, K.L., Muellegger, R.R., Means, T.K., Lee, M., Glickstein, L.J., Damle, N., Sikand, V.K., Luster, A.D., and Steere, A.C. (2008). Higher mRNA levels of chemokines and cytokines associated with macrophage activation in erythema migrans skin lesions in patients from the United States than in patients from Austria with Lyme borreliosis. *Clin Infect Dis*, 46, 85–92.

Jones, R.T., Tusting, L.S., Smith, H.M.P., Segbaya, S., Macdonald, M.B., Bangs, M.J., Logan, J.G. (2018). The impact of industrial activities on vector-borne disease transmission. *Acta Tro,* 188, 142–151.

Joseph, N.M., Mukouyama, Y.S., Mosher, J.T., Jaegle, M., Crone, S.A., Dormand, E.L., Lee, K.F., Meijer, D., Anderson, D.J., and Morrison, S.J. (2004). Neural crest stem cells undergo multilineage differentiation in developing peripheral nerves to generate endoneurial fibroblasts in addition to Schwann cells. *Development*, 131, 5599–5612.

Kahl, O., Janetzki-Mittmann, C., Gray, J. S., Jonas, R., Stein, J., and De Boer, R. (1998). Risk of infection with *Borrelia burgdorferi* sensu lato for a host in relation to the duration of nymphal *Ixodes ricinus* feeding and the method of tick removal. *Zentralblatt Fur Bakteriologie*, 287, 41–52.

Kalish, R.A., Kaplan, R.F., Taylor, E., Jones-Woodward, L., Workman, K., and Steere AC. (2001). Evaluation of study patients with Lyme disease, 10–20-year follow-up. *J Infect Dis*, 183, 453–460.

Kamholz, J., Sessa, M., Scherer, S., Vogelbacker, H., Mokuno, K., Baron, P., Wrabetz, L., Shy, M., and Pleasure, D. (1992). Structure and expression of proteolipid protein in the peripheral nervous system. *J Neurosci Res*, 31, 231–244.

Kamil, K., Yazid, M.D., Idrus, R.B.H., Das, S., Kumar, J. (2019). Peripheral Demyelinating Diseases: From Biology to Translational Medicine. *Front Neurol*, 10, 87.

Katona, I., and Weis, J. (2017). Diseases of the peripheral nerves. *Handb Clin Neurol*, 145, 453–474.

Kaukua, N., Shahidi, M. K., Konstantinidou, C., Dyachuk, V., Kaucka, M., Furlan, A., An, Z., Wang, L., Hultman, I., Ahrlund-Richter, L., Blom, H., Brismar, H., Lopes, N.A., Pachnis, V., Suter, U., Clevers, H., Thesleff, I., Sharpe, P., Ernfors, P., Fried, K., and Adameyko, I. (2014). Glial origin of mesenchymal stem cells in a tooth model system. *Nature*, 513, 551–554.

Kawai, T., Lal, A., Yang, X., Galban, S., Mazan-Mamczarz, K., and Gorospe, M. (2006). Translational control of cytochrome c by RNA-binding proteins TIA-1 and HuR. *Mol Cell Biol*, 26, 3295–3307.

Keene, J.D., Komisarow, J.M., and Friedersdorf, M.B. (2006). RIP-Chip: the isolation and identification of mRNAs, microRNAs and protein components of ribonucleoprotein complexes from cell extracts. *Nat Protoc*, 1, 302–307.

Kidd G.J., Ohno, N., and Trapp, B.D. (2013). Biology of Schwann cells. *Handb Clin Neurol*, 115, 55–79.

Kim, A., Stewart, D.R., Reilly, K.M., Viskochil, D., Miettinen, M.M., and Widemann, B.C. (2017). Malignant Peripheral Nerve Sheath Tumors State of the Science: Leveraging Clinical and Biological Insights into Effective Therapies. *Sarcoma*, 2017:7429697.

King, R.H., Chandler, D., Lopaticki, S., Huang, D., Blake, J., Muddle, J.R., Kilpatrick, T., Nourallah, M., Miyata, T., Okuda, T., Carter, K.W., Hunter, M., Angelicheva, D., Morahan, G., and Kalaydjieva, L. (2011). Ndrg1 in development and maintenance of the myelin sheath. *Neurobiol dis,* 42, 368–380.

Koedel, U., Fingerle, V., and Pfister, H.W. (2015). Lyme neuroborreliosis-epidemiology, diagnosis and management. *Nat Rev Neurol*, 11, 446–456.

Korfhage, J., and Lombard, D.B. (2019). Malignant Peripheral Nerve Sheath Tumors: From Epigenome to Bedside. *Mol Cancer Res*, 17, 1417–1428.

Kotsyfakis, M., Sá-Nunes, A., Francischetti, I.M., Mather, T.N., Andersen, J.F., and Ribeiro, J.M. (2006). Antiinflammatory and immunosuppressive activity of sialostatin L, a salivary cystatin from the tick Ixodes scapularis. *J Biol Chem*, 281, 26298-307.

Kress, T.R., Sabo, A., and Amati, B. (2015). MYC: connecting selective transcriptional control to global RNA production. *Nat Rev Cancer*, 15, 593–607.

Kristoferitsch, W., Sluga, E., Graf, M., Partsch, H., Neumann, R., Stanek, G., and Budka, H. (1988). Neuropathy associated with acrodermatitis chronica atrophicans. *Ann N Y Acad Sci*, 538:35–45.

Kullmann, M., Gopfert, U., Siewe, B., and Hengst, L. (2002). ELAV/Hu proteins inhibit p27 translation via an IRES element in the p27 5'UTR. *Genes Dev*, 16, 3087–3099.

Kuwano, Y., Rabinovic, A., Srikantan, S., Gorospe, M., and Demple, B. (2009). Analysis of nitric oxide-stabilized mRNAs in human fibroblasts reveals HuR-dependent heme oxygenase 1 upregulation. *Mol Cell Biol*, 29, 2622–2635.

Lafarga, V., Cuadrado, A., López de Silanes, I., Bengoechea, R., Fernandez-Capetillo, O., and Nebreda, A.R. (2009). p38 Mitogen-activated protein kinase- and HuR-dependent stabilization of p21(Cip1) mRNA mediates the G(1)/S checkpoint. *Mol Cell Biol*, 29, 4341–4351.

Lal, A., Kawai, T., Yang, X., Mazan-Mamczarz, K., and Gorospe M. (2005). Antiapoptotic function of RNA- binding protein HuR effected through prothymosin alpha. *EMBO J*, 24, 1852–1862.

Lambert, A.W., Pattabiraman, D.R., and Weinberg, R.A. (2017). Emerging Biological Principles of Metastasis. *Cell*, 168, 670-691.

Leandersson, K., Riesbeck, K., and Andersson, T. (2006). Wnt-5a mRNA translation is suppressed by the Elav-like protein HuR in human breast epithelial cells. *Nucleic Acids Res*, 34, 3988–3999.

Lee, S.J., Park, H.J., Kim, Y.H., Kim, B.Y., Jin, H.S., Kim, H.J., Han, J.H., Yim, H., and Jeong, S.Y. (2012). Inhibition of Bcl-xL by ABT-737 enhances chemotherapy sensitivity in neurofibromatosis type 1-associated malignant peripheral nerve sheath tumor cells. *Int J Mol Med*, 30, 443–450.

Lees, M.B., and Brostoff, S.W. (1984). Proteins of myelin. 197–217. In: Morell, P. (ed.). Myelin. *New York: Plenum*. 2nd edition.

Lemke, G. (2006). Neuregulin-1 and myelination. *Sci STKE*, 2006, pe11.

Levine, J., Buchman, C.A., and Fregien, N. (2003). Influenza A virus infection of human Schwann cells in vitro. *Acta Otolaryngo*, 123, 41–45.

Levy, N.S., Chung, S., Furneaux, H., and Levy, A.P. (1998). Hypoxic stabilization of vascular endothelial growth factor mRNA by the RNA-binding protein HuR. *J Biol Chem*, 273, 6417–6423.

Li, B., and Dewey, C.N. (2011). RSEM: accurate transcript quantification from RNA-Seq data with or without a reference genome. *BMC Bioinformatics*, 12, 323.

Lin, W.N., Lin, C.C., Cheng, H.Y., and Yang, C.M. (2011). Regulation of cyclooxygenase-2 and cytosolic phospholipase A2 gene expression by lipopolysaccharide through the RNA-binding protein HuR: Involvement of NADPH oxidase reactive oxygen species and mitogen-activated protein kinases. *Br J Pharmacol*, 163, 1691–1706.

Lindgren, E., and Jaenson, T.G.T. (2006). Lyme borreliosis in Europe: influences of climate and climate change, epidemiology, ecology and adaptation measures. *EUR/04/5046250. World Health Organization (WHO)*, Regional Office for Europe, Geneva.

Linnskog, R., Jonsson, G., Axelsson, L., Prasad, C.P., and Andersson, T. (2014). Interleukin-6 drives melanoma cell motility through p38alpha-MAPK-dependent up- regulation of WNT5A expression. *Mol Oncol*, 8, 1365–1378.

Longo, J.F., Weber, S.M., Turner-Ivey, B.P., and Carroll, S.L. (2018). Recent Advances in the Diagnosis and Pathogenesis of Neurofibromatosis Type 1 (NF1)-associated Peripheral Nervous System Neoplasms. *Adv Anat Pathol*, 25, 353–368.

López de Silanes, I., Zhan, M., Lal, A., Yang, X., and Gorospe, M. (2004). Identification of a target RNA motif for RNA-binding protein HuR. *Proc Natl Acad Sci U S A*, 101, 2987–2992.

Lopez, G., Torres, K., Liu, J., Hernandez, B., Young, E., Belousov,. R, Bolshakov, S., Lazar, A.J., Slopis, J.M., McCutcheon, I.E., McConkey, D., and Lev, D. (2011). Autophagic survival in resistance to histone deacetylase inhibitors: novel strategies to treat malignant peripheral nerve sheath tumors. *Cancer Res*, 71, 185–196.

Loven, J., Hoke, H.A., Lin, C.Y., Lau, A., Orlando, D.A., Vakoc, C.R., Bradner, J.E., Lee, T.I., and Young, R.A. (2013). Selective inhibition of tumor oncogenes by disruption of super-enhancers. *Cell*, 153, 320–334.

Ma, W.J., and Furneaux, H. (1997). Localization of the human HuR gene to chromosome 19p13.2. *Hum Genet*, 99, 32–33.

Ma, W.J., Cheng, S., Campbell, C., Wright, A., and Furneaux, H. (1996). Cloning and characterization of HuR, a ubiquitously expressed Elav-like protein. *J Biol Chem*, 271, 8144–8151.

Mac, S., da Silva, S.R., and Sander, B. (2019). The economic burden of Lyme disease and the cost-effectiveness of Lyme disease interventions: A scoping review. *PLoS ONE,* 14, e0210280.

MacCollin, M., Chiocca, E.A., Evans, D.G., Friedman, J.M., Horvitz, R., Jaramillo, D., Lev, M., Mautner, V.F., Niimura, M., Plotkin, S.R., Sang, C.N., Stemmer-Rachamimov, A., and Roach, E.S. (2005). Diagnostic criteria for schwannomatosis. Neurology, 64, 11, 1838–1845.

Mans, B.J., de Klerk, D., Pienaar, R., De Castro, M.H., and Latif, A.A. (2012). The mitochondrial genomes of *Nuttalliella namaqua* (Ixodoidea: Nuttalliellidae) and *Argas africolumbae* (Ixodoidae: Argasidae): estimation of divergence dates for the major tick lineages and reconstruction of ancestral blood- feeding characters. *PloS ONE*, 7, e49461.

Manzoni, L., Zucal, C., Maio, D.D., D'Agostino, V.G, Thongon, N., Bonomo, I., Lal, P., Miceli, M., Baj, V., Brambilla, M., Cerofolini, L., Elezgarai, S., Biasini, E., Luchinat, C., Novellino, E., Fragai, M., Marinelli, L., Provenzani, A., and Seneci, P. (2018). Interfering with HuR-RNA Interaction: Design, Synthesis and Biological Characterization of Tanshinone Mimics as Novel, Effective HuR Inhibitors. *J Med Chem*, 61, 1483–1498.

Margos, G., Vollmer, S.A., Ogden, N.H., and Fish, D. (2011). Population genetics, taxonomy, phylogeny and evolution of *Borrelia burgdorferi* sensu lato. *Infect Genet Evol*, 11, 1545–1563.

Margos, G., Fingerle, V., Cutler, S., Gofton, A., Stevenson, B., and Estrada-Peña, A. (2020). Controversies in bacterial taxonomy: The example of the genus *Borrelia. Ticks Tick Borne Dis*, 17:101335.

Marques, A.R. (2015). Laboratory diagnosis of Lyme disease: advances and challenges. *Infect Dis Clin North A,* 29, 295–307.

Martenson, R.E., and Uyemura, K. (1992). Myelin P2, a neuritogenic member of the family of cytoplasmic lipid-binding proteins. 509–528. In: Martenson R.E. (ed.). Myelin: Biology and Chemistry. Boca Raton, FL: *CRC Press*.

Martin, M. (2011). Cutadapt removes adapter sequences from high-throughput sequencing reads. *EMBnet.Journal*, 17, 10–12.

Martini, R., Mohajeri, M.H., Kasper, S., Giese, K.P., and Schachner, M. (1995). Mice doubly deficient in the genes for P0 and myelin basic protein show that both proteins contribute to the formation of the major dense line in peripheral nerve myelin. *J* Neurosci, 15, 4488–4495.

Martyn, C.N., and Hughes, R.A. (1997). Epidemiology of peripheral neuropathy. *J Neurol Neurosurg Psychiatry*, 62, 310–318.

Masaki, T., Qu, J., Cholewa-Waclaw, J., Burr, K., Raaum, and R., Rambukkana, A. (2013). Reprogramming adult Schwann cells to stem cell-like cells by leprosy bacilli promotes dissemination of infection. Cell, 152, 51–67.

Masuzawa, T. (2004). Terrestrial distribution of the Lyme borreliosis agent *Borrelia burgdorferi* sensu lato in East Asia. *Jpn J Infect Dis*, 57, 229–235.

Mazan-Mamczarz, K., Galban, S., López de Silanes, I., Martindale, J.L., Atasoy, U., Keene, J.D., and Gorospe, M. (2003). RNA-binding protein HuR enhances p53 translation in response to ultraviolet light irradiation. *Proc Natl Acad Sci U S A*, 100, 8354–8359.

McMullen, M.R., Cocuzzi, E., Hatzoglou, M., and Nagy, L.E. (2003). Chronic ethanol exposure increases the binding of HuR to the TNFalpha 3'-untranslated region in macrophages. *J Biol Chem*, 278, 38333–38341.

Medlock, J.M., and Leach, S.A. (2015). Effect of climate change on vector-borne disease risk in the UK. *Lancet Infect Dis*, 15, 721–30.

Mei, L., and Xiong, W.C. (2008). Neuregulin 1 in neural development, synaptic plasticity and schizophrenia. *Nat Rev Neurosci*, 9, 437–452.

Meisner, N.C., Hintersteiner, M., Mueller, K, Bauer, R., Seifert, J.M., Naegeli, H.U., Ottl, J., Oberer, L., Guenat, C., Moss, S., Harrer, N., Woisetschlaeger, M., Buehler, C., Uhl, V., and Auer, M. (2007). Identification and mechanistic characterization of low-molecular-weight inhibitors for HuR. *Nat Chem Biol*, 3, 508–515.

Michailov, G.V., Sereda, M.W., Brinkmann, B.G., Fischer, T.M., Haug, B., Birchmeier, C., Role, L., Lai, C., Schwab, M.H., and Nave, K.A. (2004). Axonal neuregulin-1 regulates myelin sheath thickness. *Science*, 304, 700–703.

Miller, S.J., Rangwala, F., Williams, J., Ackerman, P., Kong, S., Jegga, A.G., Kaiser, S., Aronow, B.J., Frahm, S., Kluwe, L., Mautner, V., Upadhyaya, M., Muir, D., Wallace, M., Hagen, J., Quelle, D.E., Watson, M.A., Perry, A., Gutmann, D.H., and Ratner, N. (2006). Large-scale molecular comparison of human schwann cells to malignant peripheral nerve sheath tumor cell lines and tissues. *Cancer Res*, 66, 2584–2591.

Miller, S.J., Jessen, W.J., Mehta, T., Hardiman, A., Sites E., Kaiser, S., Jegga, A.G., Li, H., Upadhyaya, M., Giovannini, M., Muir, D., Wallace, M.R., Lopez, E., Serra, E., Nielsen, G.P., Lazaro, C., Stemmer-Rachamimov, A., Page, G., Aronow, B.J., and Ratner, N. (2009). Integrative genomic analyses of neurofibromatosis tumours identify SOX9 as a biomarker and survival gene. *EMBO Mol Med*, 1, 236–248.

Monk, K.R., Naylor, S.G., Glenn, T.D., Mercurio, S., Perlin, J.R., Dominguez, C., Moens, C.B., and Talbot, W.S. (2009). A G protein-coupled receptor is essential for Schwann cells to initiate myelination. *Science*, 325, 1402–1405.

Monk, K.R., Naylor, S.G., Glenn, T.D., Mercurio, S., Perlin, J.R., Dominguez, C., Moens, C.B., and Talbot, W.S. (2009). A G protein-coupled receptor is essential for Schwann cells to initiate myelination. *Science*, 325, 1402–1405.

Monk, K.R., Oshima, K., Jörs, S., Heller, S., and Talbot, W.S. (2011). Gpr126 is essential for peripheral nerve development and myelination in mammals. *Dev Camb Engl*, 138, 2673–2680.

Morell, P., and Quarles, R.H. (1999). Characteristic Composition of Myelin. In: Siegel, G.J., Agranoff, B.W., Albers, R.W., Fisher, S.K., and Uhler, M.D. (ed). Basic Neurochemistry: Molecular, Cellular and Medical Aspects. 6th edition.

Morgello, S. (2018). HIV neuropathology. *Handb Clin Neurol*, 152, 3–19.

Moriarty, T.J., Shi, M., Lin, Y.P., Ebady, R., Zhou, H., Odisho, T., Hardy, P.O., Salman-Dilgimen, A., Wu, J., Weening, E.H., Skare, J.T., Kubes, P., Leong, J., and Chaconas, G. (2012). Vascular binding of a pathogen under shear force through mechanistically distinct sequential interactions with host macromolecules. *Mol. Microbiol*, 86, 1116–1131.

Morris, J.H., Hudson, A.R., and Weddell, G. (1972). A study of degeneration and regeneration in the divided rat sciatic nerve based on electron microscopy. II. The development of the ‘‘regenerating unit’’. *Z Zellforsch Mikrosk Anat*, 124, 103–130.

Mukherjee, N., Corcoran, D.L., Nusbaum, J.D., Reid, D.W., Georgiev, S., Hafner, M., Ascano, M. Jr., Tuschl, T., Ohler, U., and Keene, J.D. (2011). Integrative regulatory mapping indicates that the RNA-binding protein HuR (ELAVL1) couples pre-mRNA processing and mRNA stability. *Mol Cell*, 43, 327–339.

Müllegger, R.R., McHugh, G., Ruthazer, R., Binder, B., Kerl, H., and Steere, A.C. (2000). Differential expression of cytokine mRNA in skin specimens from patients with erythema migrans or acrodermatitis chronica atrophicans. *J Investig Dermatol*, 115, 1115–1123.

Nadelman, R.B., Hanincova, K., Mukherjee, P., Liveris, D., Nowakowski, J., McKenna, D., Brisson, D., Cooper, D., Bittker, S., Madison, G., Holmgren, D., Schwartz, I., and Wormser, G.P. (2012). Differentiation of reinfection from relapse in recurrent Lyme disease. *N Engl J Med*, 367, 1883–90.

Napoli, I., Noon, L.A., Ribeiro, S., Kerai, A.P., Parrinello, S., Rosen-berg, L.H., Collins, M.J., Harrisingh, M.C., White, I.J., Woodhoo, A., and Lloyd, A.C. (2012). A central role for the ERK-signaling path- way in controlling Schwann cell plasticity and peripheral nerve regeneration *in vivo*. *Neuron*, 73, 729–742.

Natalie Wu, L.M., and Lu, Q.R. (2019). Therapeutic targets for malignant peripheral nerve sheath tumors. *Future Neurology*, 14, FNL7.

Nave, K.A. (2010). Myelination and the trophic support of long axons. *Nat Rev Neurosci*, 11, 275–283.

Nave, K.A., and Werner, H.B. (2014). Myelination of the nervous system: mechanisms and functions. *Annu Rev Cell Dev Biol*, 30, 503–33.

Nelson, C. A., Saha, S., Kugeler, K.J., Delorey, M.J., Shankar, M.B., and Hinckley, A.F. (2015). Incidence of Clinician-Diagnosed Lyme Disease. *Emerg Infect Dis*, 21, 1625–1631.

Nguyen, L.H., Robinton, D.A., Seligson, M.T., Wu, L., Li, L., Rakheja, D., Comerford, S.A., Ramezani, S., Sun, X., Parikh, M.S., Yang, E.H., Powers, J.T., Shinoda, G., Shah, S.P., Hammer, R.E., Daley, G.Q., and Zhu, H. (2014). Lin28b is sufficient to drive liver cancer and necessary for its maintenance in murine models. *Cancer Cell*, 26, 248–261.

NIH (no authors listed). (1998). Neurofibromatosis. Conference statement. National Institutes of Health Consensus Development Conference. *Arch Neurol*, 45, 575–578.

Nikolsky, Y., Ekins, S., Nikolskaya, T., and Bugrim, A. (2005). A novel method for generation of signature networks as biomarkers from complex high throughput data. *Toxicol Lett*, 158, 20–29.

Ogden, N.H., Lindsay, L.R., Morshed, M., Sockett, P.N., and Artsob, H. (2009). The emergence of Lyme disease in Canada. *CMAJ* 180, 1221–1224.

Ogrinc, K., Lusa, L., Lotrič-Furlan, S., Bogovič, P., Stupica, D., Cerar, T., Ružić-Sabljić, E., and Strle, F. (2016). Course and Outcome of Early European Lyme Neuroborreliosis (Bannwarth Syndrome): Clinical and Laboratory Findings. *Clin Infect Dis*, 63, 346–53.

Okuda, T., Higashi, Y., Kokame, K., Tanaka, C., Kondoh, H., and Miyata, T. (2004). *Ndrg1*-Deficient Mice Exhibit a Progressive Demyelinating Disorder of Peripheral Nerves. *Mol Cell Biol* 24, 3949–3956.

Ortiz-Zapater, E., Pineda, D., Martínez-Bosch, N., Fernández-Miranda, G., Iglesias, M., Alameda, F., Moreno, M., Eliscovich, C., Eyras, E., Real, F.X., Méndez, R., and Navarro, P. (2011). Key contribution of CPEB4-mediated translational control to cancer progression. *Nat Med*, 18, 83–90.

Oschmann P., Dorndorf, W., Hornig, C., Schäfer, C., Wellensiek, H.J., and Pflughaupt, K.W. (1998). Stages and syndromes of neuroborreliosis. (1998). *J Neurol*, 245, 262–272.

Pal, U., Li, X., Wang, T., Montgomery, R. R., Ramamoorthi, N., DeSilva, A. M., Yang, X., Pypaert, M., Pradhan, D., Kantor, FS., Telford, S., Anderson, JF., and Fikrig, E. (2004). TROSPA, an *Ixodes scapularis* receptor for *Borrelia burgdorferi*. *Cell*, 119, 457–468.

Palmer, E., Rees, R.J., and Weddell, G. (1965). Experimental studies on nerve fibers in leprosy. I. The reaction of rat Schwann cells toward carbon particles, Mycobacterium lepraemurium and Mycobacterium leprae. *Int J Lepr*, 33, 137–159.

Pannese, E. (1981). The satellite cells of the sensory ganglia. *Adv Anat Embryol Cell Biol*, 65, 1–111.

Parkinson, D.B., Dong, Z., Bunting, H., Whitfield, J., Meier, C., Marie, H., Mirsky, R., and Jessen, K.R. (2001). Transforming growth factor beta (TGFbeta) mediates Schwann cell death *in vitro* and *in vivo*: examination of c-Jun activation, interactions with survival signals, and the relationship of TGFbeta-mediated death to Schwann cell differentiation. *J Neurosci*, 21, 8572–8585.

Parrinello, S., Noon, L.A., Harrisingh, M.C., Digby, P.W., Rosenberg, L.H., Cremona, C.A., Echave, P., Flanagan, A.M., Parada, L.F., and Lloyd, A.C. (2008). NF1 loss disrupts Schwann cell–axonal interactions: a novel role for semaphorin 4F. *Genes Dev*, 22, 3335–3348.

Parrinello, S., and Lloyd, A.C. (2009). Neurofibroma development in NF1--insights into tumour initiation. *Trends Cell Biol*, 19, 395–403.

Parry GJ. (1988). Peripheral neuropathies associated with human immunodeficiency virus infection. *Ann Neurol*, 23 Suppl, S49–53.

Parthasarathy, G., Fevrier, H.B., and Philipp, M.T. (2013). Non-viable Borrelia burgdorferi induce inflammatory mediators and apoptosis in human oligodendrocytes. *Neurosci Lett*, 556, 200–203.

Pascale, A., Amadio, M., and Quattrone, A. (2008). Defining a neuron: neuronal ELAV proteins. *Cell Mol Life Sci*, 65, 128–140.

Patel, A.J., Liao, C.P., Chen, Z., Liu, C., Wang, Y., and Le, L.Q. (2014). BET bromodomain inhibition triggers apoptosis of NF1-associated malignant peripheral nerve sheath tumors through Bim induction. *Cell Rep*, 6, 81–92.

Patel, A..V, Eaves, D., Jessen, W.J., Rizvi, T.A., Ecsedy, J.A., Qian, M.G., Aronow, B.J., Perentesis, J.P., Serra, E., Cripe, T.P., Miller, S.J., and Ratner, N. (2012). Ras-driven transcriptome analysis identifies aurora kinase A as a potential malignant peripheral nerve sheath tumor therapeutic target. *Clin Cancer Res*, 18, 5020–5030.

Pereira, B., Billaud, M., and Almeida, R. (2017). RNA-Binding Proteins in Cancer: Old Players and New Actors. *Trends Cancer*, 3, 506–528.

Pereira, J.A., Lebrun-Julien, F., and Suter, U. (2012). Molecular mechanisms regulating myelination in the peripheral nervous system. *Trends Neurosci*, 35, 123–134.

Perron, G., Jandaghi, P., Solanki, S., Safisamghabadi, M., Storoz, C., Karimzadeh, M., Papadakis, A.I., Arseneault, M., Scelo, G., Banks, R.E., Tost, J., Lathrop, M., Tanguay, S., Brazma, A., Huang, S., Brimo, F., Najafabadi, H.S., and Riazalhosseini, Y. (2018). A General Framework for Interrogation of mRNA Stability Programs Identifies RNA-Binding Proteins that Govern Cancer Transcriptomes. *Cell Rep*, 23, 1639–1650.

Peters, A., Palay, S.L., and Webster, H.D. (1991). The fine structure of the nervous system. *Oxford University Press*, New York.

Petnicki-Ocwieja, T., Chung, E., Acosta, D.I., Ramo,s L.T., Shin, O.S., Ghosh, S., Kobzik, L., Li, X., and Hu, L.T. (2013). TRIF mediates Toll-like receptor 2-dependent inflammatory responses to *Borrelia burgdorferi*. *Infect Immun*, 81, 402–10.

Petzke, M.M., Brooks, A., Krupna, M.A., Mordue, D. and Schwartz, I. (2009). Recognition of Borrelia burgdorferi, the Lyme disease spirochete, by TLR7 and TLR9 induces a type I IFN response by human immune cells. *J Immunol*, 183, 5279–5292.

Piesman, J., and Gern, L. (2004). Lyme borreliosis in Europe and North America. *Parasitology,* 129, 191–S220.

Plotkin, S.A. (2011). Correcting a public health fiasco: the need for a new vaccine against Lyme disease. *Clin Infect Dis*, 52 (suppl 3), s271–75.

Preac-Mursic, V., Wilske, B., and Schierz, G. (1986). European *Borrelia burgdorferi* isolated from humans and ticks culture conditions and antibiotic susceptibility. *Zentralbl Bakteriol Mikrobiol Hyg* A, 263, 112–18.

Previtali, S.C., Nodari, A., Taveggia, C., Pardini, C., Dina, G., Villa, A., Wrabetz, L., Quattrini, A., and Feltri, M.L. (2003). Expression of laminin receptors in Schwann cell differentiation: Evidence for distinct roles. *J Neurosci*, 23, 5520–5530.

Pritt, B.S., Respicio-Kingry, L.B., Sloan, L.M., Schriefer, M.E., Replogle, A.J., Bjork, J., Liu, G., Kingry, L.C., Mead, P.S., Neitzel, D.F., Schiffman, E., Johnson, D.K.H., Davis, J.P., Paskewitz, S.M., Boxrud, D., Deedon, A., Lee, X., Miller, T.K., Feist, M.A., Steward, C.R., Theel, E.S., Patel, R., Irish, C.L. and Petersen, J.M. (2016). *Borrelia mayonii* sp. nov., a member of the *Borrelia burgdorferi* sensu lato complex, detected in patients and ticks in the upper midwestern United States. *Int J Syst Evol Microbiol*, 66, 4878–4880.

Quarles, R.H., Macklin, W.B., and Morell, P. (2006). Myelin Formation, Structure and Biochemistry. 51–72. In: Siegel, G.J., Albers, R.W., Brady, S.T., and Price, D.L. (ed). Basic Neurochemistry. Molecular, cellular and medical aspects. American Society for Neurochemistry. *Elsevier Academic Press*. 7th edition.

Raasakka, A., Ruskamo, S., Kowal, J., Han, H., Baumann, A., Myllykoski, M., Fasano, A., Rossano, R., Riccio, P., Bürck, J., Ulrich, A.S., Stahlberg, H., Kursula, P. (2019). Molecular structure and function of myelin protein P0 in membrane stacking. *Sci Rep*, 9, 642.

Radolf, J.D., Caimano, M.J., Stevenson, B.T., and Linden, H. (2012). Of ticks, mice and men: understanding the dual-host lifestyle of Lyme disease spirochaetes. *Nat Rev Microbiol*, 10, 87–99.

Rahrmann, E.P., Watson, A.L., Keng, V.W., Choi, K., Moriarity, B.S., Beckmann, D.A., Wolf, N.K., Sarver, A., Collins, M.H., Moertel, C.L., Wallace, M.R., Gel, B., Serra, E., Ratner, N., and Largaespada, D.A. (2013). Forward genetic screen for malignant peripheral nerve sheath tumor formation identifies new genes and pathways driving tumorigenesis. *Nat Genet*, 45, 756–766.

Rambukkana, A., Zanazzi, G., Tapinos, N., and Salzer, J.L. (2002). Contact-dependent demyelination by Mycobacterium leprae in the absence of immune cells. *Science*, 296, 927–931.

Ramesh, G., Santana-Gould, L., Inglis, F.M., England, J.D. and Philipp, M.T. (2013). The Lyme disease spirochete Borrelia burgdorferi induces inflammation and apoptosis in cells from dorsal root ganglia. *J Neuroinflammation,* 10, 88.

Ramesh, G., Didier, P.J., England, J.D., Santana-Gould, L., Doyle-Meyers, L.A., Martin, D.S., Jacobs, M.B., and Philipp, M.T. (2015a). Inflammation in the Pathogenesis of Lyme Neuroborreliosis. *Am J Pathol*, 185, 1344–1360.

Ramesh, G., Meisnerand, O.C, and Philipp, M.T. (2015b). Anti-inflammatory effects of dexamethasone and meloxicam on Borrelia burgdorferi-induced inflammation in neuronal cultures of dorsal root ganglia and myelinating cells of the peripheral nervous system. *J Neuroinflammation* 12, 240.

Ranvier, L. (1872). Recherches sur l'histologie et la physiologie des nerfs. *Arch Physiol Norm Pathol*, 4, 129–149.

Rebane, A., Aab, A., and Steitz, J.A. (2004). Transportins 1 and 2 are redundant nuclear import factors for hnRNP A1 and HuR. *RNA*, 10, 590–599.

Ritchie, M.E., Phipson, B., Wu, D., Hu, Y., Law, C.W., Shi, W., and Smyth, G.K. (2015). Limma powers differential expression analyses for RNA-sequencing and microarray studies. *Nucleic Acids Res,* 43, e47.

Roberts, E.D., Bohm, R.P.Jr., Lowrie, R.C. Jr., Habicht, G., Katona, L., Piesman, J., and Philipp, M.T. (1998). Pathogenesis of Lyme neuroborreliosis in the rhesus monkey: the early disseminated and chronic phases of disease in the peripheral nervous system. *J Infect Dis*, 178, 722–732.

Roberts, S.L., Dun, X.P., Doddrell, R.D.S., Mindos, T., Drake, L.K., Onaitis, M.W., Florio, F., Quattrini, A., Lloyd, A.C., D'Antonio, M., and Parkinson, D.B. (2017). Sox2 expression in Schwann cells inhibits myelination in vivo and induces influx of macrophages to the nerve. *Development*, 144, 3114–3125.

Robitaille, R. (1998). Modulation of synaptic efficacy and synaptic depression by glial cells at the frog neuromuscular junction. *Neuron*, 21, 847–855.

Rotshenker, S. (2011). Wallerian degeneration: The innate- immune response to traumatic nerve injury. *J Neuroinflamm*, 8: 109.

Rupprecht, T.A., Koedel, U., Fingerle, V., and Pfister, H.-W. (2008). The Pathogenesis of Lyme Neuroborreliosis: From Infection to Inflammation. *Mol Med*, 14, 205–212.

Rupprecht, T.A., Manz, K.M., Fingerle, V., Lechner, C., Klein, M., Pfirrmann, M., and Koedel, U. (2018). Diagnostic value of cerebrospinal fluid CXCL13 for acute Lyme neuroborreliosis. A systemic review and meta- analysis. *Clin Microbiol Infect*, 24, 1234–1240.

Saher, G., Quintes, S., and Nave, K.A. (2011). Cholesterol: a novel regulatory role in myelin formation. *Neuroscientist*, 17, 79–93.

Salazar, J.C., Pope, C.D., Sellati, T.J., Feder, H.M.Jr, Kiely, T.G., Dardick, K.R., Buckman, R.L., Moore, M.W., Caimano, M.J., Pope, J.G., Krause, P.J., and Radolf, J.D. (2003). Coevolution of markers of innate and adaptive immunity in skin and peripheral blood of patients with erythema migrans. *J Immunol*, 171, 2660–2670.

Salzer, J.L. (2003). Polarized domains of myelinated axons. *Neuron*, 40, 297–318.

Salzer, J.L., Brophy, P.J., and Peles, E. (2008). Molecular domains of myelinated axons in the peripheral nervous system. *Glia*, 56, 1532–1540.

Salzer, J.L. (2015). Schwann Cell Myelination. *Cold Spring Harb Perspect Biol*, 7:a020529.

Samuels, D.S., and Radolf, J.D. (2010). *Borrelia*: Molecular Biology, Host Interaction and Pathogenesis. *Caister Academic Press*. 547ISBN 978-1-904455-58-5.

Sanchez, E., Vannier, E., Wormser, G.P., and Hu, L.T. (2016). Diagnosis, treatment, and prevention of Lyme disease, human granulocytic anaplasmosis, and babesiosis: a review. *JAMA,* 315, 1767–1777.

Scherer, S.S., and Arroyo, E.J. (2002). Recent progress on the molecular organization of myelinated axons. *J Peripher Nerv Syst*, 7, 1–12.

Schmid, D., Zeis, T., and Schaeren-Wiemers, N. (2014). Transcriptional regulation induced by cAMP elevation in mouse Schwann cells. *ASN Neuro*, 6, 137–157.

Schmitt, S., Castelvetri, L.C., and Simons, M. (2014). Metabolism and functions of lipids in myelin. *Biochim Biophys Acta*, 1851, 999–1005.

Schoen, R.T. (2020). Challenges in the Diagnosis and Treatment of Lyme Disease. *Curr Rheumatol Rep,* 22:3.

Schroder, J.M. (1972). Altered ratio between axon diameter and myelin sheath thickness in regenerated nerve fibers. *Brain Res*, 45, 49–65.

Schwarzova, K., Ciznar, I., Svihrova, V., and Hudeckova, H. (2019). Initial attachment of Borrelia burgdorferi spirochetes to Vero cells. *Bratisl Lek Listy*, 120, 872–875.

Serrano-Coll, H., Salazar-Peláez, L., Acevedo-Saenz, L., and Cardona-Castro, N. (2018). Mycobacterium leprae-induced nerve damage: direct and indirect mechanisms. *Pathog Dis*, 76.

Seshu, J., Esteve-Gassent, M.D., Labandeira-Rey, M., Kim, J.H., Trzeciakowski, J.P., Höök, M., Skare, J.T. (2006). Inactivation of the fibronectin-binding adhesin gene *bbk32* significantly attenuates the infectivity potential of *Borrelia burgdorferi*. *Mol Microbiol*, 59, 1591–1601.

Shannon, P., Markiel, A., Ozier, O., Baliga, N.S., Wang, J.T., Ramage, D., Amin, N., Schwikowski, B., and Ideker, T. (2003). Cytoscape: a software environment for integrated models of biomolecular interaction networks. *Genome Res*, 13, 2498–2504.

Sheflin, L.G., Zhang, W., and Spaulding, S.W. (2001). Androgen regulates the level and subcellular distribution of the AU-rich ribonucleic acid-binding protein HuR both in vitro and in vivo. *Endocrinology*, 142, 2361–2368.

Shimamoto, K., Tanimoto, K., Fukazawa, T., Nakamura, H., Kanai, A., Bono, H., Ono, H., Eguchi, H., and Hirohashi, N. (2020). GLIS1, a novel hypoxia-inducible transcription factor, promotes breast cancer cell motility via activation of WNT5A. *Carcinogenesis*, pii: bgaa010.

Shin, O.S., Isberg, R.R., Akira, S., Uematsu, S., Behera, A.K. and Hu, L.T. (2008). Distinct roles for MyD88 and Toll-like receptors 2, 5, and 9 in phagocytosis of Borrelia burgdorferi and cytokine induction. *Infect Immun*, 76, 2341–2351.

Sigal, L.H., Zahradnik, J.M., Lavin, P., Patella, S.J., Bryant, G., Haselby, R., Hilton, E., Kunkel, M., Adler-Klein, D., Doherty, T., Evans, J., Molloy, P.J., Seidner, A.L., Sabetta, J.R., Simon, H.J., Klempner, M.S., Mays, J., Marks, D., and Malawista, S.E. (1998). A vaccine consisting of recombinant Borrelia burgdorferi outer-surface protein A to prevent Lyme disease. Recombinant Outer- Surface Protein A Lyme Disease Vaccine Study Consortium. *N Engl J Med*, 339, 216–222.

Simone, L.E., and Keene, J.D. (2013). Mechanisms coordinating ELAV/Hu mRNA regulons. *Curr Opin Genet Dev*, 23, 35–43.

Sjöwall, J., Fryland, L., Nordberg, M., Sjögren, F., Garpmo, U., Jansson, C., Carlsson, S.A, Bergström, S., Ernerudh, J., Nyman, D., Forsberg, P., and Ekerfelt, C. (2011). Decreased Th1-type inflammatory cytokine expression in the skin is associated with persisting symptoms after treatment of erythema migrans. *PLoS ONE,* 6, e18220.

Skerman, V.B.D., McGowan, V., and Sneath, P.H.A. (1989). Approved list of bacterial names (amended). *ASM Press*, Washington (DC).

Skotheim, R.I., Kallioniemi, A., Bjerkhagen, B., Mertens, F., Brekke, H.R., Monni, O., Mousses, S., Mandahl, N., Soeter, G., Nesland, J.M., Smeland, S., Kallioniemi, O.P., and Lothe, R.A. (2003). Topoisomerase-II alpha is upregulated in malignant peripheral nerve sheath tumors and associated with clinical outcome. *J Clin Oncol*, 21, 4586–4591.

Small, J.R., Ghabriel, M.N., and Allt, G. (1987). The development of Schmidt–Lanterman incisures: An electron microscope study. *J Anat*, 150, 277–286.

Sobue, G., and Pleasure, D. (1984). Schwann cell galactocerebroside induced by derivatives of adenosine3',5'-monophosphate. *Science*, 224, 72–74.

Srikantan, S., and Gorospe, M. (2011). UneCLIPsing HuR nuclear function. Mol Cell, 43, 319–321.

Srikantan, S., and Gorospe, M. (2012). HuR function in disease. *Front Biosci*, 17, 189–205.

Stanek, G., and Wormser, G.P., Gray, J., and Strle, F. (2012). Lyme borreliosis. *Lancet*, 379, 461–473.

Steere, A.C., Grodzicki, R.L., Kornblatt, A.N., Craft, J.E., Barbour, A.G., Burgdorfer W., Schmid, G.P., Johnson, E., and Malawista, S.E. (1983). The spirochetal etiology of Lyme disease. *N Engl J Med*, 308, 733–740.

Steere, A.C., Sikand, V.K., Meurice, F., Parenti, D.L., Fikrig, E., Schoen, R.T., Nowakowski, J., Schmid, C.H., Laukamp, S., Buscarino, C., Krause, D.S. (1998). Vaccination against Lyme disease with recombinant *Borrelia burgdorferi* outer-surface lipoprotein A with adjuvant. Lyme Disease Vaccine Study Group. *N Engl J Med*, 339, 209–215.

Steere, A.C., and Sikand, V.K. (2003). The presenting manifestations of Lyme disease and the outcomes of treatment. *N Engl J Med*, 348, 2472–2474.

Steere, A.C., Coburn, J., and Glickstein, L. (2004). The emergence of Lyme disease. *J. Clin. Invest.* 113, 1093–1101.

Steere, A.C., and Livey, I. (2012). Lyme disease vaccines. In: Plotkin SA, Orenstein WA, Offit PA, eds. Vaccines, 6th edn. Philadelphia, PA: *Elsevier*, 1122–32.

Steere, A.C., Strle, F., Wormser, G.P., Hu, L.T., Branda, J.A., Hovius, J.W.R., Li, X., and Mead, P.S. (2016). Lyme borreliosis. *Nature reviews. Disease primers*, 2, 16090.

Sterman, A.B., Nelson, S., and Barclay, P. (1982). Demyelinating neuropathy accompanying Lyme disease. *Neurology*, 32, 1302–1305.

Stierli, S., Napoli, I., White, I. J., Cattin, A. L., Monteza Cabrejos, A., Garcia Calavia, N., Malong, L., Ribeiro, S., Nihouarn, J., Williams, R., Young, K.M., Richardson, W.D., and Lloyd, A.C. (2018). The regulation of the homeostasis and regeneration of peripheral nerve is distinct from the CNS and independent of a stem cell population. *Development*, 145: dev170316.

Strle, K., Drouin, E.E., Shen, S., El Khoury, J., McHugh, G., Ruzic-Sabljic, E., Strle, F., and Steere, A.C. (2009). *Borrelia burgdorferi* stimulates macrophages to secrete higher levels of cytokines and chemokines than *Borrelia afzelii* or *Borrelia garinii*. *J Infect Dis,* 200, 1936–43.

Stübs, G., Fingerle, V., Wilske, B., Göbel, U.B., Zähringer, U., Schumann, R.R., and Schröder, N.W. (2009). Acylated cholesteryl galactosides are specific antigens of *Borrelia* causing lyme disease and frequently induce antibodies in late stages of disease. *J Biol Chem*, 284, 13326–34.

Stünzner, D., Hubálek, Z., Halouzka, J., Wendelin, I., Sixl, W., and Marth, E. (2006). Prevalence of *Borrelia burgdorferi* sensu lato in the tick *Ixodes ricinus* in the Styrian mountains of Austria. *Wien Klin Wochenschr*, 118, 682–685.

Subramanian, A., Tamayo, P., Mootha, V.K., Mukherjee, S., Ebert, B.L., Gillette, M.A., Paulovich, A., Pomeroy, S.L., Golub, T.R., Lander, E.S., and Mesirov, J.P. (2005). Gene set enrichment analysis: a knowledge-based approach for interpreting genome-wide expression profiles. *Proc Natl Acad Sci U S A*, 102, 15545–15550.

Suter, U., and Snipes, G.J. (1995). Peripheral myelin protein-22: Facts and hypotheses. *J Neurosci Res*, 40, 145–151.

Svaren, J., and Meijer, D. (2008). The molecular machinery of myelin gene transcription in Schwann cells. *Glia*, 56, 1541–1551.

Syroid, D.E., Maycox, P.J., Soilu-Hänninen, M., Petratos, S., Bucci, T., Burrola, P., Murray, S., Cheema, S., Lee, K.-F., Lemke, G., and Kilpatrick, T.J. (2000). Induction of postnatal Schwann cell death by the low-affinity neurotrophin receptor in vitro and after axotomy. *J Neurosci*, 20, 5741–5747.

Szabo, A., Dalmau, J., Manley, G., Rosenfeld, M., Wong, E., Henson, J., Posner, J.B., and Furneaux, H.M. (1991). HuD, a paraneoplastic encephalomyelitis antigen, contains RNA- binding domains and is homologous to Elav and Sex-lethal. *Cell*, 67, 325–333.

Taveggia, C., Zanazzi, G., Petrylak, A., Yano, H., Rosenbluth, J., Einheber, S., Xu, X., Esper, R.M., Loeb, J.A., Shrager, P., Chao, M.V., Falls, D.L., Role, L., and Salzer, J.L. (2005). Neuregulin-1 type III determines the ensheath- ment fate of axons. *Neuron*, 47, 681–694.

Taveggia, C., and Bolino, A. (2018). DRG Neuron/Schwann Cells Myelinating Cocultures. *Methods Mol Biol*, 1791, 115–129.

Tong, J., Hannan, F., Zhu, Y., Bernards, A., and Zhong, Y. (2002). Neurofibromin regulates G protein-stimulated adenylyl cyclase activity. *Nat Neurosci*, 5, 95–96.

Tremblay, A.M., Missiaglia, E., Galli, G.G., Hettmer, S., Urcia, R., Carrara, M., Judson, R.N., Thway, K., Nadal, G., Selfe, J.L., Murray, G., Calogero, R.A., De Bari, C., Zammit, P.S., Delorenzi, M., Wagers, A.J., Shipley, J., Wackerhage, H., and Camargo, F.D. (2014). The Hippo transducer YAP1 transforms activated satellite cells and is a potent effector of embryonal rhabdomyosarcoma formation. *Cancer Cell*, 26, 273–287.

Tu, Y., Luo, R., Li, X., Lin, M., and Qiu, M. (2012). Hypermyelination and overexpression of neuregulin-1 in thoracic sympathetic nerves in patients with primary palmar hyperhidrosis. *J Clin Neurosci*, 19, 1651–1653.

Tyagi, N., Maheswaran, T., and Wimalaratna, S. (2015). Neuroborreliosis: the Guillain-Barré mimicker. *BMJ Case Rep*, 2015: bcr2014209080.

Uesaka, T., Nagashimada, M., and Enomoto, H. (2015). Neuronal differentiation in Schwann cell lineage underlies postnatal neurogenesis in the enteric nervous system. *J Neurosci*, 35, 9879–9888.

Uyemura, K., Asou, H., and Takeda, Y. (1993). Structure and function of peripheral nerve myelin proteins. *Prog Brain Res*, 105, 311–318.

van den Wijngaard, C.C., Hofhuis, A., Wong, A., Harms, M.G., de Wit, G.A., Lugnér, A.K., Suijkerbuijk, A.W.M., Mangen, M.J., and van Pelt, W. (2017). The cost of Lyme borreliosis. *Eur J Public Health*, 27, 538–547.

Varela-Rey, M., Iruarrizaga-Lejarreta, M., Lozano, J.J., Aransay, A.M., Fernandez, A.F., Lavin, J.L., Mósen-Ansorena, D., Berdasco, M., Turmaine, M., Luka, Z., Wagner, C., Lu, S.C., Esteller, M., Mirsky, R., Jessen, K.R., Fraga, M.F., Martínez-Chantar, M.L., Mato, J.M., and Woodhoo, A. (2014). *Neuron*, 81, 1024–1039

Vedeler, C.A., Matre, R., Kristoffersen, E.K., and Ulvestad, E. (1991). IgG Fc receptor heterogeneity in human peripheral nerves*. Acta Neurol Scand*, 84, 177–180.

Veinović, G., Ružić-Sabljić2, E., Strle, F., and Cerar, T. (2016). Comparison of Growth of *Borrelia afzelii*, *Borrelia garinii*, and *Borrelia burgdorferi* Sensu Stricto at Five Different Temperatures. *PLoS ONE*, *11, e0157706.*

Verma, A., Brissette, C.A., Bowman, A., and Stevenson, B. (2009). *Borrelia burgdorferi* BmpA is a laminin-binding protein. *Infect Immun*, 77, 4940–4946.

Wallquist, W., Plantman, S., Thams, S., Thyboll, J., Kortesmaa, J., Lannergren, J., Domogatskaya, A., Ogren, S.O., Risling, M., Hammarberg, H., et al. (2005). Impeded interaction be- tween Schwann cells and axons in the absence of laminin α4. *J Neurosci*, 25, 3692–3700.

Wang, J., Guo, Y., Chu, H., Guan, Y., Bi ,J., and Wang, B. (2013). Multiple functions of the RNA-binding protein HuR in cancer progression, treatment responses and prognosis. *Int J Mol Sci*, 14, 10015-10041.

Wang, J., Zhang, S., Li, L., and Zhang, L. (2015). Involvement of Wnt5a within the cerebrospinal fluid-contacting nucleus in nerve injury-induced neuropathic pain. *Int J Neurosci*, 125, 147–153.

Wang, J.T., Medress, Z.A., and Barres, B.A. (2012). Axon degeneration: Molecular mechanisms of a self-destruction pathway. *J Cell Biol*, 196, 7–18.

Wang, P., Dadhwal, P., Cheng, Z., Zianni, M.R., Rikihisa, Y., Liang, F.T., and Li, X. (2013). *Borrelia burgdorferi* oxidative stress regulator BosR directly represses lipoproteins primarily expressed in the tick during mammalian infection. *Mol Microbiol*, 89, 1140–53.

Wang, W., Furneaux, H., Cheng, H., Caldwell, M.C., Hutter, D., Liu, Y., Holbrook, N., and Gorospe, M. (2000). HuR regulates p21 mRNA stabilization by UV light. *Mol Cell Biol*, 760–769.

Wanner, I.B., Guerra, N.K., Mahoney, J., Kumar, A., Wood, P.M., Mirsky, R., and Jessen K.R. (2006). Role of N-cadherin in Schwann cell precursors of growing nerves. *Glia*, 54, 439–459.

Watson, A.L., Rahrmann, E.P., Moriarity, B.S., Choi, K., Conboy, C.B., Greeley, A.D., Halfond, A.L., Anderson, L.K., Wahl, B.R., Keng, V.W., Rizzardi, A.E., Forster, C.L., Collins, M.H., Sarver, A.L., Wallace, M.R., Schmechel, S.C., Ratner, N., and Largaespada, D.A. (2013). Canonical

Wnt/beta-catenin signaling drives human schwann cell transformation, progression, and tumor maintenance. *Cancer Discov*, 3, 674–689.

Winseck, A.K., Caldero, J., Ciutat, D., Prevette, D., Scott, S.A., Wang, G., Esquerda, J.E., and Oppenheim, R.W. (2002). In vivo analysis of Schwann cell programmed cell death in the embryonic chick: regulation by axons and glial growth factor. *J Neurosci*, 22, 4509–4521.

Wiśniewski, J.R., Zougman, A., Nagaraj, N., and Mann, M. (2009). Universal sample preparation method for proteome analysis. *Nat Methods,* 6, 359–62.

Wolpowitz, D., Mason, T.B., Dietrich, P., Mendelsohn, M., Talmage, D.A., and Role, L.W. (2000). Cysteine-rich domain isoforms of the neuregulin-1 gene are required for maintenance of peripheral synapses. *Neuron*, 25, 79–91.

Woodhoo, A., Alonso, M.B., Droggiti, A., Turmaine, M., D'Antonio, M., Parkinson, D.B., Wilton, D.K., Al-Shawi, R., Simons, P., Shen, J., Guillemot, F., Radtke, F., Meijer, D., Feltri, M.L., Wrabetz, L., Mirsky, R., and Jessen, K.R. (2009). Notch controls embryonic Schwann cell differentiation, postnatal myelination and adult plasticity. *Nat Neurosci*, 12, 839–847.

Wormser G.P., Dattwyler, R.J., Shapiro, E.D., Halperin, J.J., Steere, A.C., Klempner, M.S., Krause, P.J., Bakken, J.S., Strle, F., Stanek, G., Bockenstedt, L., Fish, D., Dumler, J.S., and Nadelman, R.B. (2006). The clinical assessment, treatment, and prevention of lyme disease, human granulocytic anaplasmosis, and babesiosis: clinical practice guidelines by the Infectious Diseases Society of America. *Clin Infect Dis*, 43, 1089–134.

Wressnigg, N., Po¨llabauer, E.M., Aichinger, G., Portsmouth, D., Low-Baselli, A., Fritsch, S., Livey, I., Crowe, B.A., Schwendinger, M., Brühl, P., Pilz, A., Dvorak, T., Singer, J., Firth, C., Luft, B., Schmitt, B., Zeitlinger, M., Müller, M., Kollaritsch, H., Paulke-Korinek, M., Esen, M., Kremsner, P.G., Ehrlich, H.J., and Barrett, P.N. (2013). Safety and immunogenicity of a novel multivalent OspA vaccine against Lyme borreliosis in healthy adults: a double-blind, randomised, dose-escalation phase 1/2 trial. *Lancet Infect Dis*, 13, 680–689.

Wu, J., Williams, J.P., Rizvi, T.A., Kordich, J.J., Witte, D., Meijer, D., Stemmer-Rachamimov, A.O., Cancelas, J.A., and Ratner, N. (2008) Plexiform and dermal neurofibromas and pigmentation are caused by Nf1 loss in desert hedgehog-expressing cells. *Cancer Cell*, 13, 105–116.

Wu, L.M.N., Deng, Y., Wang, J., Zhao, C., Wang, J., Rao, R., Xu, L., Zhou, W., Choi, K., Rizvi, T.A., Remke, M., Rubin, J.B., Johnson, R.L., Carroll, T.J., Stemmer-Rachamimov, A.O., Wu, J., Zheng, Y., Xin, M., Ratner, N., and Lu, Q.R. (2018). Programming of Schwann Cells by Lats1/2-TAZ/YAP Signaling Drives Malignant Peripheral Nerve Sheath Tumorigenesis. *Cancer Cell*, 33, 292–308 e297.

Wurth, L., Papasaikas, P., Olmeda, D., Bley, N., Calvo, G.T., Guerrero, S., Cerezo-Wallis, D., Martinez-Useros, J., García-Fernández, M., Hüttelmaier, S., Soengas, M.S., and Gebauer, F. (2016). UNR/CSDE1 Drives a Post-transcriptional Program to Promote Melanoma Invasion and Metastasis. Cancer Cell, 30, 694–707.

Wurth, L., and Gebauer, F. (2015). RNA-binding proteins, multifaceted translational regulators in cancer. *Biochim Biophys Acta*, 1849, 881–886.

Xiang, X., Yang, Y., Du, J., Lin, T., Chen, T., Yang, X. F., and Lou, Y. (2017). Investigation of *ospC* Expression Variation among *Borrelia burgdorferi* Strains. *Frontiers in cellular and infection microbiology*, 7, 131.

Xiao, G.H., Gallagher, R., Shetler, J., Skele, K., Altomare, D.A., Pestell, R.G., Jhanwar, S., and Testa, J.R. (2005). The NF2 tumor suppressor gene product, merlin, inhibits cell proliferation and cell cycle progression by repressing cyclin D1 expression. *Mol Cell Biol*, 25, 2384–2394.

Xu, Q., Seemanapalli, S.V., Reif, K.E., Brown, C.R., and Liang, F.T. (2007). Increasing the recruitment of neutrophils to the site of infection dramatically attenuates *Borrelia burgdorferi* infectivity. *J Immunol*, 178, 5109–5115.

Yang, D.P., Zhang, D.P., Mak, K.S., Bonder, D.E., Pomeroy, S.L., and Kim, H.A. (2008). Schwann cell proliferation during Wallerian degeneration is not necessary for regeneration and remyelination of the peripheral nerves: Axon-dependent removal of newly generated Schwann cells by apoptosis. *Mol Cell Neurosci*, 38, 80–88.

Zambrano, M.C., Beklemisheva, A.A., Bryksin, A.V., Newman, S.A., and Cabello, F.P. (2004). Borrelia burgdorferi Binds to, Invades, and Colonizes Native Type I Collagen Lattices. *Infect Immun*, 72, 3138–3146.

Zhang, J.R., Hardham, J.M., Barbour, A.G., and Norris, S.J. (1997). Antigenic variation in Lyme disease borreliae by promiscuous recombination of VMP-like sequence cassettes. *Cell*, 89, 275–285.

Zhang, X., Meltzer, M.I., Pena, C.A., Hopkins, A.B., Wroth, L., and Fix, A.D. (2006). Economic impact of Lyme disease. *Emerg Infect Dis*, 12, 653–660.

Zhang, Y., Liu, T., Meyer, C.A., Eeckhoute, J., Johnson, D.S., Bernstein, B.E., Nusbaum, C., Myers, R.M., Brown, M., Li, W., and Liu, X.S. (2008). Model-based analysis of ChIP-Seq (MACS). *Genome Biol*, 9, R137.

Zheng, H., Chang, L., Patel, N., Yang, J., Lowe, L., Burns, D.K., and Zhu, Y. (2008). Induction of abnormal proliferation by nonmyelinating schwann cells triggers neurofibroma formation. *Cancer Cell*, 13, 117–128.

Zhi, H., Weening, E.H., Barbu, E.M., Hyde, J.A., Höök, M., and Skare, J.T. (2015). The BBA33 lipoprotein binds collagen and impacts *Borrelia burgdorferi*pathogenesis. *Mol Microbiol*, 96, 68–83.

Zhou A, et al. RNA Binding Protein, HuR, Regulates SCN5A Expression Through Stabilizing MEF2C transcription factor mRNA. J Am Heart Assoc. 2018;7(9).

Zhu, Y., Ghosh, P., Charnay, P., Burns, D.K., and Parada, L.F. (2002). Neurofibromas in NF1: Schwann cell origin and role of tumor environment. *Science*, 296, 920–922.

Zitvogel, L., Kepp, O., and Kroemer, G. (2010). Decoding cell death signals in inflammation and immunity. *Cell*, 140, 798–804.

SUPPLEMENTARY MATERIAL

Supplementary Table 1:

List of List of HuR targets (fold-change >1.5; adjusted p-value<0.05) identified after RIP-chip in neurofibroma samples

ProbeID	SYMBOL	Acc_No	Fold Change	P-Value	Adjusted P-Value	Mean Signal (HuR IP)	Mean Signal (IgG IP)
ILMN_1869109		AK095855	11.89	1.91E-06	0.000660274	8.68454	5.11286
ILMN_2152131	ACTB	NM_001101.2	81.2304	4.50E-10	8.53E-07	11.73842	5.39448
ILMN_1657283	ALKBH5	NM_017758.3	6.2082	4.89E-07	0.000206134	7.24846	4.6143
ILMN_1703477	ARHGEF2	NM_004723.2	8.6818	1.81E-05	0.00339241	7.93748	4.81948
ILMN_1758918	BRD2	NM_005104.2	4.9547	3.15E-05	0.00488611	7.53158	5.22277
ILMN_1768870	CAPZA2	NM_006136.2	6.2161	3.18E-06	0.000949275	7.41389	4.77788
ILMN_1738075	CMIP	NM_030629.1	61.698	7.70E-13	1.02E-08	10.96292	5.01576
ILMN_1811648	DCAKD	NM_024819.3	7.2111	4.98E-07	0.000206561	7.36123	4.51101
ILMN_1770127	DNAJA2	NM_005880.2	10.8066	2.07E-06	0.000695643	7.98767	4.55383
ILMN_3272378	EZR	NM_003379.4	6.0972	4.71E-05	0.00669565	8.21747	5.60933
ILMN_1703330	FEM1C	NM_020177.2	4.9192	1.33E-06	0.000482913	7.2957	4.99727
ILMN_1687384	IFI6	NM_022873.2	15.7898	1.81E-05	0.00339241	9.82157	5.84065
ILMN_1723467	ITGB1	NM_002211.2	7.4209	5.81E-05	0.00771731	8.2881	5.39652
ILMN_1810214	JUND	NM_005354.3	93.4441	1.40E-10	3.10E-07	13.03501	6.48898
ILMN_3210917	LOC389168	XR_019471.2	5.6767	7.85E-05	0.00946314	7.35711	4.85205
ILMN_1780861	LOC653506	XM_927769.1	4.1868	1.53E-05	0.00294781	6.62863	4.5628
ILMN_1757106	Mar-06	NM_005885.2	18.1587	1.34E-11	7.12E-08	9.13837	4.95578
ILMN_1724907	NUDT3	NM_006703.2	5.6172	4.63E-05	0.00660764	6.78017	4.29033
ILMN_1682699	PBX2	NM_002586.4	5.4453	6.75E-05	0.00862275	6.70092	4.25592
ILMN_2151817	PFN1	NM_005022.2	12.5648	8.90E-09	7.88E-06	8.88084	5.22953
ILMN_3241758	POTEF	NM_001099771.1	48.0562	3.36E-11	1.27E-07	10.12707	4.54042
ILMN_1810467	PPP2R1A	NM_014225.3	3.3428	5.90E-05	0.00779865	7.05536	5.31431
ILMN_1664921	PPP6C	NM_002721.3	3.3444	1.88E-05	0.00348282	5.97299	4.23126
ILMN_2338997	PTP4A2	NM_080392.2	13.7479	1.16E-06	0.000437019	9.52729	5.74615
ILMN_1752582	RAB5B	NM_002868.2	6.366	2.57E-05	0.00437656	7.39325	4.72288
ILMN_1716524	RAB7A	NM_004637.5	3.0189	3.77E-05	0.00552441	6.8136	5.21959
ILMN_1735360	SDAD1	NM_018115.2	4.1722	3.71E-05	0.00550918	6.28254	4.22173
ILMN_1697670	SRRM1	NM_005839.3	7.9294	7.60E-09	7.21E-06	8.51041	5.5232
ILMN_1770338	TM4SF1	NM_014220.2	7.2972	1.48E-05	0.00289129	8.07903	5.21168
ILMN_1793829	TMCO1	NM_019026.2	2.6558	2.89E-05	0.00470884	6.25253	4.8434
ILMN_1792508	TMEM59	NM_004872.3	8.5536	1.51E-07	8.90E-05	8.35455	5.25801
ILMN_1683271	TMSB4X	NM_021109.2	22.91	1.40E-06	0.000501058	12.16864	7.65074
ILMN_1656066	TNPO2	NM_013433.3	3.4409	3.01E-05	0.00480487	6.44281	4.66001
ILMN_2150654	ZSWIM4	NM_023072.1	3.7871	5.71E-05	0.0076602	6.37791	4.45681
ILMN_1730995	AFAP1L2	NM_001001936.1	1.8923	0.000555549	0.0386667	5.31942	4.39931
ILMN_2188204	ATG12	NM_004707.2	4.0786	0.000331547	0.0273434	6.94318	4.9151
ILMN_1719224	C17orf45	NM_152350.2	4.2921	0.000150019	0.014921	7.38229	5.2806
ILMN_1680132	CADM1	NM_014333.3	4.0821	0.000150947	0.0149573	7.24278	5.21348
ILMN_1803429	CD44	NM_001001391.1	4.1078	0.000582276	0.0399558	6.5288	4.49042
ILMN_1693014	CEBPB	NM_005194.2	4.817	0.000476726	0.0349722	7.24914	4.98101
ILMN_1782439	CNN3	NM_001839.2	7.0266	8.87E-05	0.0102888	7.56387	4.75104
ILMN_1701308	COL1A1	NM_000088.3	4.7808	0.000100305	0.0111452	7.48556	5.2283
ILMN_1706643	COL6A3	NM_057165.2	4.1235	0.000231804	0.0208671	7.53606	5.49219
ILMN_2415235	CSNK1E	NM_152221.2	4.9261	0.000226554	0.0204638	7.47532	5.17488
ILMN_1728478	CXCL16	NM_022059.1	5.7475	0.000277603	0.0238577	7.06276	4.53984
ILMN_2174127	DCBLD2	NM_080927.3	2.8138	0.000110035	0.0119856	6.12446	4.63193
ILMN_1665455	DCUN1D3	NM_173475.1	2.2786	0.000135472	0.0136791	6.01645	4.82833
ILMN_1706502	EIF2AK2	NM_002759.1	4.3353	0.000288333	0.0244631	6.89688	4.78075
ILMN_1673682	GATAD2A	NM_017660.2	2.1831	0.000138441	0.0138733	6.04054	4.91416
ILMN_2130411	KDELR1	NM_006801.2	2.4628	0.000484897	0.0351465	5.802	4.50169
ILMN_1673936	KHSRP	NM_003685.2	4.0095	0.0004071	0.0312455	6.94906	4.94563
ILMN_1703949	KPNB1	NM_002265.4	3.0771	0.00026875	0.0233233	6.6344	5.01282
ILMN_1739325	LOC284023	XM_941810.2	1.7397	0.000782212	0.0491074	5.42118	4.62231
ILMN_1704750	LOC647000	XM_929980.2	3.1257	8.78E-05	0.0102644	6.76619	5.12202
ILMN_1735180	NCSTN	NM_015331.2	4.172	0.000285658	0.0243714	6.13039	4.06964
ILMN_1759154	PABPN1	NM_004643.1	6.1835	9.20E-05	0.0104813	7.59528	4.96686
ILMN_2312296	PCBP2	NM_005016.3	5.8208	0.000381486	0.0299817	7.41217	4.87096
ILMN_2342695	PDGFA	NM_033023.3	1.9677	0.000684442	0.0454401	5.83078	4.85425
ILMN_1745329	PRR14	NM_024031.2	2.3519	0.000756519	0.0481105	5.77851	4.54467
ILMN_1659206	RARA	NM_000964.2	2.1821	0.000749922	0.0481037	5.613	4.48731
ILMN_1666739	RBM15	NM_022768.4	1.9553	0.000301504	0.0253378	5.10071	4.13334
ILMN_1808157	RUNDC3B	NM_138290.1	2.0568	0.000499884	0.0356852	5.8283	4.78793
ILMN_1655595	SERPINE2	NM_006216.2	9.9343	0.000283066	0.0242487	8.37039	5.05798
ILMN_1697469	SFRS6	NM_006275.4	2.8006	0.000599738	0.0409426	6.54814	5.06239
ILMN_3229770	SKP1	NM_006930.3	2.8525	0.000133466	0.0135798	6.10648	4.59425
ILMN_1676010	SP1	NM_138473.2	2.1447	0.000556209	0.0386667	6.43591	5.33512
ILMN_2345872	SUMF2	NM_001042470.1	4.6119	0.000153533	0.0150451	6.69027	4.4849

ProbeID	SYMBOL	Acc_No	Fold Change	P-Value	Adjusted P-Value	Mean Signal (HuR IP)	Mean Signal (IgG IP)
ILMN_1714623	TOMM22	NM_020243.4	1.6265	0.000275435	0.0238256	4.96276	4.26099
ILMN_2383693	UPF2	NM_080599.1	2.9799	0.000327265	0.0270743	5.85966	4.28439
ILMN_2307903	VCAM1	NM_001078.2	8.1288	0.000572422	0.0394915	7.1527	4.12966
ILMN_1728512	YWHAH	NM_003405.3	1.8359	0.000744399	0.0480979	5.80743	4.93096

Supplementary Table 2:

List of List of HuR targets (fold-change >1.5; adjusted p-value<0.05) identified after RIP-chip in MPNST samples

ProbeID	SYMBOL	Acc_No	Fold Change	P-Value	Adjusted P-Value	Mean Signal (HuR IP)	Mean Signal (IgG IP)
ILMN_1856634		BX537823	3.3464	3.65E-06	0.00102439	6.47719	4.73456
ILMN_2152131	ACTB	NM_001101.2	33.5269	1.28E-09	2.00E-06	11.25032	6.18307
ILMN_1657283	ALKBH5	NM_017758.3	5.3254	2.93E-06	0.000893711	7.36541	4.95253
ILMN_2226304	ANKRD50	NM_020337.1	2.3485	2.44E-05	0.00423377	5.51789	4.28613
ILMN_1728471	ARFGEF1	NM_006421.3	2.7533	2.70E-07	0.000134985	6.43034	4.9692
ILMN_1703477	ARHGEF2	NM_004723.2	5.0208	1.16E-05	0.00232117	7.78286	5.45495
ILMN_1759915	ARPC1A	NM_006409.2	2.1163	8.43E-06	0.0018391	6.02477	4.94321
ILMN_2059505	ARPP19	NM_006628.4	2.1087	3.46E-05	0.0052232	5.99567	4.91929
ILMN_3245057	ASAP1	NM_018482.2	3.2869	2.82E-06	0.000871204	7.0227	5.30596
ILMN_2358783	ASB3	NM_145863.1	2.0208	3.11E-05	0.00485799	6.02832	5.01339
ILMN_2188204	ATG12	NM_004707.2	5.2892	4.23E-07	0.00019029	8.76965	6.36661
ILMN_1704452	BCL9	NM_004326.2	2.0724	4.94E-10	8.75E-07	6.11812	5.06681
ILMN_1758918	BRD2	NM_005104.2	2.8365	1.46E-06	0.000517486	7.00414	5.50005
ILMN_1666208	C14orf106	NM_018353.3	3.3895	1.13E-08	9.62E-06	6.38886	4.62778
ILMN_1708906	C20rf29	NM_017546.3	2.5643	8.32E-06	0.0018391	6.41047	5.05193
ILMN_1671116	C3orf21	NM_152531.3	4.2401	4.33E-09	4.60E-06	6.41207	4.32796
ILMN_1777318	C9orf64	NM_032307.3	3.0706	5.88E-06	0.00148677	6.88354	5.26502
ILMN_1736256	CALR	NM_004343.2	2.3752	2.88E-05	0.00470884	5.9734	4.72535
ILMN_1768870	CAPZA2	NM_006136.2	5.6467	8.88E-11	2.14E-07	7.25615	4.75875
ILMN_1803429	CD44	NM_001001391.1	3.1172	1.12E-05	0.00228567	6.24041	4.60016
ILMN_1693014	CEBPB	NM_005194.2	2.5667	2.88E-05	0.00470884	6.18436	4.82447
ILMN_1738075	CMIP	NM_030629.1	27.095	1.53E-13	4.06E-09	11.12037	6.36042
ILMN_1782439	CNN3	NM_001839.2	2.9213	4.55E-05	0.00653817	6.52734	4.98071
ILMN_1706643	COL6A3	NM_057165.2	4.4282	5.60E-05	0.00755051	7.90028	5.75358
ILMN_1782788	CSDA	NM_003651.3	8.6287	1.28E-06	0.000470953	8.0511	4.94196
ILMN_1785988	CSNK1A1	NM_001025105.1	2.4856	3.17E-05	0.00488742	5.75708	4.44347
ILMN_2415235	CSNK1E	NM_152221.2	3.161	8.16E-05	0.00970999	7.39674	5.73635
ILMN_1728478	CXCL16	NM_022059.1	7.3705	1.67E-10	3.41E-07	7.67744	4.79568
ILMN_1684321	CYB5B	NM_030579.2	2.1029	7.47E-06	0.0017111	6.22329	5.15089
ILMN_1658411	CHD4	NM_001273.2	2.3766	2.59E-06	0.000811862	5.6679	4.41901
ILMN_1679428	CHIC2	NM_012110.2	2.03	5.81E-05	0.00771731	5.67924	4.65778
ILMN_1791576	CHSY1	NM_014918.3	2.5091	3.02E-05	0.00480487	5.9864	4.65921
ILMN_2128428	DAB2	NM_001343.1	4.75	7.60E-08	5.17E-05	8.15316	5.90522
ILMN_1811648	DCAKD	NM_024819.3	6.7993	2.41E-09	3.05E-06	7.51731	4.75192
ILMN_1777340	DDX6	NM_004397.3	2.6962	3.00E-05	0.00480487	5.84962	4.4187
ILMN_1770127	DNAJA2	NM_005880.2	13.0177	3.93E-12	3.48E-08	8.40965	4.70725
ILMN_1672503	DPYSL2	NM_001386.4	2.415	5.26E-06	0.00135718	6.04739	4.77535
ILMN_1783448	DYNC1LI2	NM_006141.2	2.2771	6.83E-06	0.0016193	6.3212	5.13397
ILMN_1706502	EIF2AK2	NM_002759.1	4.4334	9.21E-07	0.000364922	7.49883	5.35042
ILMN_1789596	ETV6	NM_001987.4	2.1071	3.09E-07	0.000143819	6.01276	4.93751
ILMN_1727041	EWSR1	NM_005243.2	2.3056	1.84E-08	1.36E-05	6.27691	5.07178
ILMN_3272378	EZR	NM_003379.4	5.6588	1.96E-06	0.000666425	8.5461	6.04561
ILMN_2189870	FCF1	NM_015962.4	2.2018	2.51E-07	0.000128541	6.41618	5.27746
ILMN_1703330	FEM1C	NM_020177.2	4.762	2.68E-09	3.23E-06	7.10035	4.84878
ILMN_1673682	GATAD2A	NM_017660.2	2.4396	2.15E-06	0.000703007	6.31002	5.02339
ILMN_1754912	GLE1	NM_001003722.1	3.154	1.70E-05	0.00323	6.55115	4.89395
ILMN_1690268	HNRPUL1	NM_144732.1	3.6088	6.98E-06	0.00164054	6.39163	4.54009
ILMN_1687384	IFI6	NM_022873.2	4.28	7.65E-05	0.00941662	8.18502	6.0874
ILMN_1723467	ITGB1	NM_002211.2	7.7939	6.82E-06	0.0016193	8.75759	5.79525
ILMN_1810214	JUND	NM_005354.3	31.2964	6.12E-12	4.06E-08	11.68119	6.71327
ILMN_2130411	KDELR1	NM_006801.2	2.2904	5.98E-06	0.00149933	5.96425	4.76862
ILMN_1673936	KHSRP	NM_003685.2	6.0881	1.42E-09	2.10E-06	8.20917	5.60317
ILMN_1703949	KPNB1	NM_002265.4	4.4417	2.26E-08	1.62E-05	7.64208	5.49098
ILMN_1811104	KTELC1	NM_020231.3	3.3128	7.11E-09	7.00E-06	6.94049	5.21242
ILMN_3176090	LOC100130919	XM_001722872.1	2.0934	7.66E-05	0.00941662	6.56501	5.49916
ILMN_3285198	LOC389168	XR_039278.1	2.2366	1.24E-05	0.00245199	6.20904	5.04773
ILMN_3235221	LOC644936	NR_004845.1	2.8016	7.27E-06	0.00167942	6.15759	4.67133
ILMN_1704750	LOC647000	XM_929980.2	3.2227	8.19E-05	0.00970999	7.47598	5.78771
ILMN_1660775	LOC650152	XR_018707.1	2.5312	3.24E-06	0.000954982	6.17069	4.83085
ILMN_1780861	LOC653506	XM_927769.1	5.9352	2.19E-09	2.91E-06	7.13196	4.56268
ILMN_1757106	Mar-06	NM_005885.2	12.7956	3.35E-11	1.27E-07	9.30957	5.63199
ILMN_2224143	MCM3	NM_002388.3	2.1254	2.01E-05	0.00360552	5.89972	4.81197
ILMN_1777526	MED20	NM_004275.3	2.8373	2.10E-06	0.000696406	6.27638	4.77187
ILMN_1746408	MIDN	NM_177401.4	2.7654	7.90E-09	7.24E-06	6.54423	5.07674
ILMN_1773763	MTA2	NM_004739.2	2.5607	6.93E-08	4.84E-05	5.93684	4.58032

ILMN_1814230	MTCP1	NM_014221.3	2.1598	4.69E-07	0.000204393	5.74411	4.63321
ILMN_1735180	NCSTN	NM_015331.2	4.6159	3.70E-06	0.00102439	6.53824	4.33164
ILMN_1724907	NUDT3	NM_006703.2	8.2794	4.53E-11	1.50E-07	7.345	4.29546
ILMN_2330495	OCIAD1	NM_001079842.1	2.2521	1.06E-06	0.000408703	8.89082	7.71957
ILMN_1759154	PABPN1	NM_004643.1	7.1603	6.05E-11	1.62E-07	8.09356	5.25354
ILMN_1686871	PARP1	NM_001618.2	6.4372	1.27E-07	7.86E-05	8.07222	5.38578
ILMN_1682699	PBX2	NM_002586.4	5.4135	2.05E-07	0.000109063	7.23138	4.79481
ILMN_1673215	PCBP1	NM_006196.2	3.4026	2.79E-05	0.00465267	6.53557	4.76893
ILMN_2312296	PCBP2	NM_005016.3	5.8435	1.58E-05	0.00302052	7.86208	5.31524
ILMN_2151817	PFN1	NM_005022.2	7.7159	2.60E-06	0.000811862	9.04984	6.102
ILMN_1802905	PIAS4	NM_015897.2	2.2836	7.86E-05	0.00946314	6.844	5.65271
ILMN_1771599	PLOD2	NM_000935.2	5.7946	1.30E-08	1.04E-05	7.89239	5.35768
ILMN_3241758	POTEF	NM_001099771.1	23.9473	6.10E-11	1.62E-07	9.55731	4.97552
ILMN_1810467	PPP2R1A	NM_014225.3	4.4114	9.64E-10	1.60E-06	7.70878	5.56754
ILMN_3248975	PPP4C	NM_002720.1	2.9817	3.58E-07	0.000163715	6.77989	5.20376
ILMN_1664921	PPP6C	NM_002721.3	3.5373	9.37E-07	0.000365971	6.16062	4.33796
ILMN_1769517	PRKDC	NM_001081640.1	2.8993	1.16E-08	9.62E-06	6.19921	4.66349
ILMN_1745329	PRR14	NM_024031.2	2.4214	2.01E-05	0.00360552	6.23207	4.95624
ILMN_2392674	PRR3	NM_001077497.1	2.6228	1.26E-07	7.86E-05	5.96881	4.57769
ILMN_1720926	PSMD5	NM_005047.2	2.1094	6.18E-06	0.001534	5.17558	4.09872
ILMN_2353202	PTK7	NM_152880.2	6.2426	3.57E-09	3.96E-06	7.20658	4.56443
ILMN_2338997	PTP4A2	NM_080392.2	7.0424	7.12E-06	0.00165933	10.4136	7.59754
ILMN_1752582	RAB5B	NM_002868.2	4.8978	4.77E-07	0.000204423	7.02964	4.73752
ILMN_1760858	RAB8A	NM_005370.4	2.7263	8.48E-06	0.0018391	5.5911	4.14417
ILMN_2109156	RANBP1	NM_002882.2	2.3426	2.52E-07	0.000128541	6.25827	5.03016
ILMN_1700604	RBM14	NM_006328.2	2.5966	1.87E-07	0.000101163	6.52936	5.15275
ILMN_1666739	RBM15	NM_022768.4	2.0417	5.13E-05	0.00713255	5.53003	4.50024
ILMN_1743104	RBM4B	NM_031492.2	2.4582	3.34E-06	0.000968841	5.86935	4.57173
ILMN_1720124	RCC2	NM_018715.1	2.4271	4.49E-05	0.00647915	6.45306	5.1738
ILMN_1661002	RFWD2	NM_022457.5	2.5053	6.72E-06	0.0016193	5.90019	4.57518
ILMN_1665877	RNF149	NM_173647.2	2.2438	3.04E-05	0.00480755	6.14723	4.98125
ILMN_1721842	RYBP	NM_012234.4	2.5308	7.83E-05	0.00946314	5.90721	4.56762
ILMN_1735360	SDAD1	NM_018115.2	4.1656	4.56E-07	0.000201862	6.71387	4.65535
ILMN_1784238	SEC22B	NM_004892.4	4.1283	1.40E-07	8.48E-05	6.72886	4.68332
ILMN_1751028	SERPINH1	NM_001235.2	2.749	3.37E-05	0.00511413	6.42455	4.96566
ILMN_1697469	SFRS6	NM_006275.4	2.7127	3.90E-06	0.00106823	6.74365	5.3039
ILMN_1808501	SH3KBP1	NM_031892.1	2.1703	6.98E-05	0.00874215	6.14177	5.02385
ILMN_3229770	SKP1	NM_006930.3	2.3636	7.98E-06	0.00179635	6.00723	4.76621
ILMN_2191167	SLC30A4	NM_013309.4	3.5357	1.72E-07	9.74E-05	5.88118	4.05916
ILMN_1789999	SLC30A7	NM_133496.3	2.2806	2.19E-05	0.00385532	6.39097	5.20153
ILMN_1676010	SP1	NM_138473.2	2.5408	3.36E-06	0.000968841	6.65313	5.30783
ILMN_2181432	SPC24	NM_182513.1	2.9727	1.16E-05	0.00232117	7.0389	5.46714
ILMN_1804277	SPRED1	NM_152594.1	2.407	8.52E-06	0.0018391	5.96026	4.69303
ILMN_2089329	SPRY2	NM_005842.2	3.1434	7.98E-06	0.00179635	5.72165	4.06934
ILMN_1697670	SRRM1	NM_005839.3	4.1051	3.16E-09	3.65E-06	7.62499	5.58759
ILMN_1711383	STK4	NM_006282.2	2.6749	2.83E-07	0.00013683	7.14158	5.72209
ILMN_1663002	STOML2	NM_013442.1	2.3391	3.26E-05	0.00498087	5.42767	4.20172
ILMN_2345872	SUMF2	NM_001042470.1	3.0667	1.14E-05	0.00231789	6.4459	4.82919
ILMN_1656399	TCEAL8	NM_001006684.1	2.7689	8.92E-06	0.00191051	5.79541	4.32612
ILMN_2368068	TCF20	NM_181492.1	3.3175	9.95E-08	6.61E-05	6.24922	4.51913
ILMN_1814657	TFAP4	NM_003223.1	2.9978	2.90E-07	0.00013759	6.34641	4.7625
ILMN_1793829	TMCO1	NM_019026.2	2.432	1.75E-08	1.36E-05	6.22805	4.94591
ILMN_1792508	TMEM59	NM_004872.3	5.9435	6.70E-09	6.85E-06	7.88695	5.31563
ILMN_1710962	TMEM97	NM_014573.2	2.6591	7.63E-05	0.00941662	6.10159	4.69065
ILMN_1683271	TMSB4X	NM_021109.2	8.9789	2.17E-06	0.000703007	11.99719	8.83064
ILMN_1656066	TNPO2	NM_013433.3	3.3247	1.52E-05	0.00294192	6.94333	5.2101
ILMN_1692731	TTYH3	NM_025250.2	2.6397	5.17E-06	0.00134681	6.52891	5.12853
ILMN_1814789	UBAP2L	NM_014847.2	3.4089	4.46E-06	0.00119671	6.57599	4.8067
ILMN_2383693	UPF2	NM_080599.1	3.0929	5.36E-07	0.000219058	6.04757	4.41862
ILMN_3236765	UPLP	NM_001114403.1	2.8968	1.33E-05	0.00261526	7.13617	5.60172
ILMN_2307903	VCAM1	NM_001078.2	6.8835	4.84E-05	0.00683717	7.2229	4.43976
ILMN_1777220	VCP	NM_007126.2	2.4673	1.05E-05	0.00219701	5.59033	4.28741
ILMN_1795937	VIL2	NM_003379.3	4.361	2.61E-05	0.00441995	7.28471	5.16003
ILMN_2104106	XPR1	NM_004736.2	2.557	1.84E-08	1.36E-05	6.3242	4.96974
ILMN_2252136	YWHAE	NM_006761.3	2.0795	6.67E-05	0.00857697	4.8367	3.78048
ILMN_1728512	YWHAH	NM_003405.3	2.1658	1.17E-06	0.000437019	6.16302	5.04815
ILMN_1656413	ZMPSTE24	NM_005857.3	2.4151	6.70E-07	0.0002697	5.97797	4.70588
ILMN_2150654	ZSWIM4	NM_023072.1	5.066	1.75E-09	2.45E-06	7.14876	4.80791
ILMN_1656676	ZYG11B	NM_024646.1	2.7707	5.40E-05	0.00737348	6.45742	4.98716
ILMN_3237396	AAGAB	NM_024666.3	1.9754	3.69E-06	0.00102439	6.18282	5.20069
ILMN_1665945	ACBD3	NM_022735.3	1.8804	8.04E-05	0.00962108	6.05433	5.14329
ILMN_2095653	AFMID	NM_001010982.1	1.7222	2.92E-05	0.00472192	5.66558	4.8813

ILMN_1703791	ANXA7	NM_004034.1	2.4138	0.000306208	0.0255712	5.45635	4.18503
ILMN_3307651	APOBEC3D	NM_152426.3	1.6163	0.00026119	0.0229675	5.2977	4.60497
ILMN_1768394	ARPC5	NM_005717.2	2.05	0.000345984	0.028012	6.15208	5.11646
ILMN_1658071	ATP1B1	NM_001677.3	2.0572	0.000738762	0.0478502	5.17125	4.13058
ILMN_2140207	ATPBD4	NM_080650.2	1.949	3.18E-05	0.00488742	5.20043	4.23772
ILMN_1725696	ATXN3	NM_004993.4	1.7031	0.000799199	0.0496695	4.97492	4.20675
ILMN_1651826	BASP1	NM_006317.3	2.81	0.000334357	0.0274049	7.29015	5.79961
ILMN_2255133	BCL11A	NM_022893.2	3.2343	0.000111785	0.0120401	5.70649	4.01304
ILMN_1711543	C14orf169	NM_024644.2	1.5877	6.69E-05	0.00857697	4.84686	4.17993
ILMN_1690442	C18orf45	NM_032933.4	2.3366	0.000257846	0.0228245	5.69744	4.47304
ILMN_1812688	C20rf18	NM_017877.3	1.6913	0.000416179	0.0316153	4.95532	4.19716
ILMN_1695917	C5orf15	NM_020199.1	2.2463	0.000128759	0.0133686	5.81768	4.65015
ILMN_1669831	C6orf192	NM_052831.2	1.9409	0.000392953	0.0304235	5.64608	4.68934
ILMN_1680132	CADM1	NM_014333.3	2.583	0.000223381	0.0202461	6.59016	5.22113
ILMN_1685580	CBLB	NM_170662.3	1.583	0.000104132	0.0114744	5.44285	4.78017
ILMN_1667081	CCND2	NM_001759.2	1.6192	0.000533855	0.0374065	5.55065	4.85537
ILMN_2261784	CCNY	NM_145012.3	1.978	7.88E-05	0.00946314	6.18876	5.20469
ILMN_1799688	CDC23	NM_004661.3	1.6676	7.74E-05	0.00946314	5.48688	4.74915
ILMN_1778557	CDC2L5	NM_003718.3	1.8146	4.77E-06	0.00126759	5.38015	4.5205
ILMN_1710326	CLDND1	NM_001040181.1	1.8927	0.000666195	0.0443395	5.28488	4.36441
ILMN_1662328	CNNM3	NM_017623.4	1.7968	0.000296495	0.0250605	5.52088	4.67544
ILMN_1701308	COL1A1	NM_000088.3	5.6806	0.000525879	0.0370431	9.13747	6.63143
ILMN_1729117	COL5A2	NM_000393.3	3.0516	0.000210326	0.0194614	6.3581	4.74854
ILMN_1751615	COQ10B	NM_025147.3	1.8031	0.000132444	0.0135736	5.80014	4.94966
ILMN_2385161	CUL4B	NM_001079872.1	1.5584	0.000263602	0.023027	5.36635	4.7263
ILMN_2106902	CHES1	NM_005197.2	2.1465	0.000575735	0.0396094	5.18279	4.08082
ILMN_1666503	DENND2A	NM_015689.2	2.0371	9.16E-05	0.0104813	5.88458	4.85804
ILMN_1785356	DENND5A	NM_015213.2	2.2698	0.000485364	0.0351465	5.86382	4.68126
ILMN_1768595	DLG4	NM_001365.2	1.8926	0.000365515	0.0292368	5.75716	4.83677
ILMN_1753243	DNAJB11	NM_016306.4	1.9595	0.000491929	0.0354222	6.373	5.40249
ILMN_2374244	DYRK2	NM_003583.2	2.0731	0.000173817	0.0166639	6.48791	5.4361
ILMN_1761463	EFHD2	NM_024329.4	2.2101	8.81E-05	0.0102644	5.82825	4.68413
ILMN_1665717	EIF2S3	NM_001415.3	2.2639	0.000390243	0.030373	5.63673	4.45793
ILMN_1794522	EIF5A	NM_001970.3	3.355	0.000220513	0.0201929	6.54578	4.79946
ILMN_1764873	ELAVL1	NM_001419.2	1.7215	0.000381601	0.0299817	5.18477	4.40114
ILMN_1784320	ELMO1	NM_014800.9	1.7674	4.97E-05	0.00696679	5.65634	4.83472
ILMN_2214910	EPHB4	NM_004444.4	1.8265	3.07E-05	0.00483122	4.85768	3.98859
ILMN_2352131	ERBB2	NM_004448.2	1.7866	5.58E-05	0.00755051	5.2911	4.45386
ILMN_1739222	ETV5	NM_004454.1	1.7066	1.08E-05	0.00224636	5.09009	4.319
ILMN_1746314	EVI5	NM_005665.4	1.8749	0.000177682	0.0168519	6.64986	5.74301
ILMN_1719985	FEM1A	NM_018708.2	1.7904	2.00E-05	0.00360552	5.85613	5.01582
ILMN_1764314	FGD1	NM_004463.2	2.2121	0.000103039	0.0114012	5.7305	4.58505
ILMN_1805796	FLYWCH2	NM_138439.1	1.5417	0.000733816	0.0477628	5.04484	4.42036
ILMN_1736510	FOXN2	NM_002158.3	1.9942	5.06E-06	0.00133103	5.29099	4.29515
ILMN_1748473	GIMAP4	NM_018326.2	1.7518	5.83E-06	0.00148677	5.97391	5.16507
ILMN_1652631	GLIPR2	NM_022343.2	2.6341	0.000802389	0.0496695	5.98038	4.58309
ILMN_1750130	GSPT1	NM_002094.2	1.5547	0.00012962	0.0133686	5.56077	4.92412
ILMN_1705570	H2AFY2	NM_018649.2	2.5363	0.000801881	0.0496695	5.36617	4.02345
ILMN_1767747	HDAC2	NM_001527.2	3.0816	0.000175373	0.0167525	6.43941	4.81574
ILMN_1804150	HIBADH	NM_152740.2	2.0674	0.000185946	0.0175106	5.63362	4.58582
ILMN_2087646	HLX	NM_021958.2	1.7672	0.000596551	0.0408299	4.31531	3.49384
ILMN_2321451	HNRNPD	NM_031369.2	1.9852	2.70E-05	0.00454353	6.46674	5.47745
ILMN_3246409	HNRNPH1	NM_005520.2	1.5753	0.000100228	0.0111452	4.96976	4.31414
ILMN_1719975	HOXC4	NM_014620.4	1.7493	0.000467872	0.0346095	4.89402	4.08721
ILMN_1709882	ICK	NM_016513.3	1.7047	1.11E-05	0.0022805	5.43407	4.66456
ILMN_1752283	ITCH	NM_031483.3	1.6161	6.83E-05	0.00864998	5.58659	4.89408
ILMN_1668535	JOSD1	NM_014876.3	1.6355	0.000772996	0.0487593	4.95892	4.24916
ILMN_1682572	KIAA0528	NM_014802.1	1.9169	0.000164889	0.0160396	5.65687	4.71806
ILMN_1743034	KIF1B	NM_183416.2	1.8192	1.90E-05	0.00351093	6.06065	5.19738
ILMN_1712452	KIF20B	NM_016195.2	1.5432	8.99E-05	0.0103814	5.74343	5.11751
ILMN_1702279	KIF3B	NM_004798.2	1.7393	1.51E-06	0.000528153	5.3195	4.52098
ILMN_1735930	KLF2	NM_016270.2	1.8642	0.000387125	0.0303259	5.73992	4.84137
ILMN_2400448	L3MBTL3	NM_001007102.1	1.8815	0.00012988	0.0133686	4.34049	3.42858
ILMN_1782292	LAMP1	NM_005561.2	1.7038	0.000124012	0.0131731	5.85564	5.0869
ILMN_1733390	LARP1B	NM_032239.2	1.9107	3.75E-05	0.00552441	5.02262	4.08853
ILMN_1774890	LAS1L	NM_031206.3	1.8911	2.23E-06	0.000714537	5.78276	4.86351
ILMN_2129563	LDLRAD3	NM_174902.2	1.6715	0.00080194	0.0496695	4.87865	4.13751
ILMN_3282321	LOC643336	XM_001718563.1	1.5902	0.00064245	0.0431922	5.13678	4.46761
ILMN_1697024	LOC730432	XM_001125680.1	1.7285	0.000110577	0.0119856	5.63018	4.84067
ILMN_2216265	LONP2	NM_031490.2	1.9847	0.000572534	0.0394915	5.29719	4.30825
ILMN_2218450	LSM1	NM_014462.1	1.7208	0.000601984	0.0409904	5.93575	5.15267
ILMN_1702698	LSM11	NM_173491.2	1.5285	0.000413899	0.0316153	5.70175	5.08964

ILMN_2092693	LSM12	NM_152344.1	2.3464	0.00024035	0.0214907	5.59457	4.36409
ILMN_2079803	LSM14A	NM_015578.1	2.4643	0.000716404	0.047229	6.14122	4.84002
ILMN_2162972	LYZ	NM_000239.1	1.6158	5.41E-05	0.00737348	5.31995	4.62766
ILMN_1723020	MAP3K1	NM_005921.1	1.9026	2.81E-05	0.00466499	5.81422	4.88628
ILMN_1807042	MARCKS	NM_002356.5	2.9885	0.00015578	0.0152092	6.61465	5.03522
ILMN_1745699	METTL2A	NM_181725.2	1.686	0.000514724	0.0364507	5.14229	4.3887
ILMN_2347068	MKNK2	NM_017572.2	1.7554	3.63E-05	0.00544914	5.60153	4.78975
ILMN_1775744	MRPS16	NM_016065.3	1.9301	2.13E-05	0.00376827	5.59491	4.64626
ILMN_1716678	NPC2	NM_006432.3	2.3474	0.000451273	0.0337578	6.18105	4.94997
ILMN_2079786	NUAK1	NM_014840.2	1.9743	6.84E-05	0.00864998	5.62453	4.64316
ILMN_1706376	OSBP	NM_002556.2	1.6657	0.000738487	0.0478502	5.74569	5.00956
ILMN_1746618	PAQR7	NM_178422.4	1.5914	0.000779676	0.0490642	4.6613	3.99099
ILMN_2216852	PGK1	NM_000291.2	2.2148	9.38E-05	0.0106405	5.56019	4.41303
ILMN_1733666	PLDN	NM_012388.2	1.5989	0.000438723	0.0330049	5.28068	4.60358
ILMN_2277252	PPFIBP1	NM_003622.2	1.6267	0.000276907	0.0238577	5.84656	5.1446
ILMN_2405018	PPP1CB	NM_206876.1	1.5367	0.000136249	0.0137055	4.78531	4.1655
ILMN_1722858	PPP2CA	NM_002715.2	1.8211	9.60E-06	0.00203912	6.42689	5.56208
ILMN_1759954	PTMA	NM_001099285.1	1.5232	0.000342204	0.027876	4.82149	4.21438
ILMN_1757552	PTRF	NM_012232.3	2.9793	0.000114465	0.012257	6.23824	4.66326
ILMN_1712312	RAB11A	NM_004663.3	2.3054	0.000555235	0.0386667	6.09486	4.88987
ILMN_1768117	RBM25	NM_021239.1	1.6394	3.67E-05	0.00547714	5.65248	4.93928
ILMN_1753008	REXO1	NM_020695.3	1.8602	0.000111986	0.0120401	5.4718	4.57635
ILMN_1801441	RFTN2	NM_144629.1	1.6485	0.000389694	0.030373	4.70658	3.98545
ILMN_1802205	RHOB	NM_004040.2	1.7173	6.08E-05	0.00797138	5.2034	4.42323
ILMN_1714809	RPIA	NM_144563.2	1.5697	0.00018861	0.0176987	5.58108	4.93058
ILMN_1660533	RPN1	NM_002950.3	1.8571	0.000761451	0.0482604	6.00175	5.1087
ILMN_1808157	RUNDC3B	NM_138290.1	1.8488	0.000391157	0.030373	5.64639	4.75978
ILMN_1674955	SCP2	NM_001007098.1	1.6088	0.000492198	0.0354222	4.62329	3.9373
ILMN_1655595	SERPINE2	NM_006216.2	6.2217	0.000239582	0.0214907	8.47029	5.83299
ILMN_1720513	SETBP1	NM_015559.1	1.562	0.000746989	0.0481037	5.94214	5.29871
ILMN_1795341	SFRS1	NM_001078166.1	2.0394	0.000769558	0.048658	6.20269	5.17458
ILMN_1665538	SKP2	NM_032637.2	1.7242	0.000121438	0.0129514	5.45624	4.67031
ILMN_2053103	SLC40A1	NM_014585.3	2.8943	0.000415269	0.0316153	6.01956	4.48635
ILMN_1706553	SMG7	NM_173156.1	1.7505	0.000168613	0.0163419	5.69741	4.88963
ILMN_2409078	SNHG10	NR_001459.2	1.7586	0.000461709	0.0344414	5.69691	4.88246
ILMN_3247064	SNRNP40	NM_004814.2	1.9202	9.68E-05	0.0109384	5.62079	4.67956
ILMN_1787415	SNX16	NM_022133.2	2.235	0.000132894	0.0135736	5.14876	3.98848
ILMN_1814165	SSBP3	NM_018070.3	1.7398	0.000223252	0.0202461	5.86113	5.06219
ILMN_1655163	STK24	NM_003576.3	2.1717	9.17E-05	0.0104813	5.77943	4.6606
ILMN_2172969	STXBP6	NM_014178.6	1.7616	0.000728097	0.047507	5.40134	4.58449
ILMN_1697793	SYNJ2BP	NM_018373.1	2.2474	0.000654724	0.0437956	6.34224	5.17396
ILMN_1790953	TBCB	NM_001281.2	1.6087	0.000755788	0.0481105	5.85929	5.17336
ILMN_1682781	TEAD2	NM_003598.1	1.518	0.000713382	0.047229	5.85104	5.24883
ILMN_1715661	TFAM	NM_003201.1	1.6526	0.000152328	0.015038	4.87343	4.14868
ILMN_1707124	TFPI	NM_006287.4	1.6988	0.000353295	0.0285171	5.67531	4.91076
ILMN_1651346	TICAM2	NM_021649.3	1.7251	0.000200236	0.0187235	4.89492	4.10822
ILMN_1692511	TMEM106C	NM_024056.2	1.9476	0.000264975	0.023071	4.94809	3.98639
ILMN_2042941	TMEM159	NM_020422.3	1.6557	0.000259596	0.0229031	5.85377	5.12634
ILMN_3240316	TMSL3	NM_183049.2	2.4561	0.000126011	0.0133321	5.96599	4.66962
ILMN_1685005	TNFRSF1A	NM_001065.2	1.6379	0.000181438	0.0171469	5.29888	4.58702
ILMN_1726786	TNRC6B	NM_015088.2	1.5231	0.000749146	0.0481037	5.71986	5.11284
ILMN_1672908	TWIST1	NM_000474.3	1.5097	0.000207432	0.0193283	5.67829	5.08402
ILMN_2368576	UBA52	NM_003333.3	2.4917	0.000797305	0.0496695	5.67055	4.35342
ILMN_2301083	UBE2C	NM_181800.1	2.0893	0.000563111	0.0390443	5.6873	4.62428
ILMN_1707475	UBE2E2	NM_152653.2	1.5778	0.000485102	0.0351465	5.78245	5.12456
ILMN_2360291	UGCGL1	NM_020120.2	2.0844	0.000324667	0.0269433	5.7295	4.66985
ILMN_1729563	UGDH	NM_003359.2	1.7317	3.05E-06	0.000920849	5.92471	5.13256
ILMN_2094587	USP8	NM_005154.2	1.5699	0.000416681	0.0316153	4.9028	4.25216
ILMN_2376625	VHL	NM_198156.1	1.7354	0.000304738	0.0255288	5.11757	4.32232
ILMN_1676448	WDFY1	NM_020830.3	2.4497	0.000171286	0.0165406	6.22699	4.93436
ILMN_1707506	YTHDC1	NM_001031732.2	2.4426	0.000323816	0.0269433	5.76133	4.47291
ILMN_1798533	ZNF22	NM_006963.3	1.7447	3.81E-05	0.00555413	5.94782	5.14484
ILMN_1686968	ZNF362	NM_152493.2	1.7579	0.000511308	0.0363056	5.01153	4.19764
ILMN_1672940	ZNF562	NM_017656.2	2.1707	0.000658986	0.0439699	5.83371	4.71554
ILMN_1702384	ZNF706	NM_016096.3	1.8759	0.000286333	0.0243714	5.6865	4.7789
ILMN_1812856	ZSWIM1	NM_080603.3	2.0535	0.000108729	0.0119315	5.51738	4.47926
ILMN_1777061	ZSWIM6	XM_035299.8	1.8745	1.76E-07	9.74E-05	6.05235	5.14587

Supplementary Table 3:

GSEA report for putative HuR targets identified after RIP-chip in MPNST samples

NAME	SIZE	ES	NES	NOM p-val	FDR q-val	FWER p-val	RANK AT MAX	LEADING EDGE
HALLMARK_G2M_CHECKPOINT	110	0.66091704	2.2007105	0	0	0	1642	tags=40%, list=15%, signal=47%
HALLMARK_WNT_BETA_CATENIN_SIGNALING	25	0.78778225	2.0969403	0	0	0	522	tags=32%, list=5%, signal=34%
HALLMARK_EPITHELIAL_MESENCHYMAL_TRANSITION	135	0.5895362	2.0109563	0	0	0	1836	tags=36%, list=17%, signal=42%
HALLMARK_MTORC1_SIGNALING	115	0.5973246	1.9983793	0	0	0	1675	tags=43%, list=16%, signal=51%
HALLMARK_UNFOLDED_PROTEIN_RESPONSE	66	0.6169456	1.9491183	0	0	0	1392	tags=38%, list=13%, signal=43%
HALLMARK_UV_RESPONSE_DN	86	0.586251	1.903825	0	7.66E-04	0.004	1199	tags=29%, list=11%, signal=32%
HALLMARK_MITOTIC_SPINDLE	110	0.5334939	1.7825989	0	0.006466026	0.04	1796	tags=32%, list=17%, signal=38%
HALLMARK_PI3K_AKT_MTOR_SIGNALING	61	0.5641523	1.7556522	0.00120919	0.006801055	0.046	1181	tags=30%, list=11%, signal=33%
HALLMARK_PEROXISOME	50	0.55628026	1.6787007	0.004968944	0.018492453	0.131	1263	tags=28%, list=12%, signal=32%
HALLMARK_APOPTOSIS	105	0.49836984	1.6635113	0.003340757	0.020388661	0.157	1374	tags=30%, list=13%, signal=35%
HALLMARK_GLYCOLYSIS	105	0.49525842	1.6402197	0.001119821	0.023897646	0.199	1499	tags=30%, list=14%, signal=35%
HALLMARK_TNFA_SIGNALING_VIA_NFKB	104	0.48929134	1.6331859	0.002252252	0.02339069	0.209	2112	tags=38%, list=20%, signal=46%
HALLMARK_APICAL_JUNCTION	104	0.49044627	1.6322346	0.001116072	0.021929914	0.212	1377	tags=21%, list=13%, signal=24%
HALLMARK_ANGIOGENESIS	24	0.6194995	1.6268386	0.015647227	0.021904958	0.23	800	tags=33%, list=7%, signal=36%
HALLMARK_PROTEIN_SECRETION	51	0.5395127	1.6265352	0.008760951	0.020524971	0.231	1441	tags=31%, list=13%, signal=36%
HALLMARK_KRAS_SIGNALING_UP	97	0.47857574	1.5667709	0.008	0.03583513	0.399	1305	tags=26%, list=12%, signal=29%
HALLMARK_IL2_STAT5_SIGNALING	110	0.45464563	1.5261422	0.012235818	0.051514674	0.533	1918	tags=30%, list=18%, signal=36%
HALLMARK_E2F_TARGETS	103	0.4570279	1.5065614	0.019296255	0.058281112	0.599	2424	tags=39%, list=23%, signal=50%
HALLMARK_MYC_TARGETS_V1	125	0.43638206	1.4668849	0.007608695	0.07842948	0.721	1460	tags=30%, list=14%, signal=34%
HALLMARK_COMPLEMENT	92	0.4429166	1.4631652	0.025287356	0.0766934	0.737	1308	tags=23%, list=12%, signal=26%
HALLMARK_TGF_BETA_SIGNALING	32	0.5188074	1.4178389	0.07493188	0.1104575	0.861	1992	tags=47%, list=19%, signal=57%
HALLMARK_HYPOXIA	121	0.40840784	1.3906022	0.043141592	0.12912361	0.913	1482	tags=26%, list=14%, signal=30%
HALLMARK_INFLAMMATORY_RESPONSE	87	0.41521847	1.3527392	0.06342016	0.16534793	0.962	1697	tags=29%, list=16%, signal=34%
HALLMARK_IL6_JAK_STAT3_SIGNALING	42	0.46002385	1.3494619	0.10602094	0.16181342	0.962	1892	tags=36%, list=18%, signal=43%
HALLMARK_MYOGENESIS	98	0.4137025	1.3434615	0.073578596	0.1631277	0.967	978	tags=16%, list=9%, signal=18%
HALLMARK_MYC_TARGETS_V2	29	0.478168	1.3149215	0.1401099	0.19196516	0.988	1266	tags=28%, list=12%, signal=31%
HALLMARK_ESTROGEN_RESPONSE_EARLY	81	0.4036203	1.3027929	0.08741259	0.19942532	0.992	1992	tags=35%, list=19%, signal=42%
HALLMARK_XENOBIOTIC_METABOLISM	75	0.4054729	1.2860401	0.12880562	0.21394835	0.997	497	tags=11%, list=5%, signal=11%
HALLMARK_UV_RESPONSE_UP	73	0.40425426	1.2719775	0.14285715	0.22587061	0.998	1327	tags=25%, list=12%, signal=28%
HALLMARK_NOTCH_SIGNALING	24	0.48087007	1.2595494	0.1988555	0.23480763	0.998	1854	tags=33%, list=17%, signal=40%
HALLMARK_ESTROGEN_RESPONSE_LATE	83	0.38209093	1.235678	0.16991964	0.25913045	0.999	1820	tags=28%, list=17%, signal=33%
HALLMARK_BILE_ACID_METABOLISM	39	0.42276612	1.2304164	0.20915033	0.25940308	0.999	639	tags=15%, list=6%, signal=16%
HALLMARK_P53_PATHWAY	107	0.36603296	1.2129018	0.17117117	0.27646855	1	1143	tags=17%, list=11%, signal=19%
HALLMARK_APICAL_SURFACE	19	0.4819313	1.2029262	0.27098674	0.282939	1	2122	tags=47%, list=20%, signal=59%
HALLMARK_CHOLESTEROL_HOMEOSTASIS	37	0.40666175	1.148678	0.26778784	0.3601674	1	1160	tags=14%, list=11%, signal=15%
HALLMARK_ANDROGEN_RESPONSE	56	0.37425527	1.1463497	0.28607595	0.35416937	1	2019	tags=32%, list=19%, signal=39%
HALLMARK_FATTY_ACID_METABOLISM	72	0.35421097	1.122274	0.3038741	0.38514337	1	1602	tags=22%, list=15%, signal=26%
HALLMARK_HEDGEHOG_SIGNALING	15	0.47174457	1.119419	0.33333334	0.37997162	1	1916	tags=40%, list=18%, signal=49%
HALLMARK_HEME_METABOLISM	86	0.3279731	1.0723225	0.3787529	0.4474676	1	1965	tags=28%, list=18%, signal=34%
HALLMARK_ADIPOGENESIS	114	0.31826487	1.0704817	0.36574584	0.43867436	1	1848	tags=26%, list=17%, signal=31%
HALLMARK_INTERFERON_GAMMA_RESPONSE	101	0.3143803	1.0297027	0.43249428	0.49463367	1	1439	tags=19%, list=13%, signal=22%
HALLMARK_KRAS_SIGNALING_DN	61	0.2778541	0.87647456	0.6658625	0.7462542	1	2550	tags=26%, list=24%, signal=34%
HALLMARK_COAGULATION	63	0.2773195	0.86546314	0.6816525	0.74789935	1	879	tags=13%, list=8%, signal=14%
HALLMARK_ALLOGRAFT_REJECTION	105	0.24082597	0.79747456	0.8103638	0.8350867	1	1693	tags=19%, list=16%, signal=22%
HALLMARK_REACTIVE_OXIGEN_SPECIES_PATHWAY	27	0.27147785	0.73852396	0.818705	0.8931917	1	902	tags=15%, list=8%, signal=16%
HALLMARK_DNA_REPAIR	84	0.22432286	0.7244512	0.87283236	0.89092064	1	2210	tags=25%, list=21%, signal=31%
HALLMARK_SPERMATOGENESIS	47	0.23561779	0.69741	0.8802548	0.90089965	1	1588	tags=17%, list=15%, signal=20%

Supplementary Table 4:

GSEA report for genes associated with ShCtr-infected cells

NAME	SIZE	ES	NES	NOM p-val	FDR q-val	FWER p-val	RANK AT MAX	LEADING EDGE
CSR_LATE_UP.V1_UP	161	0.6463217	2.026948	0	0	0	7554	tags=58%, list=13%, signal=67%
RPS14_DN.V1_DN	179	0.60663754	1.9231466	0	0	0	5608	tags=47%, list=10%, signal=52%
RB_P107_DN.V1_UP	135	0.6183999	1.8919705	0	0	0	6012	tags=56%, list=11%, signal=62%
PRC2_EZH2_UP.V1_UP	182	0.59619594	1.8788438	0	0	0	3123	tags=38%, list=6%, signal=41%
GCNP_SHH_UP_LATE.V1_UP	173	0.58318806	1.8233163	0	0	0	3248	tags=34%, list=6%, signal=36%
E2F1_UP.V1_UP	179	0.57013875	1.805654	0	0	0	6918	tags=47%, list=12%, signal=53%
HOXA9_DN.V1_DN	183	0.57443297	1.8028847	0	0	0	6728	tags=44%, list=12%, signal=50%
VEGF_A_UP.V1_DN	189	0.5392788	1.7186297	0	7.17E-04	0.009	5838	tags=42%, list=10%, signal=46%
CORDENONSI_YAP_CONSERVED_SIGNATURE	57	0.625357	1.6881859	0	7.86E-04	0.011	3980	tags=47%, list=7%, signal=51%
PRC2_EED_UP.V1_DN	187	0.5278528	1.6847965	0	8.31E-04	0.013	7405	tags=42%, list=13%, signal=48%
RB_P130_DN.V1_UP	126	0.5470712	1.634776	0	0.00160963	0.027	3464	tags=33%, list=6%, signal=35%
GCNP_SHH_UP_EARLY.V1_UP	163	0.5051882	1.5741572	0	0.003955163	0.069	7276	tags=40%, list=13%, signal=46%
MYC_UP.V1_UP	163	0.49637333	1.5591592	0	0.004583201	0.086	7203	tags=45%, list=13%, signal=51%
BMI1_DN_MEL18_DN.V1_UP	140	0.5100883	1.5514046	0	0.004670326	0.095	7496	tags=51%, list=13%, signal=58%
ESC_J1_UP_LATE.V1_DN	179	0.4785535	1.5299935	0	0.006708479	0.136	7240	tags=40%, list=13%, signal=46%
ERB2_UP.V1_DN	185	0.44723895	1.4340094	0	0.018547483	0.358	6705	tags=36%, list=12%, signal=40%
STK33_DN	263	0.4047926	1.3371545	0.002873563	0.05775106	0.765	6610	tags=36%, list=12%, signal=41%
STK33_SKM_DN	257	0.3825717	1.2545364	0.01907357	0.13202493	0.974	3143	tags=27%, list=6%, signal=28%
BMI1_DN.V1_UP	142	0.40230384	1.246761	0.033254158	0.13612205	0.984	3771	tags=29%, list=7%, signal=31%
MTOR_UP.V1_UP	161	0.40020773	1.2454468	0.05707196	0.13068776	0.984	5268	tags=29%, list=9%, signal=31%
RB_DN.V1_UP	130	0.4052772	1.2372407	0.0530504	0.1349215	0.991	7074	tags=39%, list=13%, signal=45%
MEL18_DN.V1_UP	136	0.4008568	1.2277946	0.07263923	0.14207262	0.994	6674	tags=39%, list=12%, signal=44%
LTE2_UP.V1_DN	190	0.3812306	1.2164211	0.036458332	0.15159744	0.996	5911	tags=31%, list=10%, signal=35%
HINATA_NFKB_IMMU_INF	16	0.604309	1.2118691	0.1971831	0.15200374	0.997	5674	tags=50%, list=10%, signal=56%
E2F3_UP.V1_UP	175	0.38684732	1.2116122	0.06806283	0.14621256	0.997	6742	tags=37%, list=12%, signal=42%
SRC_UP.V1_DN	160	0.3809992	1.195038	0.078085646	0.16436355	1	7583	tags=34%, list=13%, signal=39%
TGFB_UP.V1_UP	184	0.37824148	1.1847157	0.06818182	0.17407961	1	6971	tags=30%, list=12%, signal=34%
JNK_DN.V1_DN	184	0.3669385	1.1626757	0.08163265	0.20641711	1	6133	tags=28%, list=11%, signal=32%
STK33_NOMO_DN	260	0.35340944	1.1574258	0.07520892	0.20890447	1	5207	tags=29%, list=9%, signal=32%
NFE2L2.V2	443	0.33444002	1.1482269	0.043209877	0.21954389	1	5163	tags=23%, list=9%, signal=25%
LEF1_UP.V1_UP	189	0.35781455	1.1402278	0.13054188	0.22859871	1	6613	tags=34%, list=12%, signal=38%
KRAS.AMP.LUNG_UP.V1_DN	137	0.36763945	1.1303136	0.1598063	0.24194734	1	5172	tags=25%, list=9%, signal=27%
PRC2_SUZ12_UP.V1_UP	180	0.36056408	1.129645	0.1484375	0.23572789	1	5801	tags=26%, list=10%, signal=28%
P53_DN.V1_UP	188	0.3551615	1.1239165	0.14285715	0.24101885	1	6313	tags=32%, list=11%, signal=36%
NRL_DN.V1_DN	130	0.3683067	1.1220392	0.17085427	0.23828094	1	6219	tags=32%, list=11%, signal=36%
ATF2_S_UP.V1_UP	184	0.35174403	1.1180388	0.15167095	0.23962294	1	7869	tags=35%, list=14%, signal=41%
IL15_UP.V1_UP	180	0.34741217	1.0986463	0.20408164	0.27593216	1	5079	tags=26%, list=9%, signal=28%
EGFR_UP.V1_DN	188	0.33923462	1.0757606	0.21505377	0.3239593	1	2944	tags=22%, list=5%, signal=23%
TBK1.DN.48HRS_DN	50	0.41038764	1.0738732	0.3272311	0.32051444	1	7426	tags=38%, list=13%, signal=44%
CSR_EARLY_UP.V1_UP	152	0.34655768	1.0694181	0.24939467	0.3240171	1	8190	tags=39%, list=15%, signal=45%
JAK2_DN.V1_UP	174	0.33457637	1.0504899	0.28533334	0.36530247	1	6929	tags=26%, list=12%, signal=30%
SIRNA_EIF4GI_DN	92	0.3565203	1.0272043	0.37588653	0.42244884	1	5997	tags=28%, list=11%, signal=32%
PDGF_ERK_DN.V1_UP	138	0.33252293	1.0162523	0.39099526	0.44549736	1	5762	tags=27%, list=10%, signal=30%
P53_DN.V2_UP	145	0.32177395	0.99758	0.4555256	0.4955497	1	3347	tags=19%, list=6%, signal=20%
BRCA1_DN.V1_DN	133	0.3277704	0.9953412	0.44652405	0.49176452	1	7812	tags=29%, list=14%, signal=33%
KRAS.LUNG.BREAST_UP.V1_UP	138	0.32414296	0.9873838	0.47921762	0.50743544	1	8698	tags=36%, list=15%, signal=43%
CTIP_DN.V1_DN	126	0.3256546	0.9829276	0.45343137	0.5109972	1	6141	tags=27%, list=11%, signal=30%
PRC1_BMI_UP.V1_UP	182	0.30172926	0.9559453	0.58	0.5925697	1	4613	tags=20%, list=8%, signal=22%
BCAT_GDS748_DN	45	0.33781058	0.8585551	0.7276888	0.9142249	1	4760	tags=24%, list=8%, signal=27%
BCAT_BILD_ET_AL_DN	46	0.29015687	0.75080264	0.9326087	0.99237084	1	14542	tags=52%, list=26%, signal=70%

Supplementary Table 5:

GSEA report for genes associated with shHuR#1-infected cells

NAME	SIZE	ES	NES	NOM p-val	FDR q-val	FWER p-val	RANK AT MAX	LEADING EDGE
BMI1_DN_MEL18_DN.V1_DN	140	-0.65756273	-1.9316547	0	0	0	6383	tags=53%, list=11%, signal=59%
MEL18_DN.V1_DN	140	-0.6470315	-1.9101604	0	0	0	6830	tags=54%, list=12%, signal=62%
STK33_UP	273	-0.5978454	-1.888939	0	4.30E-04	0.001	8476	tags=49%, list=15%, signal=58%
STK33_NOMO_UP	272	-0.58234036	-1.8480598	0	3.22E-04	0.001	7740	tags=47%, list=14%, signal=55%
PRC2_EED_UP.V1_UP	182	-0.5965234	-1.8123351	0	2.58E-04	0.001	6805	tags=46%, list=12%, signal=52%
STK33_SKM_UP	268	-0.55316085	-1.7442031	0	0.002238993	0.011	7054	tags=38%, list=13%, signal=43%
BMI1_DN.V1_DN	138	-0.5773672	-1.6887712	0	0.00365305	0.02	6830	tags=43%, list=12%, signal=49%
MTOR_UP.N4.V1_DN	169	-0.55986893	-1.6829	0	0.00351008	0.022	6973	tags=40%, list=12%, signal=45%
ERB2_UP.V1_UP	183	-0.548108	-1.6590604	0	0.004342172	0.03	6402	tags=43%, list=11%, signal=48%
KRAS.KIDNEY_UP.V1_UP	140	-0.56736267	-1.6563841	0.001655629	0.004284753	0.033	2844	tags=38%, list=5%, signal=40%
ATF2_S_UP.V1_DN	180	-0.5472791	-1.6556194	0	0.00389523	0.033	6668	tags=48%, list=12%, signal=55%
IL2_UP.V1_DN	183	-0.53921	-1.6400353	0	0.004720663	0.044	7629	tags=38%, list=14%, signal=44%
CAHOY_ASTROGLIAL	96	-0.5661811	-1.6217597	0	0.005484538	0.056	6804	tags=45%, list=12%, signal=51%
ESC_V6.5_UP_LATE.V1_UP	185	-0.53170925	-1.6210804	0	0.005177034	0.057	6374	tags=40%, list=11%, signal=45%
ATF2_UP.V1_DN	180	-0.53176725	-1.6154956	0	0.00532063	0.062	4385	tags=37%, list=8%, signal=40%
RPS14_DN.V1_UP	187	-0.5262576	-1.6150908	0.001650165	0.00498809	0.062	7404	tags=40%, list=13%, signal=45%
RB_P130_DN.V1_DN	130	-0.55093676	-1.6129909	0	0.004769147	0.063	7701	tags=46%, list=14%, signal=53%
HOXA9_DN.V1_UP	181	-0.53509647	-1.6123956	0	0.004504195	0.063	6915	tags=41%, list=12%, signal=47%
E2F1_UP.V1_DN	183	-0.5256635	-1.5868429	0	0.006698331	0.097	6804	tags=43%, list=12%, signal=48%
CSR_EARLY_UP.V1_DN	139	-0.54012334	-1.5828733	0.001675042	0.00648976	0.099	8014	tags=45%, list=14%, signal=53%
ESC_J1_UP_LATE.V1_UP	186	-0.5178298	-1.566775	0.001620746	0.007163001	0.115	6374	tags=42%, list=11%, signal=47%
AKT_UP.V1_DN	179	-0.510245	-1.5351222	0.001633987	0.010299	0.174	7583	tags=42%, list=13%, signal=48%
LEF1_UP.V1_DN	181	-0.50430536	-1.5283473	0	0.010674264	0.187	6892	tags=45%, list=12%, signal=51%
CSR_LATE_UP.V1_DN	157	-0.5095311	-1.5267802	0	0.010275873	0.188	3803	tags=32%, list=7%, signal=34%
WNT_UP.V1_DN	164	-0.50823104	-1.5252419	0	0.009965336	0.19	5912	tags=36%, list=10%, signal=40%
P53_DN.V1_DN	187	-0.50242114	-1.5183854	0.001666667	0.010564892	0.207	7369	tags=45%, list=13%, signal=52%
PDGF_UP.V1_DN	126	-0.5178902	-1.5111766	0	0.010716772	0.215	6840	tags=36%, list=12%, signal=41%
CRX_DN.V1_DN	131	-0.5105873	-1.5057538	0.001692047	0.010831025	0.224	5824	tags=34%, list=10%, signal=38%
RELA_DN.V1_DN	130	-0.5106599	-1.502233	0	0.010917531	0.233	6327	tags=32%, list=11%, signal=36%
SNF5_DN.V1_DN	156	-0.505419	-1.5021679	0.003174603	0.010553614	0.233	4278	tags=31%, list=8%, signal=33%
IL15_UP.V1_DN	172	-0.4874963	-1.4768474	0.001639344	0.014126416	0.3	4935	tags=26%, list=9%, signal=29%
IL21_UP.V1_DN	172	-0.48531935	-1.4578557	0.004942339	0.018886749	0.397	8422	tags=35%, list=15%, signal=42%
CTIP_DN.V1_UP	130	-0.4980072	-1.4321824	0.003350084	0.025314162	0.505	6327	tags=25%, list=11%, signal=29%
KRAS.LUNG_UP.V1_DN	136	-0.48795864	-1.4268856	0.00174216	0.02614274	0.524	6526	tags=33%, list=12%, signal=37%
PRC1_BMI_UP.V1_DN	177	-0.46813366	-1.4235611	0.00331675	0.026448129	0.537	8339	tags=40%, list=15%, signal=46%
KRAS.600.LUNG.BREAST_UP.V1_DN	274	-0.4455334	-1.4080275	0.001545595	0.032223556	0.609	6536	tags=30%, list=12%, signal=34%
PIGF_UP.V1_UP	187	-0.4598211	-1.4061472	0.009771987	0.03257395	0.622	8646	tags=36%, list=15%, signal=42%
KRAS.LUNG.BREAST_UP.V1_DN	136	-0.47849157	-1.4030654	0.010327023	0.033116005	0.635	6499	tags=34%, list=12%, signal=38%
PKCA_DN.V1_UP	166	-0.4687581	-1.3980176	0.00487013	0.03395229	0.657	7992	tags=39%, list=14%, signal=45%
PRC2_EZH2_UP.V1_DN	183	-0.4541471	-1.3906862	0.003378379	0.036799826	0.695	6425	tags=43%, list=11%, signal=48%
VEGF_A_UP.V1_UP	189	-0.45748687	-1.3872037	0.007898894	0.03729289	0.714	6768	tags=34%, list=12%, signal=39%
EGFR_UP.V1_UP	185	-0.4549511	-1.3788	0.003284072	0.040864076	0.762	7308	tags=45%, list=13%, signal=52%
MEK_UP.V1_UP	188	-0.45373976	-1.378503	0.011217949	0.0401403	0.763	5729	tags=34%, list=10%, signal=38%
PTEN_DN.V2_UP	136	-0.46210852	-1.3765156	0.015463918	0.040344935	0.773	4212	tags=30%, list=7%, signal=33%
ESC_J1_UP_EARLY.V1_UP	168	-0.45925367	-1.3724189	0.006493507	0.041627586	0.781	7031	tags=39%, list=12%, signal=45%
MTOR_UP.V1_DN	178	-0.45521936	-1.3679518	0.011627907	0.043126527	0.796	7705	tags=37%, list=14%, signal=43%
KRAS.50_UP.V1_UP	47	-0.5499441	-1.365234	0.04920914	0.043695517	0.806	6035	tags=43%, list=11%, signal=48%
CAHOY_NEURONAL	95	-0.4838539	-1.3634824	0.021922428	0.043876994	0.815	5980	tags=37%, list=11%, signal=41%
ALK_DN.V1_UP	137	-0.46332282	-1.3590385	0.016920473	0.045335766	0.828	8093	tags=38%, list=14%, signal=44%
MYC_UP.V1_DN	157	-0.4463858	-1.3410349	0.012965964	0.055599816	0.894	6881	tags=34%, list=12%, signal=38%
SIRNA_EIF4GI_UP	91	-0.4781993	-1.3376204	0.04042179	0.057057574	0.91	7772	tags=40%, list=14%, signal=46%
TGFB_UP.V1_DN	183	-0.43953583	-1.3299516	0.014218009	0.06085203	0.928	5341	tags=29%, list=9%, signal=32%
RAF_UP.V1_UP	187	-0.43491796	-1.3236665	0.017271157	0.064317055	0.943	6708	tags=39%, list=12%, signal=44%
AKT_UP.V1_UP	163	-0.4465274	-1.3232546	0.010256411	0.0634152	0.943	5341	tags=29%, list=9%, signal=32%
PRC2_SUZ12_UP.V1_DN	178	-0.43630323	-1.3204952	0.01584786	0.06416449	0.946	7343	tags=33%, list=13%, signal=38%
EIF4E_DN	97	-0.47950608	-1.3200814	0.03691275	0.06344434	0.947	7612	tags=37%, list=14%, signal=43%
ESC_V6.5_UP_EARLY.V1_DN	171	-0.43647343	-1.3151157	0.011382114	0.06571491	0.959	6383	tags=36%, list=11%, signal=41%
JNK_DN.V1_UP	182	-0.43130216	-1.3147677	0.01618123	0.06481554	0.959	6822	tags=31%, list=12%, signal=36%
KRAS.BREAST_UP.V1_DN	138	-0.4474425	-1.3136595	0.031719532	0.06449671	0.961	6421	tags=30%, list=11%, signal=34%
GCNP_SHH_UP_EARLY.V1_DN	164	-0.43535474	-1.3025784	0.032312926	0.072718576	0.974	6259	tags=29%, list=11%, signal=32%
LTE2_UP.V1_UP	180	-0.4305646	-1.3000975	0.014925373	0.07323898	0.976	6681	tags=33%, list=12%, signal=38%
BCAT_BILD_ET_AL_UP	44	-0.5213563	-1.2990202	0.07509158	0.07285976	0.977	6584	tags=39%, list=12%, signal=44%
CYCLIN_D1_KE_.V1_UP	188	-0.42368215	-1.2925098	0.031719532	0.0770856	0.985	7522	tags=35%, list=13%, signal=40%
KRAS.600_UP.V1_DN	275	-0.40660927	-1.2846336	0.009188362	0.08312739	0.988	6570	tags=27%, list=12%, signal=30%
ATM_DN.V1_DN	145	-0.43178657	-1.2720134	0.0539629	0.0936025	0.992	4076	tags=21%, list=7%, signal=23%
MEK_UP.V1_DN	187	-0.4179306	-1.2624791	0.034941763	0.10203829	0.996	8636	tags=37%, list=15%, signal=44%
AKT_UP_MTOR_DN.V1_UP	174	-0.41666472	-1.2565967	0.04399323	0.10667876	0.996	5768	tags=28%, list=10%, signal=31%
GCNP_SHH_UP_LATE.V1_DN	178	-0.4182879	-1.2528129	0.046357617	0.109699294	0.997	8615	tags=38%, list=15%, signal=44%
YAP1_DN	42	-0.50460243	-1.2466412	0.11588785	0.11543524	0.999	5806	tags=33%, list=10%, signal=37%
AKT_UP_MTOR_DN.V1_DN	177	-0.40857023	-1.2437973	0.0539629	0.11731986	0.999	6792	tags=32%, list=12%, signal=36%

CYCLIN_D1_UP.V1_UP	184	-0.40996936	-1.2426367	0.041467305	0.11701133	0.999	7729	tags=32%, list=14%, signal=37%
KRAS.600_UP.V1_UP	267	-0.39482123	-1.2404662	0.031722054	0.11752298	0.999	5107	tags=25%, list=9%, signal=28%
RAF_UP.V1_DN	186	-0.40824127	-1.2385556	0.04639175	0.11826252	0.999	7391	tags=34%, list=13%, signal=39%
RAPA_EARLY_UP.V1_DN	188	-0.4034595	-1.229752	0.05409836	0.12861106	1	8071	tags=40%, list=14%, signal=47%
SNF5_DN.V1_UP	167	-0.4062797	-1.2276385	0.053658538	0.12961918	1	6971	tags=34%, list=12%, signal=39%
ESC_V6.5_UP_EARLY.V1_UP	164	-0.4069866	-1.2189118	0.07559055	0.14075077	1	7791	tags=38%, list=14%, signal=44%
BCAT_GDS748_UP	48	-0.49227807	-1.2180996	0.13186814	0.14029224	1	3250	tags=33%, list=6%, signal=35%
KRAS.KIDNEY_UP.V1_DN	132	-0.41603586	-1.215755	0.08280255	0.14170973	1	6043	tags=24%, list=11%, signal=27%
RAPA_EARLY_UP.V1_UP	170	-0.40015364	-1.2105435	0.06259542	0.14767988	1	8281	tags=32%, list=15%, signal=38%
IL21_UP.V1_UP	179	-0.39640853	-1.1967514	0.07096774	0.16624704	1	5944	tags=30%, list=11%, signal=34%
DCA_UP.V1_DN	172	-0.39655963	-1.1931783	0.08674304	0.16995634	1	8647	tags=34%, list=15%, signal=40%
P53_DN.V2_DN	144	-0.39602318	-1.1818166	0.094527364	0.18789166	1	4017	tags=22%, list=7%, signal=24%
TBK1.DF_UP	274	-0.3752914	-1.1801769	0.0748503	0.1880153	1	6836	tags=35%, list=12%, signal=39%
PTEN_DN.V1_UP	178	-0.39142367	-1.1790795	0.09737249	0.18758051	1	7096	tags=30%, list=13%, signal=34%
CAHOY_ASTROCYTIC	98	-0.4201239	-1.1784772	0.13416816	0.18634637	1	5631	tags=32%, list=10%, signal=35%
GLI1_UP.V1_DN	25	-0.5265167	-1.1754428	0.19855596	0.18937056	1	11987	tags=68%, list=21%, signal=86%
WNT_UP.V1_UP	174	-0.3880947	-1.1652383	0.10981697	0.20461807	1	5463	tags=22%, list=10%, signal=25%
RB_P107_DN.V1_DN	124	-0.40116835	-1.1642183	0.13879599	0.20420375	1	8647	tags=39%, list=15%, signal=46%
KRAS.300_UP.V1_UP	137	-0.4008654	-1.1640077	0.13565217	0.20229357	1	4934	tags=28%, list=9%, signal=30%
CRX_NRL_DN.V1_DN	121	-0.39857513	-1.1579727	0.14262295	0.21177538	1	5320	tags=29%, list=9%, signal=32%
KRAS.DF.V1_DN	188	-0.3757507	-1.1439826	0.14379086	0.23671098	1	5254	tags=24%, list=9%, signal=26%
RB_DN.V1_DN	120	-0.39151672	-1.1425174	0.16440678	0.23713848	1	6315	tags=32%, list=11%, signal=36%
ATM_DN.V1_UP	142	-0.38630423	-1.139042	0.1826923	0.24180397	1	8213	tags=35%, list=15%, signal=41%
BRCA1_DN.V1_UP	130	-0.39138877	-1.1367528	0.17478992	0.2443973	1	6046	tags=18%, list=11%, signal=20%
BCAT.100_UP.V1_DN	39	-0.46870634	-1.1356789	0.2410072	0.24386278	1	5586	tags=23%, list=10%, signal=26%
ESC_J1_UP_EARLY.V1_DN	172	-0.37756443	-1.1302017	0.17462933	0.25283358	1	6792	tags=30%, list=12%, signal=34%
TBK1.DF_DN	271	-0.354238	-1.110956	0.16850394	0.29304767	1	8807	tags=34%, list=16%, signal=40%
KRAS.PROSTATE_UP.V1_DN	140	-0.37569675	-1.107071	0.20921986	0.29909995	1	6090	tags=26%, list=11%, signal=29%
KRAS.AMP.LUNG_UP.V1_UP	134	-0.3755756	-1.1046449	0.22222222	0.30164874	1	11014	tags=37%, list=20%, signal=46%
SINGH_KRAS_DEPENDENCY_SIGNATURE_	20	-0.5250638	-1.1036365	0.31690142	0.3010787	1	5035	tags=30%, list=9%, signal=33%
KRAS.300_UP.V1_DN	136	-0.37628254	-1.1031575	0.22824302	0.29914707	1	8854	tags=34%, list=16%, signal=40%
KRAS.LUNG_UP.V1_UP	134	-0.37086076	-1.0970467	0.22704507	0.31044355	1	4833	tags=18%, list=9%, signal=20%
DCA_UP.V1_UP	177	-0.36171275	-1.0921688	0.24203822	0.3186584	1	7648	tags=28%, list=14%, signal=32%
KRAS.BREAST_UP.V1_UP	135	-0.37284163	-1.0911309	0.2594417	0.31776333	1	6327	tags=27%, list=11%, signal=30%
BCAT.100_UP.V1_UP	48	-0.43644738	-1.0902193	0.28623852	0.31710854	1	5236	tags=31%, list=9%, signal=34%
IL2_UP.V1_UP	181	-0.3569956	-1.0815799	0.252443	0.33586597	1	7391	tags=31%, list=13%, signal=36%
PKCA_DN.V1_DN	160	-0.3623502	-1.0806458	0.26554623	0.33467913	1	7471	tags=27%, list=13%, signal=31%
PTEN_DN.V1_DN	174	-0.35588032	-1.0788217	0.24088748	0.33641726	1	6236	tags=26%, list=11%, signal=29%
MTOR_UP.N4.V1_UP	190	-0.352475	-1.0739225	0.2651391	0.3454366	1	6703	tags=30%, list=12%, signal=34%
NOTCH_DN.V1_DN	177	-0.35606456	-1.0691338	0.277865	0.35474998	1	3906	tags=22%, list=7%, signal=24%
E2F3_UP.V1_DN	139	-0.35568857	-1.0588322	0.312187	0.3780714	1	6324	tags=23%, list=11%, signal=26%
KRAS.DF.V1_UP	184	-0.3455789	-1.0588236	0.30819672	0.37473845	1	7505	tags=35%, list=13%, signal=41%
CYCLIN_D1_KE_.V1_DN	187	-0.34854963	-1.0541956	0.30769232	0.3834846	1	5989	tags=25%, list=11%, signal=27%
CAMP_UP.V1_DN	194	-0.33900616	-1.038234	0.31726283	0.42363483	1	7150	tags=30%, list=13%, signal=34%
CAHOY_OLIGODENDROCUTIC	90	-0.36661395	-1.0233443	0.375	0.46248755	1	5278	tags=28%, list=9%, signal=31%
ESC_V6.5_UP_LATE.V1_DN	177	-0.34053668	-1.0189543	0.4130809	0.47102657	1	4010	tags=21%, list=7%, signal=23%
NOTCH_DN.V1_UP	177	-0.33687726	-1.0186822	0.40097404	0.46767175	1	5873	tags=24%, list=10%, signal=26%
RELA_DN.V1_UP	147	-0.34391066	-1.0186015	0.3993232	0.46389627	1	7564	tags=27%, list=13%, signal=31%
KRAS.600.LUNG.BREAST_UP.V1_UP	274	-0.31640318	-1.0032834	0.43317232	0.5042312	1	6527	tags=24%, list=12%, signal=27%
TBK1.DN.48HRS_UP	50	-0.39224413	-1.0005885	0.45137614	0.50812435	1	7006	tags=34%, list=12%, signal=39%
CYCLIN_D1_UP.V1_DN	186	-0.32892182	-0.9993821	0.45033112	0.50747675	1	5255	tags=23%, list=9%, signal=25%
NRL_DN.V1_UP	131	-0.3396588	-0.9910634	0.45890412	0.52836514	1	3957	tags=19%, list=7%, signal=20%
ATF2_UP.V1_UP	186	-0.3272957	-0.98880756	0.47460318	0.5308636	1	7359	tags=28%, list=13%, signal=33%
CRX_DN.V1_UP	131	-0.33606824	-0.98316747	0.48681897	0.5439377	1	7597	tags=27%, list=13%, signal=32%
PIGF_UP.V1_DN	185	-0.32482016	-0.9805442	0.5109375	0.54723155	1	6518	tags=27%, list=12%, signal=30%
SRC_UP.V1_UP	158	-0.32862654	-0.98052436	0.50161815	0.542925	1	7056	tags=27%, list=13%, signal=31%
KRAS.PROSTATE_UP.V1_UP	131	-0.33539593	-0.9757101	0.5147059	0.5532125	1	5782	tags=26%, list=10%, signal=29%
PDGF_UP.V1_UP	142	-0.32810605	-0.9740319	0.5074135	0.5537849	1	8728	tags=34%, list=15%, signal=40%
PDGF_ERK_DN.V1_DN	144	-0.32522762	-0.95591176	0.5565217	0.6048704	1	8609	tags=34%, list=15%, signal=40%
CAMP_UP.V1_UP	192	-0.31045902	-0.94301784	0.5972222	0.64022213	1	8887	tags=35%, list=16%, signal=42%
PTEN_DN.V2_DN	132	-0.31941798	-0.9429997	0.61435723	0.63538134	1	6248	tags=24%, list=11%, signal=27%
CRX_NRL_DN.V1_UP	134	-0.3177159	-0.9251622	0.66883117	0.68720186	1	7718	tags=27%, list=14%, signal=31%
JAK2_DN.V1_DN	129	-0.31307027	-0.9120055	0.6923077	0.7234041	1	4312	tags=20%, list=8%, signal=22%
EIF4E_UP	92	-0.31982827	-0.89133775	0.7325175	0.78107285	1	6048	tags=21%, list=11%, signal=23%
YAP1_UP	43	-0.35468942	-0.8805186	0.687389	0.8077706	1	7557	tags=33%, list=13%, signal=38%
KRAS.50_UP.V1_DN	45	-0.35012364	-0.8783998	0.6666667	0.80817103	1	12197	tags=42%, list=22%, signal=54%
ALK_DN.V1_DN	132	-0.30028018	-0.8743522	0.77759475	0.81399626	1	9043	tags=32%, list=16%, signal=38%
GLI1_UP.V1_UP	25	-0.32332292	-0.72717	0.9073084	0.9948409	1	6973	tags=28%, list=12%, signal=32%

ACKNOWLEDGEMENTS

This path could never have been possible without the support and help of many people, so listing all of them would make another book as long as the thesis itself. Anyway, I would try to make it shorter. And of course, thanks Tim Berners-lee for the World Wide Web!

Esta historia no habría sido posible sin cada uno de vosotros.

1. SCIENCE

1.1. CIC bioGUNE

First of all, I want to thank the director of this thesis, **Ashwin,** because this thesis has been based in your brilliant ideas, that could make me think in more experiments and scientific projects for the future. With your desire to try new experiments and the newest protocols you discovered, I have grown like a scientist, thank you very much for believing in me. I would always be grateful to have had the possibility to work in many different projects learning more every day and making me more passion for the science.

Quiero agradecer también, a **Jesús Barbero y José María Mato** por haberme dado esta oportunidad de empezar como pequeña científica y poder acabar con esta tesis doctoral en CIC bioGUNE, gracias de corazón.

Gracias a **Malu y a todo su laboratorio (Gotxi, Vir, David, Teresa, Fer…)**, por enseñarme tanto. Aquí es donde empecé mi andadura y donde tanto aprendí. Cómo tú bien dices, Malu, yo crecí en ese laboratorio. Gracias por todos tus consejos y por ser una de las brillantes científicas que no dejaré de admirar nunca.

Me gustaría dar las gracias a **Juan Anguita**, porque sin tus queridas *Borrelia* esto no hubiera empezado. Estoy agradecida por haber podido tenerte como lab neighbour. Siempre me has ayudado con lo que he necesitado, gracias.

Arkaitz Carracedo, eskerrak eman nahi dizkizut beti entzuteko prest egon zarelako, zure iritzia emanez eta, zure jakinduria transmititzeagatik, erreferentzi gisa hartuko zaitut beti.

Sandra Blanco, gracias por estar dispuesta a enseñarme, a colaborar, a querer saber y transmitirme esas ganas por ir al extranjero, gracias a ti tuve la oportunidad de conocer a una gran investigadora de Cambridge y siempre te estaré agradecida.

José María Falcon, quiero darte las gracias por haber podido aconsejarme sobre este mundo de exosomas, que tan desconocido era para mí. **Felix**, **Espe**, eskerrik asko, por ayudarme y darme vuestra opinión siempre que lo he necesitado. **Ariane**, eskerrik asko zuri ere por introducirme en el mundo de los exosomas.

Itziar Gil, Bego y Carla, gracias por estar siempre ayudándonos en todo lo que podáis.

1.2. UPV/EHU

José Luis Zugaza, gracias por ser mi maestro y compañero. Gracias por enseñar tanto a todo el que quiera aprender, y estar siempre dispuesto a ayudar y escuchar. De ti aprendí antes de empezar esta etapa, en estos 4 años y, sé que seguiré haciéndolo siempre.

Tengo que agradecer también a **Pedro Grandes,** tutor de esta tesis**,** por dejarnos su laboratorio y microtomo cada vez que lo necesitábamos, y como no, a mi maestro en esto del microscopio electrónico y el mundo del sistema nerviosos central **Svein**, porque, ¿mejor persona puede haber?, siempre dispuesto a ayudar y enseñar.

1.3. EUSKO JAURLARITZA, BOEHRINGER INGELHEIM & EMBO

Eusko Jaurlaritzari eskertzea gustatuko litzaidake, emandako dirulaguntzagatik, abentura hau astea posible egin izan baituen.

I cannot be more delighted and grateful to have had the opportunity to go to work in a foreign country because of **Boehringer Ingelheim** travel grant, really amazing and unforgettable experience! It was really a unique opportunity that without this Boehringer Ingelheim grant I could not have visited the host laboratory of Randy Schekman Nobel laureate in Berkeley, University of California.

Although finally, I could not have time to benefit from **EMBO** travel grant in order to visit **Dr. Ragnhildur Thora Karadottir** Lab in Cambridge, I remember exactly when I received the acceptance notification as if it was yesterday. It was one of the happiest moments in my life, that It will remain with me forever.

1.4. UC BERKELEY

Randy Schekman, thank you for all your help and knowledge, for giving me the opportunity to go to your lab, because without your permission I couldn't never had this working experience in an outstanding lab as yours; **Bob and Stephanie** thanks, for all your support in everything regarding paperwork and lab material, without your help I wouldn't have had my visa for USA Ps. Bob continue learning Spanish and Basque:) **Morayma**, I think you already know how much I have learned with you, you are the future Nobel laureate! I remember the first week I arrived to the lab you were so busy but you took some time to explain me exosomes isolation protocol, thank you; **Patrick**, **Xioman** and **Justin**, thank you for being always ready to help me. **Arup**, even if you are not a real Schekmanity :), I am so grateful to have had the opportunity to work with primary skin cells and learned about this amazing world, trying to explain exosomes function between fibroblast and keratinocytes communication. **All the other lab members**, I am grateful to have worked with you, thanks.

1.5. UNIVERSIDAD DE LEÓN

Vega y Elsa, porque empezó siendo un proyecto, pero ahora me llevo conmigo a dos grandes personas. Estaré encantada siempre de trabajar con vosotras y volver a León para compartir ideas con vinos y raciones por medio.

1.6. BIOCRUCES

Paco, uno de los mejores directores de tesis que he conocido en estos 4 años, no solo como investigador, sino como profesor. Siempre queriendo formar y preocupándose por sus estudiantes, un ejemplo a seguir. Eskerrik asko, por haberme ayudo siempre que lo he necesitado.

1.7. UNIVERSITY OF CAMBRIDGE

Dr. Ragnhildur Thora Karadottir, I am really grateful for believing in me to share and continue your projects, thanks again for giving me the opportunity to go to your lab in Cambridge to enjoy learning about the marvelous central nervous system world. We need to fight against demyelinating neuropathies!

2. FAMILIA

Ama, mila esker egunero zure bizitza neregatik ematen baituzu, hainbeste ikasi dut zuregandik! Eskerrik asko esperimentuen arazoak entzuten aspertu arren, hor egoteagatik, Schwann zelulen arazoak behin eta berriz entzuten.

Papi, **Tati**, **Fran**, sense vosaltres rés d'això hauria sigut possible, començant per l'interès per la ciència que meu donat inconscientment, per les ganes que em vau donar per aprendre**,** moltes gracies per creure en la ciència. **Papi,** tant de bo pugui demanar una beca, potser pugui compartir projectes amb el teu laboratori en un futur proper, per que allà he crescut, i es on vaig aprendrà que amb constància y dedicació (i una mica de positivisme amb un mateix) es poden complir els teus somnis.

Oier, egunero lezio bat ikasten dudalako zurekin, nik eta inguratzen zaituen guztiek. Bakoitzak bizitza bere erara koloreztatu dezakeela erakustsi didazulako, zure gogoekin, iraukortasunarekin edonora iritsiko zarelako.

Agur, familiaren parte zarelako, eskerrik asko beti laguntzeaz prest egoteagatik, beti!

3. THE BIG FAMILY, FRIENDS

Mención especial a **mis amigos**, que puedo llamar **mi gran familia,** siempre haciéndome sentir tan especial, TODOS y cada uno de ellos. Vosotros habéis sido parte de esta tesis:

Ashguitos (Ashwitos: Señora madre, Vermouth friend, **Adri el agobiado** & **La Cierva**) porque mejor equipo no me puedo llevar, cada uno fundamental para que el equipo funcione, porque con vosotros el equipo siempre gana. Ojalá pudiera llevaros conmigo en la siguiente etapa y siempre fuerais vosotros mi equipo, haceis que trabajar sea una fiesta. **Encarni**, esto no hubiera sido posible sin ti, no puedo estar más contenta por haber compartido tantos años mano con mano, codo con codo, eskerrik asko. **Miguel**, porque ahora mis momentos favoritos vermoutheros son compartidos contigo, ¡gracias por ser como eres! **Laura**, ¿por qué no pediste la Juan de la Cierva antes? Pero, agradecida de poder haber compartido estos últimos momentos más intensos y de tus consejos sabios. **Adri,** desde el minuto 1 que te conocí parecía que te conocía de hace 28 años y siempre has estado cuando lo he necesitado, por todo lo compartido fuera del ámbito laboral, no puedo estar más agradecida a esta tesis, a CIC bioGUNE…por haberte conocido.

Anguitos, alegráis todos los días el laboratorio y yo diría que el centro. Seguir tal y como sois que de vosotros deberíamos aprender. **H**, padre de Evaristo, me llevo todas y cada una de las conversaciones que he tenido contigo, no he conocido persona con mayor interés de aprender. Y, por supuesto, pieza fundamental de parte de este proyecto. **Leti**, porque allá donde vaya siempre tendré en cuenta tus consejos, gracias por estar siempre dispuesta a escuchar. Ana, porque con tu ayuda ¡pude superar al súper confocal! **Nico**, porque aquí te conocí y parte de este proyecto empezó contigo. Sé que puedo contar con un amigo en León☺. **Jul** "The Future Nobel Prize", quizá me tengas que acoger en tu futuro laboratorio, y lo harías con los brazos abiertos, beti egin duzun bezala, eskerrik zaren bezalako izateagatik.

La pandi del frontenis (**Isk**, **Lau**, **Tere**, **Llavero** & **Juan**) porque todo menos frontenis…comer, beber y el rollo de siempre…No, con vosotros nada es igual, siempre es diferente, y hacéis que todos los días científicos sean divertidos. **Lau,** siempre dispuesta a ayudarme, creo que la única persona que me puede ganar en positivismo, gracias por transmitir esa felicidad y alegría, tanto como **Juan**. **Isk,** aunque demasiado cursi para ti, pero no dejaré que te alejes nunca, quiero seguir compartiendo momentos por siempre. **Llavero**, por estar siempre, desde el inicio de esta etapa. Gracias a las afortunadas que acabaron esta andadura mucho antes **Esti y Vir**, por haber podido compartir los últimos años de esta tesis con vosotras.

Aitor, afortunada de haber conocido a una de las personas más felices de este planeta, gracias por querer sacar sonrisas a los tuyos e intentar que estén felices, lo consigues ☺.

Vosotras chicas bellas, **Urra** y **Santa**, ¿que hubieran sido mis tardes de laboratorio sin vosotras? Gracias por todos los momentos, comidas y cenas que hemos compartido, eskerrik asko politak!

Nuria, gracias por estar siempre ahí, y por ser tan paciente, gracias por las comilonas y charlitas, largas....

Onin, ¿cómo se puede coger tanto cariño en tan poco tiempo? Otro descubrimiento de la tesis que espero que esté presente en un futuro allá donde vaya.

Lei, porque aquí estamos, ¡Consiguiéndolo! Por apoyarnos mutuamente, eskerrik asko, por comprendernos y poder compartir contigo la subida a la cumbre de la montaña.

No puedo estar más agradecida de haber empezado esta aventura con las mejores personas que podía haber tenido, gracias **Pau**, **Lu**, **Justy**, **Lau y por supuesto Marta txiki**, que hubiera hecho sin tu apoyo, gracias por hacer que fuerais tan incondicionales para mí.

Donostiako betikoengatik, hitzak soberan daudelako, urteak pasa ahala beti hor zaudete eta, urteak pasa izango ez balira bezala. **Sari,** eskerrik asko bizitza guztian zehar (2 urte genituenetik) ondoan egoteagatik.

Jowi "FlowJo", beharrezkoa zara neretzat, badakizu, eta etapa guzti hontan ondoan izan zaitut beti, eskerrik asko. Seguirás siendo parte del resto de mi aventura aunque la siguiente andadura sea lejos, sé que nos tendremos cerca. **Mari**, juntas en y por la ciencia, todovía recuerdo ese experimento a las dos de la mañana que nos demostró que nunca nos rendimos, nunca! Empezamos en esto juntas y así terminamos esta etapa, amiga. **Nere**, mejor descubrimiento de estos años, zer zorionekoa naizen zu nere bizitzaren parte izateaz; **Lore**, ¿por qué has aparecido tan tarde en mi vida? Bertan nahi zaitut beti. Eta, nola ez, **Haizea**, zoriontsu zu ezagutzeaz tesiko lehen urteetan, eta eskiatzeko asteburua bezain zeregin gehiago elkar egiteaz nago esperoan. Alaitasun horrrekin jarraitu ezazu beti.

Nando y **Sonia**, descubrimientos que me ha dado Bilbo. Gracias por los momentos vividos a lo largo de esta tesis.

Berkeley people, **who are you**? (only you would understand this, Unai, Juanma, Xabi, Pepiño traveler, Dani, Paolo, mi chino favorito, Garreth…) thank you, because all of you guys, make me happy in 9000 km away from my home, you make me strong as scientist and as a person and I learned with all of you every day. You are part of one of the best experiences of my life.

Isa, más gente como tú por favor. Sé que no haría falta repetir lo que tantas veces nos hemos dicho, pero, que quede constancia oye. Porque en tan poco tiempo hemos vivido más cosas juntas que en muchos años con mucha gente, me has conocido en todos los aspectos, mejor que nadie en menos tiempo que nadie, gracias por existir en mi vida y desde ¡ya! parte de ella por siempre.

Ko, porque cada día lo haces más bonito. Tengo que dar gracias a la última etapa de mi tesis, que hizo que descubriera a un sardo por el mundo. Dónde los otros solo ven palabras, tú ves mundo. Para nosotros, el mundo desconocido, que quizá sea más grande que el mundo conocido. *Buona notte fiorellino.*

Gracias por hacer que pueda compartir mi vida con todos vosotros. Por ello, quiero resaltar momentos que me llevo en mi corazón y que siempre viajarán conmigo allá donde vaya.

Acknowledgements

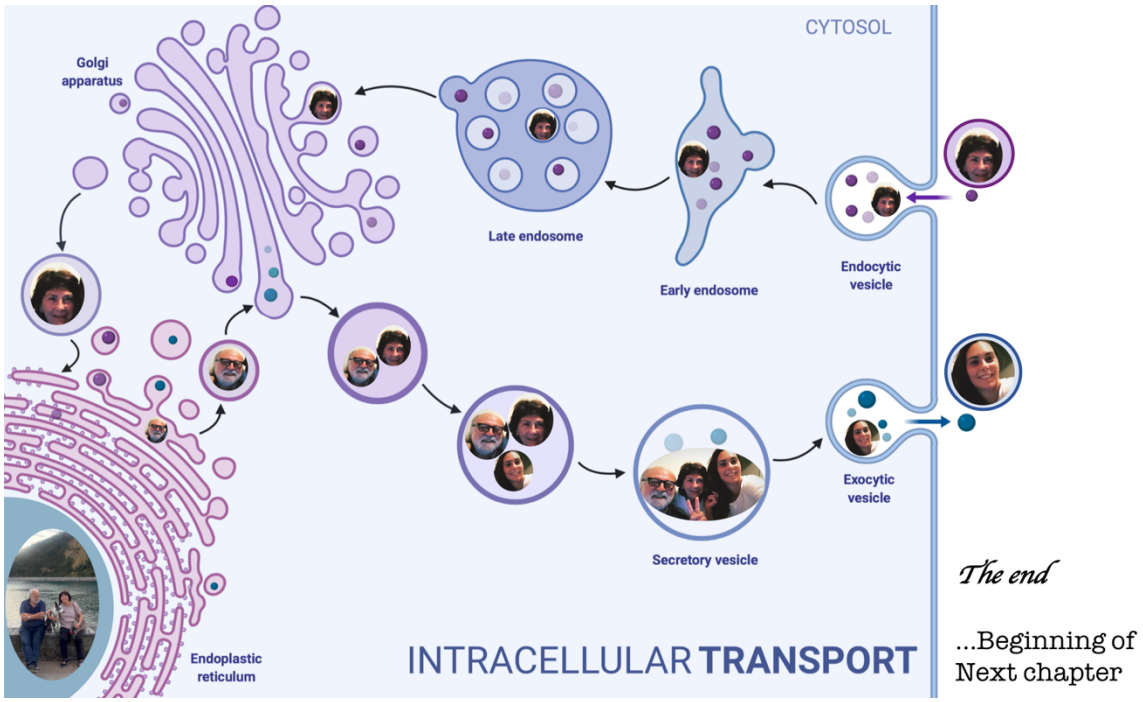

En ciencia, además de intentar conocer lo desconocido y salvar vidas, nos lo pasamos bien, ¿por qué no hacer MÁS CIENCIA?

In Science, in addition to try to know what is unknown and solve lives, we enjoy it, so why do not we do MORE SCIENCE?